

THE STRUCTURE OF VELOCITY AND DENSITY INTERFACES
IN A WEAKLY TURBULENT STRATIFIED SHEAR FLOW

BY

GREGORY M. POWELL

A DISSERTATION PRESENTED TO THE GRADUATE COUNCIL OF
THE UNIVERSITY OF FLORIDA
IN PARTIAL FULFILLMENT OF THE REQUIREMENTS FOR THE
DEGREE OF DOCTOR OF PHILOSOPHY

UNIVERSITY OF FLORIDA

1980

UNIVERSITY OF FLORIDA



3 1262 08552 3172

to my parents

ACKNOWLEDGEMENTS

Many people have contributed their time and efforts toward the completion of this study. In particular the author would like to express his gratitude to Dr. D. Max Sheppard for his continuous support and guidance. The encouragement and contributions of Dr. Y. H. Wang are also greatly appreciated. Special thanks go to Ivan Chou for his assistance in carrying out the experiments and for the many hours spent discussing key aspects of this study.

Thanks also go to Vernon Sparkman and the Coastal Engineering Laboratory staff for their assistance with equipment for these experiments. The author wishes to thank Katherine Williams for her efforts in typing the final manuscript and Rhonda Rogers, Rena Herb, Pat McGhee, Kathy Fariello, Sue Green and Cathy Nell who contributed to the typing of this manuscript in its early stages. Additional thanks go to Lillean Pieter who drafted the figures for this study.

Finally, the author wishes to thank his wife Carol for her love, support and patience.

This work was supported by the Fluid Mechanics Branch of the Mathematical and Information Sciences Division of the Office of Naval Research under Contract N00014-68-A-0173-0016.

TABLE OF CONTENTS

	PAGE
ACKNOWLEDGEMENTS	iii
LIST OF FIGURES	vi
LIST OF SYMBOLS	viii
ABSTRACT	xi
CHAPTER	
I INTRODUCTION	1
Motivation	1
Two-Layer Flows	3
A Regime Concept For Two-Layer Flows	5
Scope of This Investigation	7
II BACKGROUND DISCUSSION	9
Introduction	9
Laminar Flow	10
Stability of Stratified Shear Flows	11
Turbulent Entrainment Across Density Interfaces	14
Dynamic Structure of Stratified Mixing Layer	17
Dimensional Analysis	19
Governing Equations	21
III EXPERIMENTAL APPARATUS AND PROCEDURE	25
Facilities	25

	PAGE
Instrumentation	28
Data Acquisition Procedure	32
Data Reduction Procedure	34
IV RESULTS	48
Introduction	48
Density Structure	49
Mean Velocity	52
The Richardson Number	54
Shear Stress Profiles	55
Energy Spectra	57
V CONCLUSIONS	83
APPENDICES	
A PROFILE SHAPING ELEMENT	89
B INDIVIDUAL DENSITY PROFILES	92
C THE ERROR IN ASSUMING $D\rho/Dt = 0$	173
D ENERGY SPECTRA	177
E VERTICAL SHEAR STRESS PROFILE	196
BIBLIOGRAPHY	208
BIOGRAPHICAL SKETCH	212

LIST OF FIGURES

<u>Figure</u>	<u>Page</u>
1 THE EFFECT OF VERTICAL LENGTH SCALES ON THE RICHARDSON NUMBER PROFILE	24
2 SCHEMATIC DRAWING OF THE OVERALL FACILITY	39
3 CROSS-SECTIONAL VIEW OF THE TEST SECTION	40
4 UPSTREAM END OF TEST SECTION	41
5 DOWNSTREAM END OF TEST SECTION	42
6 BLACK BOX SCHEMATIC OF THE INSTRUMENTATION	43
7 SCHEMATIC OF THERMISTOR ELECTRONICS	44
8 CALIBRATION CURVE FOR THERMISTER	44
9 CROSS-SECTION OF CONDUCTIVITY PROBE	45
10 SCHEMATIC OF CONDUCTIVITY PROBE ELECTRONICS	45
11 CALIBRATION CURVE FOR CONDUCTIVITY PROBE	46
12 CONDUCTIVITY VOLTAGE VS. TEMPERATURE	46
13 HOT FILM CALIBRATION CURVES	47
14 EXPERIMENTS AND GLOBAL PARAMETERS	59
15 EXPERIMENTS AND MEASURED QUANTITIES	60
16 NONDIMENSIONAL DENSITY PROFILE 12/6/78	61
17 DIMENSIONLESS VAISALA FREQUENCY PROFILE 12/6/78	62
18 NONDIMENSIONAL DENSITY PROFILE 10/13/78	63
19 DIMENSIONLESS VAISALA FREQUENCY PROFILE 10/13/78	64
20 NONDIMENSIONAL DENSITY PROFILE 7/24/78	65

<u>Figure</u>	<u>Page</u>
21 DIMENSIONLESS VAISALA FREQUENCY PROFILE 7/24/78	66
22 NONDIMENSIONAL DENSITY PROFILE 10/19/77	67
23 DIMENSIONLESS VAISALA FREQUENCY PROFILE 10/19/77	68
24 NONDIMENSIONAL DENSITY PROFILE 7/6/76	69
25 DIMENSIONLESS VAISALA FREQUENCY PROFILE 7/6/76	70
26 INTERFACIAL THICKNESS VS. KEULEGAN NUMBER	71
27 NORMALIZED MEAN VELOCITY PROFILE - GROUP 1	72
28 NORMALIZED MEAN VELOCITY PROFILE - GROUP 2	73
29 MEAN VELOCITY PROFILE COMPARISON	74
30 MEAN VELOCITY PROFILE, LOG-NORMAL PLOT	75
31 NORMALIZED SHEAR STRESS PROFILE - GROUP 1	76
32 NORMALIZED SHEAR STRESS PROFILE - GROUP 2	77
33 COMPUTED SHEAR STRESS PROFILES - GROUP 1	78
34 INTERFACIAL FRICTION FACTOR VS. REYNOLDS NUMBER	79
35 VISCOUS SHEAR STRESS/TOTAL STRESS - GROUP 1	80
36 VISCOUS SHEAR STRESS/TOTAL STRESS - GROUP 2	81
37 VISCOUS SHEAR STRESS/TOTAL STRESS - COMPARISON	82

LIST OF SYMBOLS

Symbol	Definition
D	Distance from the bottom of the tank to the density interface or the depth of a channel
D_e	Equivalent pipe diameter = $4R_h$
∇	Distance from bottom of the tank to the freesurface
δ	Thickness of the density interface
δ_u	Velocity boundary layer thickness
f and f^*	Undefined or experimentally defined functions
f_i	Interfacial friction factor
f_o	Sidewall friction factor
g	Acceleration of gravity
g'	Reduced gravity = $g\Delta\rho/\rho_\ell$
γ_s	Molecular diffusion coefficient for salt in water
H	Depth of the upper layer
K	Keulegan number
k	Molecular coefficient of diffusion (heat)
κ	Von Karman's constant
ℓ	Turbulent integral length scale
ℓ_b	Buoyancy length scale
ℓ_v	Viscous length scale
λ	Kolmogorov turbulent microscale
μ	Dynamic viscosity

Symbol	Definition
N	Brunt-Vaisala frequency
NMAX	Maximum Vaisala frequency
N*	Nondimensional Vaisala frequency - N/NMAX
ν	Kinematic viscosity
ν_e	Csanady's (1978) effective viscosity
P	Pressure
P_o	Time averaged pressure
P'	Fluctuating pressure
Pe	Peclet number based on turbulent length scale
Re	Reynolds number
Re_t	Reynolds number based on turbulent velocity and length scale
Ri	Richardson number
Ri_g	Gradient Richardson number $\equiv \frac{-g(\partial\rho/\partial\xi)}{\rho(\partial U/\partial\xi)^2}$
R_h	Hydraulic radius
ρ	Fluid density
ρ_u	Density of upper layer
ρ_ℓ	Density of lower layer
ρ'	Fluctuating density
ρ_o	Time averaged density
$\Delta\rho$	Change in density across interface = $\rho_\ell - \rho_u$
ρ^*	Nondimensional density excess = $(\rho - \rho_u)/\Delta\rho$
S	Salinity (mass of salt/unit volume)
T	Temperature
t	Time
τ_i	Interfacial shear stress

Symbol	Definition
τ_v	Viscous shear stress
τ_T	Total shear stress (viscous and Reynolds)
Θ	Keulegan stability parameter
U	Time average velocity (x-direction)
\bar{U}	Free stream velocity ($\xi > 15$ cm)
U_e	Erosion velocity
U_*	Friction velocity
U_l	Turbulent velocity scale
u'	Fluctuating velocity (x-direction)
V	Time average velocity (y-direction)
v'	Fluctuating velocity (y-direction)
W	Time average transverse velocity (z-direction) or half the width of the tank
w'	Fluctuating velocity (z-direction)
x	Coordinate axis - direction of primary flow
y	Coordinate axis - vertical direction
z	Coordinate axis - transverse direction to flow
ξ	Vertical coordinate fixed to density interface
ξ^+	Nondimensional vertical coordinate fixed to density interface ($\xi^+ = \xi/\delta$)
ξ^*	Nondimensional vertical coordinate fixed to velocity interface ($\xi^* = (\xi - \eta)/\delta_u$)
η	Vertical distance between velocity and density interface
Φ	Viscous dissipation function

Abstract of Dissertation Presented to the Graduate Council
of the University of Florida in Partial Fulfillment
of the Requirements for the Degree
of Doctor of Philosophy

THE STRUCTURE OF VELOCITY AND DENSITY INTERFACES
IN A WEAKLY TURBULENT STRATIFIED SHEAR FLOW

By

GREGORY M. POWELL

JUNE 1980

Chairman: Dr. Knox Millsaps
Cochairman: Dr. D. M. Sheppard
Major Department: Engineering Sciences

Most natural fluid bodies, the ocean, the atmosphere, many lakes and most estuaries, exhibit inherent stratification. Recently, with the rapid development of coastal and offshore resources and with the recognition of environmental quality as a fundamental consideration, stratified flows have taken on a new importance for engineers and hydrologists.

In this dissertation, the mixing region between two parallel and homogeneous streams of fluid having different densities and velocities is investigated experimentally. The flow is produced in a flume with a test section 24.38 m long, 1.22 m high and 0.61 m wide by pumping the upper 0.61 m deep layer in a closed circuit. The density of each layer is controlled by the addition of sodium chloride in such a manner that the lower layer is about 2.5 percent denser than the upper layer.

Tests are conducted at two downstream locations and at several velocities between 2.7 cm/sec and 7.8 cm/sec. The mean velocity and the fluctuating velocity components are measured with hot film anemometers while the density structure is measured with a high resolution conductivity probe. Profiles of mean velocity, viscous stress, and Reynolds stress are obtained through the mixing region. Energy spectra of the fluctuating velocity components are also obtained at several points within the region and under several flow conditions.

Over the range of conditions investigated, the interface moves about and distorts a small amount in a temporally and spatially random fashion. However, it is always distinct and readily identifiable; there are no large convoluting motions of the interface. The velocity structure is similar in some ways to flow over a smooth rigid surface.

The results show that for the conditions investigated the interfacial boundary layer is marginally stable. When a well-developed turbulent boundary layer exists above the interface, the Richardson number at the inflection point in the velocity profile is of order one or less.

CHAPTER I

INTRODUCTION

Motivation

Studies of stratified¹ flows are, with few exceptions, motivated by two important facts. First, most natural fluid bodies are, to some extent, stratified. The ocean, the atmosphere, many lakes, and most estuaries exhibit inherent stratification; ostensibly, stratification is the rule, not the exception. Secondly, when effluents are discharged into the water or air there is generally a difference in density between the effluent and the receiving fluid; this produces a stratified flow.

Most aspects of oceanic and atmospheric circulation are intimately tied to the density structure of the fluid. For this reason, the dynamics of stratified flows have, for many years, been important to meteorologists and oceanographers. More recently, with the rapid

¹ Stratification denotes a layered structure. There may be a finite number of distinct layers in which case the system is referred to as an "N-layer" system. In the limit, the fluid may have an infinite number of infinitely thin layers in which case the term "continuously stratified" might be used. The property differentiating between layers can in general be any property of the fluid. However, in this paper, "stratified" will imply density stratification, since the density is the ultimate factor affecting the dynamics of the flow. The density variations can, in turn, result from temperature variations and/or variations in dissolved or suspended constituents. Nothing has been said regarding the orientation or extent of the layers with respect to other layers or the gravitational field; in this paper, the term is used loosely to imply a nonhomogeneous density structure.

development of coastal and offshore resources and with the recognition of environmental quality as a fundamental consideration, the subject has taken on a new importance for engineers and hydrologists.

Many of the world's large population centers are located on coastlines near estuaries or on lakes. These centers depend on their neighboring hydraulic systems for transportation, food, waste disposal, recreation, and a multitude of other societal requisites. Many times these requirements are mutually exclusive when the system is improperly managed. The cornerstone of proper management is an accurate and reliable model of the flow within the lake, estuary, or coastal zone. Nevertheless, many mathematical models used today are unable to accurately describe the flows when stratification is present. In some models, this is due to the use of vertically averaged equations of motion. These equations cannot account for changes in flow direction or speed within the fluid column. However, even those models that attempt to account for stratification by employing a multi-layer approach suffer from an incomplete knowledge concerning the transport of mass, momentum, and energy between layers in a stratified fluid. Consequently, the mathematical models available today require extensive calibration and may be unreliable if significant variations are made from the calibration condition. If the dynamics of natural fluid systems are to be understood, modeled effectively and reliably, the effect of stratification must be understood.

The consequences of stratification are generally three-fold:

1. The mean flow pattern is altered by the redistribution of inertia and pressure.

2. Turbulent energy is enhanced or decreased, depending on the nature of the stratification. This, in turn, alters the transfer of mass, momentum, and energy.
3. Stratification allows for the existence of gravity waves internal to the fluid. These internal waves are capable of transmitting energy and momentum across large distances with little mixing or dissipation of energy.

Any one or all three of the above can have a profound effect on the dynamics of the fluid system. For an extensive discussion of the many phenomena associated with stratified fluids, the reader is referred to Turner (1973), Phillips (1969), and Yih (1965). These books all have lengthy bibliographies for further reference.

With the increasing impact man exerts upon nature and therefore himself comes the need to better understand the dynamics of natural fluid systems and the effects of density stratification.

Two-Layer Flows

Many studies of stratified flows, including this one, are concerned with various aspects of two-layer flows. This type of flow, which is characterized by the presence of two thick layers of nearly homogeneous fluid separated by a thin transition region in which the density changes abruptly, continues to receive considerable attention for a number of important reasons.

The first and most basic reason is the geometric simplicity of the flow. As with all investigations of complicated phenomena, stratified flows must first be broken down into basic structural units;

when these units are understood, more complicated phenomena can be considered.

Secondly, and perhaps more important in terms of the engineering application, the two-layer flow closely represents many natural and man-made occurrences. For example, salt-wedge and fjord-type estuaries often exhibit a density structure which is closely modeled as a two-layer flow. Additionally, when heated water or effluents from industrial processes are discharged into the environment the resulting flow many times approximates a two-layer flow, the dynamics being controlled in large part by the processes taking place at the interface. Finally, the formation and evolutionary development of the oceanic thermocline and the atmospheric inversion are strongly dependent on the mixing process at the thermocline or inversion. These phenomena are often modeled as two-layer stratified flows. This is, of course, a limited list of the possible occurrences; many other examples exist.

A third reason for studying two-layer flows, which has far-reaching implications for the study of continuously stratified fluids, is the observance of step-like density structures in many continuously stratified flows. Using high resolution instruments to document the fine scale structure of continuously stratified fluids, several investigators have found that in many natural fluid bodies the vertical density and velocity profiles are not smoothly varying, as was originally expected, but are step-like in appearance. Thick layers of nearly homogeneous fluid are separated by thin transition regions in which the velocity and density change abruptly.¹ In the ocean this

¹The term "fine structure" is sometimes used in the literature when referring to this type of stratification.

structure has been documented by Woods (1968), Woods and Wiley (1972), and Osborne and Cox (1972). Woods referred to the nearly homogeneous regions as "layers" and the high gradient regions as "sheets."¹ This fine structure has also been observed numerous times in the atmosphere; see, for example, Browning (1971), Browning and Watkins (1970), and Emmanuel (1973). The step-like structure has even been observed in the fluff layer of a tidal channel where stratification is a consequence of fine suspended sediments.² It is increasingly apparent that this density structure is a widespread phenomenon, and the formation depending little, if at all, on the stratifying agent. This step-like density structure might possibly be modeled as the superposition of many two-layer flows.

A Regime Concept for Two-Layer Flows

In fluid mechanics, the concept of regimes is a useful tool for describing or defining the characteristics of a flow. For example, flows are often described as falling within the compressible or incompressible, laminar or turbulent regimes. In the study of two-layer stratified shear flows, a differentiation can be made on the basis of interfacial dynamics. Observations reported by numerous investigators Thorpe (1968), Koop (1976), Kantha (1975), and Browand and Wang (1972), to mention just a few, reveal that interfacial instabilities can produce two distinctly different modes of interfacial mixing.

¹In this paper the high gradient region may be alternatively referred to as the interfacial region.

²Seminar presented at the University of Florida by Dr. W. R. Parker of the Institute of Oceanographic Sciences, November 18, 1977.

First, under conditions of high shear and/or low static stability, large vortical structures, known as Kelvin-Helmholtz billows, form at the interface. These large coherent structures produce an overturning of the density interface, entraining fluid from the upper and lower layers into the vortex spiral. Many studies, beginning with Helmholtz (1868) and Kelvin (1871) and continuing to the present, have dealt with various aspects of this instability. Recent experimental studies in both liquids and gases--Thorpe (1973, 1969), Roshko (1976), Koop (1976), Browand and Winant (1973), Browand and Wang (1972), Scotti and Corcos (1969)--have greatly increased the understanding of the initiation, growth, and decay of this type of instability. Some of these papers have excellent photographic plates showing the Kelvin-Helmholtz billow. The correlation between experiment and theory strongly substantiates the idea that these structures are the result of inviscid instabilities. In this regime, the interface, in an unbounded flow, diffuses rapidly with time and/or space until at some point it again becomes stable.

The second regime exists when the shear is small and/or the static stability is large. In this case the mixing seems to result from the breaking of small wavelets which develop a sharp cusp-like shape at the crest and/or trough, ejecting fluid from one layer into the other. The interface in this regime, unlike the first regime, remains distinct and easily identifiable. The mixing process, in this case, more closely approximates turbulent entrainment than diffusion. The origin and nature of the motions which produce this mode of mixing are not as well understood as those which produce the Kelvin-Helmholtz billow. They might be the end result of viscous or inviscid instabilities which can

originate at the interface or at a distant location. Benjamin (1963) has identified three types of instabilities which can arise in the region of a flexible boundary. His results indicate that viscous instabilities of the Tollmein-Schlichting type can arise before the Kelvin-Helmholtz instability. Browand and Wang (1973), however, have proposed that the two different types of mixing result from two different modes of an inviscid instability.

Thus, because of the dissimilarities between the two modes of mixing and the fundamental questions which still remain, it is useful at this time to study and model the two regimes separately. Eventually, as more data are obtained, it may be possible to consider the two regimes¹ through one comprehensive model.

Scope of This Investigation

The intent of this dissertation is to document experimentally, as accurately as possible, the density and velocity structure of the interfacial region in a weakly turbulent stratified shear flow. Previous investigations, many of which are discussed in Chapter II, have either provided qualitative descriptions of the mixing process, documented interlayer transfer rates for mass momentum and energy or established stability parameters for transition from laminar to turbulent flow. Few have accurately measured the density and velocity structure in the transition region between the layers. This study documents the time averaged mean density and velocity profiles, the turbulent and viscous shear stress profiles and the turbulent energy spectra through the

¹In this paper, when the terms "regime one" or "regime two" are used alone, the reference will be to the conditions described above.

interfacial region of a weakly turbulent (regime 2) stratified shear flow. The intent is to provide accurate baseline data needed to establish sound theories describing the entrainment of fluid from one layer to another or the shear stress at the interface between fluids with different densities and velocities. These two generic problems form the basis for more specific problems such as the dynamics of salt-wedge and fjord-type estuaries, the development and evolution of the oceanic thermocline and the dynamics of atmospheric inversions.

In Chapter II, many papers published to date are categorized and several important results from these studies are briefly discussed. Chapter III describes the facilities, instrumentation, and procedures used to obtain the data presented in Chapter IV. The last chapter discusses the conclusions reached from this study and makes recommendations regarding future work in this area.

CHAPTER II

BACKGROUND DISCUSSION

Introduction

Numerous articles on the dynamics of flow near a density interface have been published in a wide variety of journals. Generally, these studies fall into one of three categories: (1) studies of laminar flow, (2) investigations into the dynamic stability of two-layer stratified shear flows, and (3) studies concerned with the turbulent transfer of mass, momentum, and energy across a density interface. This last group can be further divided on the basis of where the turbulent energy originates. Sometimes mixing is induced by a turbulent energy source located far from the density interface. This situation is usually characterized by the absence of mean flow vorticity in the region of the interface. Other times the transfer results from the production of turbulent energy at the interface. In this case, a mean velocity gradient is required at the interface in order to maintain production of turbulence. Still other times both energy sources are present. This is the most common condition found in nature; however, it is also the most complicated.

Studies of laminar flow and hydrodynamic stability are based on firmly established and highly developed mathematical theories. The theory of turbulent flow, however, has not yet been developed to the point where complex flows can be predicted from basic equations.

Investigations of turbulent flow, therefore, must rely on experimental observation augmented by less well developed mathematical models.

Although there is no direct link between linear stability theory and fully developed turbulent flow, much insight into the origin of turbulent motions can be obtained by examining the results of linear stability theory. This is the primary reason for including, in this chapter, the brief discussion on stability.

Laminar Flow

Keulegan (1944) and Lock (1951) analyzed the laminar boundary layer between two streams of fluid with differing density and viscosity. The fluids were assumed to be incompressible, nondiffusive and immiscible, such that the density and viscosity were discontinuous across the interface. They used the standard boundary layer assumptions and solved for the velocity in each layer by matching the solutions at the interface. As one would expect, their solutions show that the boundary layer grows with the square root of the downstream distance, the constant of proportionality depending on the viscosity in the respective layer. The exact shape of the velocity profile is dependent on the product of the density and viscosity ratios. Since the requirement of laminar flow is seldom realized, studies of this type have limited direct practical application toward problems in engineering and geophysics. They are important, however, since they supply the basic mean flow required for stability analysis, and they form a limiting case upon which to build more applicable models.

Stability of Stratified Shear Flows

Helmholtz (1868) and Kelvin (1871), interested in the generation of water waves by wind, were the first to investigate analytically the stability of stratified shear flows. Their studies examined the case where the density and velocity are discontinuous at the interface and uniform within each layer (the stratified vortex sheet). Later, Taylor (1931), Goldstein (1931), and Holmboe (1962), to list some of the more widely quoted examples, analyzed piecewise linear velocity and density profiles. Holmboe (1962) and Miles (1961, 1963) extended the analysis to include hyperbolic tangent velocity and density profiles. For a lengthy discussion on the stability of parallel inviscid flows the reader is referred to the review article by Drazin and Howard (1966).

Two important general observations grow out of these analytic solutions. The first is Miles' $1/4$ Theorem: if the gradient Richardson number is everywhere greater than $1/4$, the flow will be stable. This is only a sufficient condition for stability; it states nothing about when the flow will become unstable or if stability will persist below $1/4$. The second observation is more qualitative in nature. The point at which the flow becomes unstable and the nature of the instability depend strongly on the details of the velocity and density structure or, alternatively, the Richardson number profile. This second point is reinforced by the results from experimental studies of two-layer stratified flows. Figure 1 shows two hypothetical velocity and density profiles and their respective Richardson number profiles. Although the total change in velocity and density is the same for both cases, the shapes of the Richardson number profiles are radically different. This difference results solely from the diversities of the vertical length scales.

Thorpe (1969, 1973), Scotti and Corcos (1969), and Delisi and Corcos (1973) investigated experimentally the stability of flows where the gradient Richardson number is a minimum at the interface (see Figure 1). They found that Miles Theorem held and that Kelvin-Helmholtz billows formed when the interface became unstable. The investigations of Browand and Wang (1972) and Wang (1975), however, reveal a much different stability boundary in the Richardson number--wave number plane. It should be noted that in these experiments the viscous boundary layer was much thicker than the diffusion layer. Under these conditions, the profile of the gradient Richardson number will exhibit a local, or possibly an absolute, maximum at the interface (see Figure 1). Koop (1976), using the same facility as Wang (1975), demonstrated that two distinctly different modes of instability form at the interface, depending on the initial conditions. These two instabilities correlate well with the results of Hazel's numerical study (1972) and the analytic study of Holmboe (1962). The character of the interfacial disturbance created by these two instabilities corresponds, at least qualitatively, to the two regimes discussed in Chapter I.

To this point, only inviscid stability theory has been discussed; the effects of viscosity need to be considered. Maslowe and Thompson (1971) and Gage (1973) numerically analyzed the stability of stratified shear flows, including the effects of both viscosity and heat conduction. Their results support the idea that viscosity has a stabilizing influence. It should be noted, however, that the velocity and density profiles that were used again led to a Richardson number profile with a minimum at the interface.

Benjamin (1963) investigated the stability of a flexible boundary in an inviscid flow, and extended his results to the case of an inviscid fluid flowing over a viscous fluid. His model assumed a uniform density in both the upper and lower layers, with a Blasius velocity profile in the upper layer and zero flow below the interface. The Richardson number profile under these assumptions is undefined at and below the interface. This model, nevertheless, closely approximates many actual laboratory and geophysical flows. When the density difference is large, as with air over water, Benjamin's results show that the Kelvin-Helmholtz (K-H) instability will be the dominant instability. However, when the density difference is small, Tollmien-Schlichting (T-S) instabilities can arise at half the velocity required for a K-H instability. Since the T-S instability requires energy dissipation to grow, viscosity must be considered a destabilizing factor under certain conditions. To date, no one to the author's knowledge has examined analytically or numerically the stability of an unbounded viscous stratified shear flow where the Richardson number profile has a maximum at the interface. It may be that under this condition, viscosity is a destabilizing factor, and T-S instabilities can arise before K-H instabilities. This could explain the two regimes discussed in Chapter I: regime one is undoubtedly the result of K-H instabilities; regime two might be the result of T-S instabilities. As Benjamin (1963) demonstrates, the K-H instability extracts energy from the mean flow at a much higher rate than the T-S instability; therefore, if the K-H instability exists, it will dominate.

Keulegan (1949) experimentally investigated the stability of a two-layer viscous stratified flow. Using an approach which paralleled

Jeffreys' theory (1926) for the generation of water waves, Keulegan derived a stability parameter,¹

$$\theta = \frac{(\nu g \Delta\rho/\rho)^{1/3}}{U},$$

where ν is the viscosity, g the gravitational acceleration, ρ the fluid density, $\Delta\rho$ the density difference across the interface, and U the velocity of the upper layer. His experimental data showed that the critical value for the generation of interfacial wavelets is:

$$\begin{aligned}\theta &= 0.127, \text{ Re} < 450 \\ \theta &= 0.178, \text{ Re} > 450\end{aligned}$$

where Re is the Reynolds number based on the hydraulic radius of the flume. The instabilities observed by Keulegan had regime two characteristics.

Turbulent Entrainment Across Density Interfaces

Many investigators, beginning with Rouse and Dodu (1955) and Cromwell (1960), have studied, using oscillating grid tanks, the problem of turbulent mass transport across density interfaces. Within these tanks, turbulent motions are generated above and/or below a stable density interface by oscillating a grid of rigid bars. This experimental apparatus makes the measurement of entrainment rates relatively simple; however, since no mean velocity is present, measurement of turbulent properties is difficult. Hopfinger and Toly (1976) were able, nevertheless, to measure the turbulent fluctuations using a hot-film anemometer mounted on a rotating arm. Their results show that the

¹This parameter is sometimes referred to as the Keulegan number (K) where $K = \theta^3$.

turbulent structure is closely tied to the amplitude and frequency of oscillation and to the geometry of the grid. The turbulent energy is concentrated in frequency bands close to the grid oscillation frequency and harmonics of this frequency. Dispersion of the turbulent energy to wider frequency bands is slow in this type of facility since there is no mean velocity shear, and therefore only limited vortex stretching. Turbulent motions produced in this manner can generate standing waves at the interface which grow and break due to partial resonance with the oscillator.

Despite these drawbacks some significant findings have resulted from these experiments. Linden (1975) found that the rate of increase in the potential energy of the fluid column is proportional to the rate at which turbulent energy is supplied to the interfacial region. There is no simple relationship, however, between the rate of change of potential energy and the energy input at the grid. He also found that as much as half the energy supplied to the interface could be radiated away by internal waves if the Vaisala frequency below the interface is not zero.

Turner (1968) and Crapper and Linden (1974) studied the effect of molecular diffusivity on the mixing rate. They found, for low turbulent Reynolds numbers,

$$Re_t \equiv \frac{U_1 \ell}{\nu} < 50 \quad ,$$

that the mechanics of the mixing process and the rate of mixing were dependent on the turbulent Peclet number:

$$Pe \equiv \frac{U_1 \ell}{k} \quad ,$$

where U_1 , is a turbulent velocity scale, λ is a turbulent length scale, k the coefficient of molecular diffusivity, and ν the kinematic viscosity. When $Pe < 200$, the interface has a diffusive core and the thickness of the interface depends on the value of Peclet number. When $Pe > 200$, there is no dependence on Peclet number; the turbulent eddies completely penetrate the interface, and molecular diffusion across the interface is insignificant. Turner (1968) also found when Peclet number is large (the case when salt is used as a stratifying agent) that:

$$\frac{U_e}{U_1} \propto Ri^{-3/2}, \quad Ri \equiv \frac{g\Delta\rho\lambda}{\rho_u U_1^2},$$

where U_e is the entrainment velocity and the Richardson number is based on U_1 , and λ .

Ellison and Turner (1959), Kato and Phillips (1969), and Moore and Long (1971) have investigated the problems of turbulent entrainment across a density interface in the presence of a mean velocity shear. Their results support the relationship:

$$\frac{U_e}{U_1} \propto Ri^{-1}.$$

The discrepancy between the above two power laws has been the source of much debate [see Long (1975)]. It is not clear which expression is correct or if, as Long (1975) argues, the difference is due to the presence of a mean velocity shear. It is clear, however, that, in general,

$$\frac{U_e}{U_1} = f(Ri, Pe, Re) \text{ and}$$

that only when Reynolds number and Peclet numbers are large is

$$\frac{U_e}{U_1} = f(Ri) \quad .$$

Dynamic Structure of a Stratified Mixing Layer

To date, there is no model for the turbulent stratified half-jet or mixing layer that is valid over a wide range of Richardson numbers. There are, however, two limiting cases that have been studied and modeled extensively. First, as the Richardson number approaches zero, the homogenous turbulent half-jet results. At the other extreme, the Richardson number approaches infinity and the static stability of the interface becomes so large that the interface acts much like a solid plate. The flow of air over water is an example of this extreme case. The turbulent structures exhibited by these two limiting flows are vastly different. For example, the eddy viscosity is almost constant near the center of the homogeneous half-jet, while at a rigid plate the eddy viscosity approaches the fluid viscosity. When a turbulent stratified two-layer flow is in regime one, its dynamic structure is more closely approximated by the homogeneous half-jet than flow over a flat plate; however, when in regime two the situation is reversed. This dissertation is concerned with the dynamic structure of a regime two stratified mixing layer. Therefore, the many aspects of a regime one mixing layer will not be discussed. Readers interested in this type of flow are referred to Roshko (1976) and Brown and Roshko (1974).

Lofquist (1960) made extensive measurements of velocity and density through the interfacial region of a regime two stratified flow. Because hot film anemometers were in their infancy at the time his

work was done, Lofquist was able to directly measure only the pressure gradient and the mean velocity and density profiles. The interfacial shear stress was calculated using the equations of motion in conjunction with the above measurements. All of Lofquist's experiments reveal a velocity structure that closely resembles the flow over a flat plate.

Csanady (1978) demonstrated, using Lofquist's (1960) data, that a "Law of the Wall" could be formulated for density interfaces. The "Law of the Interface," however, differs from the traditional "Law of the Wall" in that it depends on two parameters, Reynolds number and Keulegan number. Csanady chose to formulate the "Law of the Interface" as,

$$\frac{U(z)}{U_*} = \frac{1}{\kappa} \ln\left(\frac{zU_*}{\nu_e(K)}\right) + B(K),$$

where U_* is the interfacial friction velocity, κ the Von Karman constant, z the vertical coordinate, and ν_e an effective viscosity defined by,

$$\nu_e = \frac{U_*^2}{\left. \frac{dU}{dz} \right|_{\text{interface}}}.$$

$B(K)$ and $\nu_e(K)$ are constants which depend on the turbulent Keulegan number defined by,

$$K \equiv \frac{\Delta \rho g \nu}{\rho U_*^3},$$

where ν is the kinematic viscosity, $\Delta \rho$ the density difference across the interface, and ρ the fluid density.

Dimensional Analysis

In this section, a functional form of the velocity profile in the region of a density interface is developed from dimensional reasoning. The approach parallels the classical analysis of turbulent flow over a rigid surface, except that the roughness length used in the analysis of a rigid surface is replaced by a buoyancy length scale.

Under the Boussinesq approximation, and assuming the velocity profile in the region of the density interface is only a function of the fluid properties, the shear stress at the interface, gravity and the vertical coordinate, the following holds:

$$U = f(\rho_\ell, \mu, g', U_\star, \xi)$$

where:

ρ_ℓ is the fluid density of the lower layer;

μ is the fluid viscosity (assumed to be equal in upper and lower layers);

g' is the reduced gravity = $g\Delta\rho/\rho_\ell$;

g is the acceleration of gravity;

$\Delta\rho$ is the density jump across the interface;

U_\star is the interfacial friction velocity = τ_i/ρ_ℓ ;

τ_i is the interfacial shear stress;

ξ is the vertical distance from the interface; and

U is the mean velocity.

The above independent variables (excluding ξ) can be combined to form two length scales: a viscous length scale,

$$\ell_v \equiv \frac{\mu}{\rho_\ell U_\star}$$

and a buoyancy length scale,

$$\ell_b = \frac{U_*^2}{g'}$$

A physical interpretation of the buoyancy length scale is as follows: ℓ_b is the vertical distance an inviscid particle of density ρ_ℓ would travel, in a medium of density $\rho_\ell - \Delta\rho$, if it was given an initial vertical velocity U_* . Therefore, if U_* is a measure of the turbulent velocity scales, ℓ_b is a measure of the vertical distortions of the interface caused by the turbulent motions within the flow.

Paralleling the approach used in the analysis of flow over a rigid surface, two alternative functional expressions for the mean velocity profile near a density interface are:

$$\frac{U(\xi)}{U_*} = f \left[\frac{\rho_\ell U_* \xi}{\mu}, \frac{g' \mu}{\rho_\ell U_*^3} \right]$$

and

$$\frac{U(\xi)}{U_*} = f^* \left[\frac{g' \xi}{U_*^2}, \frac{g' \mu}{\rho_\ell U_*^3} \right]$$

where

$\frac{g' \xi}{U_*^2}$ is a Richardson number,

$\frac{\rho_\ell U_* \xi}{\mu}$ is a Reynolds number,

and

$$\frac{g' \mu}{\rho_\ell U_*^3} = \frac{\ell_v}{\ell_b} = K \text{ is a Keulegan number.}$$

When $K \gg 1$, the viscous length scale dominates the buoyancy length scale. Therefore, the distortions of the density interface (the interfacial wavelets) will be deeply imbedded within a viscous sublayer

and should have little influence on the flow. Under this condition, the first functional expression would appear most appropriate. When $K \ll 1$, the distortions of the interface would be much larger than the viscous sublayer and would therefore dominate the flow. Under this condition, the second expression would appear most appropriate.

The results from Lofquist (1960) and from this study (Figure 30) indicate the existence of a region above the interface where the velocity profile has a logarithmic shape. It should therefore be possible to represent the velocity profile in this region by:

$$\frac{U(\xi)}{U_*} = A(K) \ln \left(\frac{\rho_\ell U_* \xi}{\mu} \right) + B(K), \quad K > 1.$$

In the case of flow over a rigid surface,

$$A(K) = 1/\kappa$$

where κ is Von Karman's constant, there is no reason to assume, in the case of flow over a density interface, that A is constant. The flux of mass through the interface could alter the turbulent structure and therefore the value of A .

The above expression is similar in form to the "Law of the Interface" given by Csanady (1978), except that Csanady assumed $A = 1/\kappa$ and replaced the fluid viscosity with an "equivalent viscosity." The author feels the above expression is a more physically meaningful form. The functions $A(K)$ and $B(K)$, as well as the range of ξ over which this expression holds, remain to be determined. Finally, it seems reasonable to assume that as K becomes large, $A(K) \Rightarrow 1/\kappa$.

Governing Equations

The governing equations for turbulent stratified flow are derived from the differential form of the continuity and Navier-Stokes equations

using Reynolds decomposition technique. Specific concern here is for two-layer flow in a rectangular channel where the mean velocity is nearly unidirectional. The x-axis is positive in the primary flow direction while the y-axis is positive upward and the z-axis is perpendicular to the x and y axes using a righthanded coordinate system.

If the flow is assumed to be nearly two dimensional and free of secondary currents then at the center of the tank ($z=0$), where the measurements presented in Chapter IV were made, the continuity equation is

$$\frac{\partial U}{\partial x} + \frac{\partial V}{\partial y} = 0 \quad 2.1$$

where U and V are the time averaged mean velocities in the x and y directions, respectively.

If the pressure throughout the fluid is assumed to be hydrostatic, the y-component momentum equation is simply the hydrostatic equation

$$\frac{\partial P_o}{\partial y} = -g \rho_o(x,y), \quad 2.2$$

where P_o and ρ_o are the time mean pressure and density, respectively, and g is the acceleration of gravity.

Finally, if third order correlations and correlations between velocity and density fluctuations are assumed small, then the mean advective accelerations, the horizontal pressure gradient, the side wall shear stress and the interfacial shear stress are the only significant terms in the x-component momentum equation. Furthermore, if ρ_o is approximately equal to ρ_u , the Boussinesq approximation holds and the x-component momentum equation is

$$\frac{\partial U^2}{\partial x} + \frac{\partial UV}{\partial y} = \frac{-1}{\rho_u} \frac{\partial P_o}{\partial x} + \frac{\partial \tau_{xy}}{\partial y} + \frac{\partial \tau_{xy}}{\partial z}, \quad 2.3$$

where

$$\tau_{xz} = -\overline{u'w'} + \frac{\mu}{\rho_u} \frac{\partial U}{\partial z} ,$$

is the shear stress maintained by the side walls and

$$\tau_{xy} = -\overline{u'v'} + \frac{\mu}{\rho_u} \frac{\partial U}{\partial y} ,$$

is the shear stress maintained by the interface.

Equation 2.3 can be further simplified if one assumes that the flow does not vary with distance downstream and the side wall stresses are insignificant. Under these conditions equation 2.3 becomes

$$\frac{1}{\rho_u} \frac{\partial P_o}{\partial x} = \frac{\partial \tau_{xy}}{\partial y} . \quad 2.4$$

Appendix E contains the full form of the governing equations and presents in detail the derivation of equations 2.1 through 2.4. In addition, a seven parameter expression for the shear stress profile at the center of the tank ($z=0$) is developed from equations 2.1 through 2.3 assuming a self-similar velocity and density profile. This expression for the shear stress will be discussed further in Chapter IV.

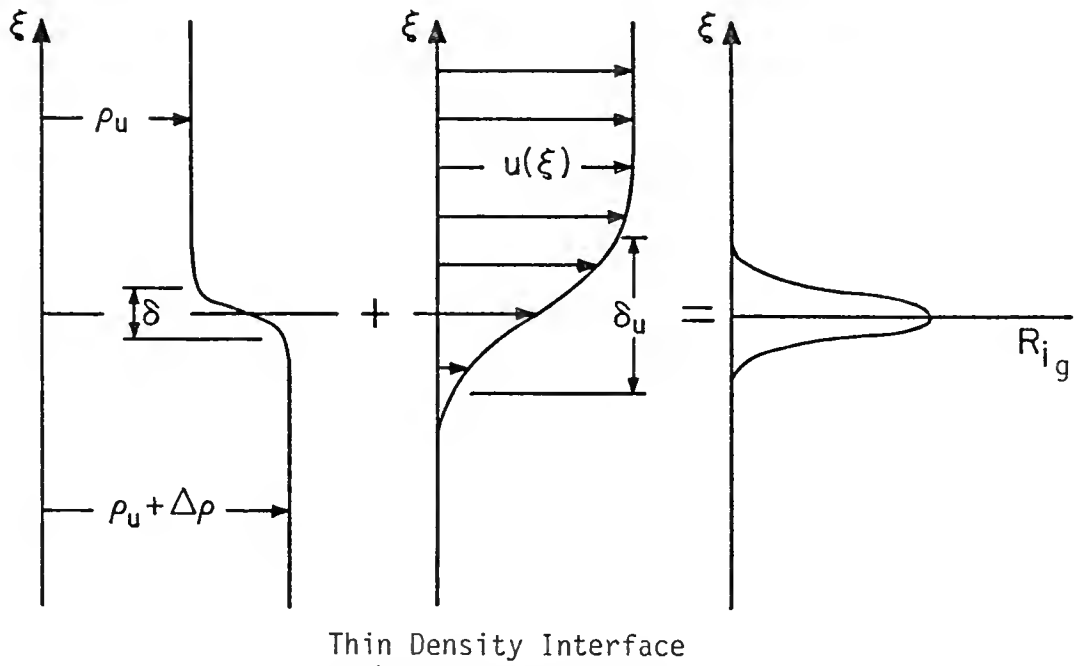
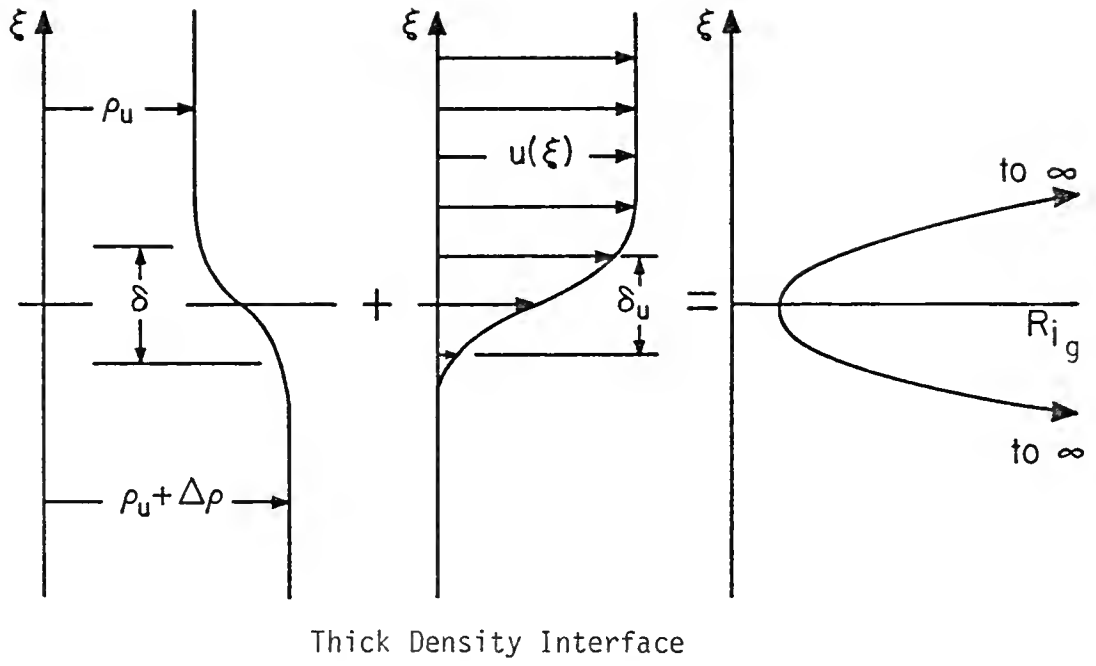


FIGURE 1: THE EFFECT OF VERTICAL LENGTH SCALES ON THE RICHARDSON NUMBER PROFILE

CHAPTER III

EXPERIMENTAL APPARATUS AND PROCEDURE

Facilities

The internal wave tank at the University of Florida's Coastal and Oceanographic Engineering Laboratory was used in this study. The tank was designed as a multi-purpose stratified flow facility; consequently, it had available many operational features which were not needed for this experiment. Only those aspects of the facility pertinent to the execution of this study will be discussed here. For a detailed description of all the capabilities of this tank, see Sheppard, Shemdin, and Wang (1973).

Figure 2, a schematic drawing of the overall facility, shows the locations of the main components. The test section is 24.38 meters long, 1.83 meters high, and 0.61 meter wide in the lower two-thirds of the tank, while the upper one-third is 0.91 meter in width. Figure 3 shows a cross-sectional view of the test section. In this study, the bottom one-third is filled with salt water, and the middle one-third with fresh water. The upper one-third of the tank is a wind tunnel designed for the generation of wind waves and wind-induced currents; it was not used during this experiment. The sides of the test section are constructed from one-half inch (1.27 cm) thick glass panels, allowing visual observation of phenomena from both sides of the tank.

The flow is produced by pumping the upper layer in a closed circuit. The pumping system consists of two centrifugal pumps connected in parallel. The 60 hp pump can produce, in the test section, velocities approximating 0.5 m/s. However, at low flow rates (velocities less than 8 cm/s) this pump heats the water excessively and is difficult to control. The second pump is only 5 hp but it can produce flows up to 8 cm/s; therefore, for low flow rates the small pump was used to minimize thermal stratification in the tank.

The saline solution is mixed before each experiment in one of two 4,000 gallon (15,140 liter) storage tanks; the fresh water is stored in the other. The saline solution is usually dyed with red food color, so that the interface between the fresh and salt water is easily identified. From the storage tanks the water is fed by gravity into the internal wave tank. The salt water enters the tank through a horizontal slot in the bottom; its inflow rate can be regulated from 0 to 5 gal/min (0.32 liter/sec) to an accuracy of ± 0.05 gal/min ($\pm .0032$ liter/sec) using a Fischer and Porter tapered tube flow meter. Fresh water from the city water supply can be continuously added to the upper layer through a tap in the 12 inch (30.48 cm) pipe which is located upstream of the pumps. The free surface level is maintained by the discharge of fresh water across a weir at the downstream end of the test section. This continuous exchange of fresh water forestalls any significant change in the upper layer density due to the entrainment of salt water across the density interface. The maximum fresh water inflow rate is limited to 12 gallons/min (0.76 liter/sec).

The entrance to the test section has been significantly modified for this experiment from that described by Sheppard et al. (1973). The new entrance section was designed with two criteria in mind: (1) to allow for a smooth transition in the flow where the fresh upper layer meets the lower salt layer, and (2) to produce a velocity profile which is straight, parallel, and as close as possible to the fully developed profile for flow in a rectangular channel. The intent of the second criterion is to minimize longitudinal variations in the velocity profile. Figure 4 shows the general layout of the entrance section. The profile shaping element is constructed from 880 pieces of 3/4-inch (1.91-cm) I.D. PVC pipe. Each tube is cut to a prescribed length based on its position within the tank cross-section. For details of the construction see Appendix A.

The transition plate, which is just downstream of the profile shaping element, is horizontal at their point of contact; the downward slope, as well as the curvature, increases with distance downstream. This design was employed to insure that the upper and lower layers meet smoothly and with no significant mixing, even though the vertical position of the interface may vary several centimeters due to set-up and entrainment. The end of the transition plate is always at least 25 cm below the interface.

The exit from the test section has also been modified for this study. Figure 5 shows the layout at the downstream end of the tank. This design minimizes saltwater entrainment and blockage close to the interface while separating the upper and lower layers. By rotating the splitter wedge about its pivotal point, the vertex of the wedge can be correspondingly adjusted to match long-term changes in the vertical

position of the interface. The vertically slotted weir, located 10 to 20 cm downstream of the wedge vertex, is designed to enhance turbulent mixing. This eliminates the build-up of a wedge of intermediate density water at the downstream end of the tank, thus reducing blockage effects near the interface.

Instrumentation

The instrument system for this investigation consists of six independent transducers, nine signal conditioners, a traverse mechanism, and an analog-to-digital (A/D) tape recorder. The output signal from each transducer is passed through one or more signal conditions and is sampled and recorded onto magnetic tape by the Kinematics Model DDS-1103 A/D tape recorder. Figure 6 shows the general arrangement of the instrument package.

The Kinematics A/D recorder can simultaneously sample up to 16 channels of data at any one of 75 predetermined sample rates between .05 and 1,000 samples/sec. The input voltage, which must be between -5.0v and +5.0v, is resolved into 4,096 discrete values. Consequently, the input resolution for this unit is limited to ± 0.0012 volts.

The traverse mechanism is driven by a variable speed electric motor which allows the speed to be continuously controlled between 0.02 cm/sec and 2.0 cm/sec. It can move, vertically, a total distance of 71.0 cm. The probes for transducers two through six, which measure temperature, conductivity, and velocity, are mounted at the end of the traverse support rod.

The first transducer, which indicates the vertical position of the traverse support rod, consists simply of a 10-turn, 10k-ohm

variable resistor in series with two fixed resistors; the potentiometer is attached to the gear drive of the traverse mechanism. The unit has a linearity of 0.05 percent over the range of the output voltage from -5.0v to ± 5.0 v. The signal from the position indicator goes to a low-pass filter with 20-Hz cutoff frequency. The output from the filter is then input to the Kinematics tape recorder. Since this voltage can be determined only to within ± 0.0012 volt by the A/D recorder, the resolution of the position indicator is limited to ± 0.085 mm.

The second transducer is a thermistor; its electronic schematic diagram is shown in Figure 7. The probe, Model SF2-42A68 manufactured by Victory Engineering Company, has a sensor only 1.5 mm in diameter and a time constant of 0.4 second in still water. The thermistor was calibrated against a mercury thermometer with a resolution of ± 0.05 degrees Fahrenheit. The thermistor resolution is assumed, therefore, to be the same. A typical calibration curve for this transducer is shown in Figure 8, and although the electronic circuit was designed to produce a linear output, a small degree of nonlinearity can be seen in the calibration curve. To compensate for this, the calibration points were fitted with a second order polynomial (three coefficients), using the method of least square error. The difference between any one of the calibration points and the curve fit value was always less than the resolution stated above. The output from the thermistor passes to a low-pass filter with a cutoff frequency of 20 Hz; the output from the filter is recorded by the A/D recorder.

The electrical conductivity of the fluid is measured by a third transducer. Knowing the conductivity and temperature, the density of the fluid can be determined. The conductivity probe, shown in

Figure 9, is constructed of acrylic plastic and has one stainless steel and one platinum electrode. When the probe is operating, the surrounding fluid is continuously drawn into the interior chamber through a 0.5 mm slit and a 0.3 mm diameter vertical hole at the bottom of the probe. The fluid exits through the plastic tube connecting the probe and the vacuum pump. The electrical current density between the electrodes is small except in the vertical hole, where it becomes very large. Thus, the resistance between the electrodes at any instant is governed by the conductivity of the fluid in the vertical hole, not by the resistance at the fluid-electrode interface. This reduces the effects caused by electrode contamination and plating. Figure 10 shows the electronic circuit diagram for the transducer. The horizontal slit in the probe is designed to enhance the selected withdrawal* of the surrounding fluid. For more on the characteristics of this unit see Sheppard and Doddington (1977).

The major advantage of this design over the so-called "single electrode" conductivity probe used by previous investigators is that the D.C. drift problem has been virtually eliminated while still maintaining the high vertical resolution needed for the study of density stratified fluids. There are, however, two important disadvantages. First, the time response for this probe is much slower than the single-point conductivity probe because the fluid must be physically drawn through the hole in the probe. Based on a comparison of temperature and conductivity time series data, a drop-off in the response curve is

*When a sink is placed in a stably stratified fluid, it tends to draw fluid only from its own level provided the velocity is not too large.

believed to occur at about 2 Hz. Second, the probe is physically larger than a single-point conductivity probe; therefore, its presence will alter the flow-field for a greater distance. In turn, this necessitates a greater spacing between the hot film probes and the conductivity probe. As a consequence of both the above, correlations between density and velocity fluctuations measured with this system are of limited significance.

A calibration curve of conductivity voltage versus density for a fluid temperature of 75.0 degrees Fahrenheit is shown in Figure 11, while Figure 12 shows the effect of temperature on conductivity voltage for two different levels of salt concentration. Using these two plots, the density can be determined to within $\pm 5.0 \times 10^{-5}$ gm/cc.

The output voltage from this transducer is again input to a low-pass filter with a 20-Hz cutoff frequency, and the output from the filter is again recorded on magnetic tape.

The last three transducers consist of three hot film sensors and their respective anemometers. The first two sensors are part of an x-type hot film probe, Thermo-Systems Model 1243-60w NaCl. This probe is used to measure both the mean velocity and the fluctuating components of velocity in the plane of the sensors. The third hot film, Model 1232w NaCl, is a wedge-type probe used only for mean velocity measurements. All three sensors use Thermo-Systems Model 1050 general purpose anemometers.

The output from each anemometer is first passed to a Thermo-Systems Model 1057 signal conditioner. This conditioner suppresses the excessive D.C. Voltage to make the signal compatible with the input requirements of the A/D recorder. From the conditioner, the

signal is sent to a low-pass filter with a cutoff frequency of 17 Hz and from there the signal goes to the A/D recorder where it is digitized and recorded onto magnetic tape.

The purpose of the low-pass filters is to prevent contamination of the signal by high frequency noise, specifically 60-cycle noise, which is picked up from the large pumps, electric motors, and other support equipment in the laboratory. The low-pass filters used with the position, temperature, and conductivity transducers are fourth-order Butterworth filters with the -3 db point at 20.2 Hz. At 10 Hz, the power loss through these filters is less than two percent. Sixth-order Butterworth filters are used with the hot film anemometers. The -3 db point for these filters is at 17.3 Hz, which assures that the power loss at 10 Hz is less than one percent. Spectral analysis of the velocity data indicates that for these experiments, negligible energy exists above 7 Hz; therefore, these low-pass filters have little or no effect on the true signal from their respective transducers.

Data Acquisition Procedure

Two different techniques were employed to obtain data during these experiments. The first is referred to as a constant speed traverse (CST), while the second is called a stepped traverse (ST).

The primary objective of the constant speed traverse was to obtain, in a quasi-instantaneous manner, the structure of the density transition region. This was accomplished by moving the probe package through the interface at a nearly constant speed between 0.5 mm/sec and 1.5 mm/sec. As the probes moved down, the position, conductivity, and thermistor voltages were each sampled and recorded at the rate of

25 Hz. Since the thickness of the interfacial region was about 1.5 cm, it took no more than 30 seconds to traverse the entire transition region. The second objective of the CST was to determine the position of the interface, defined as the point where the density equals the average density between the upper and lower layers. The position of the interface was then plotted as a function of time and all other measurements were referenced to the interface.

The stepped traverse was used to obtain information on the structure of the turbulent boundary layer in the region of the density interface. With this method the probes were placed at a pre-determined position and the time series data from the thermistor, the conductivity probe, and the three hot film anemometers were recorded. The time series were sampled at the rate of 15 Hz over a period of 540 seconds--a total of 8,100 samples. While these data were being recorded on magnetic tape, the position voltage was recorded in the lab book for a later determination of the exact probe position. The probes were then moved to another position and the time series data were again recorded. This procedure was repeated until sufficient points were obtained (15 to 20) to determine the profile through the transition region.

The drop in the position of the interface over the 540 seconds required to record the time series data at each point was much less than 0.2 mm. This is insignificant when determining the position of the probe relative to the interface. However, the total time required to complete an ST profile was as long as three hours; care was taken to account for the drop in the interface over this time interval.

The steps followed in taking data were:

1. The salt water was allowed to flow in under the fresh water at the rate of 3.5 gal/min; at this rate 15 hours were required to fill the tank. The filling process began the night before the tests.
2. The instruments were calibrated and mounted on the traverse just prior to the start of the experiment.
3. The pump was started and the flow increased to the velocity desired. This required as much as one hour since it had to be done slowly to prevent surges in the tank and seiching of the interface.
4. The pump was run for an additional hour or more before any data were taken. This allowed time for any transients to die out.
5. A CST was taken first, followed by an ST profile, which was followed in turn by another CST. This sequence of three profiles was usually repeated several times; each ST was preceded and followed by a CST.

Data Reduction Procedure

The data sets were reduced on the IBM System/370 computer at the University of Florida using the Fortran IV language. The first step in the reduction process was to convert the instrument voltages into physically significant values. Because of nonlinearities in most of the calibration curves (the position indicator is the only instrument which is linear over the entire range of operation), this must be done before any other numerical computations. To make this conversion, the least

squares method was used to fit an N^{th} order polynomial to the calibration points for each instrument. Since the position indicator is linear, $N = 1$ was used for this instrument. The thermistor and the conductivity probe, however, required $N = 2$ and $N = 4$, respectively (see Figures 8 and 11). The polynomial equations were then used within the computer program to convert instrument voltages to physical values. In the conversion of conductivity voltage to density, corrections were made for changes in temperature. Figure 12 shows the effect of temperature on the conductivity voltage for two solutions with different salinities. The shape of the hot film calibration curves (see Figure 13) and the fact that below a critical velocity the velocity can no longer be measured accurately make it desirable to fit these calibration points with a sequence of straight lines rather than a polynomial. If the hot film voltages dropped below the critical values (points 1 in Figure 13) more than five percent of the time, the data were discarded. Variations in the fluid temperature and density were accounted for when the velocity was computed.

In the reduction of the CST data, it was desirable to have the data output at nearly uniform intervals of about 0.5 mm (vertical separation distance). To accomplish this, m values of sampled data were averaged to produce one output point. The value of m depended on the speed of the traverse at the time, but it usually fell between 10 and 30. This numerical filter, which reduced the effects of high frequency electrical noise (specifically 60-cycle), was applied to all three channels of CST data (position, temperature, and conductivity).

Determination of the Vaisala frequency at a point requires the density gradient, $d\rho/dz$, at the point. The nature of differentiation

is such that the calculated value of the density gradient can fluctuate greatly due to small errors in the value of the density and/or the position. To lessen this problem, the density gradient at a point was calculated by first fitting a least-squares quadratic to five points in the density profile (the point of interest and two points on either side). The density gradient was then calculated by evaluating the derivative of the quadratic at the point of interest. The thickness of the interface δ was determined from,

$$\delta \equiv \frac{g \Delta \rho}{\rho NMAX^2} ,$$

where NMAX is the largest value of the Vaisala frequency taken from the core of the interfacial region.

The final result from the CST data was a tabulation of temperature, specific gravity, and Vaisala frequency versus position. The computer program then plotted these profiles using the Gould (series 5100) plotter. The program also printed out the position of the interface, the value of the density which defines the interface, and the exact time that the sensors crossed the interface.

The raw data from the ST runs consisted of four or five time series: thermistor voltage, conductivity voltage, and the output voltage from two or three hot film anemometers versus time. The first step in reducing these data was to convert each value of thermistor voltage to temperature in degrees Fahrenheit. The temperature at each point in time was then used to convert the conductivity voltage to the fluid density (the calibration polynomials discussed above were used to make both these conversions). Transformation of the hot film voltages to instantaneous velocities requires knowledge of the instantaneous

fluid temperature and density around the hot film sensors (see Figure 13). It should be noted that the thermistor, the conductivity probe, and the hot film probes were separated horizontally by a small but finite distance (≈ 2 cm). This horizontal separation meant that high frequency fluctuations in the temperature and conductivity at the respective probe positions were not related in general to the high frequency fluctuations in temperature and density at the hot film sensors. If these fluctuations are not filtered out they may induce fluctuations in the velocity measurements which do not actually exist. Also, since the temperature and density corrections were applied uniformly to both channels of the hot film data, these fluctuations may have resulted in unrealistic values of the velocity correlations. To reduce the effects from this source of error, the temperature and density were averaged over a one second period centered about the time point of interest. The averaged values were then used to compute the velocity at the time of interest. Mathematically, this process is as follows:

$$\bar{T}_i = \frac{1}{2n+1} \sum_{j=i-n}^{i+n} T(t=t_j) \quad , \quad \bar{\rho}_i = \frac{1}{2n+1} \sum_{j=i-n}^{i+n} \rho(t=t_j)$$

$$V(t=t_i) = V[\text{HFV}(t=t_i), \bar{T}_i, \bar{\rho}_i] \quad .$$

Where HFV is the hot film voltage, V the velocity, T the temperature, and ρ the fluid density. The functional relationship between V , HFV, T , and ρ is shown in Figure 13 and $(2n+1)\Delta t \approx 1$ second.

In order to estimate the magnitude of this potential source of error a simple experiment was conducted. Identical time series records, for a point in the interfacial region, were reduced by two different

methods. With the first method the instantaneous velocity and all the correlations were computed using a constant value of temperature and density (the average values of temperature and density for the 540 second time period). The second method used the instantaneous values of temperature and density to compute the instantaneous velocities and the velocity correlations. A comparison of the results showed that the relative difference between the values was always less than 0.1 percent. It was concluded, therefore, that fluctuations in the temperature and density do not result in a significant source of error.

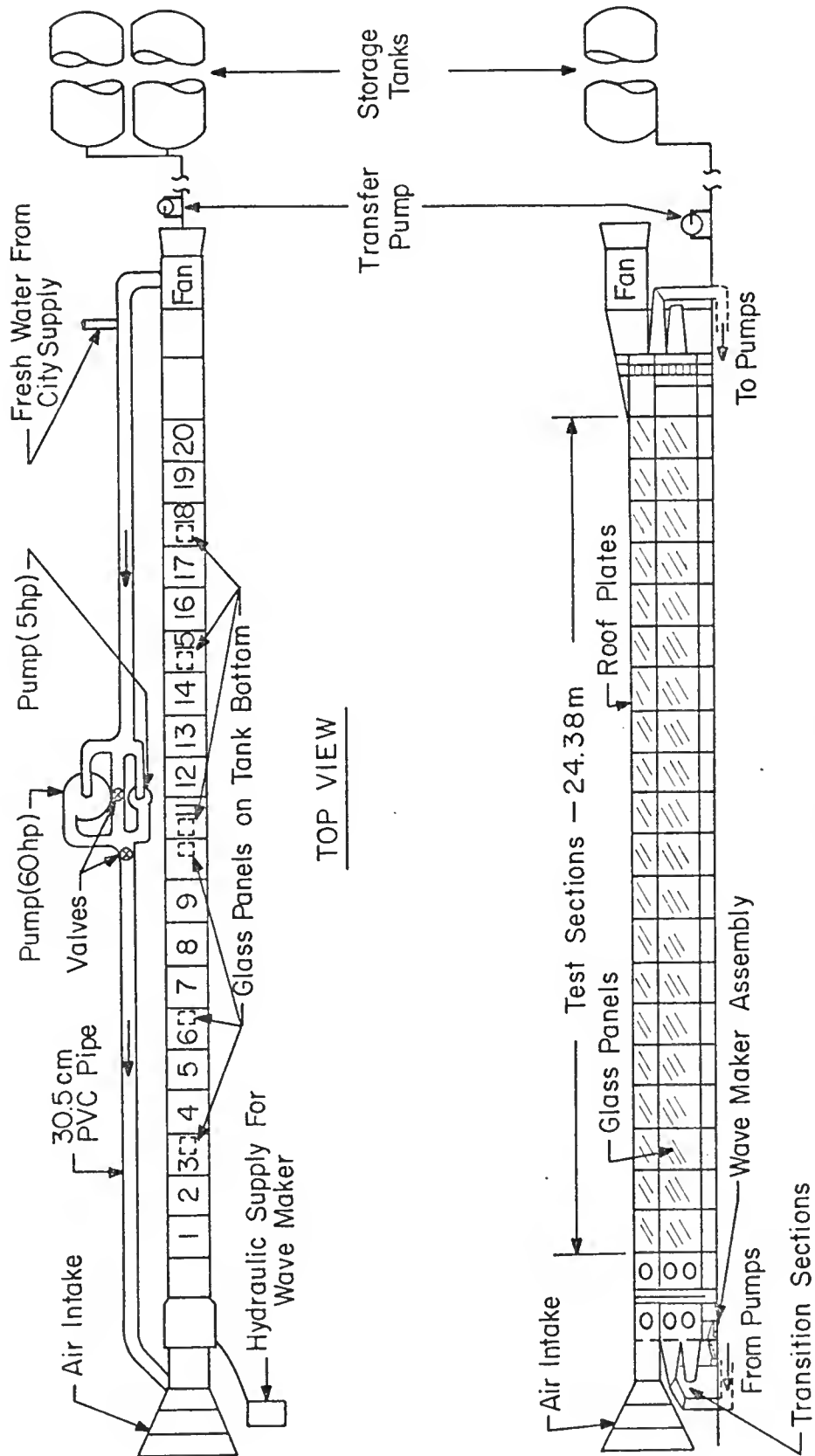


FIGURE 2: SCHEMATIC DRAWING OF THE OVERALL FACILITY

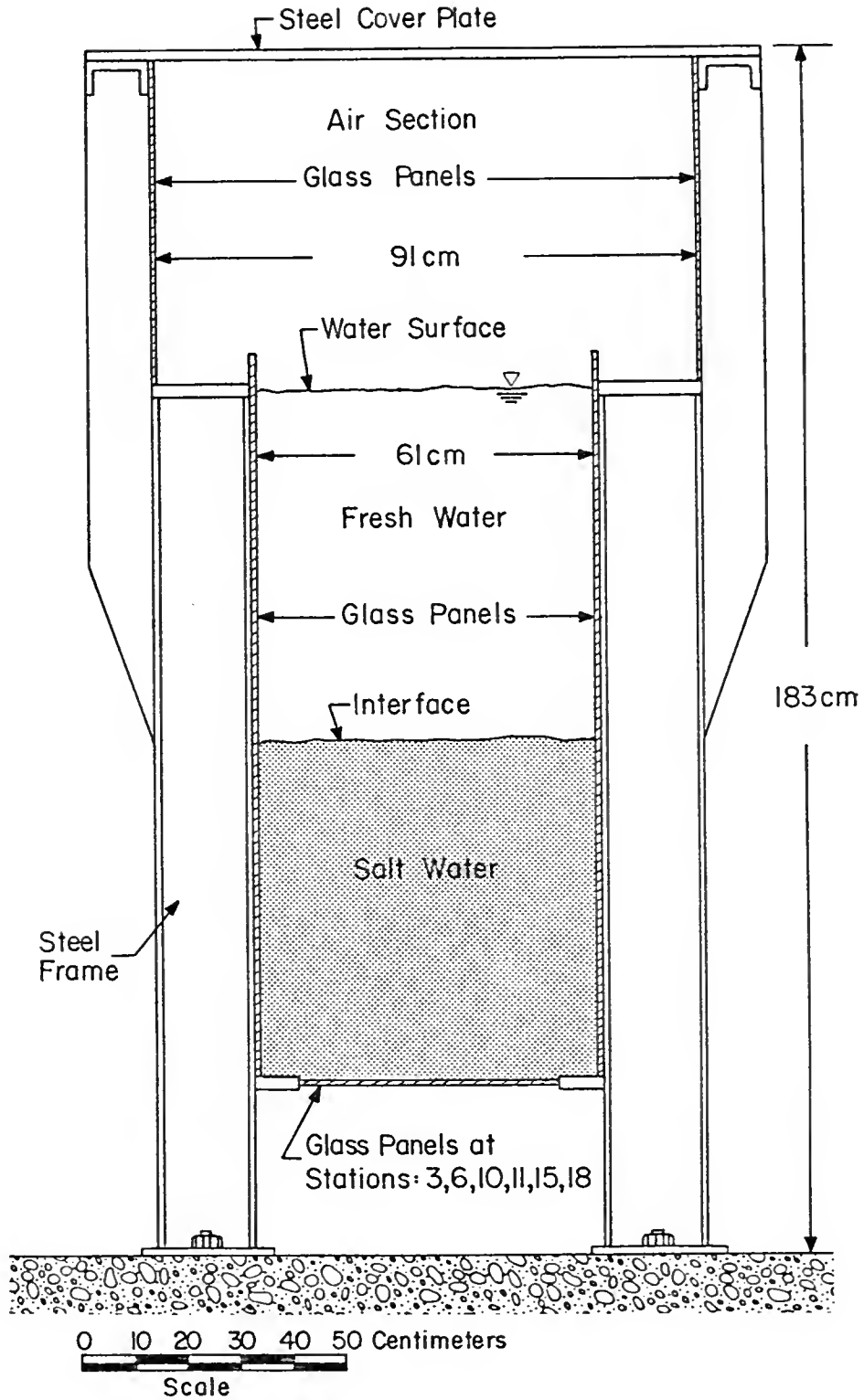


FIGURE 3: CROSS-SECTIONAL VIEW OF THE TEST SECTION

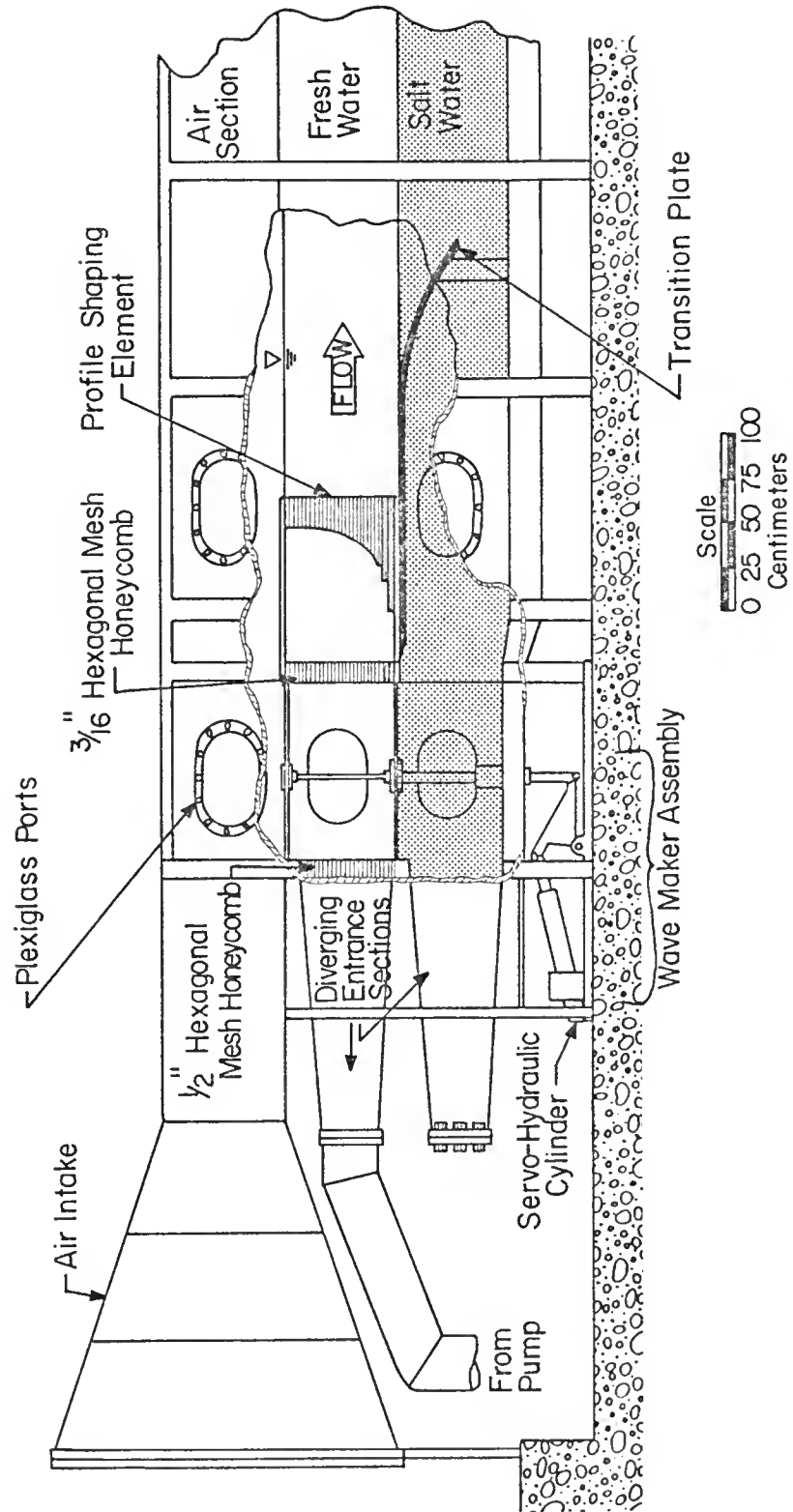


FIGURE 4: UPSTREAM END OF TEST SECTION

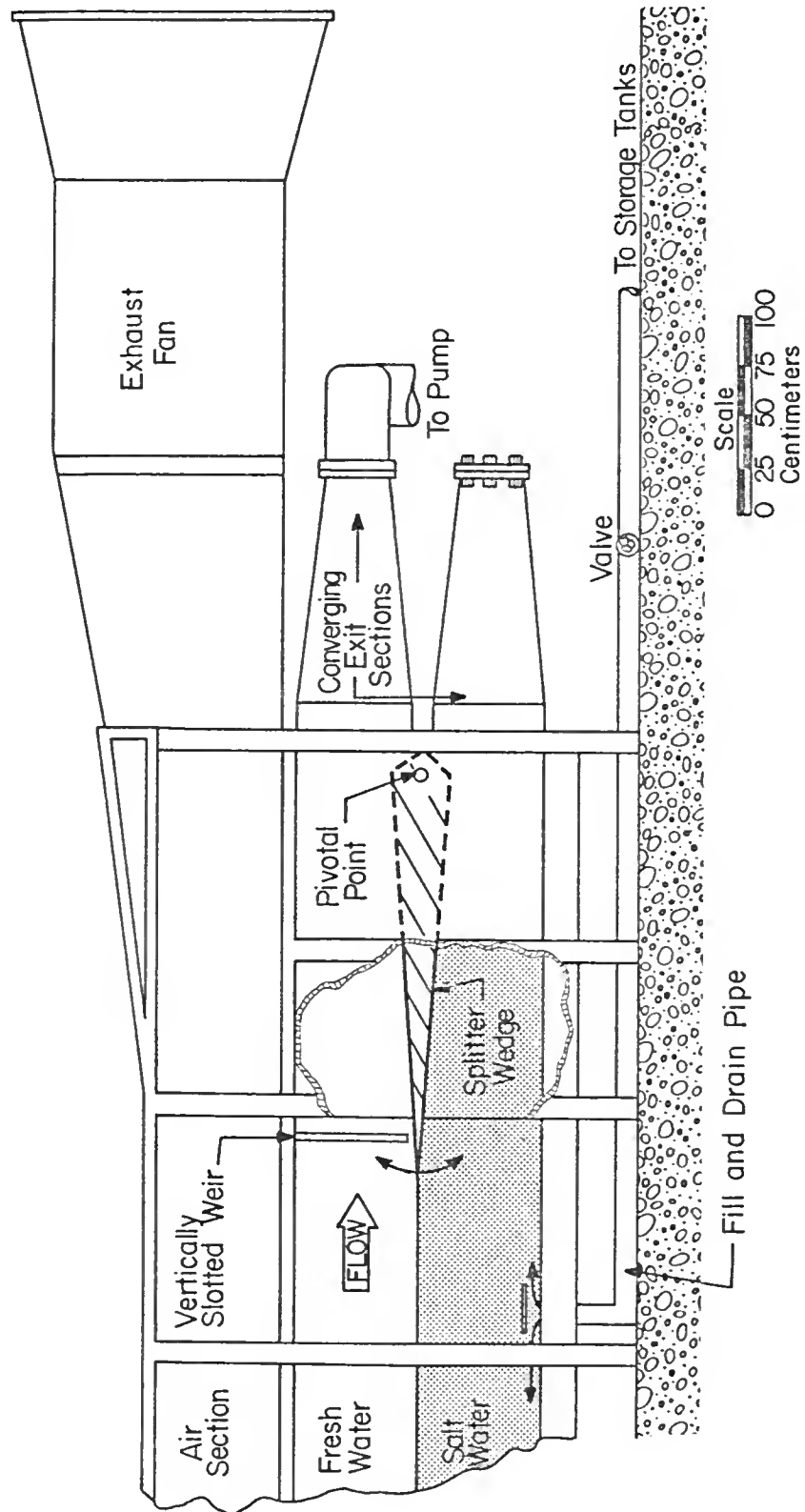


FIGURE 5: DOWNSTREAM END OF TEST SECTION

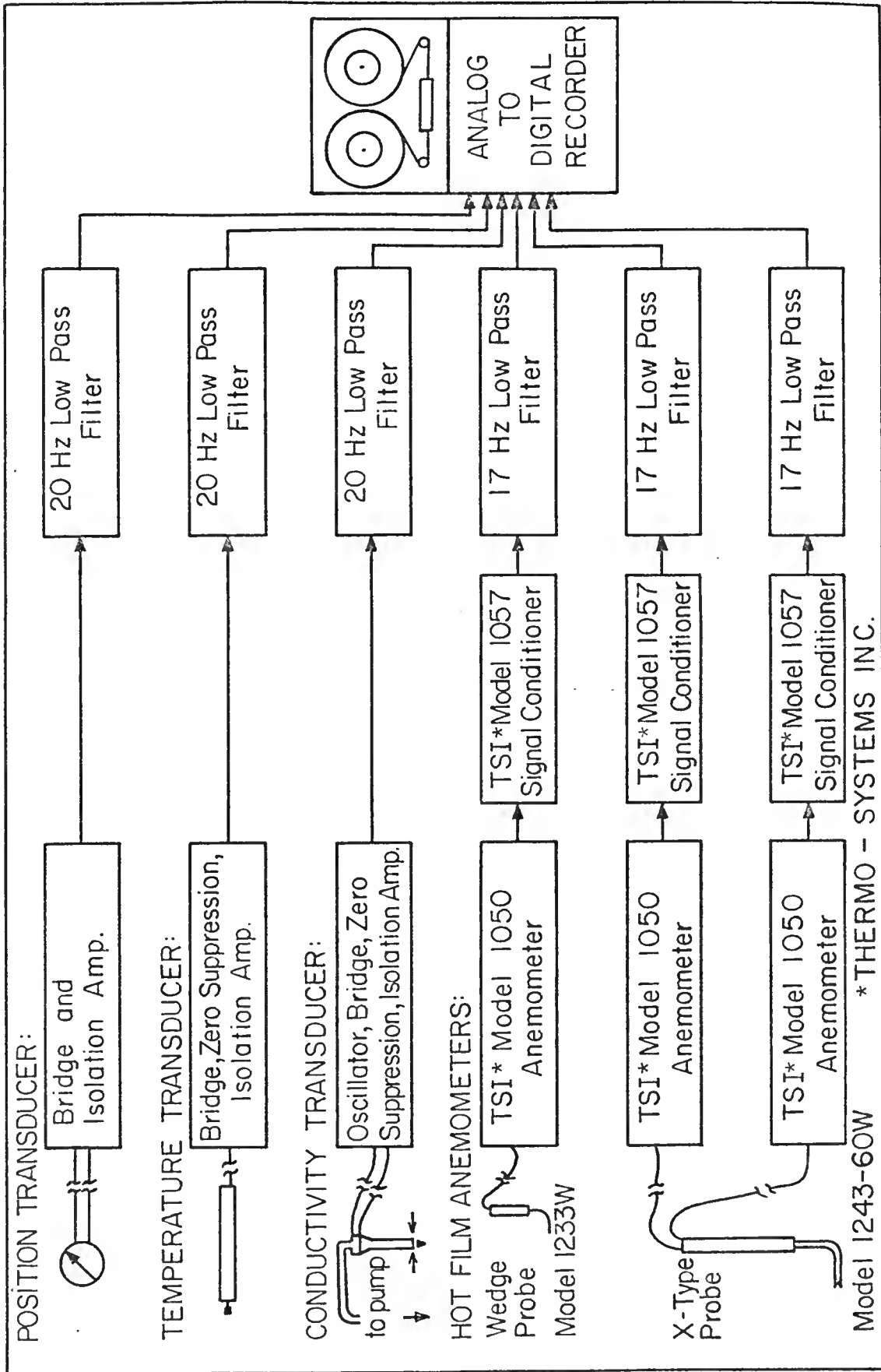


FIGURE 6: BLACK BOX SCHEMATIC OF THE INSTRUMENTATION

A graph showing the relationship between Temperature (°F) on the Y-axis and Thermistor Voltage on the X-axis. The Y-axis ranges from 60 to 90 with major ticks every 10 units. The X-axis ranges from -4.0 to 4.0 with major ticks every 2.0 units. A series of data points are plotted, showing a non-linear, slightly downward-curving relationship. A quadratic equation is fitted to the data, indicated by a line pointing to the equation: $T = 74.8489 + 3.6498V - 0.9488V^2$.

Thermistor Voltage (V)	Temperature (°F)
-4.5	55.0
-4.0	58.0
-3.5	60.5
-3.0	64.0
-2.5	66.5
-2.0	68.0
-1.5	69.0
-1.0	70.5
-0.5	72.5
0.0	74.5
0.5	76.5
1.0	78.5
1.5	80.5
2.0	82.5
2.5	84.0
3.0	85.5
3.5	87.0
4.0	88.5

FIGURE 8: CALIBRATION CURVE FOR THERMISTOR

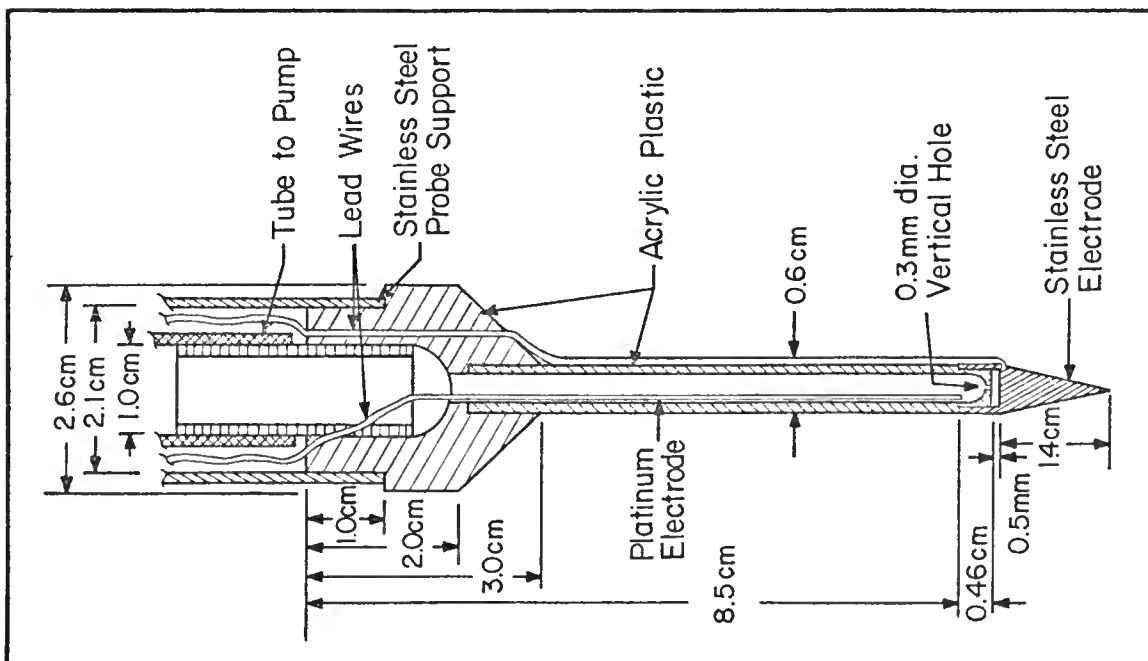


FIGURE 9: CROSS-SECTION OF CONDUCTIVITY PROBE

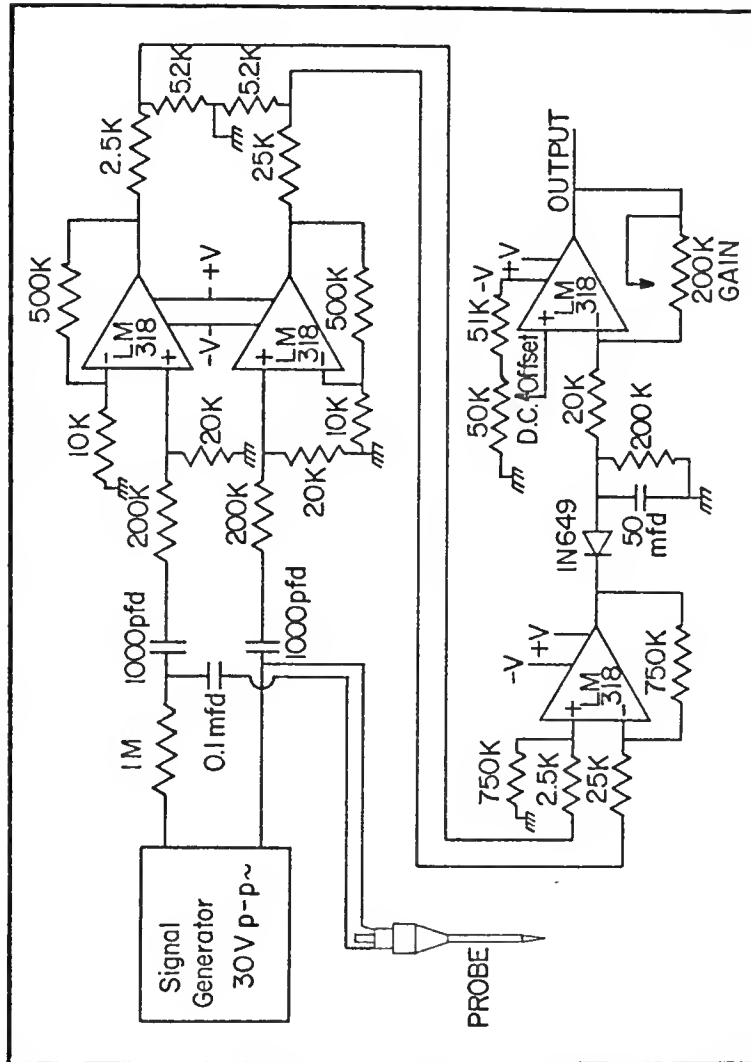


FIGURE 10: SCHEMATIC OF CONDUCTIVITY PROBE ELECTRONICS

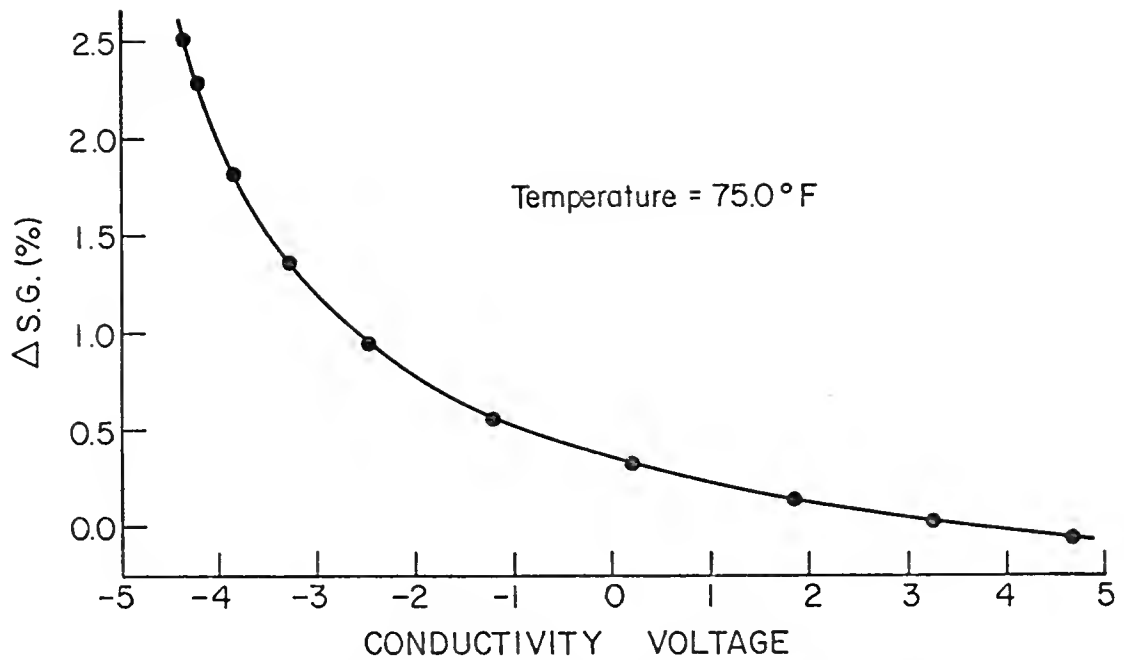


FIGURE 11: CALIBRATION CURVE FOR CONDUCTIVITY PROBE

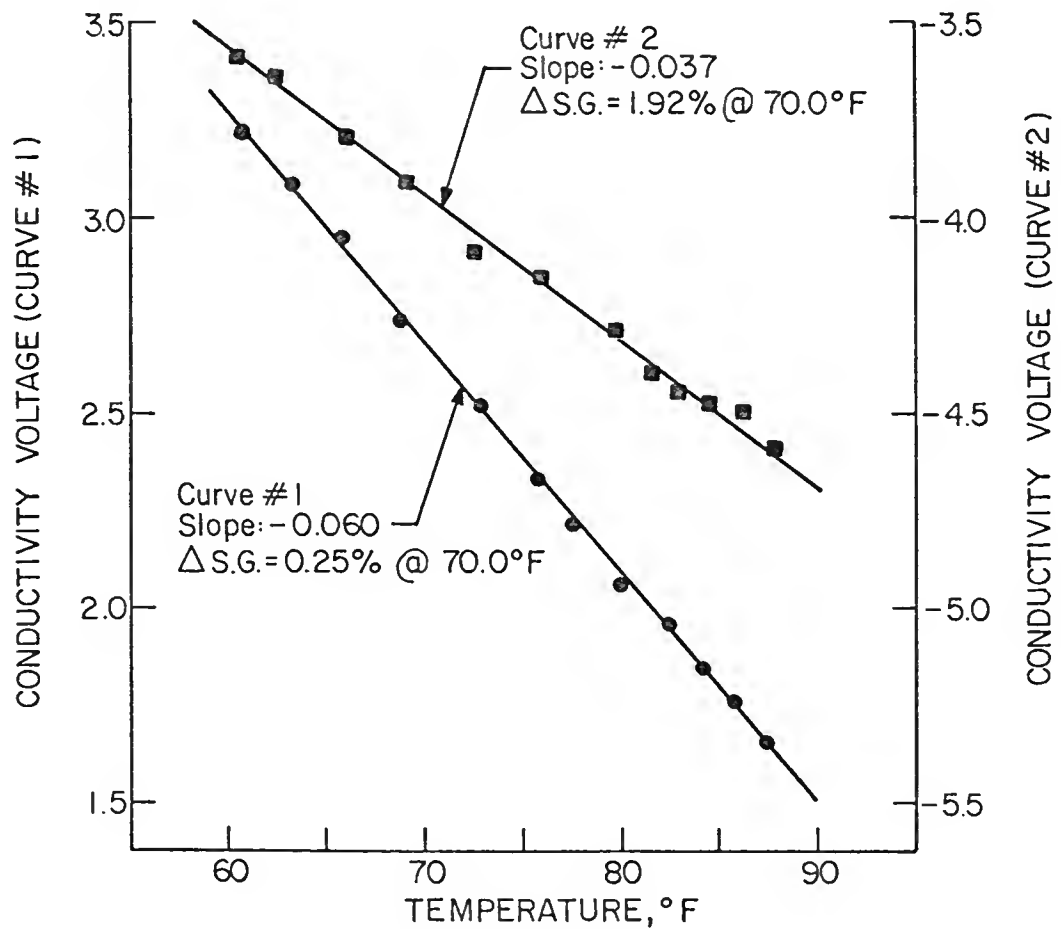


FIGURE 12: CONDUCTIVITY VOLTAGE VS. TEMPERATURE

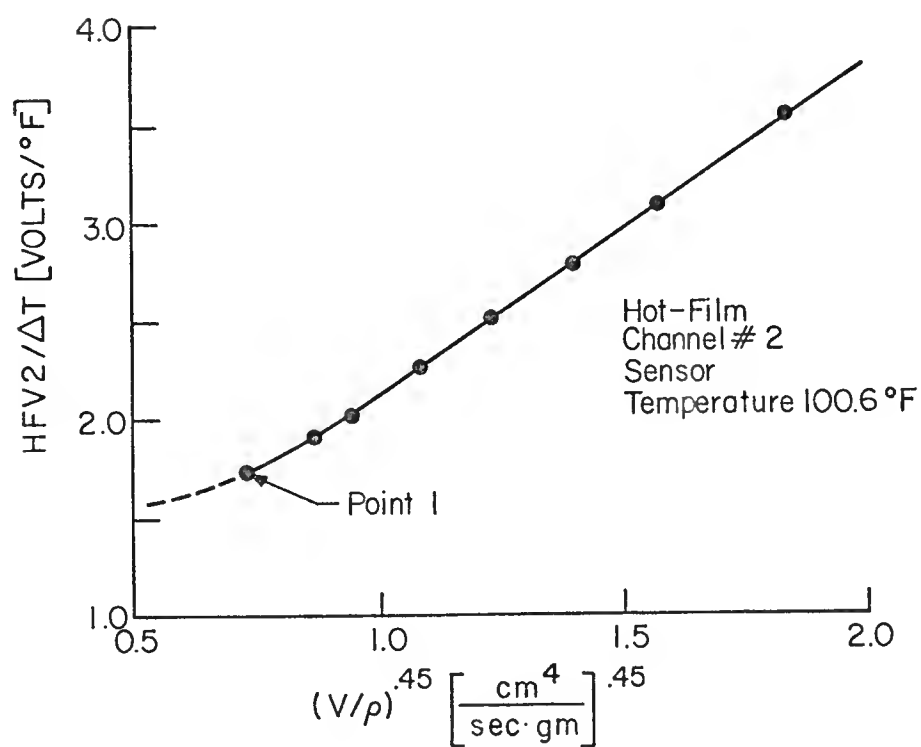
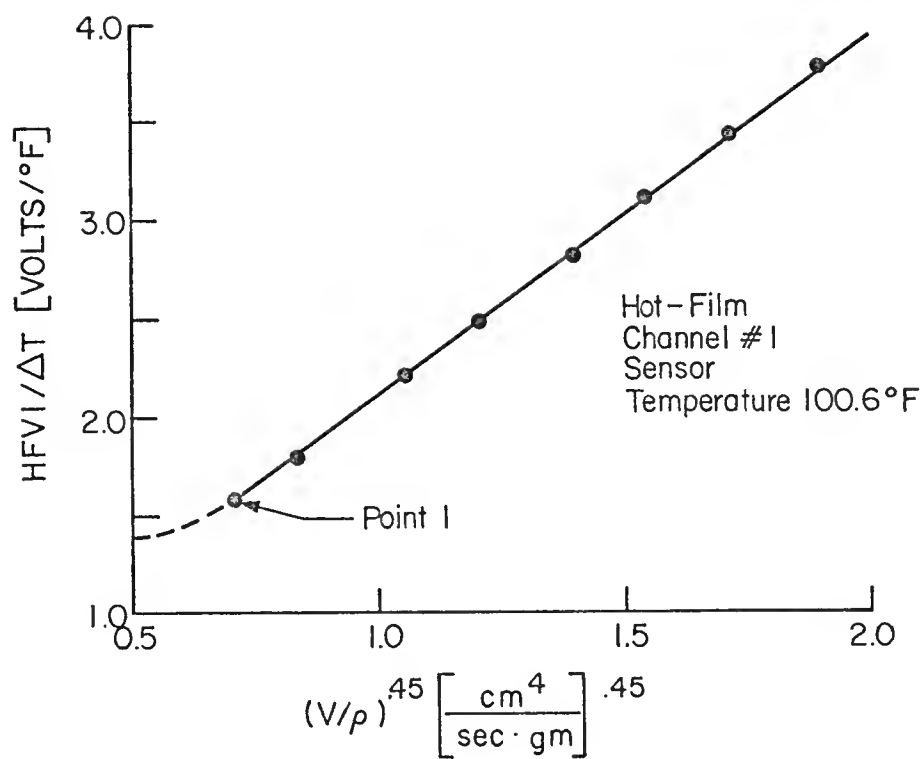


FIGURE 13: HOT FILM CALIBRATION CURVES

CHAPTER IV

RESULTS

Introduction

The data presented in this chapter are the results of those experiments considered accurate, consistent, and reliable. The primary factor in making this determination was the mean velocity. If the mean velocity at a point varied significantly over a long period of time or if the velocity profile away from the interface varied radically with position, the data were discarded as invalid.

Figure 14 gives a chronological listing of the experiments and the corresponding global parameters which define the state of flow. Figure 15 lists some of the experimentally derived quantities for each test.

Five experiments were conducted at a location 800 cm downstream from the entrance while four others were conducted at 1600 cm. The overall density difference was maintained between 2.2 and 2.7 percent while the mean velocity varied between 2.7 cm/sec and 7.8 cm/sec. The Reynolds number for the upper layer, based on the equivalent pipe diameter, was always greater than 2.0×10^4 . Thus, the upper layer was always above the critical Reynolds number for turbulent flow, while the flow deep within the bottom layer was always laminar.

Density Structure

The physical appearance of the density interface is similar to the surface of water at the point when wind first starts to generate waves, except that the time scales are longer. Small amplitude wavelets having large wave numbers and short crests move along the interface with an apparently random distribution in both space and time. The wave lengths, crest lengths and amplitudes of these waves increase very slowly with distance downstream. Many of the wavelets form sharp crests, break and eject salt water into the upper layer. At times, the ejected salt water falls back to the interface before diffusing completely. The structure of the density interface and the dynamics of the mixing process clearly indicate that this flow is always within regime two (see Chapter I). Although the interface is continuously moving, it always remains distinct and easily identifiable with no large coherent overturning structures present.

Appendix B contains the quasi-instantaneous profiles of density, temperature and Vaisala frequency obtained by the CST technique. Because the density interface is in a state of agitation there is considerable variance between density profiles, even between consecutive profiles taken under the same conditions. Some of the profiles exhibit what appear to be double interfaces or unstable regions. These structures may be aberrations resulting from the passage of a wave during the 10 to 30 seconds required for the probes to traverse the interfacial region or they may actually exist. When the structures exist, they appear in all profiles taken during the particular experiment. When the structures result from the passage of a wave, they appear and disappear at random. The density plots from October 26, 1978,

and May 3, 1977, illustrate the first case while those from October 13, 1978, illustrate the latter. The small perturbations in the density profiles found deep within each layer are most likely the result of noise on the conductivity signal. These fluctuations, most pronounced in the salt layer where the conductivity probe is least sensitive, translate into large fluctuations in the Vaisala frequency profiles.

Due to the large variance between individual profiles, a more meaningful measure of the density structure is obtained by first non-dimensionalizing the density and Vaisala frequency profiles, and then forming an ensemble average by overlaying several of these plots. Figures 16, 18, 20, 22 and 24 show the overlaid density profiles while Figures 17, 19, 21, 23 and 25 show the corresponding Vaisala frequency plots. The nondimensional density, ρ^* , is defined by

$$\rho^*(\xi/\delta) \equiv \frac{\rho(\xi/\delta) - \rho_u}{(\rho_\ell - \rho_u)}$$

where ρ_u is the density of the upper layer and ρ_ℓ the density of the lower layer. The vertical coordinate ξ is nondimensionalized by the interfacial thickness parameter, δ defined by

$$\delta \equiv \frac{2g \Delta\rho}{(\rho_\ell + \rho_u) NMAX^2}$$

where g is the acceleration of gravity and $NMAX$ is the largest value of Vaisala frequency from the core of the interfacial region. The dimensionless Vaisala frequency, N^* , is obtained by dividing the Vaisala frequency by $NMAX$. The solid line on each of the nondimensionalized density plots is given by

$$\rho^*(\xi/\delta) = \frac{1}{2} \left[1 - \tanh \left(\frac{2\xi}{\delta} \right) \right]$$

while the solid line on the nondimensionalized Vaisala frequency plots is given by

$$N^*(\xi/\delta) = \operatorname{sech} (2\xi/\delta)$$

These functional representations of the density and Vaisala frequency are generally a good fit to the experimental data. The greatest deviation usually occurs in the region above the interface where the curvature of the density profile is maximum.

Figure 26 shows a plot of the interfacial thickness parameter, δ , versus the Keulegan number, K . The solid dots represent the data taken at Station 800 while the open circles are data taken at Station 1600. The solid line is the line of least square error through the solid dots. The corresponding correlation coefficient is 0.43, which for 25 degrees of freedom, is significant at the 0.05 level. The slope of this line gives

$$\frac{d\delta}{dK} = 0.0126 \text{ cm.}$$

The data sets defined by $0 \leq K \leq 4$ indicate a positive correlation also exists between δ and x . The average interfacial thickness for the data in this range was 0.44 at Station 800 while at Station 1600 it was 0.64, thus

$$\frac{\Delta\delta}{\Delta x} = 2.5 \times 10^{-4}$$

The correlation coefficient between δ and x for these data sets was 0.59, which given the 28 degrees of freedom is again significant at 0.001 level. Due to the limited number of stations and experiments it was not possible to determine the functional relationship between

δ and x or between δ and K , but there is a positive correlation in both cases.

Mean Velocity

The mean velocity profiles fall into two distinctly different groups. The primary feature differentiating the groups in the boundary layer thickness, δ_u , defined as the point where the mean velocity reaches 95 percent of the freestream velocity. The freestream velocity, \bar{U} , is, in turn, defined as the average velocity 15 cm or more above the density interface. The velocity in this region is very nearly uniform. Figure 27 shows the nondimensionalized velocity profiles for the first group; the boundary layer thickness for these profiles is between 10.5 cm and 11.5 cm. In the second group, Figure 28, the boundary layer thickness is only between 1.15 cm and 3.2 cm. The two nondimensionalized profiles also have different shapes. For comparison, the two velocity profiles shown in Figures 27 and 28 are drawn together in Figure 29. In the region $(\xi - \eta)/\delta_u > 0.6$ the two profiles are identical, within experimental error. However, below this region the profiles are distinctly different.

No statistically significant distinction can be made between profile groups on the basis of any of the parameters listed in Figure 14. However, there is a slight tendency for the group two profiles to occur at lower velocities and at locations closer to the entrance. The small variations in the boundary layer thickness for the profiles in Figure 27 have no significant correlation with mean velocity, distance downstream or the Reynolds number based on these two quantities. Therefore, the flow is believed to be fully developed and in equilibrium. This,

however, is not the case for the group two profiles (Figure 28). The boundary layer thickness for this set correlates well with the inverse of the Reynolds number based on the downstream position. The correlation coefficient is 0.969 which, given two degrees of freedom, is still significant at the 0.03 level.

The origin of the vertical coordinate in both Figures 27 and 28 is defined as the point where the velocity equals 50 percent of the free-stream velocity. This origin is shifted a small amount, η , from the origin defined by the density interface (i.e. $\xi=0$). This small shift between the density and velocity profiles appears reasonable upon examination of the individual density profiles (Appendix B). A small discrepancy of less than 0.2 cm could result from errors in positioning the conductivity and hot film probes, while larger shifts are usually associated with the existence of a double interfacial structure. It appears that the velocity profile, in some way, "locks in" on the upper most density interface.

The experiments which exhibit the group two velocity profiles also exhibit relatively smooth density profiles having a single density interface. On the other hand, the experiments which fall into group one have density profiles which exhibit either a double interface or a highly agitated structure (see Appendix B). This correlation between velocity profiles and density structure extends to the vertical shift parameter, η . As shown in Figures 27 and 28 the group one velocity profiles have values of η ranging from 0.38 to 0.80 cm while for the group two profiles, η falls between 0.05 cm and 0.25 cm.

The mean velocity profile for group one is plotted on log-normal paper in Figure 30. This illustration points out the existence of a

region above the interface, $(\xi - \eta)/\delta_u > 0.15$, where the velocity profile has a logarithmic shape. The group two profiles have no such region.

The Richardson Number

The gradient Richardson number at any point is defined by:

$$Ri_g \equiv \frac{-g \frac{\partial \rho}{\partial \xi}}{\rho \left(\frac{\partial U}{\partial \xi} \right)^2} = \frac{N^2}{\left(\frac{\partial U}{\partial \xi} \right)^2} ,$$

where N is the Brunt-Vaisala frequency. Given the Vaisala frequency profile,

$$N(\xi) = NMAX \operatorname{sech}\left(\frac{2\xi}{\delta}\right) ,$$

where by definition,

$$NMAX^2 \equiv \frac{2g \Delta \rho}{(\rho_\ell + \rho_u) \delta} ,$$

and the velocity profile,

$$U = \bar{U} f\left(\frac{\xi - \eta}{\delta_u}\right) ,$$

The Richardson number profile can be expressed as:

$$Ri_g(\xi) = \frac{2g \Delta \rho \delta_u^2}{(\rho_\ell + \rho_u) \bar{U}^2 \delta} \left[\frac{\operatorname{sech}\left(\frac{2\xi}{\delta}\right)}{f'\left(\frac{\xi - \eta}{\delta_u}\right)} \right]^2$$

where $f'\left(\frac{\xi - \eta}{\delta_u}\right)$ is the derivative of f with respect to $\frac{\xi - \eta}{\delta_u}$.

The gradient Richardson number at the inflection point in the velocity profile ($\xi = \eta$) then becomes:

$$Ri_g(\xi=\eta) = \frac{2g \Delta \rho \delta_u^2}{\bar{U}^2(\rho_\ell + \rho_u)\delta} \left[\frac{\text{sech}(\frac{2\eta}{\delta})}{f'(0)} \right]^2$$

The gradient Richardson number at $\xi=\eta$ was calculated for each experiment using the above equation and the appropriate values listed in Figures 14 and 15 (the average value of the δ 's listed in Figure 15 was used for δ). The values of $f'(0)$ were obtained for the two velocity groups from Figures 27 and 28. The results are shown below:

<u>Exp. No.</u>	<u>Date</u>	<u>Group</u>	<u>$Ri_g(\xi=\eta)$</u>	<u>$f'(0)$</u>
2	5/3/77	1	0.08	8.0
3	10/19/77	1	0.13	8.0
6	10/26/78	1	0.52	8.0
7	10/26/78	1	1.06	8.0
8	11/8/78	1	0.07	8.0
1	7/6/76	2	88.60	0.8
4	7/24/78	2	1.23	0.8
5	10/13/78	2	7.18	0.8
9	12/6/78	2	7.06	0.8

Thus,

$$Ri_g(\xi=\eta) \leq 1.06 \text{ for group one profiles}$$

and

$$Ri_g(\xi=\eta) \geq 1.23 \text{ for group two profiles.}$$

Shear Stress Profiles

The total shear stress in a turbulent flow is the sum of the viscous and the Reynolds stresses defined as

$$\tau_T = \tau_v + \tau_t = \mu \frac{\partial U}{\partial \xi} - \overline{\rho u'v'},$$

where τ_T is the total stress, τ_v is the viscous stress, and τ_t is the Reynolds stress.

Figures 31 and 32 show the total shear stress profile corresponding to the group one and group two velocity profiles respectively. The stress has been normalized by τ_i , the total stress at the velocity interface, $\xi=\eta$. Both these profiles exhibit a marked increase in the neighborhood of the interface, dropping off rapidly on either side. The fact that the total shear stress becomes very small just below the density interface is in agreement with the observation of little or no motion in the bottom layer even after the upper layer has been moving for three to six hours. The rapid decrease in the stress profile above the interface, however, is unexpected since equations 2.2 and 2.4 predict a linear stress profile between the freesurface and the density interface. In an attempt to explain this unexpected behavior, the theoretical shear stress profile was calculated from equations 2.1 through 2.3. These equations account for the additional effects of side wall friction, mean advective accelerations and mean density gradients. The latter two result from boundary layer growth and turbulent diffusion at the interface, set-up of the density interface and set-down of the freesurface. Details of the solution techniques are presented in Appendix E. Figure 33 shows the computed shear stress profiles under group one conditions and the magnitude of the five parameters which determine the shape of the stress profiles. These profiles more closely represent the data (see Figure 31) than does the simple linear model. However, this solution is still not completely satisfactory. First, the calculated stress is only 40 to 50 percent of the measured stress at the interface. In addition, except for profiles one and two, the magnitude of the parameters are unreasonably large. A possible

explanation for why this analysis is unable to predict the shear stress profile is given in Chapter V.

The interfacial friction factor, defined by

$$f_i \equiv \frac{8 \tau_i}{\rho \bar{U}^2} ,$$

is plotted versus Reynolds number in Figure 34 along with the line corresponding to turbulent flow over a hydraulically smooth rigid surface. This figure shows that, at the same Reynolds number, the shear stress at the interface is generally less than or equal to the stress at a smooth rigid surface. The data points, except for one, cluster around a line with a -2 slope which implies the interfacial shear stress is independent of the mean flow velocity. No significant correlation is found between the interfacial friction factor and the data groups.

Figures 35 and 36 show the ratio of viscous stress to total stress for the group one and two velocity profiles. There is again an obvious difference between groups. For group one, the viscous stress drops off in an exponential manner above the interface; at the interface, the viscous stress is only 60 to 70 percent of the total stress. For group two, the viscous stress remains large above the interface until $(\xi - \eta / \delta_u) > 1.0$ and then drops off rapidly. For $(\xi - \eta / \delta_u) < 1.0$ the viscous stress accounts for nearly the entire stress and in some cases balances negative Reynolds stresses. Again for the purpose of comparison, the curves from Figures 35 and 36 are shown together in Figure 37.

Energy Spectra

Energy spectra of the horizontal and vertical velocity fluctuations were measured during four of the nine experiments at several

positions above the interface. These plots, along with pertinent facts on the measurement technique, are given in Appendix D. The spectra measured well above the interface generally have a smoothly varying shape indicating broad band phenomena denoting a turbulent flow. The energy content of the high frequency fluctuations appears to be about the same for the horizontal and vertical components indicating local isotropy. However, at lower frequencies the energy in the vertical fluctuations drops below that for the horizontal fluctuations due to the presence of the stable density interface.

The spectra measured close to or in the density interface exhibit a more erratic behavior and a rather sudden change in the slope of the energy curve between one and two Hertz; this corresponds roughly to the maximum Vaisala frequency of the interface. There is often a marked rise in the energy level in this frequency band, especially in the vertical velocity component and a rapid decrease in the energy at higher frequencies.

This characteristic of the energy spectra indicates the presence of internal wave energy. The fact that the spectra drops off rapidly above the Vaisala frequency is indicative of the fact that disturbances with frequencies above the Vaisala frequency are damped rapidly. The density interface prevents the transfer of high frequency energy from one side of the interface to the other.

Finally, the spectra measured on December 6, 1978, at $\xi = 0.37$ cm and on July 6, 1976, at $\xi = 0.46$ cm correspond to group two velocity profiles. These spectra indicate the presence of internal waves.

Exp. No.	DATE	X cm	\bar{U} cm/sec	$\frac{\Delta \rho}{\rho u}$ %	$\frac{\bar{U} D_e}{\nu}$	$\frac{\bar{U} X}{\nu 10^{-3}}$	$\frac{g \Delta \rho D_e}{\rho \bar{U}^2}$	$\frac{g \Delta \rho \nu}{\rho \bar{U}^3}$ ($\times 10^3$)
1	July 6 1976	800	2.70	2.50	21,945	216.0	273.2	12.45
2	May 3 1977	800	3.22	2.20	26,172	257.6	169.0	6.46
3	Oct 19 1977	800	4.10	2.25	33,324	364.0	106.6	2.34
4	July 24 1978	800	7.10	2.64	57,708	568.0	41.7	0.72
5	Oct 13 1978	800	4.50	2.51	36,576	360.0	98.7	2.70
6	Oct 26 1978	1600	6.52	2.50	52,995	1,043.2	46.8	0.88
7	Oct 26 1978	1600	4.76	2.50	38,689	724.8	87.9	2.64
8	Nov 8 1978	1600	7.79	2.40	63,317	1,246.1	31.5	0.50
9	Dec 6 1978	1600	4.05	2.70	33,325	656.0	131.1	3.84
$D_e = 4 R_h = 81.3 \text{ cm}, \nu = 0.01 \text{ cm}^2/\text{sec}$								

FIGURE 14: EXPERIMENTS AND GLOBAL PARAMETERS

Exp. No.	τ_i/ρ $\frac{\text{cm}^2}{\text{sec}^2}$	u_* $\frac{\text{cm}}{\text{sec}}$	f_i	δ_u cm	η cm	$\frac{g\Delta\rho\nu}{\rho u_*^3}$	Measured δ (cm) from CST
1	0.017	0.130	0.019	3.20	0.10	111.50	0.63, 0.61, 0.42, 0.38, 0.41 0.73, 0.51
2	0.040	0.200	0.031	11.0	0.80	26.95	0.63, 0.47, 0.53
3	0.051	0.226	0.024	10.8	0.62	19.10	0.41, 0.60, 0.50
4	0.0585	0.242	0.009	1.45	0.25	18.26	0.32, 0.38, 0.35, 0.50, 0.50 0.42
5	0.059	0.243	0.023	1.60	0.15	17.14	0.52, 0.53, 0.34, 0.53, 0.39 0.44, 0.33
6	0.050	0.224	0.009	10.8	0.38	21.80	0.68, 0.70, 0.79, 0.44
7	0.041	0.202	0.014	10.5	0.38	29.72	0.67, 0.76, 0.88, 1.00
8	0.052	0.228	0.007	11.5	0.65	19.84	0.51, 0.68
9	0.037	0.192	0.018	1.15	0.05	37.38	0.46, 0.47, 0.44, 0.43
$f_i = (\tau_i/\rho) 8/\bar{U}^2$							

FIGURE 15: EXPERIMENTS AND MEASURED QUANTITIES

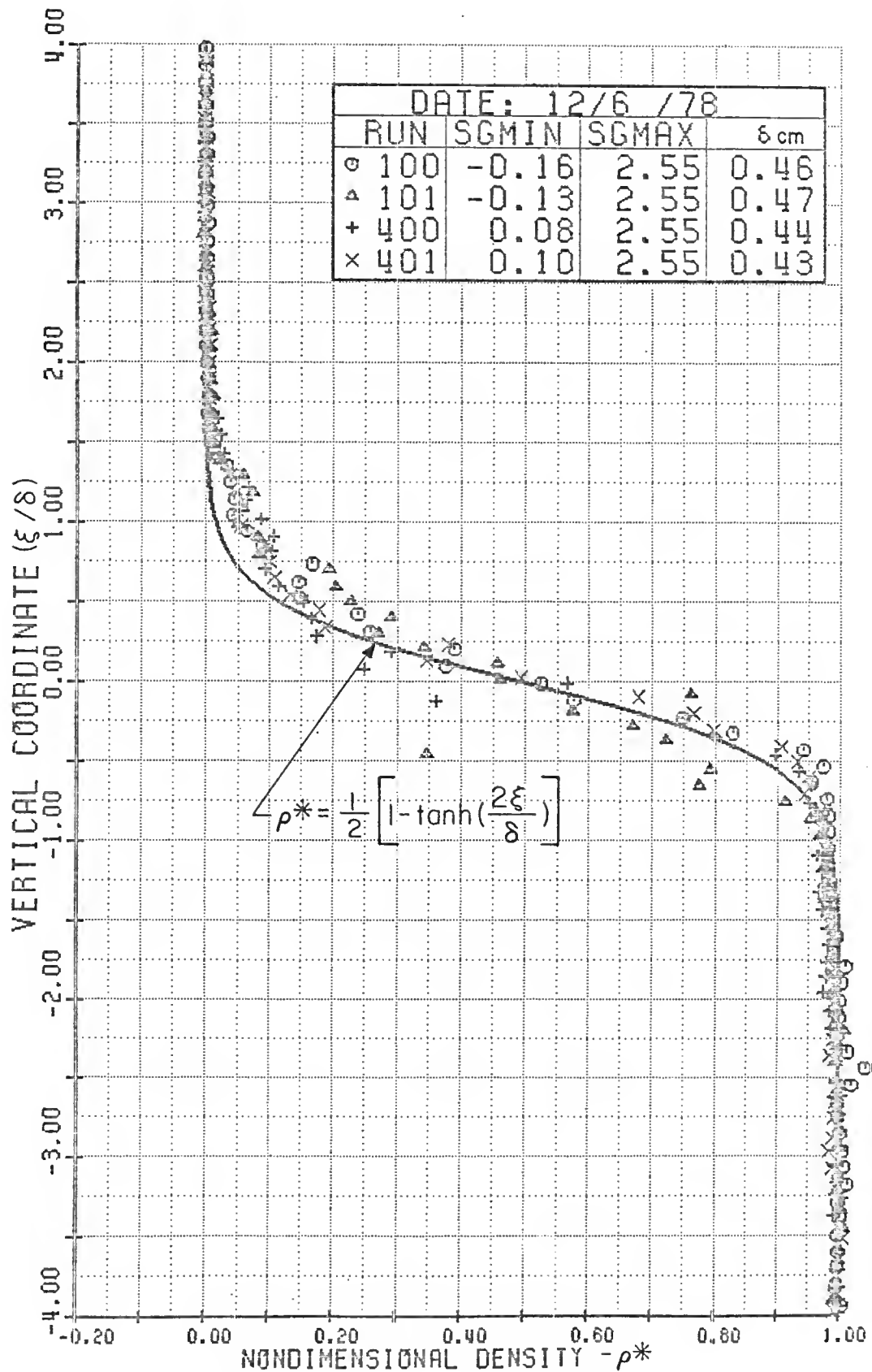


FIGURE 16: NONDIMENSIONAL DENSITY PROFILE 12/6/78

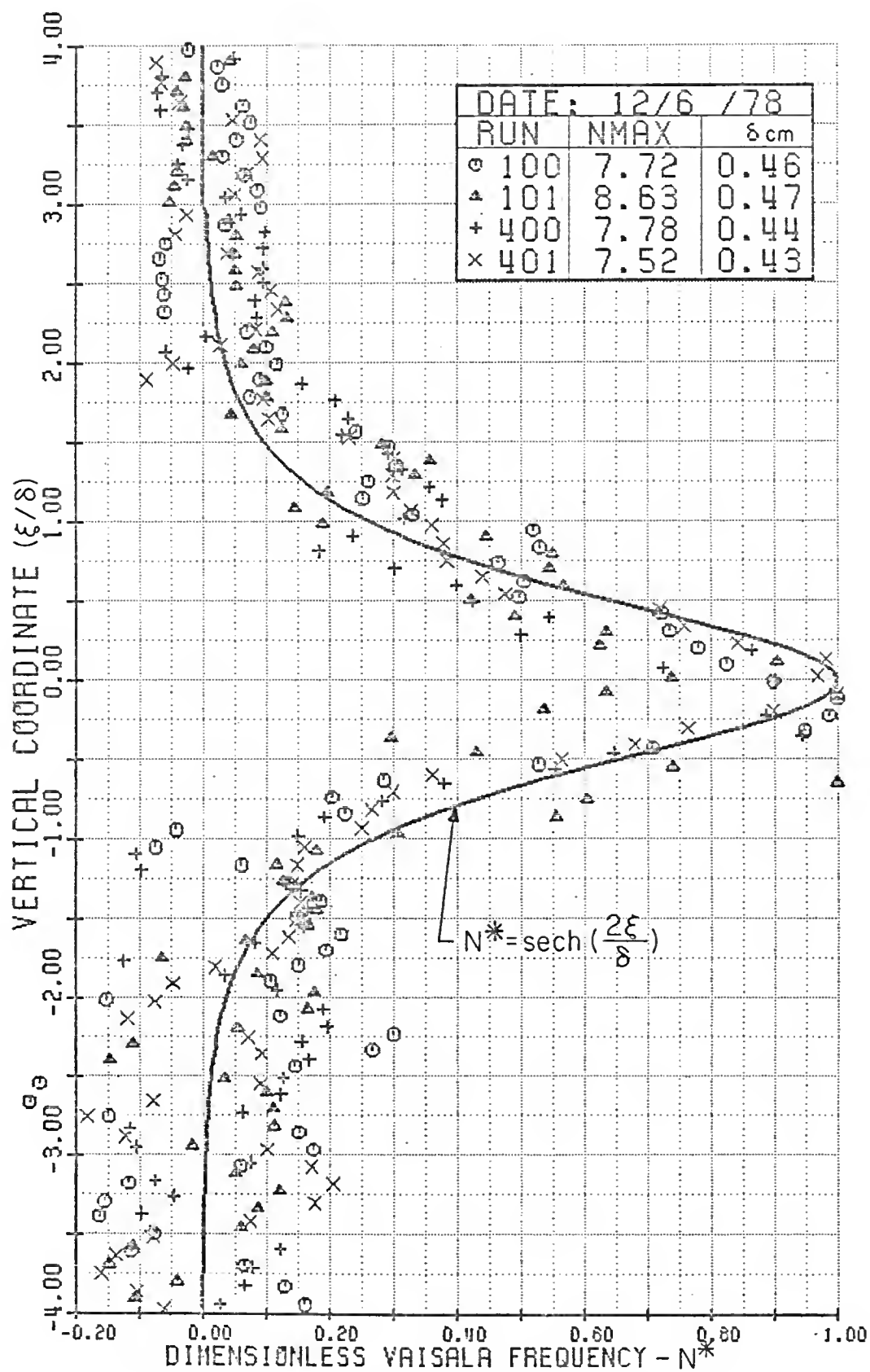


FIGURE 17: DIMENSIONLESS VAISALA FREQUENCY 12/6/78

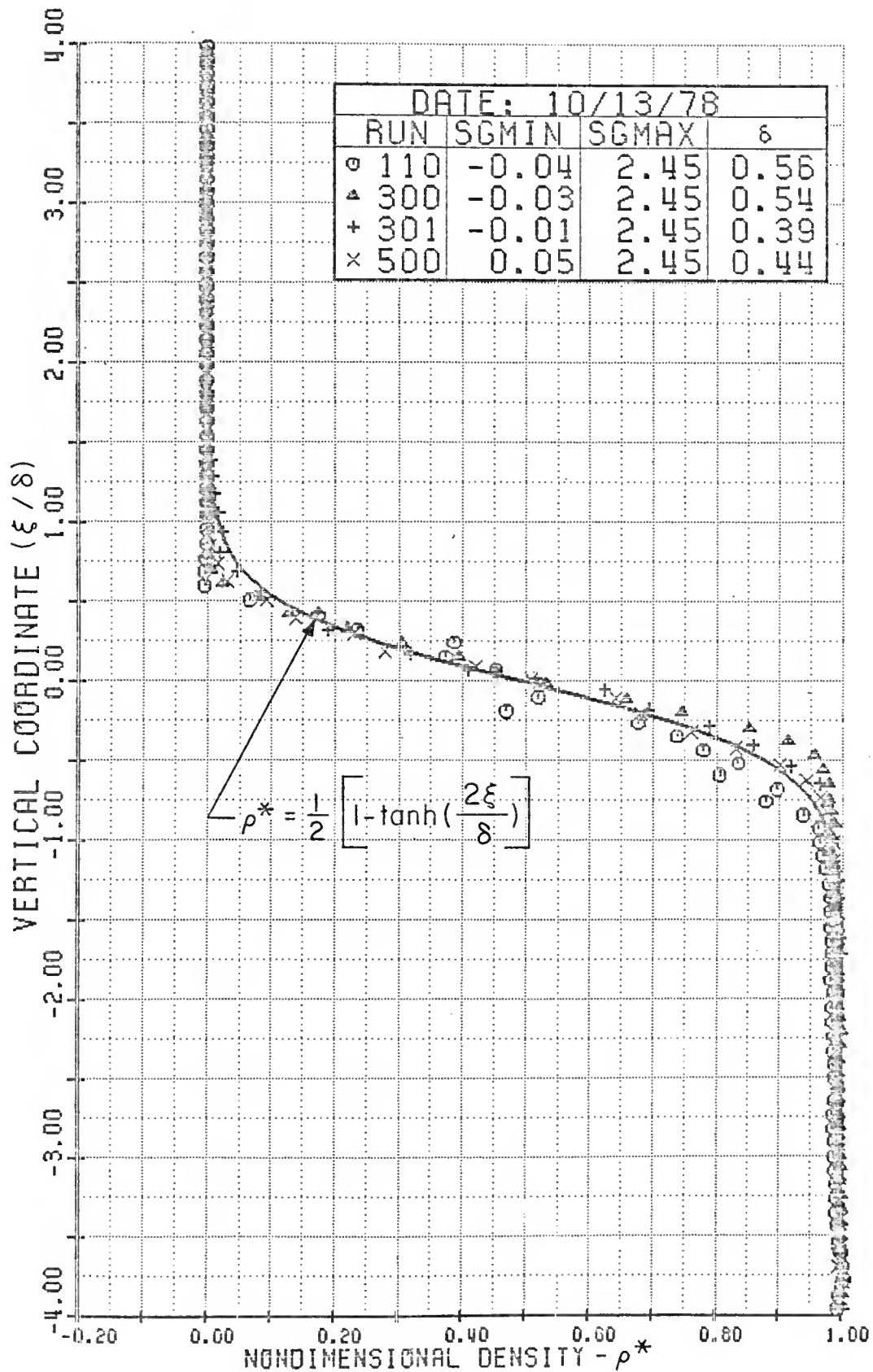


FIGURE 18: NONDIMENSIONAL DENSITY PROFILE 10/13/78

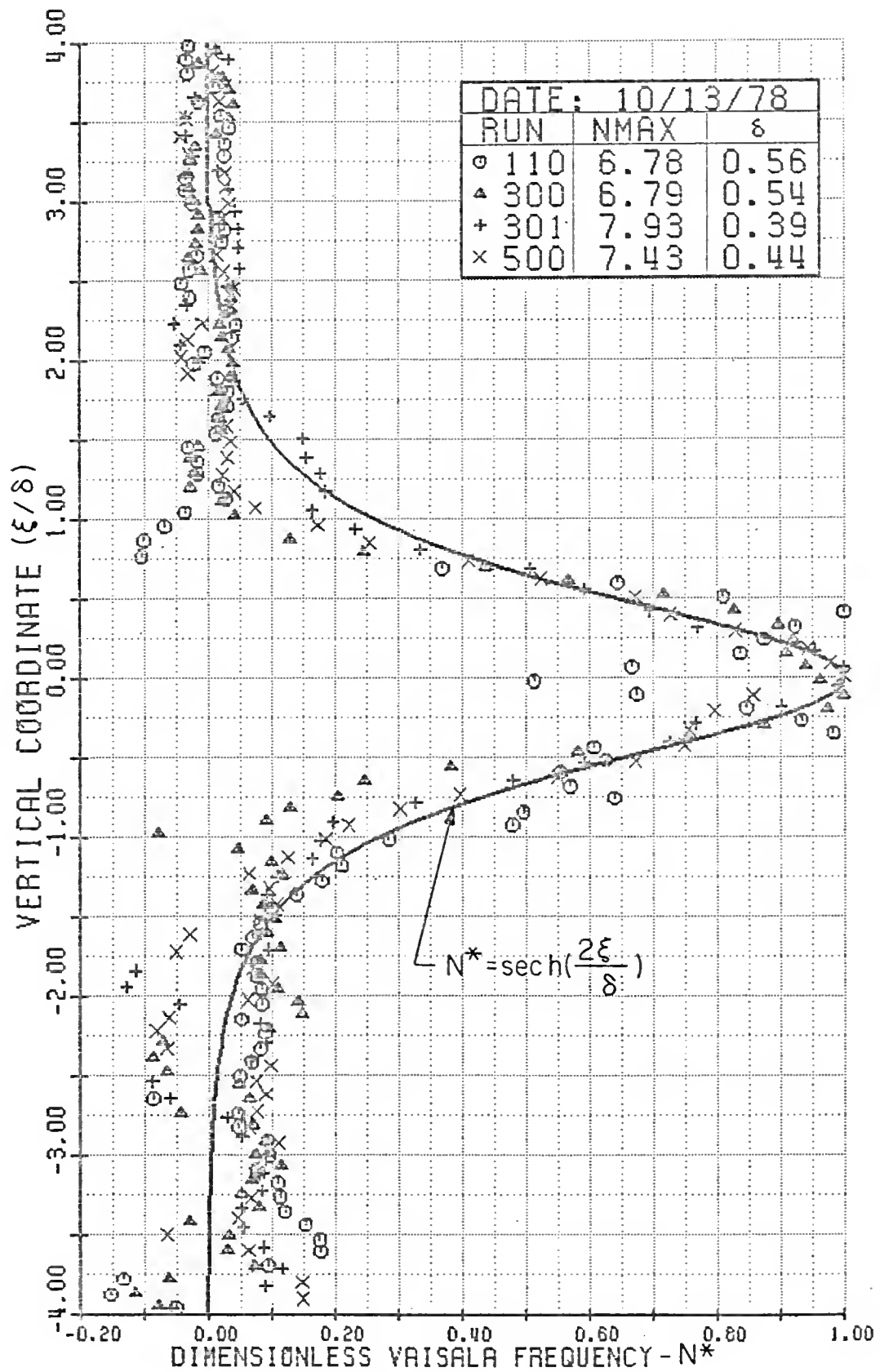


FIGURE 19: DIMENSIONLESS VAISALA FREQUENCY PROFILE 10/13/78

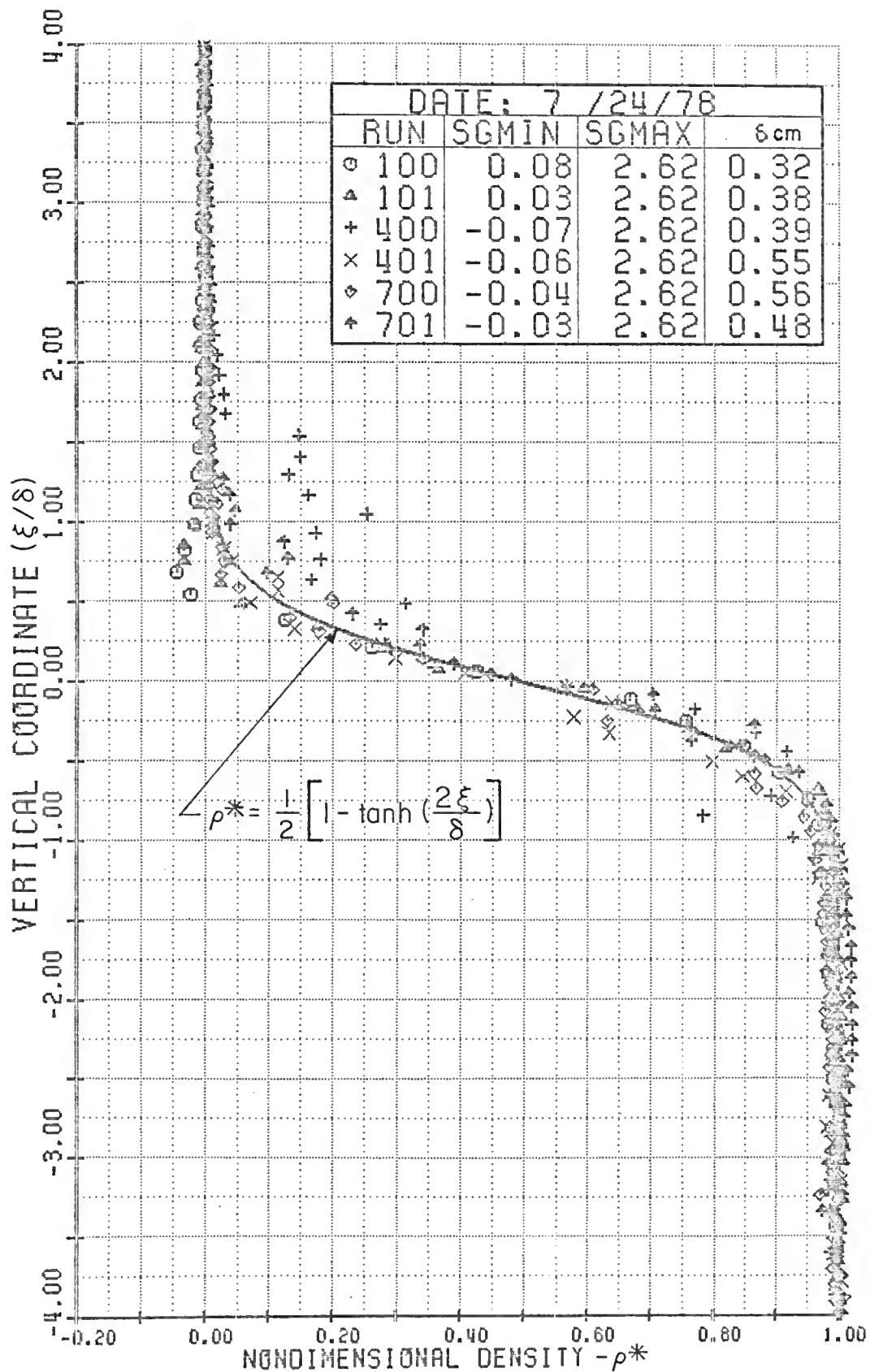


FIGURE 20: NONDIMENSIONAL DENSITY PROFILE 7/24/78

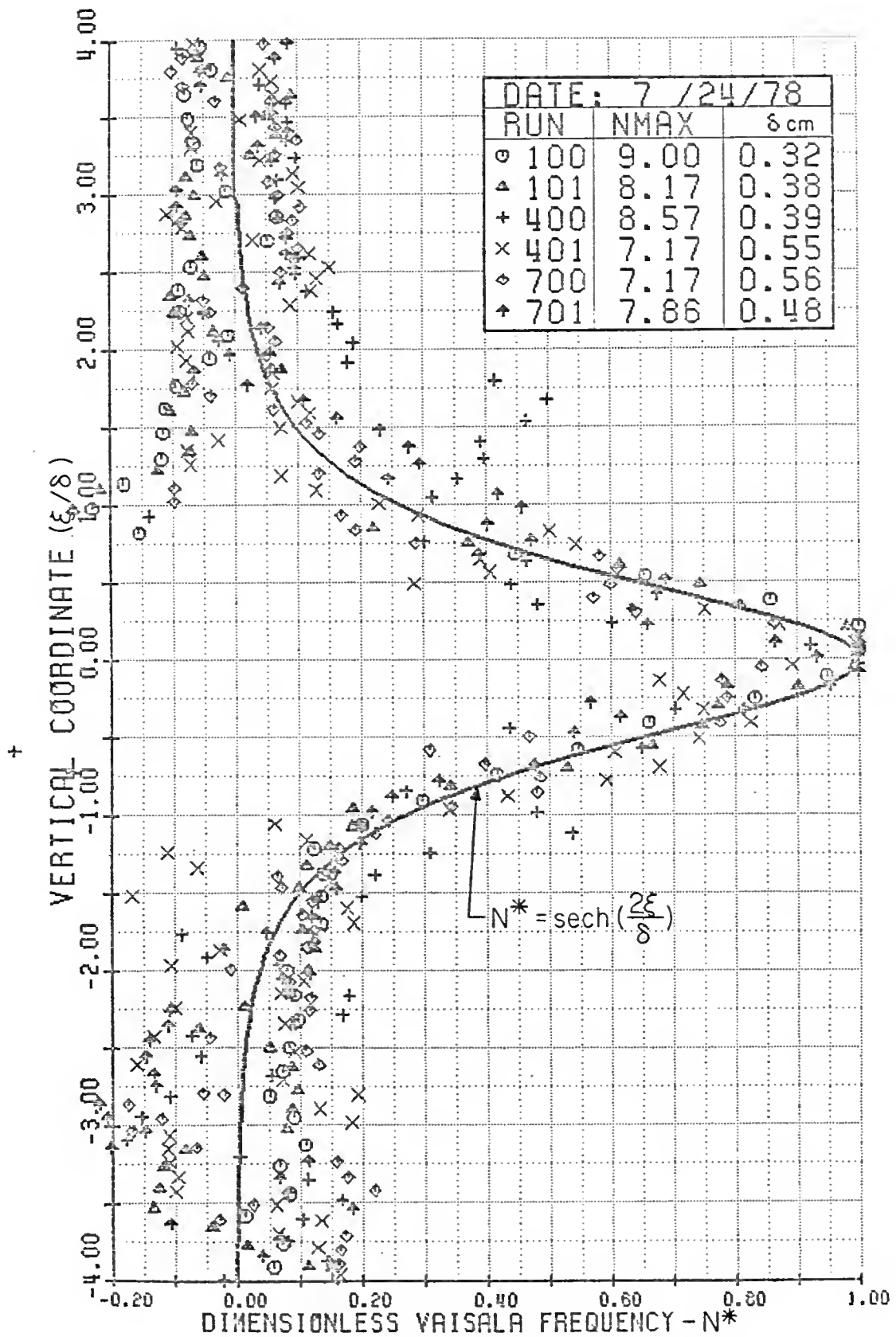


FIGURE 21: DIMENSIONLESS VAISALA FREQUENCY PROFILE 7/24/78

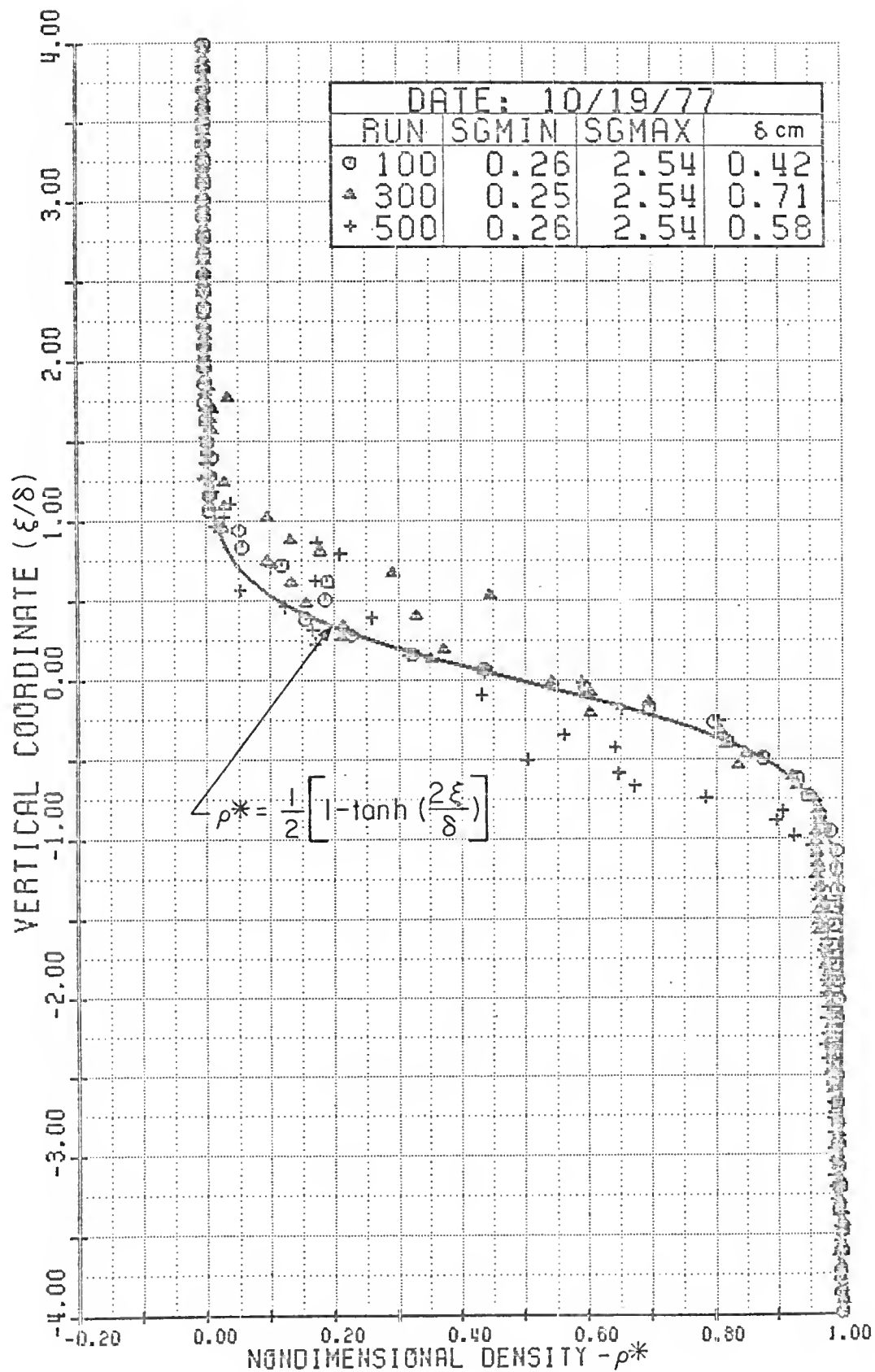


FIGURE 22: NONDIMENSIONAL DENSITY PROFILE 10/19/77

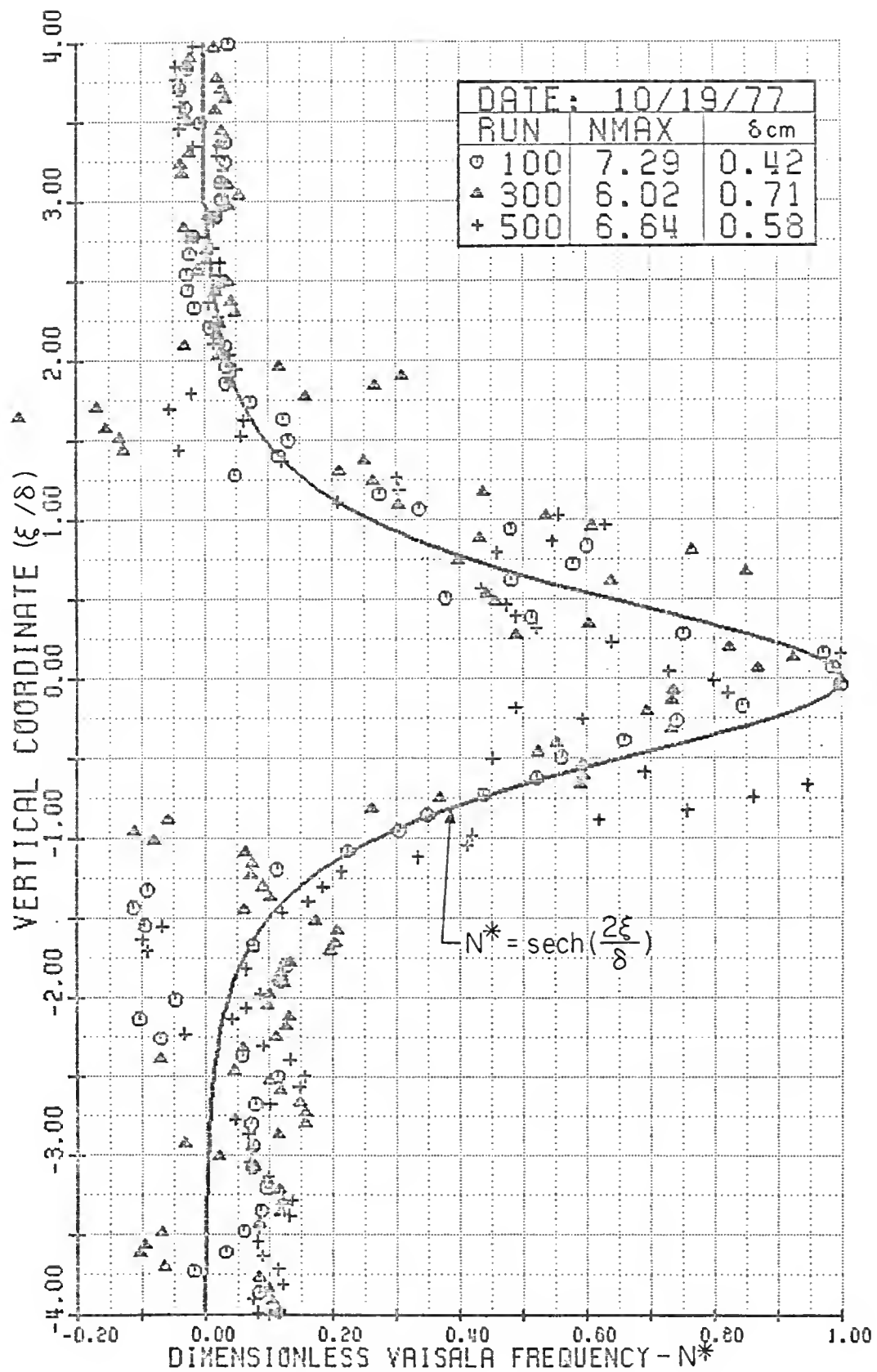


FIGURE 23: DIMENSIONLESS VAISALA FREQUENCY PROFILE 10/19/77

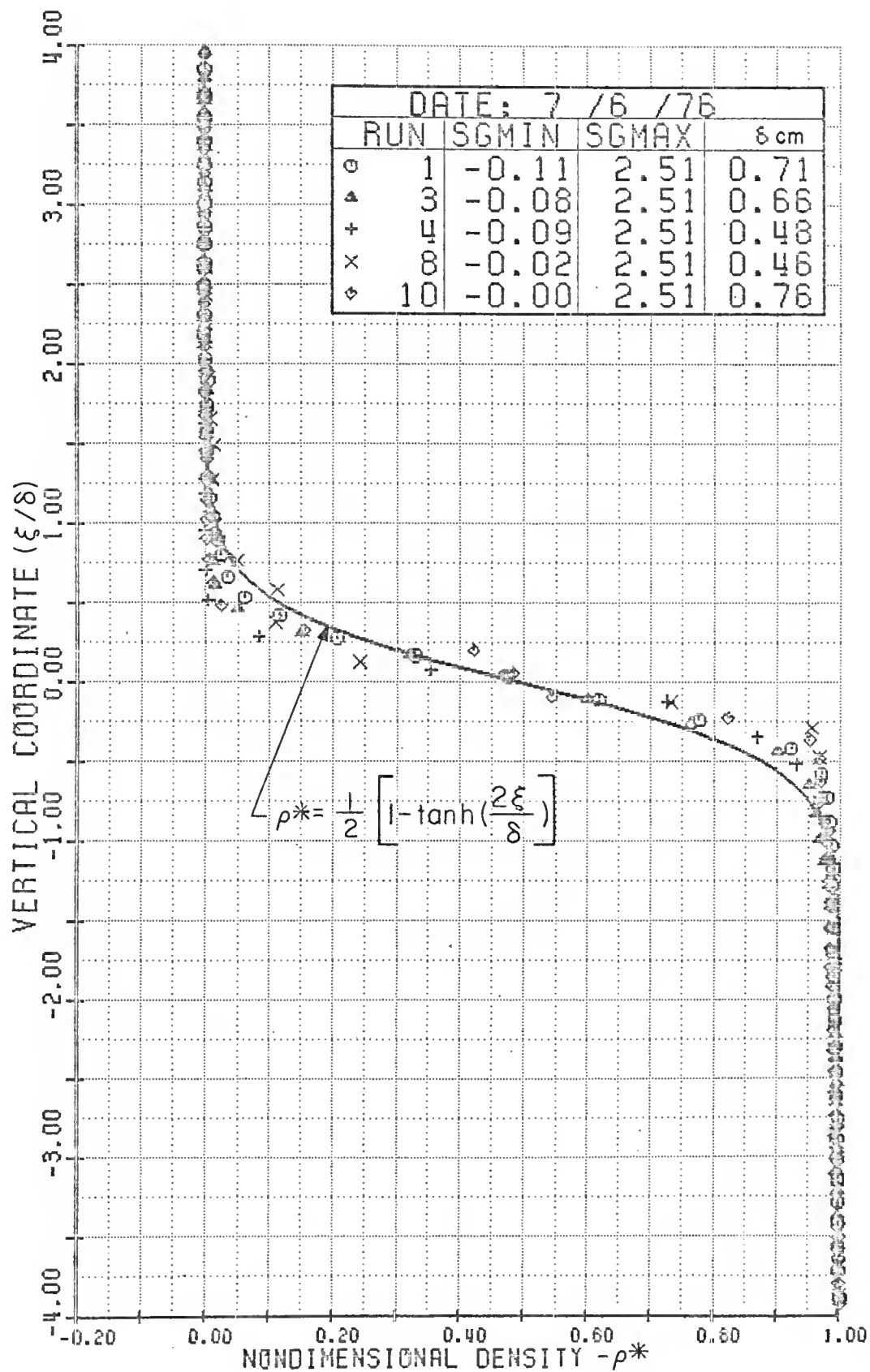


FIGURE 24: NONDIMENSIONAL DENSITY PROFILE 7/6/76

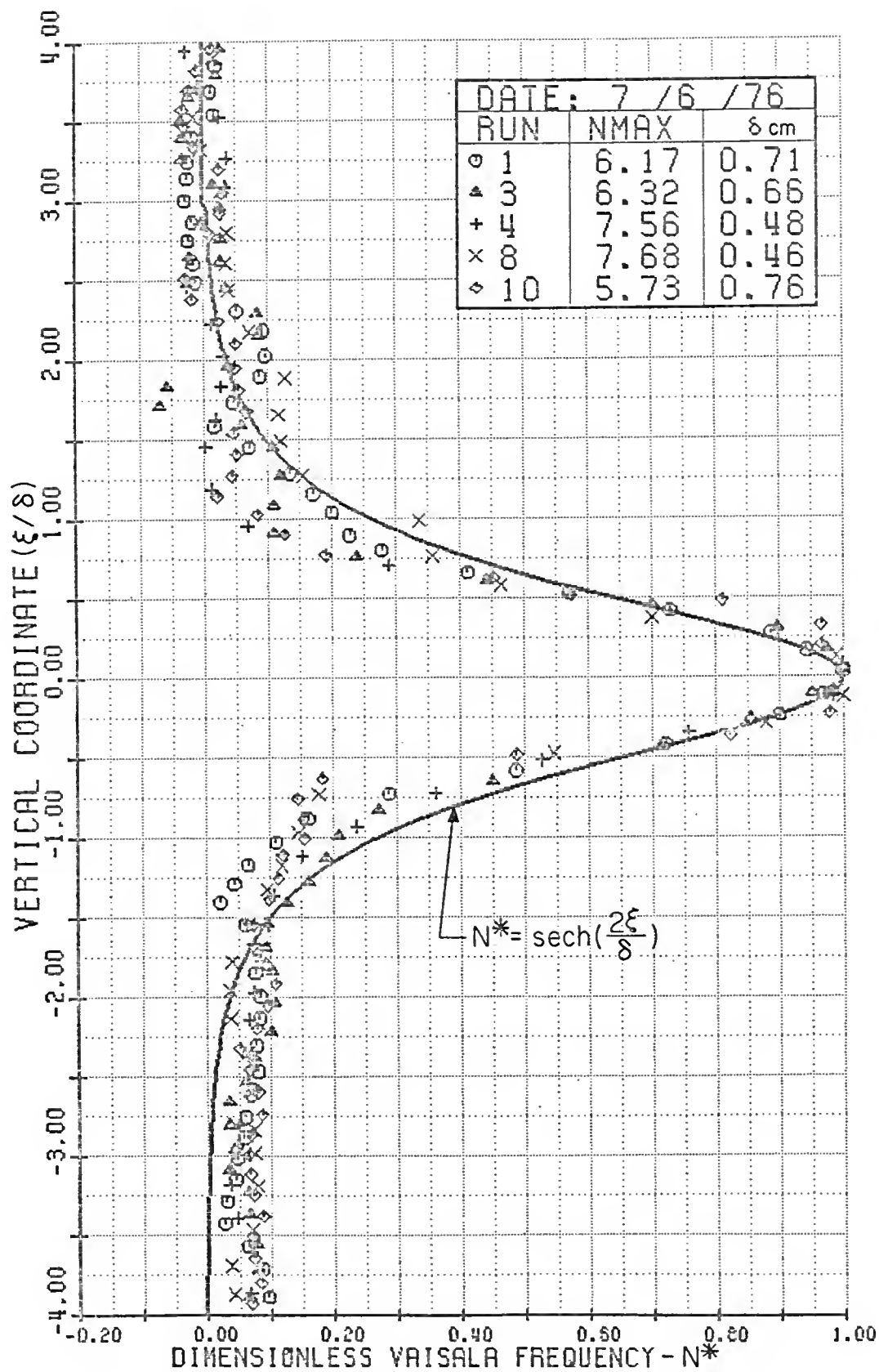


FIGURE 25: DIMENSIONLESS VAISALA FREQUENCY PROFILE 7/6/76

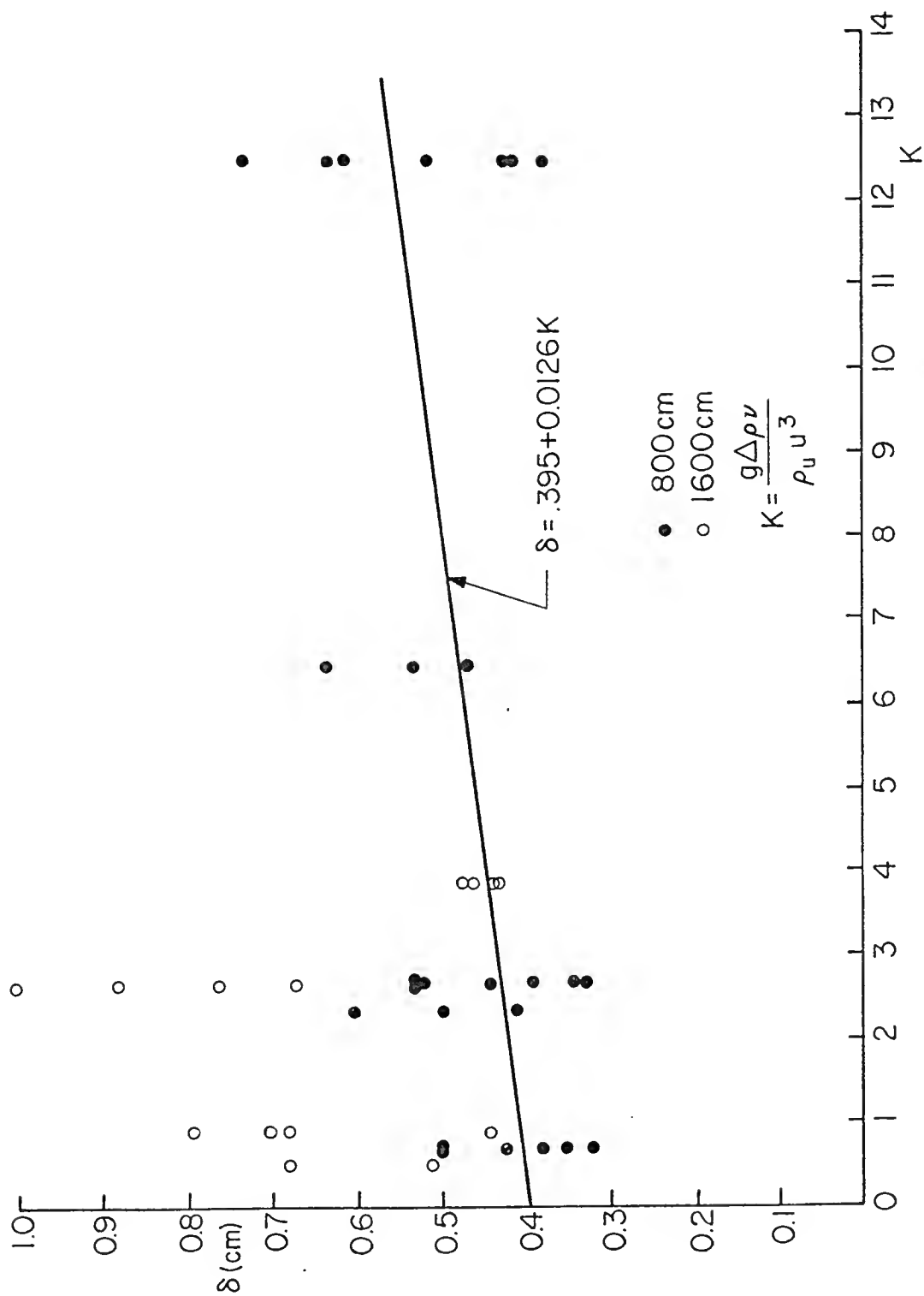


FIGURE 26: INTERFACIAL THICKNESS VS. KEULEGAN NUMBER

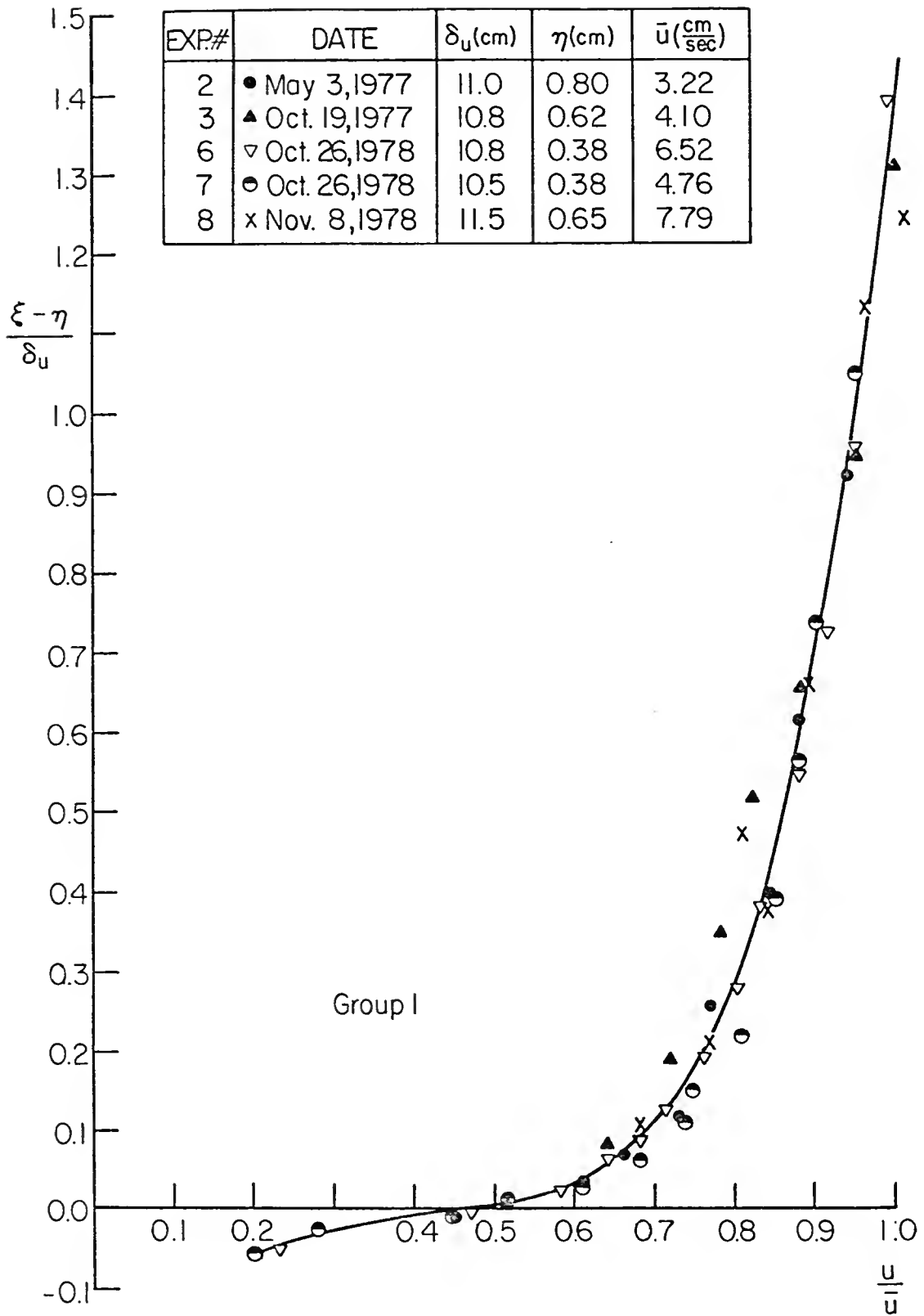


FIGURE 27: NORMALIZED MEAN VELOCITY PROFILE - GROUP 1

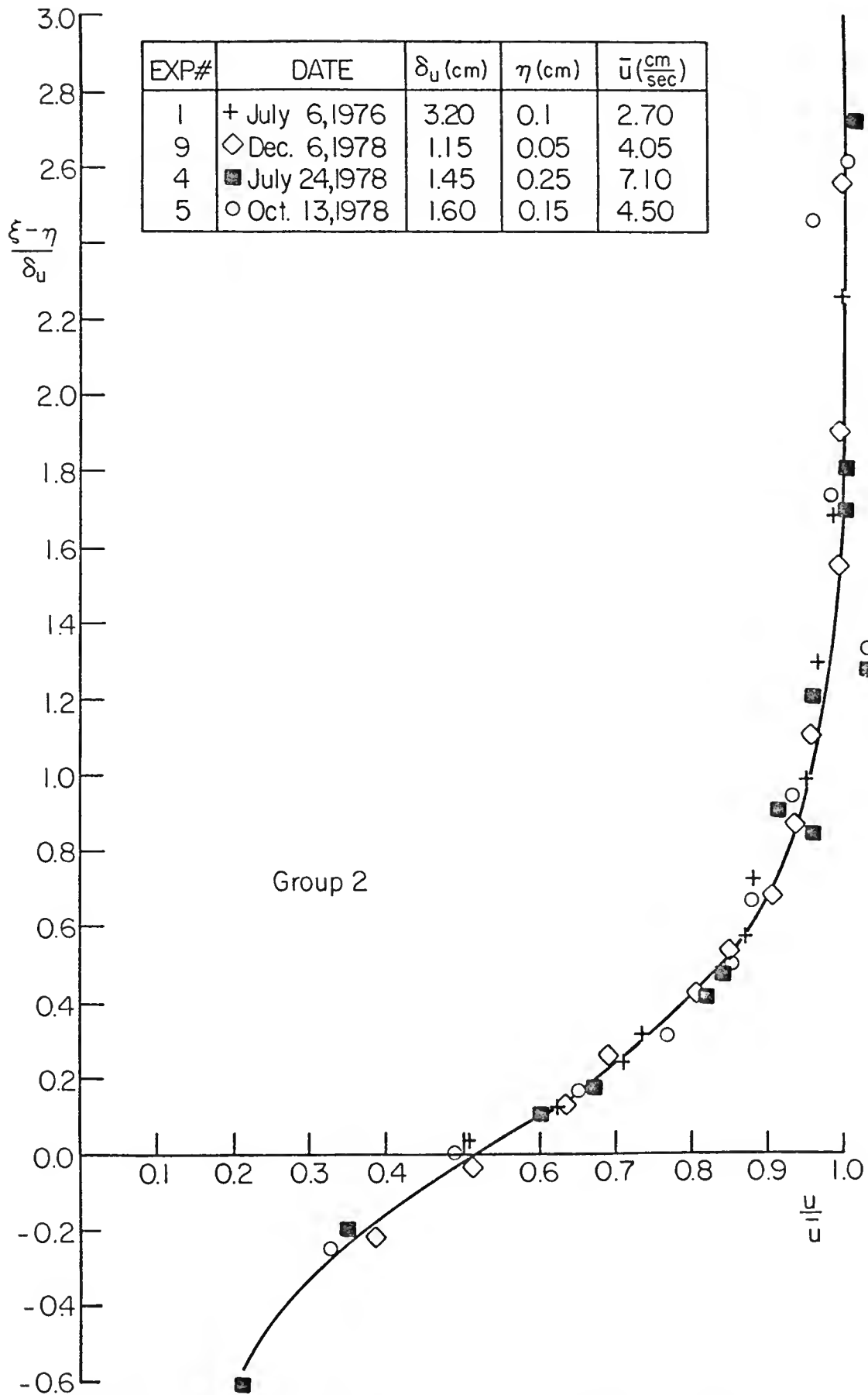


FIGURE 28: NORMALIZED MEAN VELOCITY PROFILE - GROUP 2

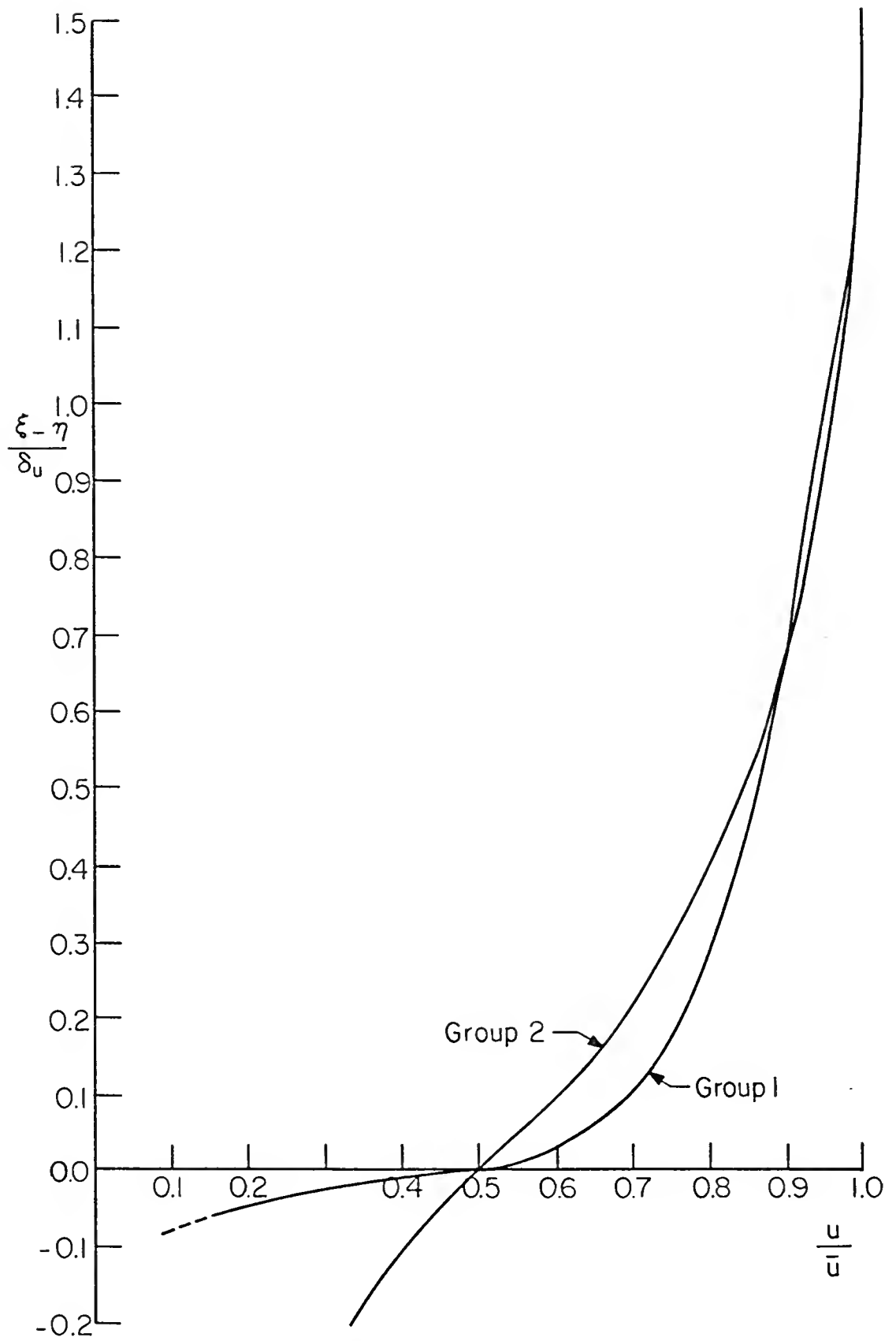


FIGURE 29: MEAN VELOCITY PROFILE COMPARISON

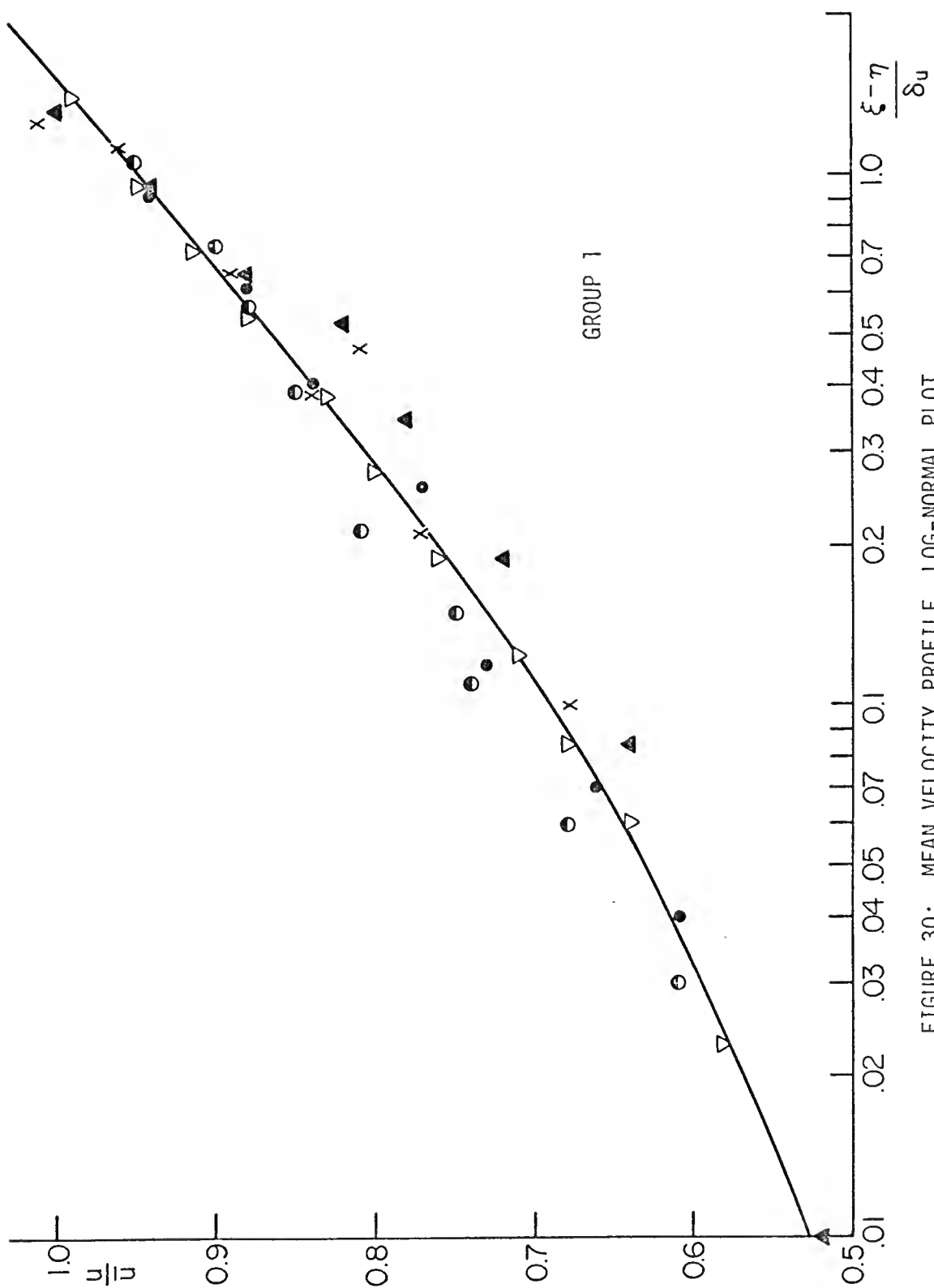


FIGURE 30: MEAN VELOCITY PROFILE, LOG-NORMAL PLOT

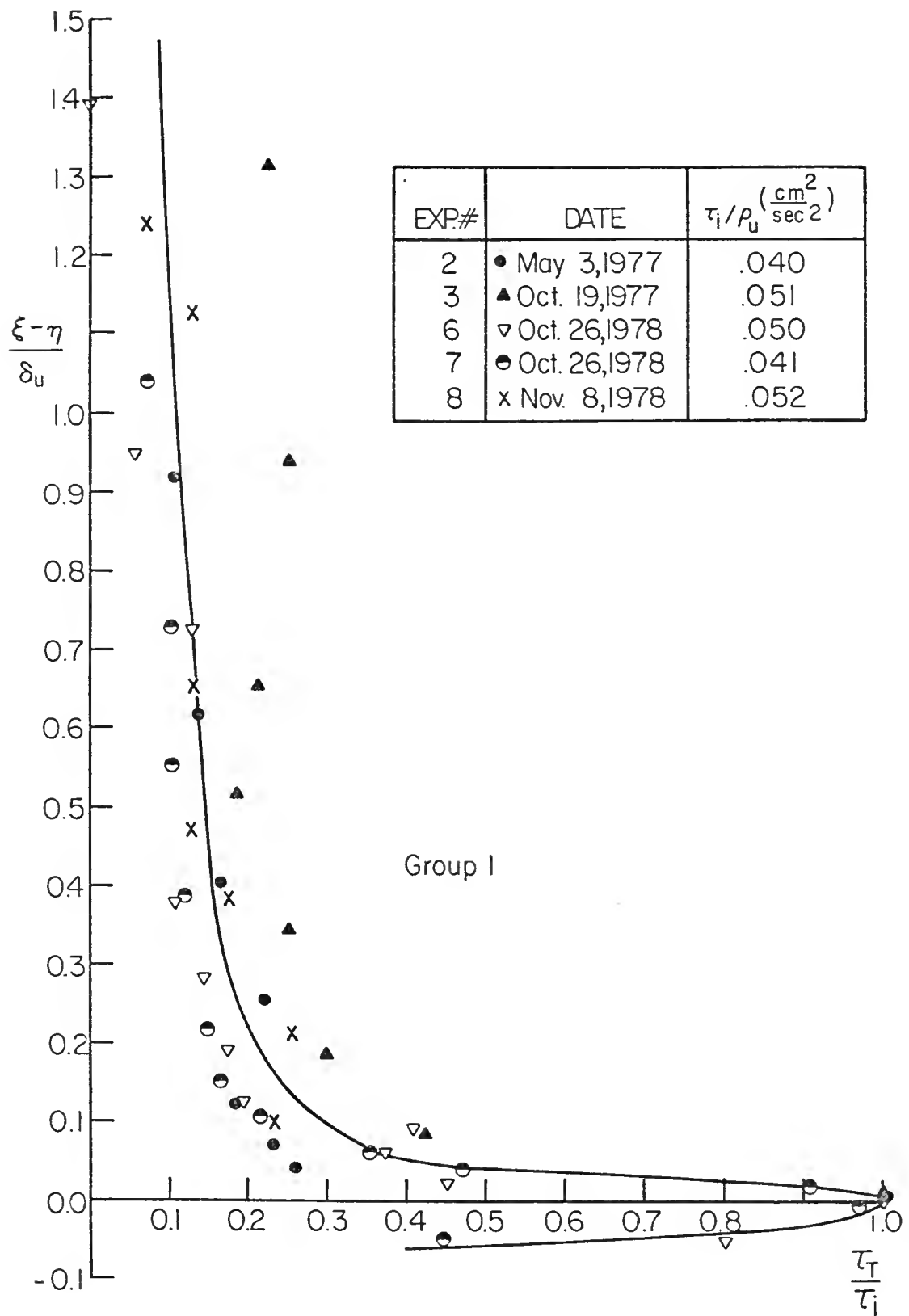


FIGURE 31: NORMALIZED SHEAR STRESS PROFILE - GROUP 1

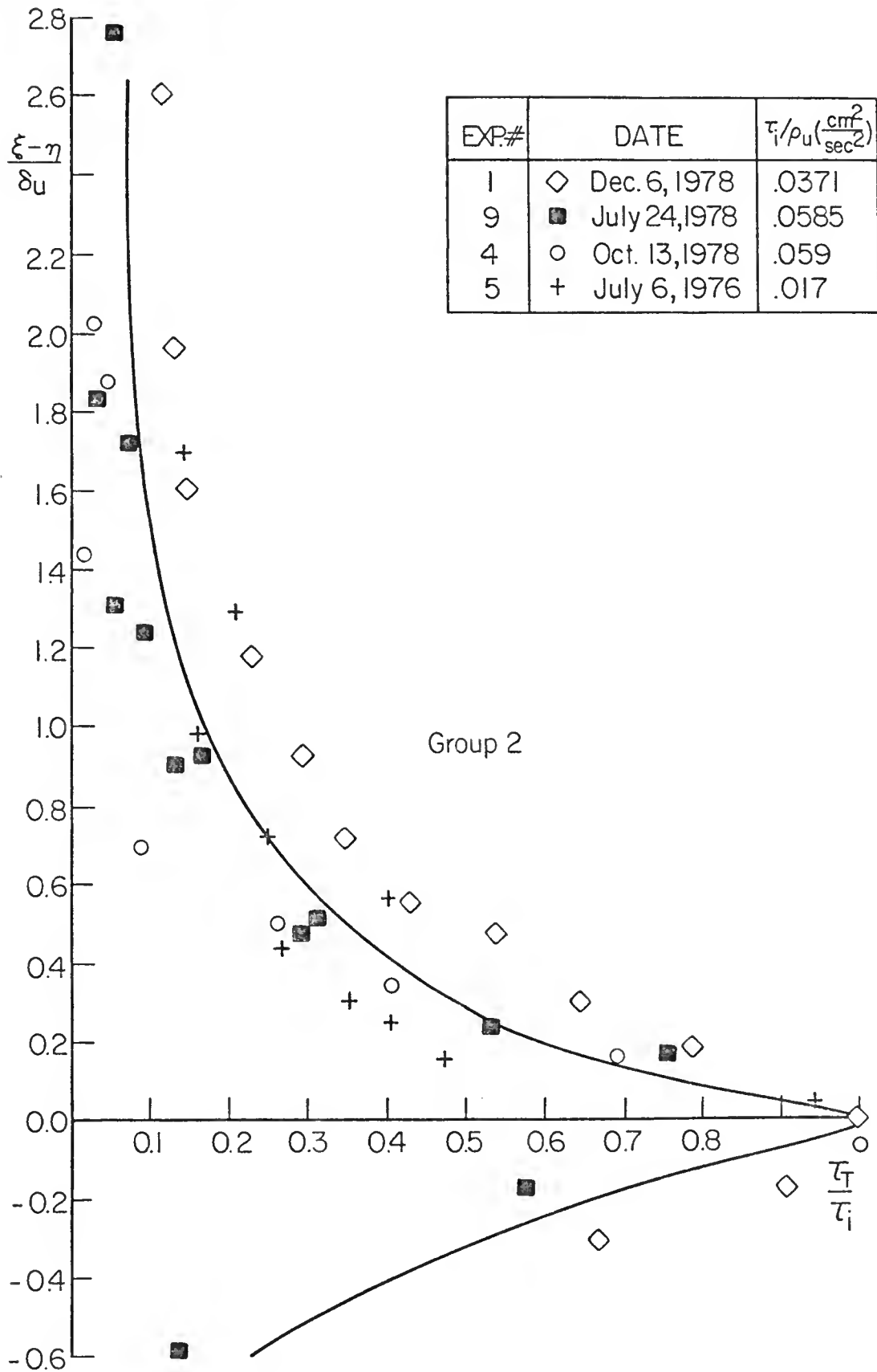


FIGURE 32: NORMALIZED SHEAR STRESS PROFILE - GROUP 2

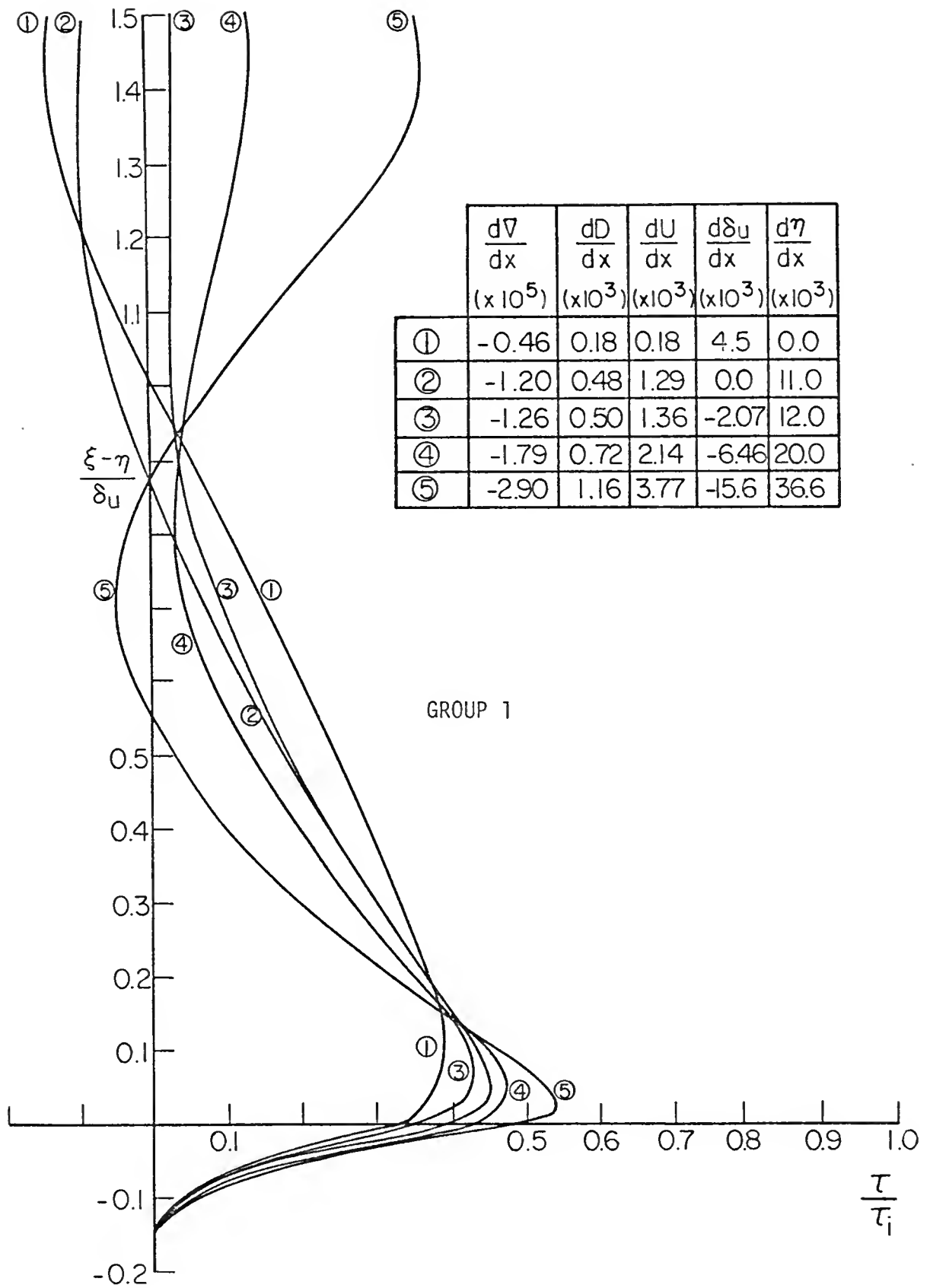


FIGURE 33: COMPUTED SHEAR STRESS PROFILES - GROUP 1

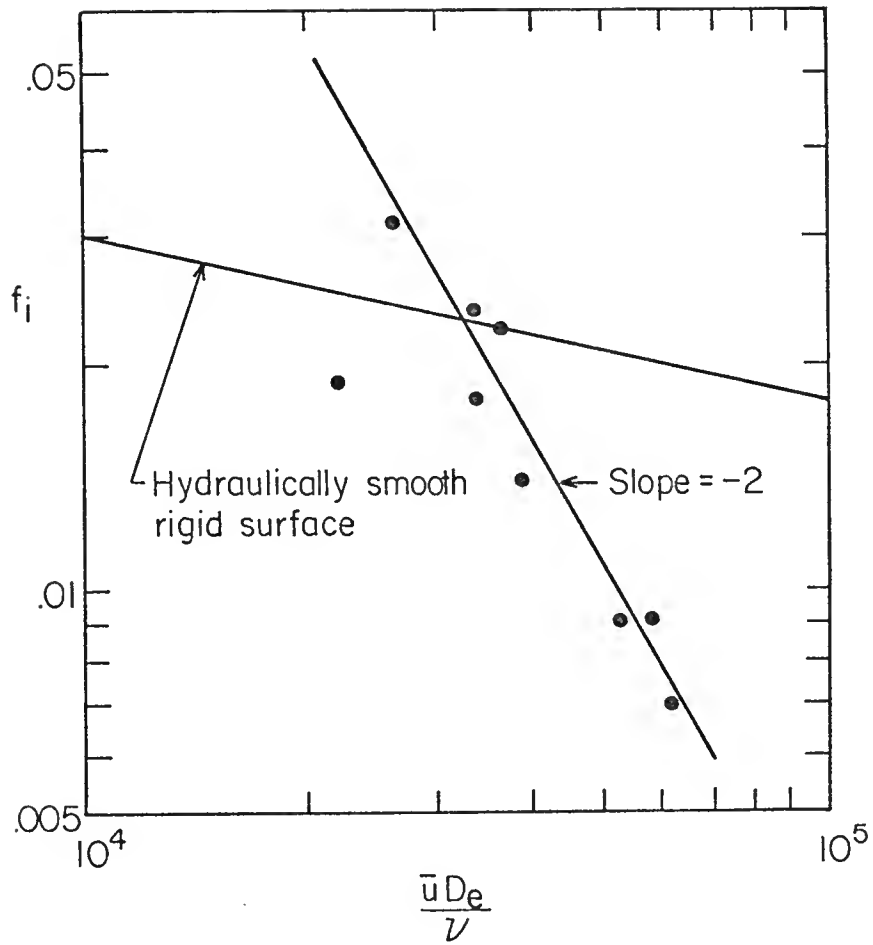


FIGURE 34: INTERFACIAL FRICTION FACTOR VS. REYNOLDS NUMBER

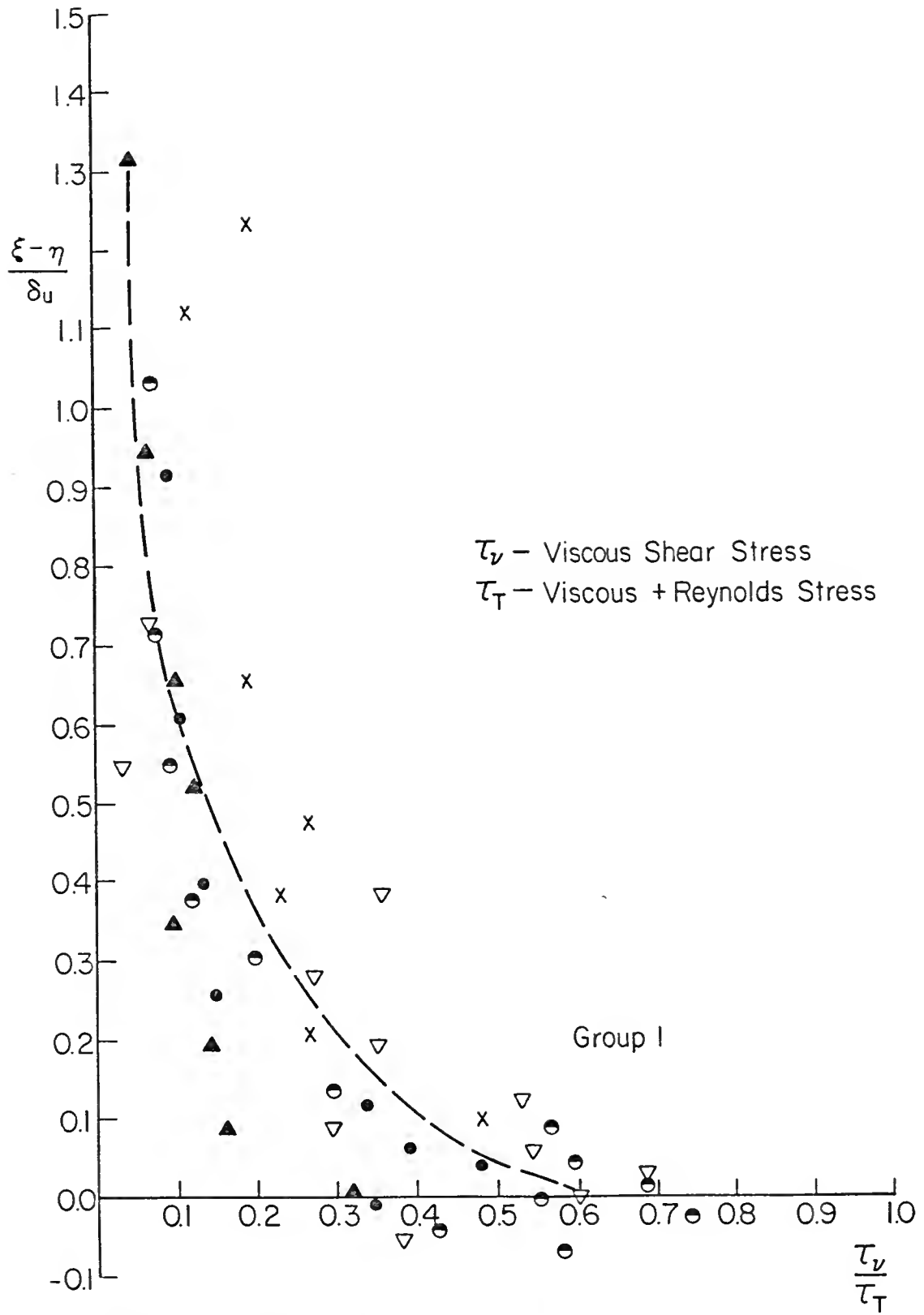


FIGURE 35: VISCOUS SHEAR STRESS/TOTAL STRESS - GROUP 1

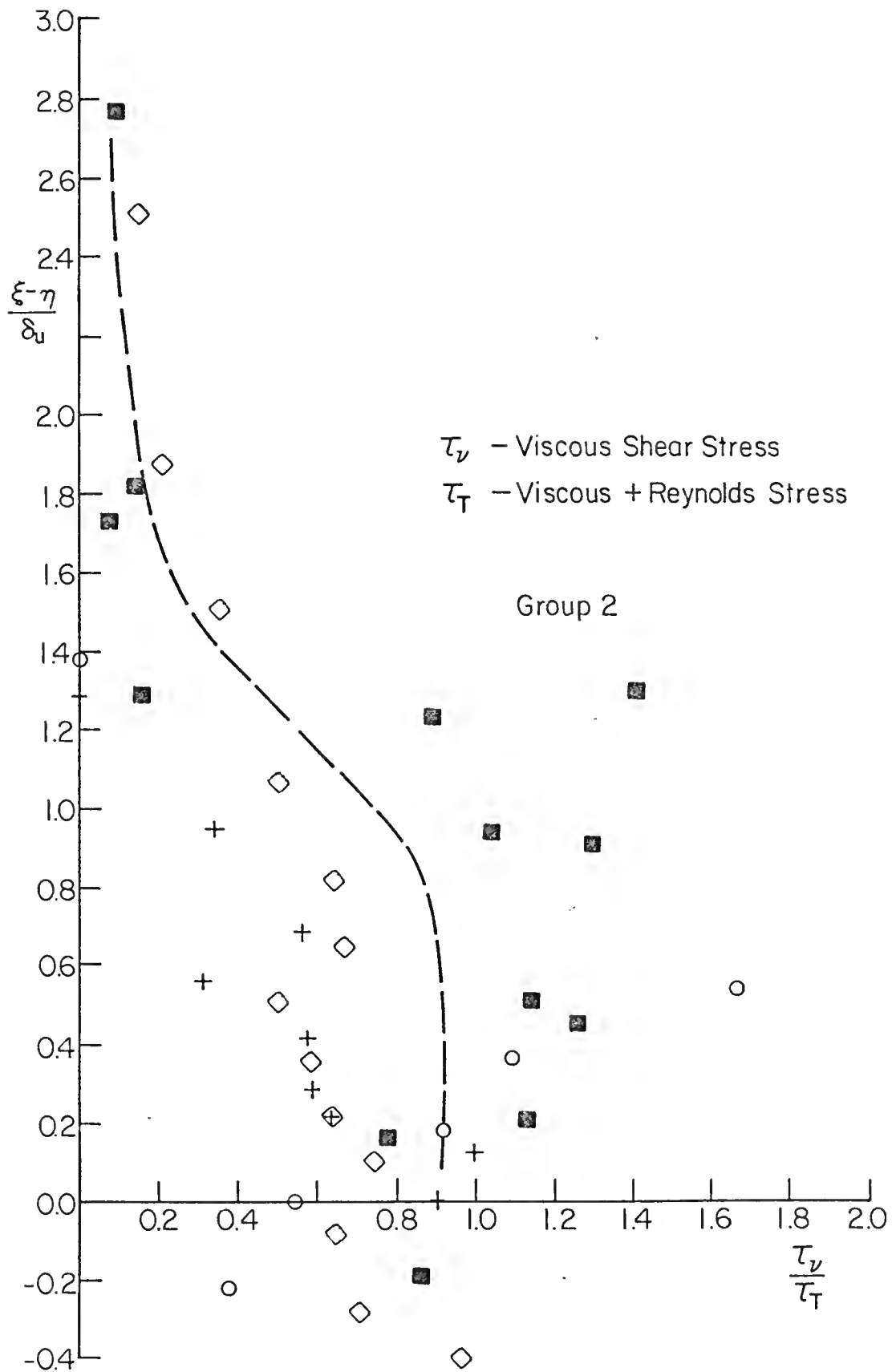


FIGURE 36: VISCOUS SHEAR STRESS/TOTAL STRESS - GROUP 2

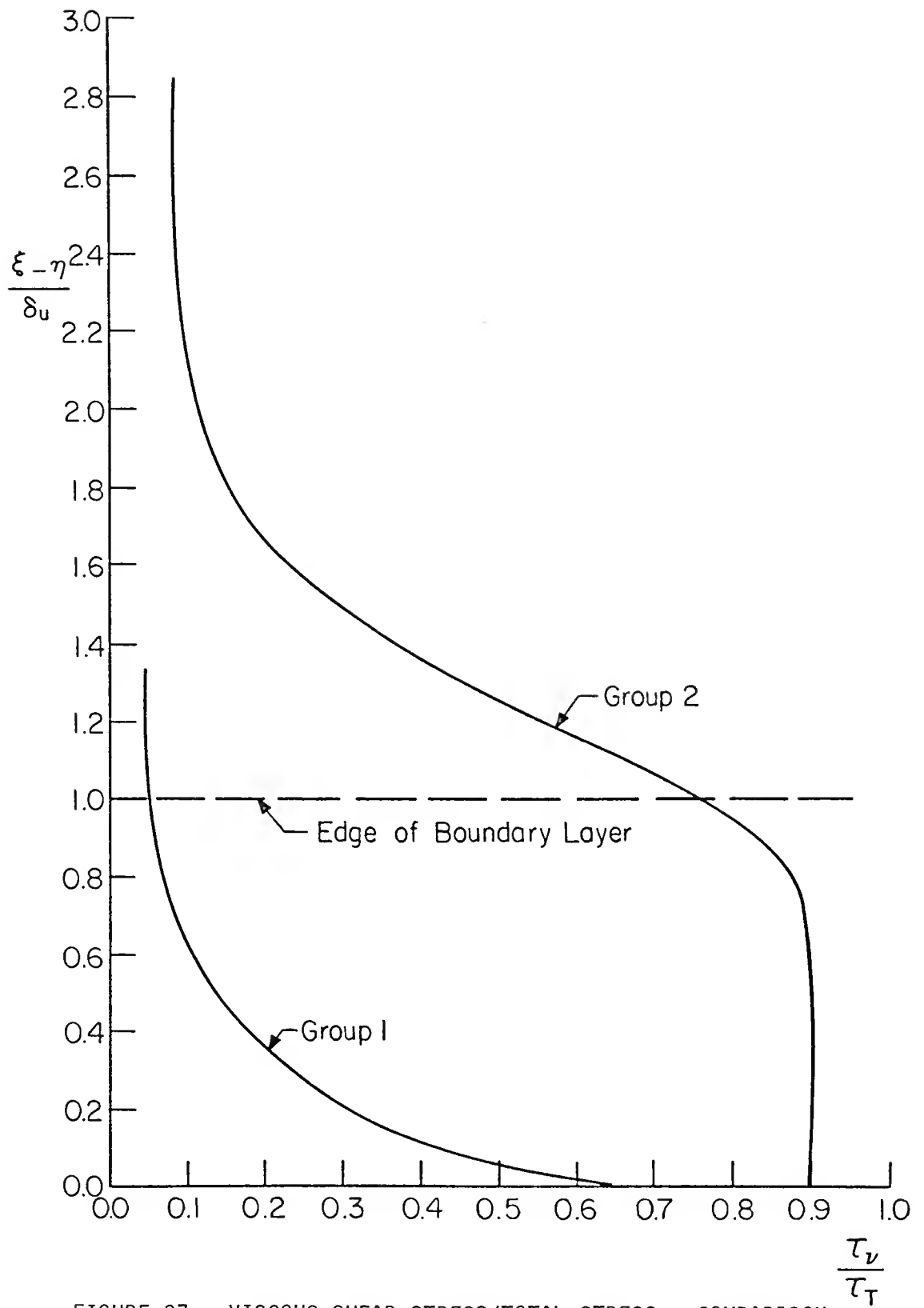


FIGURE 37: VISCOUS SHEAR STRESS/TOTAL STRESS - COMPARISON

CHAPTER V

CONCLUSIONS

This study has documented the structure of the velocity and density transition region in a two-layer flow by experimentally measuring the time mean velocity and density profiles, the turbulent and viscous shear stress and the turbulent energy spectra. In addition, the measured data were used to calculate the interfacial friction factor and the gradient Richardson number at the inflection point of the velocity profile. From these measurements, the following conclusions are reached.

1) In a weakly turbulent stratified shear flow, the interfacial region exists in one of two measurably different states. This bimodal character is not manifest in the magnitude of the flow properties, but in the distribution of these properties through the interfacial region.

2) No parameter or dimensionless number derived from global¹ or overall flow properties accurately predicts the existence of the two modes or groups. However, the gradient Richardson number at the

¹The term "global" in this context implies an integral scale property, for example the mean freestream velocity, the depth or width of the channel, the total density jump across the density interface, or the Richardson number based on the above. This is in contrast to the term "local" which refers to point properties such as the density or the gradient Richardson number based on the velocity and density gradient at a point within the flow.

inflection point of the velocity profile is distinctly different for each group. In group one the Richardson number is less than or equal to one, while in group two the converse is true.

3) The turbulent energy spectra measured within the boundary layer above the density interface indicate the presence of internal wave motions under group two conditions. Under group one conditions, no internal wave subrange is indicated by the energy spectra.

4) The total shear stress in the x-y plane is small everywhere except in a narrow region around the density interface where the stress reaches a maximum (Figures 31 and 32).

5) Over the range of conditions investigated, the interfacial friction factor is generally less than or equal to the friction factor for a hydraulically smooth surface at the same Reynolds number. Furthermore, the friction factor is proportional to Re^{-2} (see Figure 34). Therefore, the interfacial shear stress is independent of the freestream velocity when the Reynolds number is between 30,000 and 65,000.

The bimodal character of the flow near the interface is indicated by the mean velocity and shear stress profiles, the profiles of viscous/total shear stress, and the gradient Richardson number at the inflection point of the velocity profile. For each of the above, the experimental data divide into one of two distinct groups.

With respect to the mean velocity, there are two distinguishing characteristics. First, the group one profiles have a boundary layer thickness on the order of 10 cm while group two profiles have a thickness of only one to three centimeters. Secondly, when nondimensionalized, the velocity profiles for the two groups have significantly

different shapes. The group one profiles have a shape characteristic of a turbulent boundary layer over a rigid wall, possessing a log-linear distribution over a limited region. The group two profiles do not exhibit this characteristic shape. The nondimensionalized shear stress profiles also bifurcate, each group having a distinctly different shape.

The profiles of viscous/total shear stress point again to the bimodal character. For group one, the stress is 35 to 40 percent turbulent at the interface and the viscous component drops rapidly to less than 10 percent before reaching the outer edge of the boundary layer (see Figure 37). The group two data, however, show the shear stress to be about 90 percent viscous throughout the boundary layer falling off only outside this region. In addition, the data for group one have little variance while group two data are widely scattered.

The density profiles also show a character that correlates with the velocity groups. The group one experiments almost invariably exhibit an agitated density interface, many times possessing two or three distinct interfaces while the group two experiments usually have a smoothly changing density profile.

The fact that no global parameter or dimensionless number correlates significantly with the two groups indicates that the existence of the two dynamic states is not determined by the global properties of the flow. Even the interfacial friction factor, which is a measure of the maximum shear stress at the interface, shows no significant correlation with the groups. In contrast, the gradient Richardson number at the inflection point of the velocity profile is found to have a strong correlation with the two groups. This verifies the fact that the mean

velocity and density distributions through the transition region are significantly different from one group to the other. Since the gradient Richardson number is calculated from the velocity and density distribution, it can not be considered as the factor that dictates which dynamic state will exist, but must be viewed only as an indicator of which state exists at the time. The significance of the gradient Richardson number at the inflection point of the velocity profile is brought into focus when combined with two other observations. First, the velocity inflection point is always at or above the density inflection point. Second, the density transition region is always thinner than the velocity transition region (at least for this flow regime). These two factors combined imply that the gradient Richardson number everywhere above the velocity inflection point is less than or equal to the Richardson number at the velocity inflection point. Therefore, the gradient Richardson number is less than or equal to one everywhere above the inflection point for group one. For group two, this is not the case. To maintain turbulence, the gradient Richardson number must be less than or equal to one (see Turner, 1973).

The author suggests the above facts point to the following conclusions. First, the two groups represent, in one case, a well developed turbulent boundary layer (group one) and, in the second, a gravitationally stabilized boundary layer (group two). This conclusion is supported by the fact that the turbulent energy spectra, measured within the boundary layer above the density interface, indicate the existence of an internal wave subrange for group two experiments. The energy spectra measured in the same region (although not at exactly the same

point) show no such subrange for group one experiments. Second, since no correlation is found between the dynamic modes (groups) and any of the global flow parameters, the author believes the data groupings must be related to the initial conditions at the start of each experiment. Although there was no conscious or observable difference in the initiation of each experiment, subtle differences may have been present.

The shear stress profiles for both groups (Figures 31 and 32) have very unexpected shapes which are difficult to explain. The stress is small everywhere except in a narrow region around the interface, where the magnitude increases rapidly. One to three centimeters below the interface the shear stress goes to zero. This is in agreement with the observation of little or no motion below the interface, even after the flow in the upper layer has been in motion for three to six hours.

An attempt was made to solve equations 2.1 through 2.3 in order to determine the origin of the unexpected stress profile. The equations were solved (see Appendix E) under the assumption that the velocity and density profiles were each self-similar and that each required only one length scale for nondimensionalization. This approach failed to reproduce accurately the measured shear stress profiles (compare Figures 31 and 33). One can only assume that significant terms are omitted from equations 2.1 through 2.3 (terms which were assumed small, see Appendix E) or that the self-similarity assumption is incorrect. The author believes the latter is more likely, since nondimensionalizing the velocity profile by one length scale implies the boundary layer above the interface grows at the same rate as the boundary layer below

the interface. This may not be the case, because the flow above the interface appears turbulent while the flow below the interface is laminar.

APPENDIX A

PROFILE SHAPING ELEMENT

The profile shaping element (PSE) was designed to produce, at the entrance to the test section, a velocity profile which closely approximates fully developed turbulent flow in a rectangular channel, thereby minimizing longitudinal variations within the test section. The fully developed profile is closely represented by:

$$U(y,z) = U_{\max} \left(\frac{z}{D}\right)^{1/7} \left(\frac{w-y}{w}\right)^{1/7} \quad A.1$$

where $U_{\max} = U(y=0, z=D)$,

w is the half-width of the tank, D the depth of the channel, y the lateral distance from the center line of the tank, and z the vertical distance from the bottom.

The PSE consists of a bundle of thin-wall PVC tubing, each tube cut to a precise length based on its position within the cross section. The length of each tube was determined in the following way:

Assuming laminar flow through all the tubes, the total pressure drop through the tubes, P_T , is given by,

$$P_T = P_f + P_e \quad A.2$$

where P_f is the pressure loss due to friction and P_e is the pressure loss due to entrance and exit effects. P_T and P_e were assumed to be the same for all the tubes, while,

$$P_f = C U(y,z) L(y,z) \quad A.3$$

where C is a constant of proportionality, the magnitude of which depends on the fluid viscosity and the diameter of the tubes. Substituting equations A.3 and A.2 into equation A.1,

$$\frac{P_T - P_e}{C} = U_{\max} \left(\frac{z}{D}\right)^{1/7} \left(\frac{w-y}{w}\right)^{1/7} L(y,z) \quad A.4$$

at $z = D$ and $y = 0$ equation A.4 becomes,

$$\frac{P_T - P_e}{C} = U_{\max} L(0,D) \quad A.5$$

Substituting equation A.5 back into A.4:

$$L(y,z) = \frac{L(0,D)}{\left(\frac{z}{D}\right)^{1/7} \left(\frac{w-y}{w}\right)^{1/7}} \quad A.6$$

Time and labor considerations prevented the diameter of the tubes from being very small even though the requirements of laminar flow dictated the opposite. Thus, tubes with 1.91 cm (0.75-inch) I.D. and 2.13 cm (0.84-inch) O.D. were chosen. The tubes were stacked in a triangular arrangement alternating between 28 and 27 tubes per row. A total of 32 rows was stacked together requiring a total of 880 tubes.

To reduce entrance and exit effects the shortest tube, $L(0,D)$, was cut nine inches long so that all the tubes would have a length-to-diameter ratio greater than 12. The length of each tube (in inches) was determined by,

$$L(y,z) = \frac{9.0}{\left(\frac{z}{D}\right)^{1/7} \left(\frac{w-y}{w}\right)^{1/7}} \quad A.7$$

The requirement that the flow remain laminar determines the maximum allowable velocity through the PSE. The criteria for laminar flow are given by,

$$\frac{U D}{\nu} < 2200$$

for $D = 1.91 \text{ cm}$ and $\nu = 0.01 \frac{\text{cm}^2}{\text{sec}}$

$$U_{\text{max}} \leq 11.5 \text{ cm/s}$$

Due to the many assumptions made in the design of this unit, the resulting velocity profile was not expected to match the equilibrium profile exactly. Indeed, when the upper layer meets the salt layer a readjustment in the velocity profile must take place. The intent of the PSE was to minimize longitudinal variations; it was not expected to eliminate them completely.

APPENDIX B

INDIVIDUAL DENSITY PROFILES

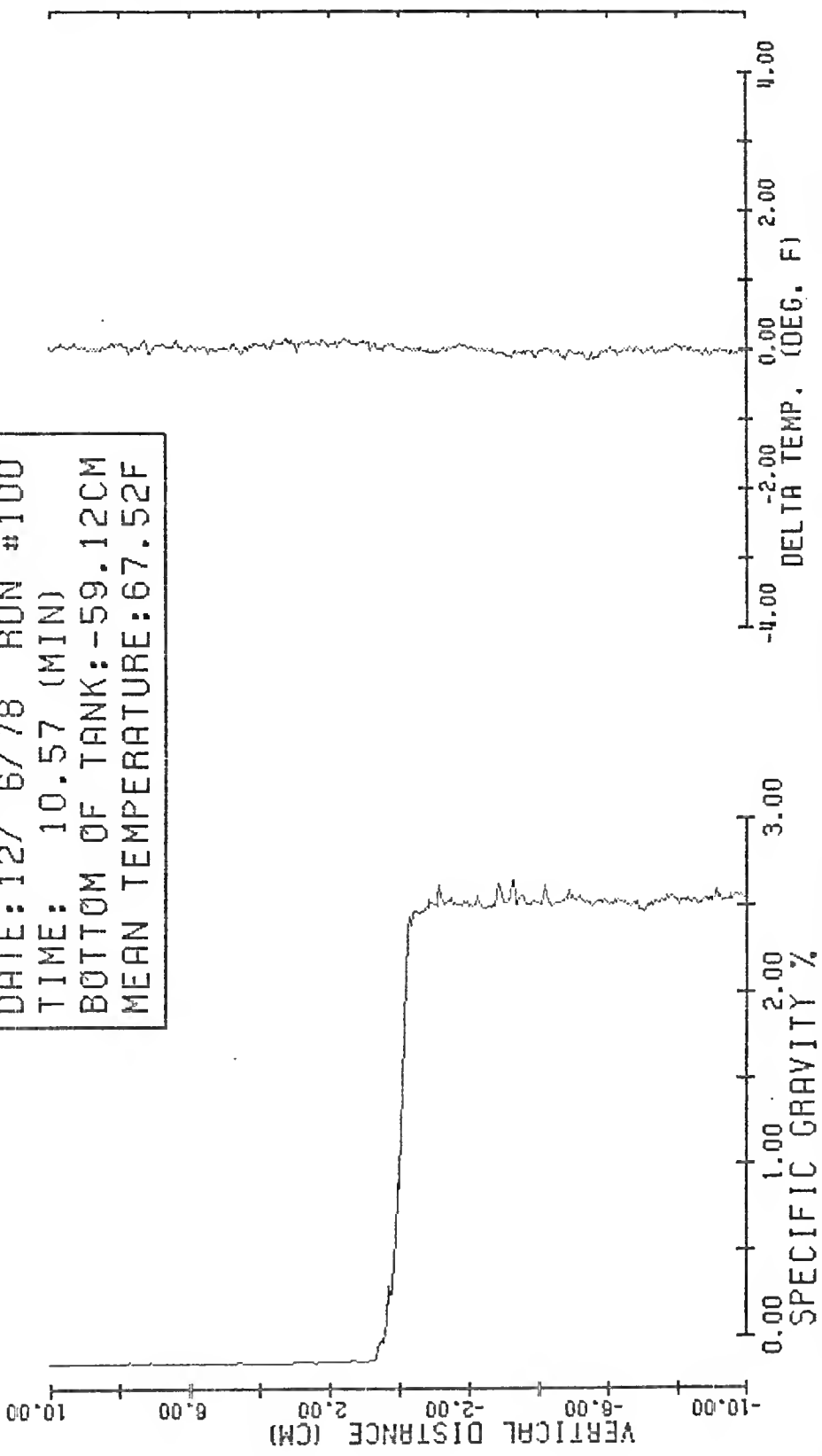
This appendix contains the individual quasi-instantaneous profiles of density, temperature, and Vaisala frequency obtained by the constant speed traverse technique. Throughout the appendix there are two plates for each run. The first contains the profiles of density and temperature, while the second shows the corresponding profiles of filtered density and Vaisala frequency.

The vertical coordinate is always referenced to the interface, defined as the point where the density equals the average density of the upper and lower layers. The interface is, in turn, referenced to the bottom of the tank. The density is given in terms of percent specific gravity (S.G. %), defined by:

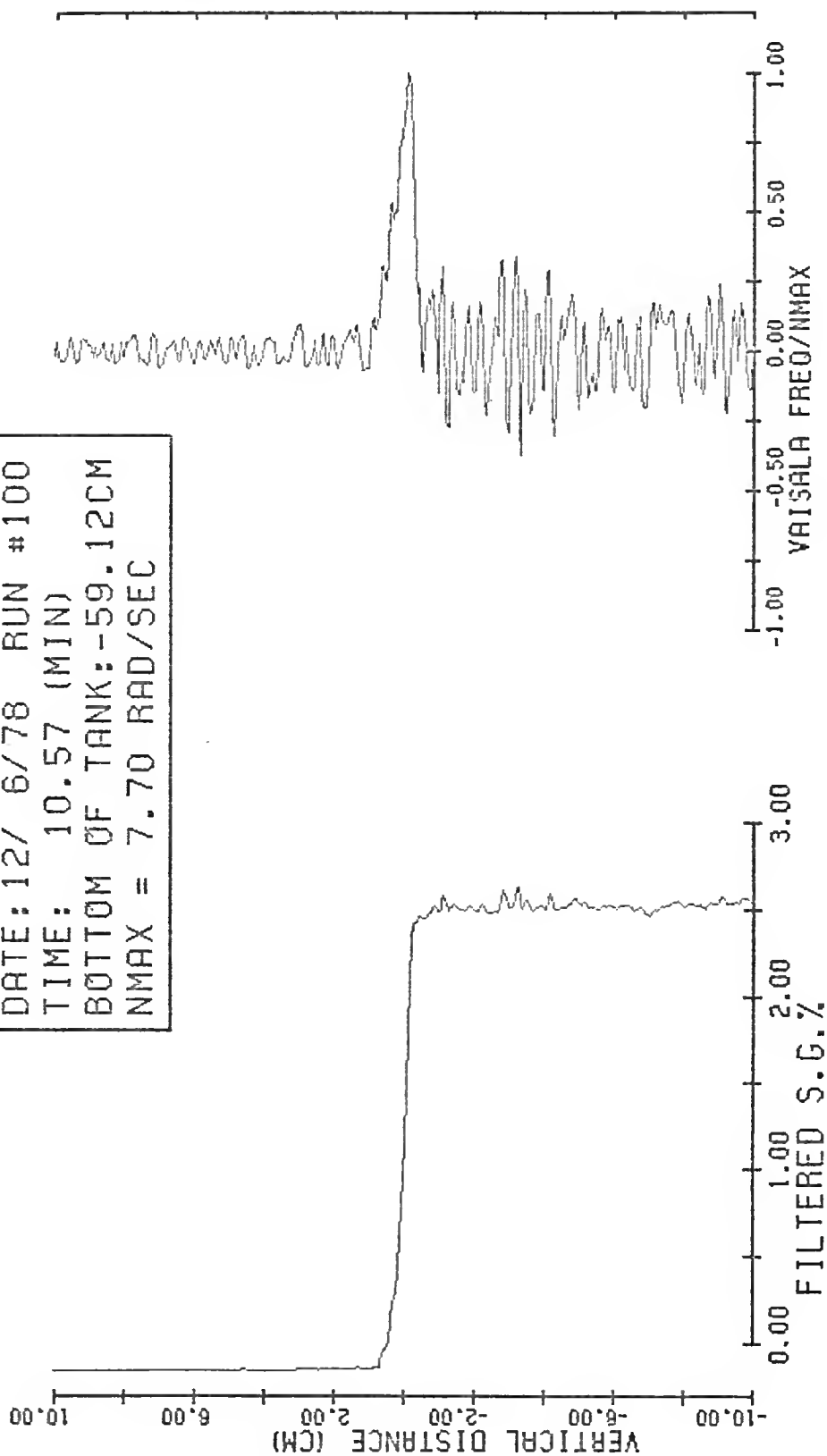
$$\text{S.G. \%} = (\text{S.G.} - 1.0) 100.0$$

The temperature profile is plotted as the deviation from the mean temperature (DELTA TEMP.), where the mean temperature is the average over the entire profile. The filtered specific gravity is the density after the least-square smoothing has been applied (see Chapter III). The Vaisala frequency is nondimensionalized by the maximum value of the Vaisala frequency for the individual profile, NMAX.

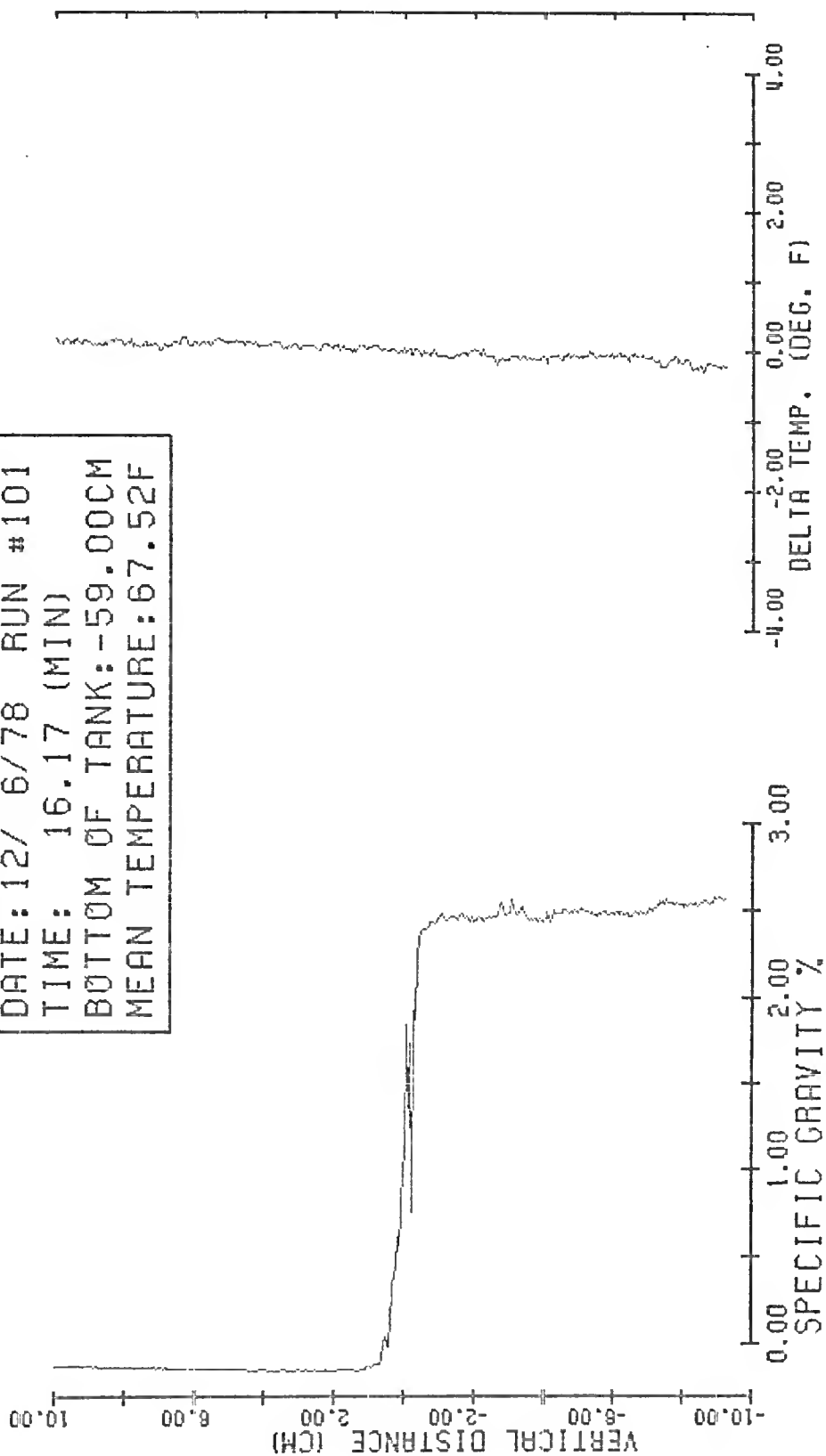
DATE: 12/ 6/78 RUN #100
TIME: 10.57 (MIN)
BOTTOM OF TANK: -59.12CM
MEAN TEMPERATURE: 67.52F



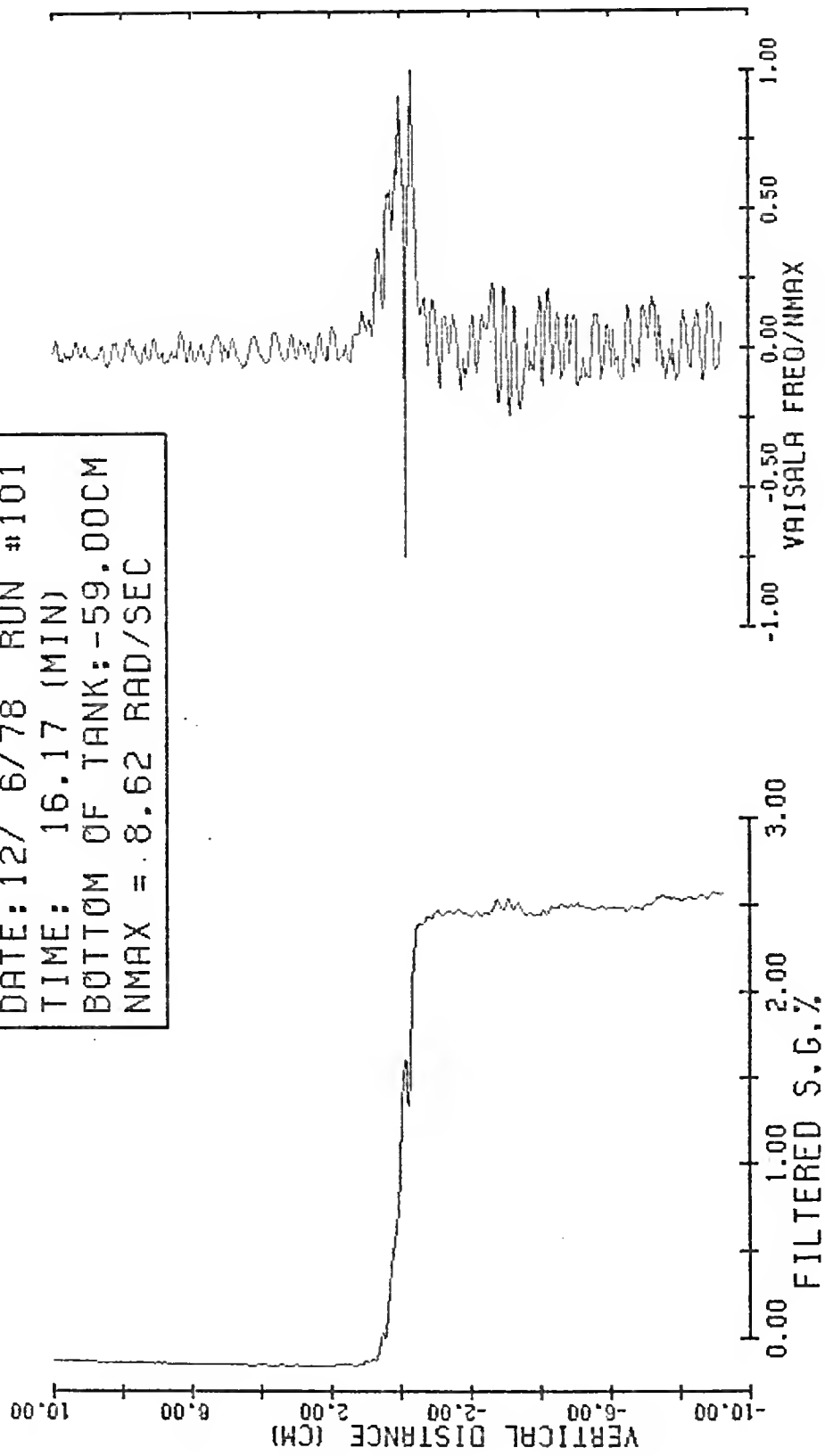
DATE: 12/ 6/78 RUN #100
TIME: 10.57 (MIN)
BOTTOM OF TANK: -59.12CM
NMAX = 7.70 RAD/SEC



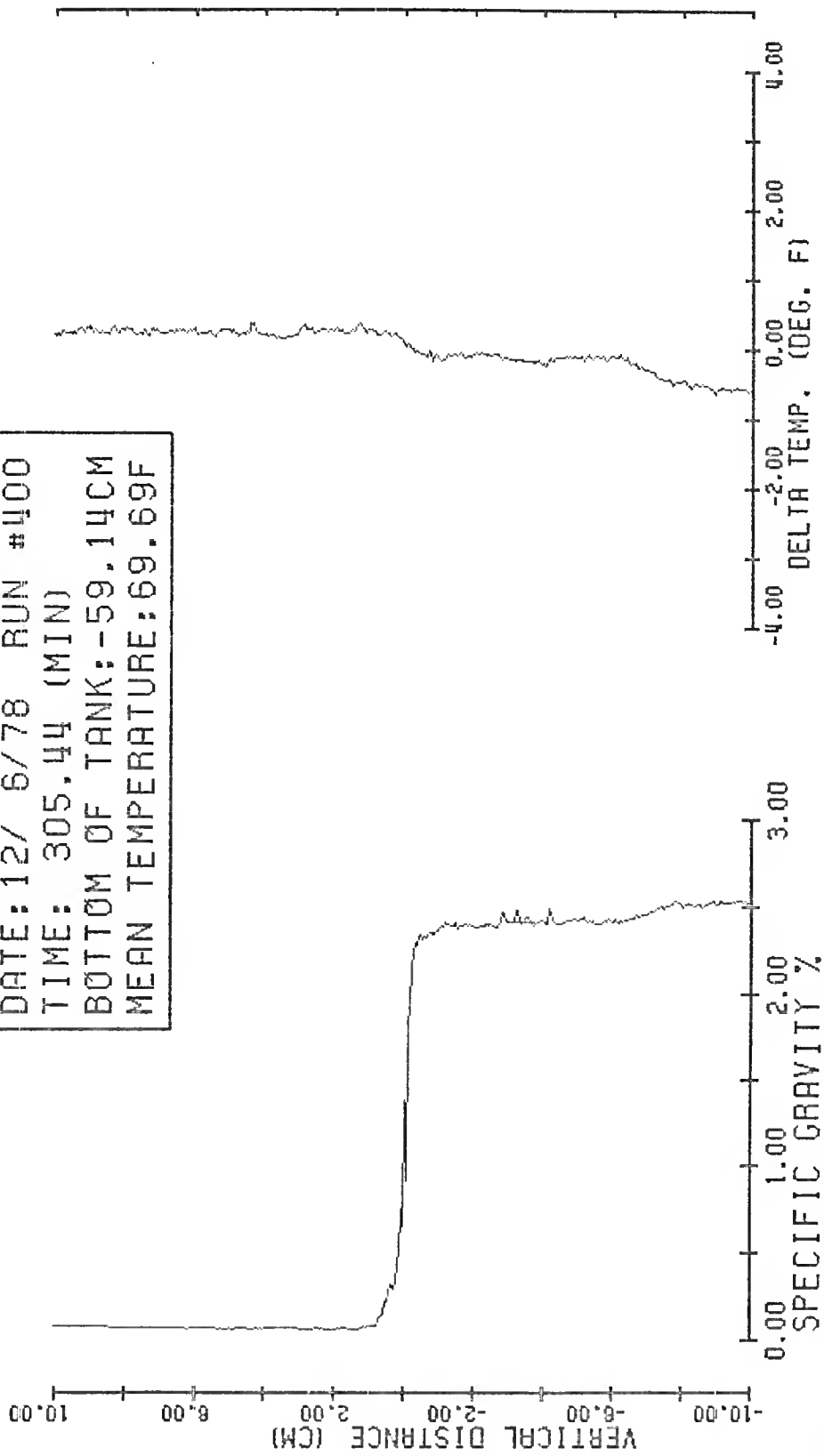
DATE: 12/ 6/78 RUN #101
TIME: 16.17 (MIN)
BOTTOM OF TANK: -59.00CM
MEAN TEMPERATURE: 67.52F



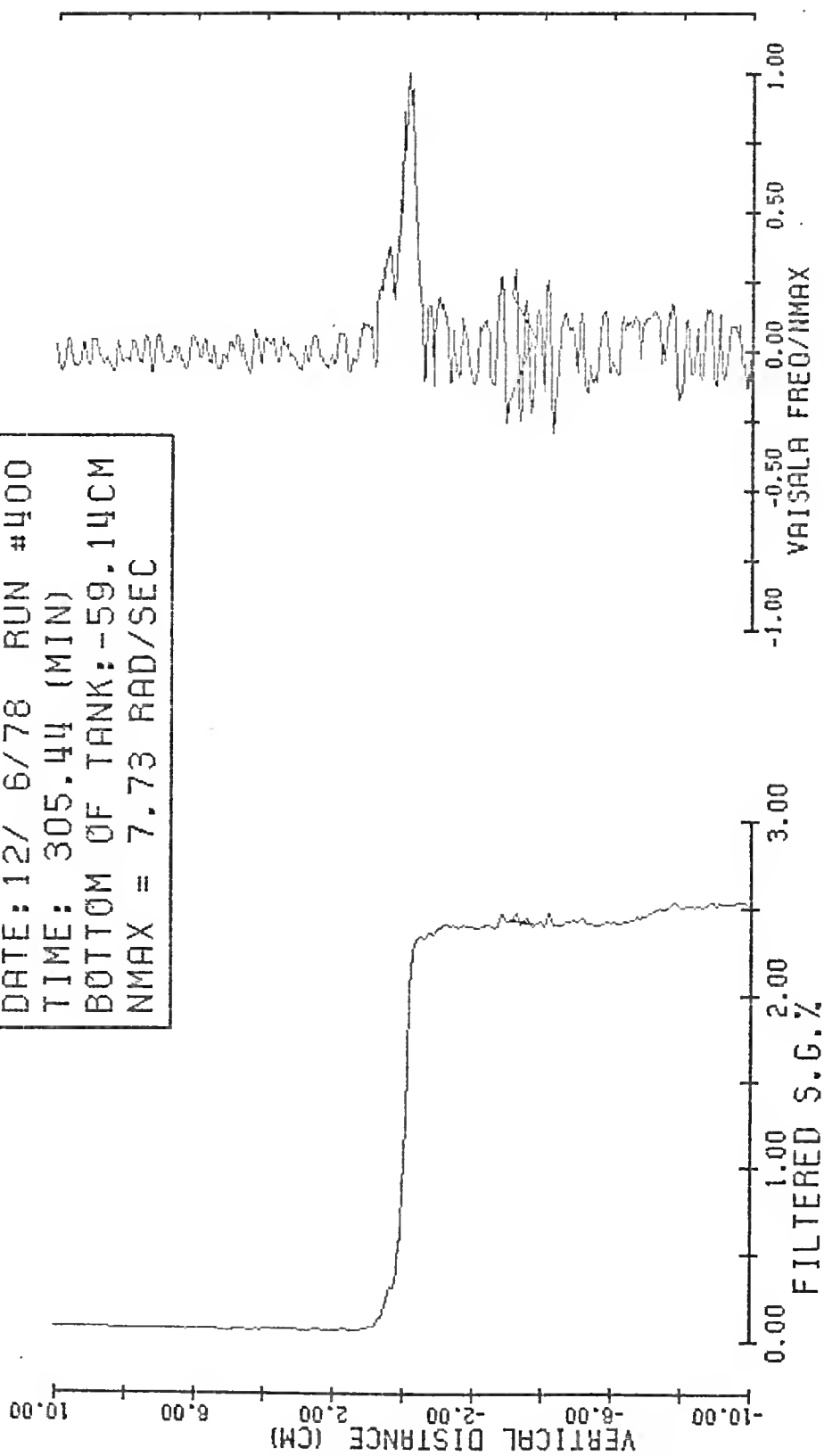
DATE: 12/ 6/78 RUN #101
TIME: 16.17 (MIN)
BOTTOM OF TANK: -59.00CM
NMAX = 8.62 RAD/SEC



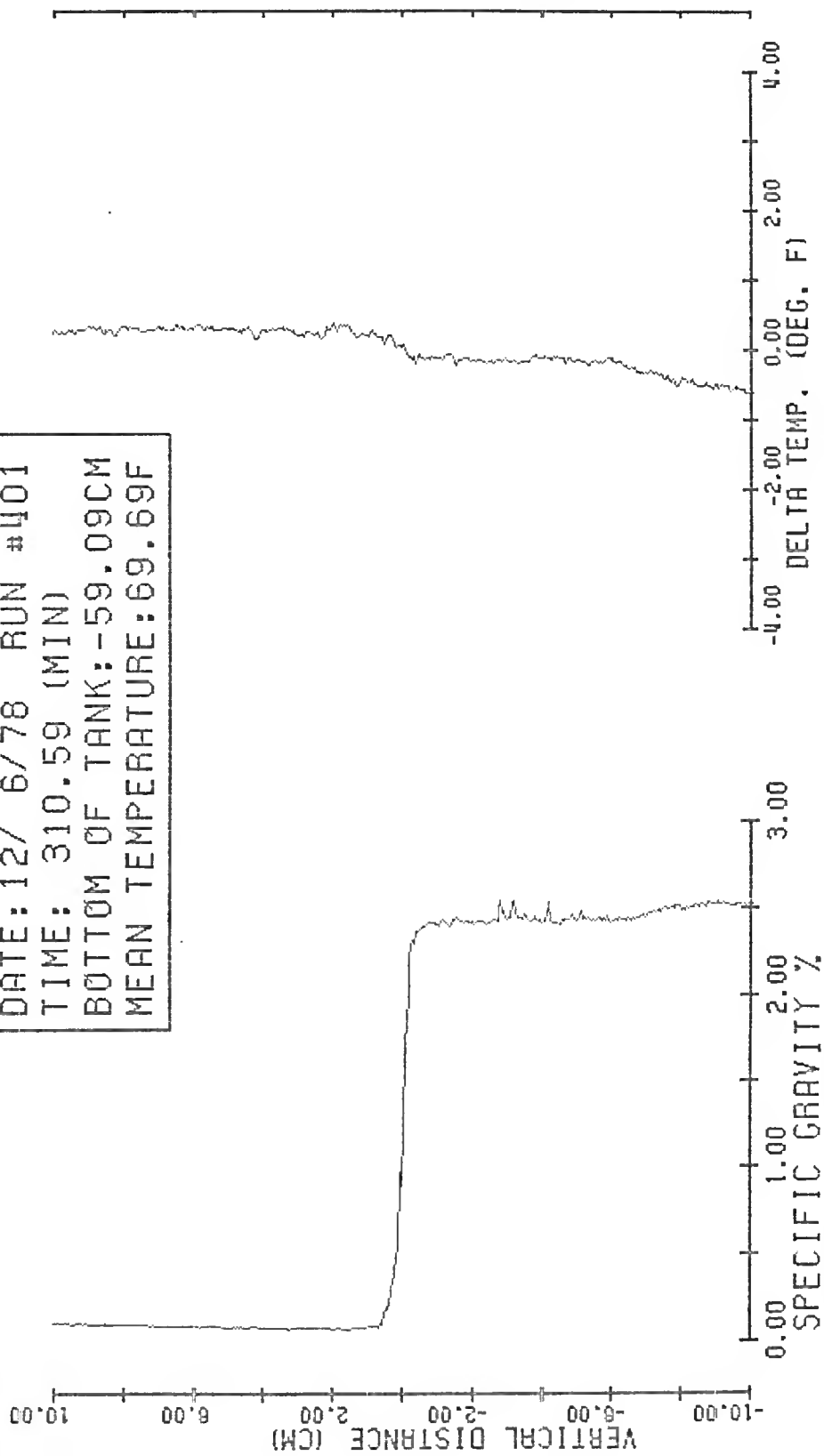
DATE: 12/ 6/78 RUN #400
TIME: 305.44 (MIN)
BOTTOM OF TANK: -59.14CM
MEAN TEMPERATURE: 69.69F



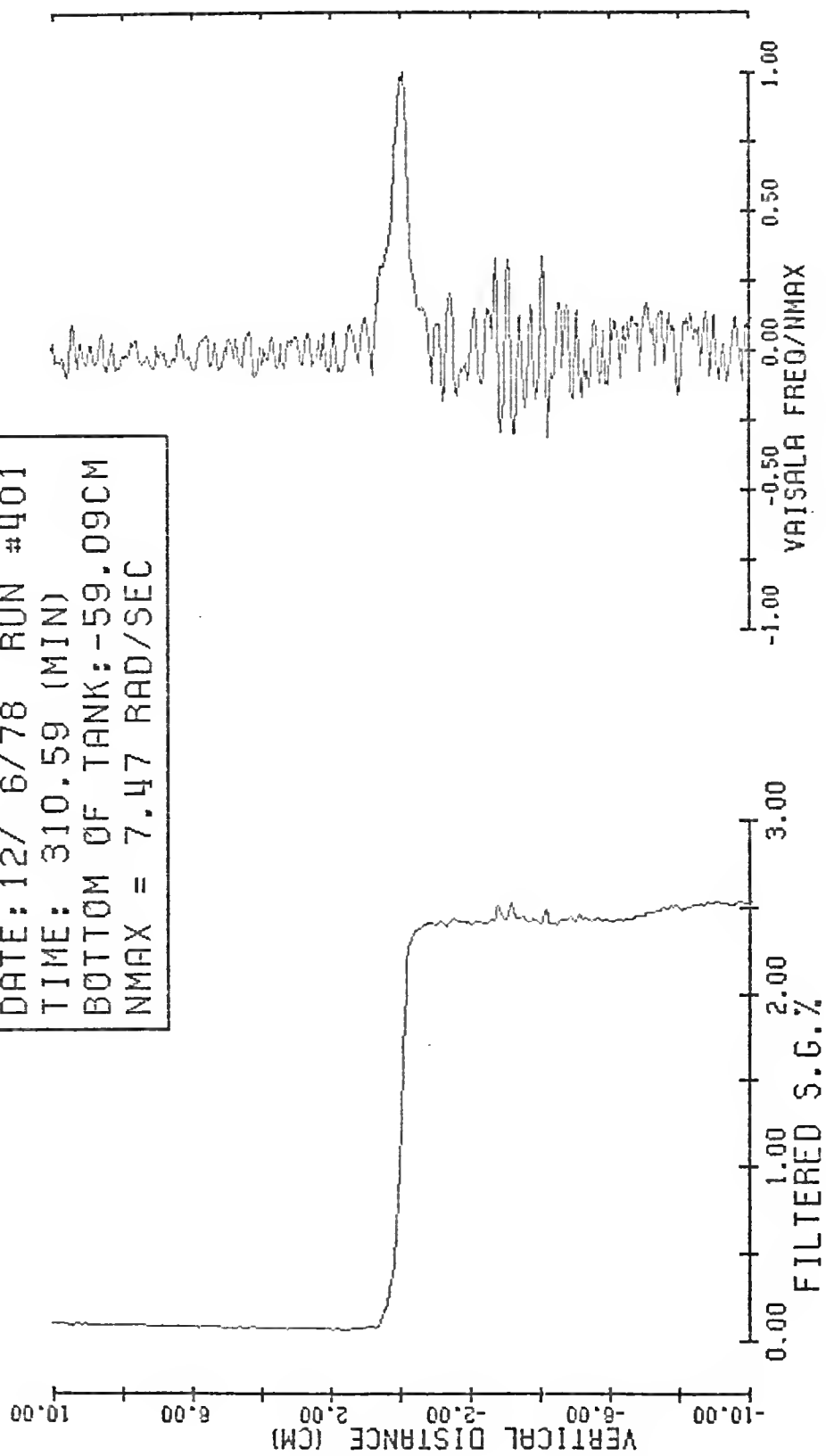
DATE: 12/ 6/78 RUN #400
TIME: 305.44 (MIN)
BOTTOM OF TANK: -59.14CM
NMAX = 7.73 RAD/SEC



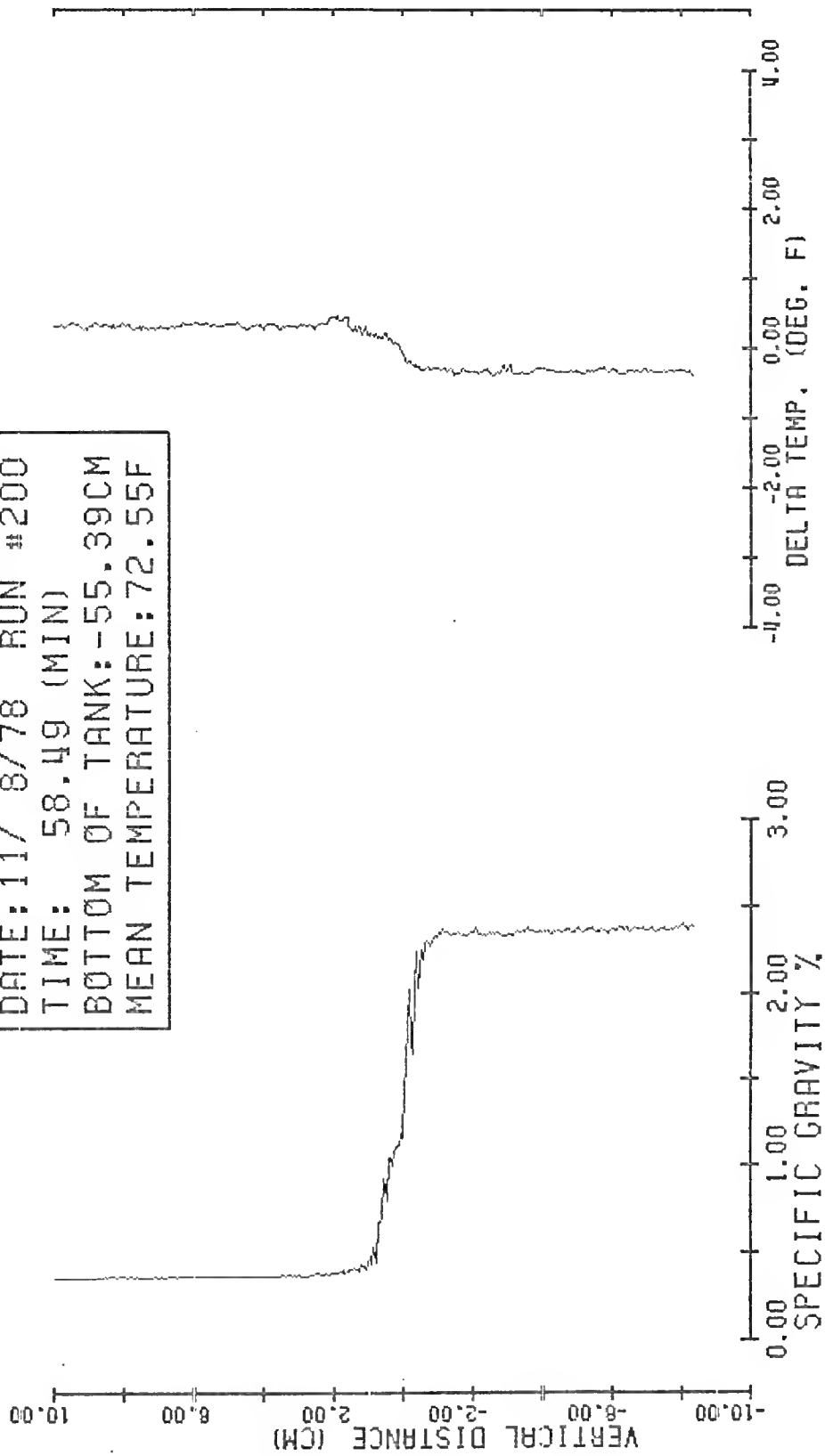
DATE: 12/ 6/78 RUN #401
TIME: 310.59 (MIN)
BOTTOM OF TANK: -59.09CM
MEAN TEMPERATURE: 69.69F



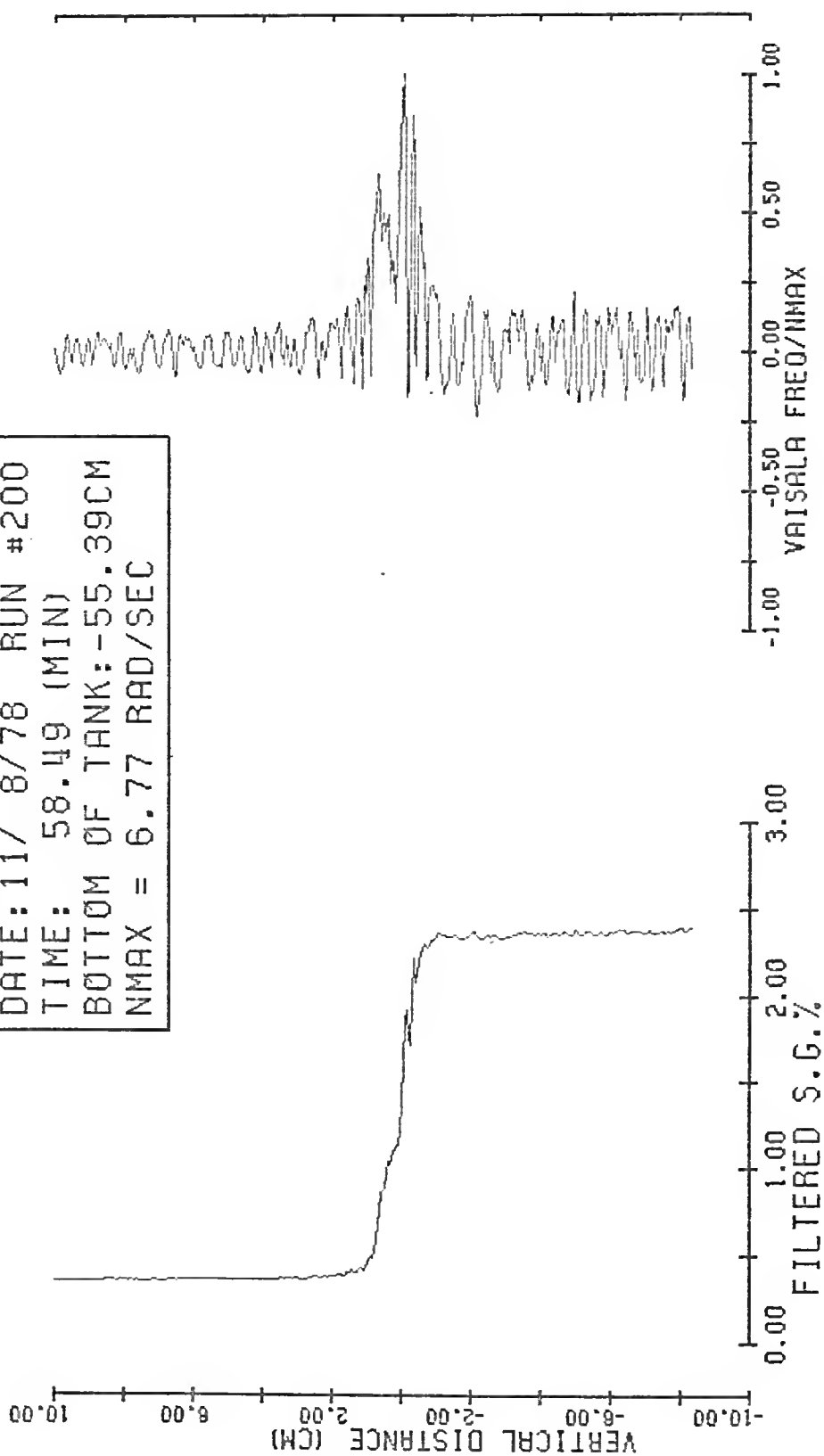
DATE: 12/ 6/78 RUN #401
TIME: 310.59 (MIN)
BOTTOM OF TANK: -59.09CM
NMAX = 7.47 RAD/SEC



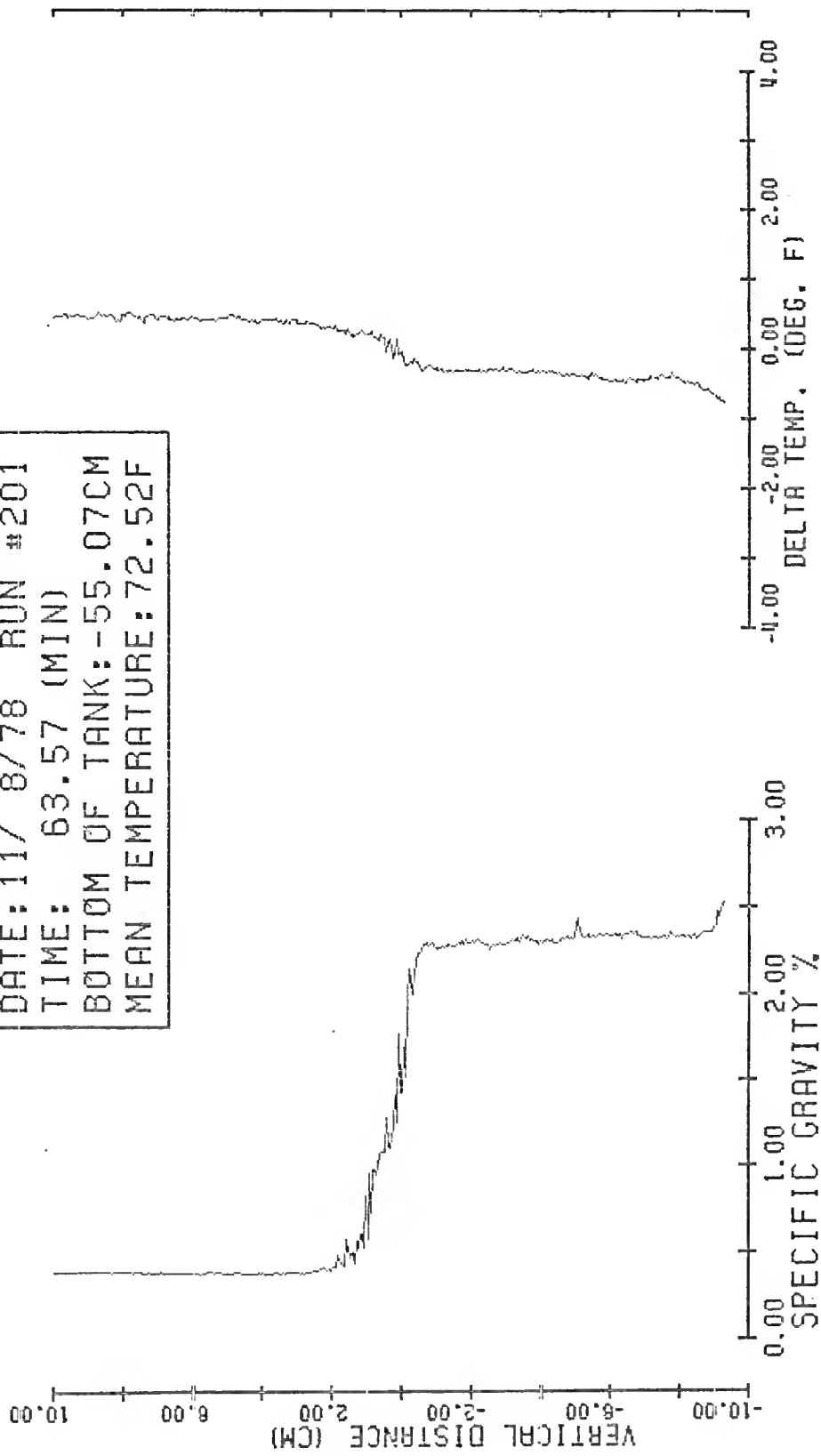
DATE: 11/ 8/78 RUN #200
TIME: 58.49 (MIN)
BOTTOM OF TANK: -55.39CM
MEAN TEMPERATURE: 72.55F



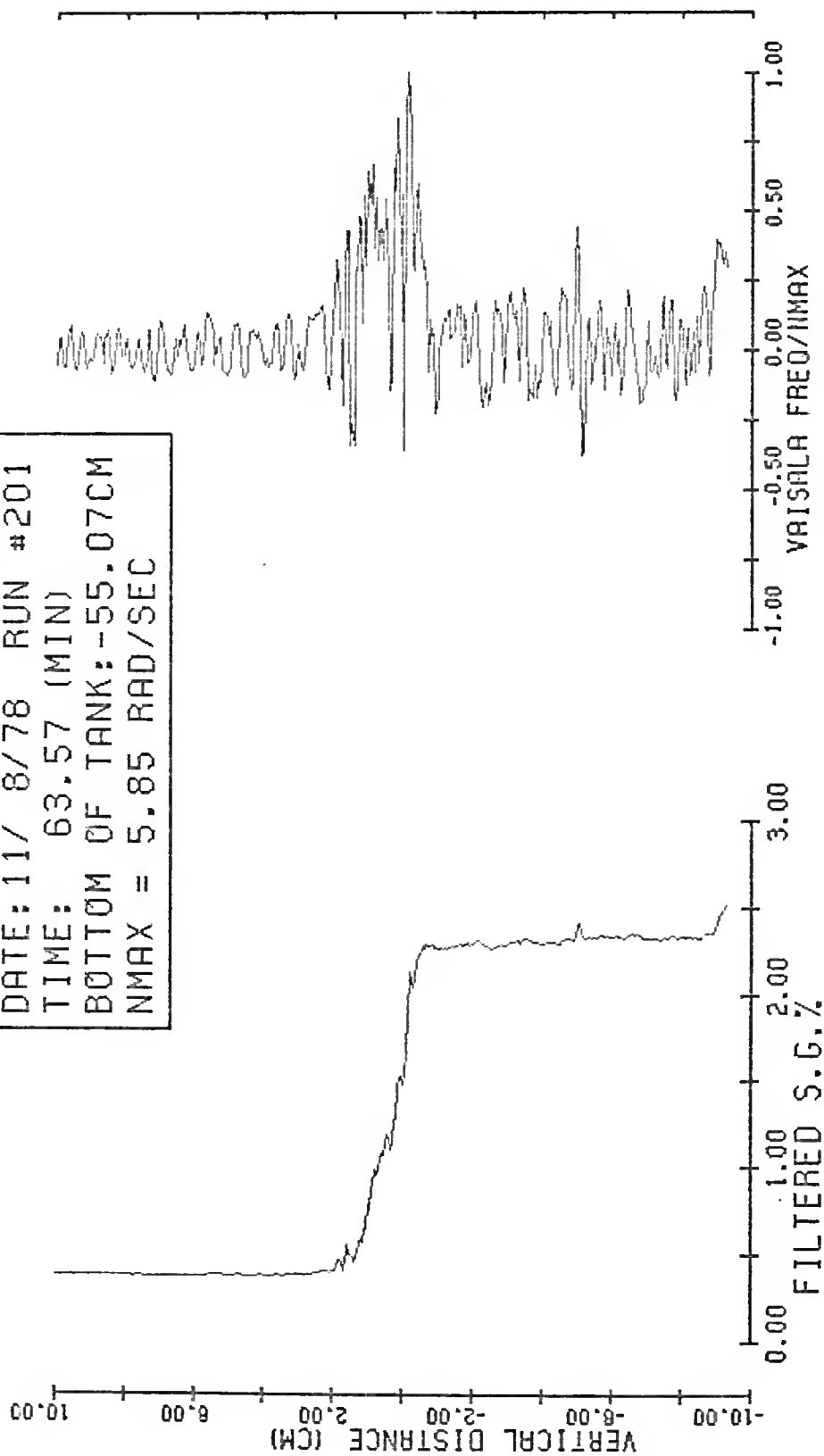
DATE: 11/ 8/78 RUN #200
TIME: 58.49 (MIN)
BOTTOM OF TANK: -55.39CM
NMAX = 6.77 RAD/SEC



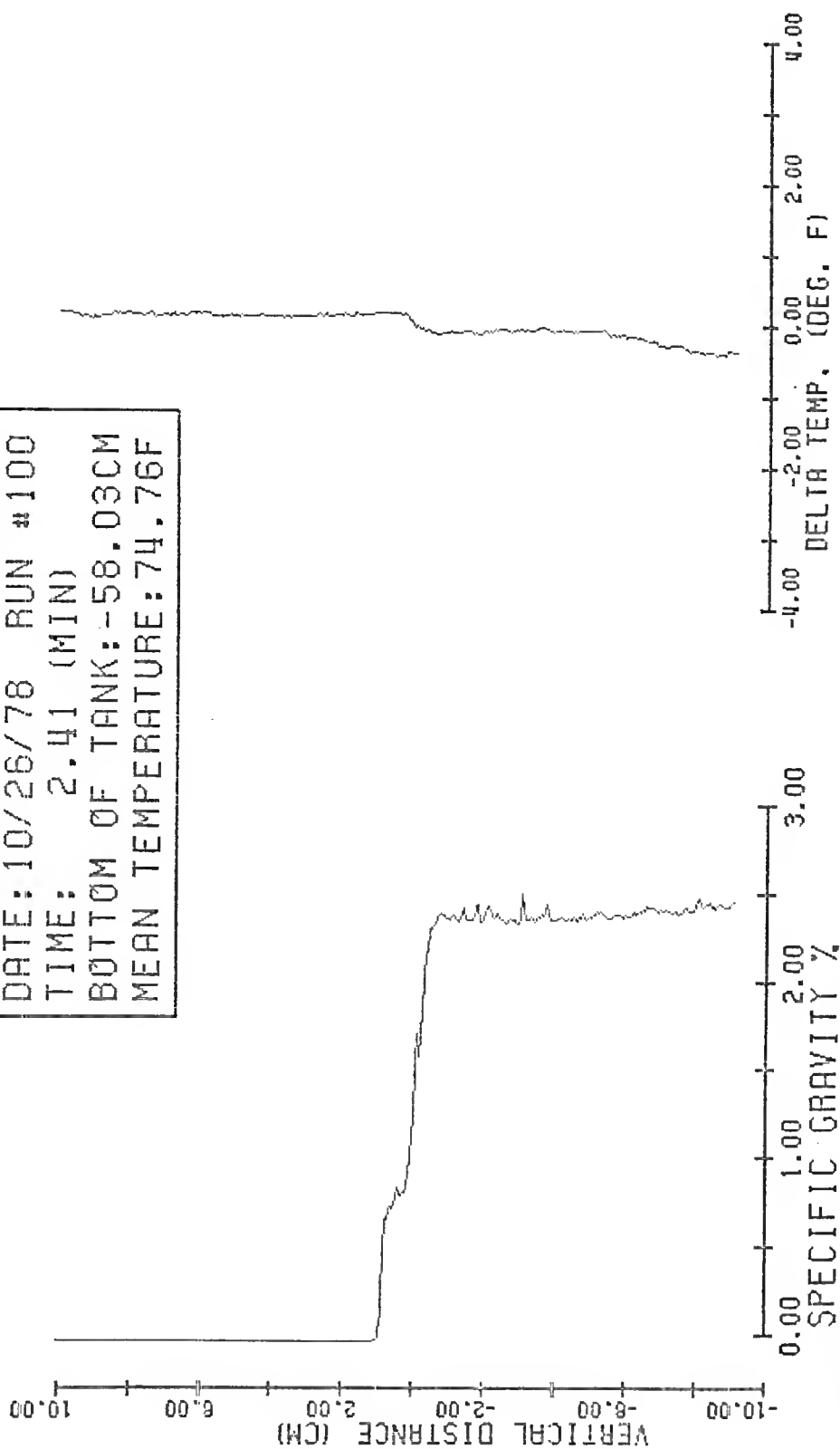
DATE: 11/ 8/78 RUN #201
TIME: 63.57 (MIN)
BOTTOM OF TANK: -55.07CM
MEAN TEMPERATURE: 72.52F

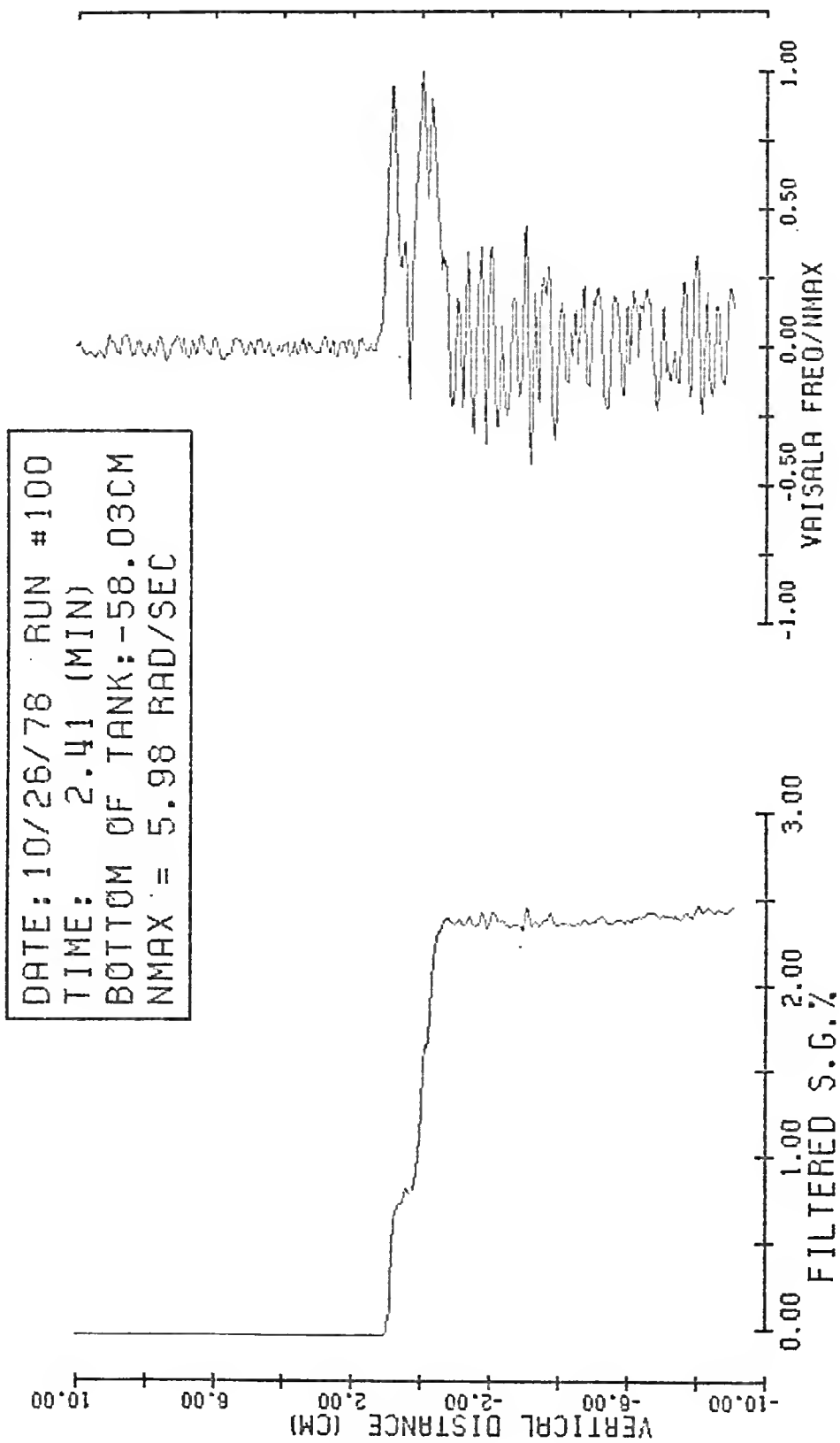


DATE: 11/ 8/78 RUN #201
TIME: 63.57 (MIN)
BOTTOM OF TANK: -55.07CM
NMAX = 5.85 RAD/SEC

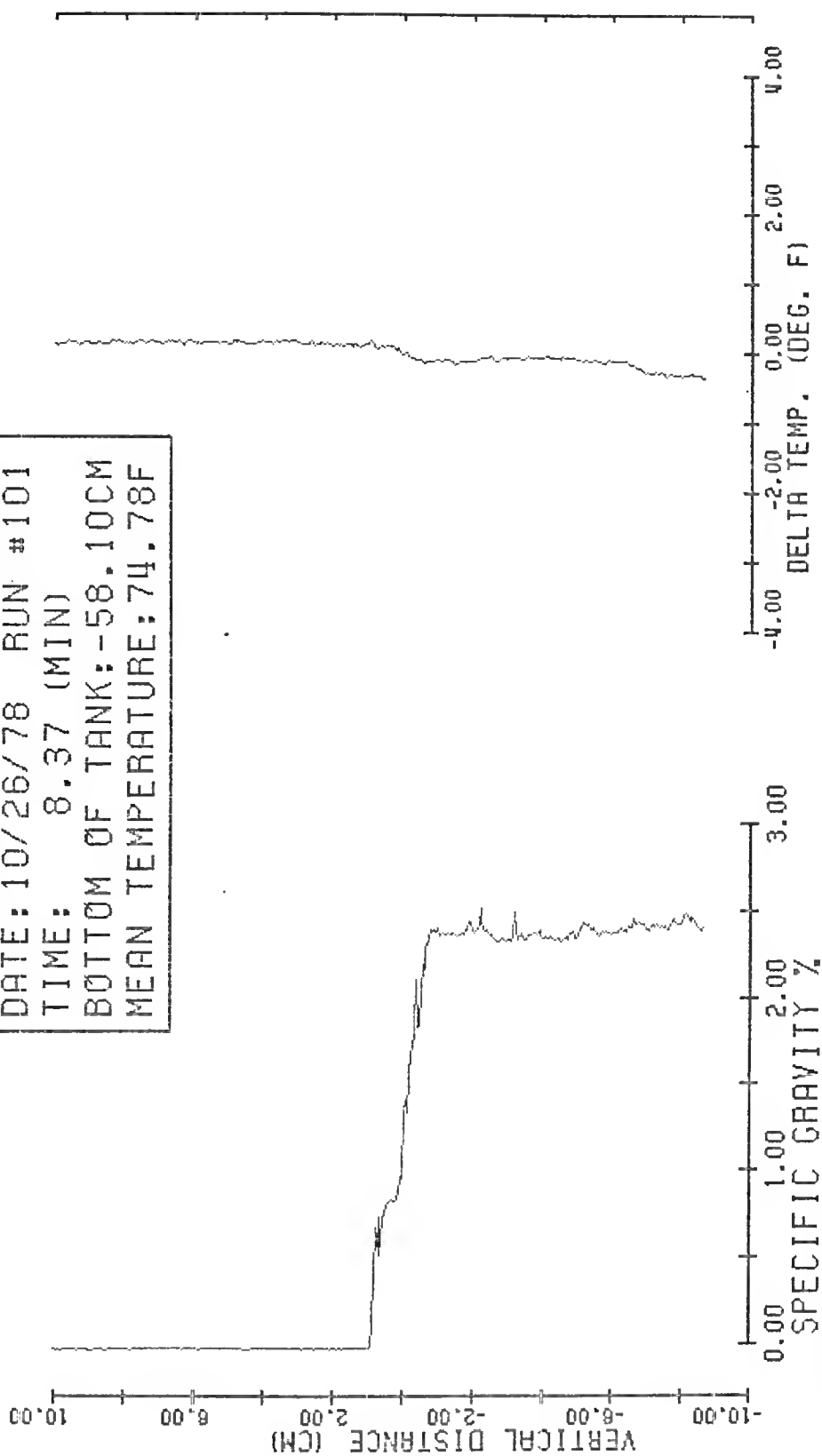


DATE: 10/26/78 RUN #100
TIME: 2.41 (MIN)
BOTTOM OF TANK: -58.03CM
MEAN TEMPERATURE: 74.76F

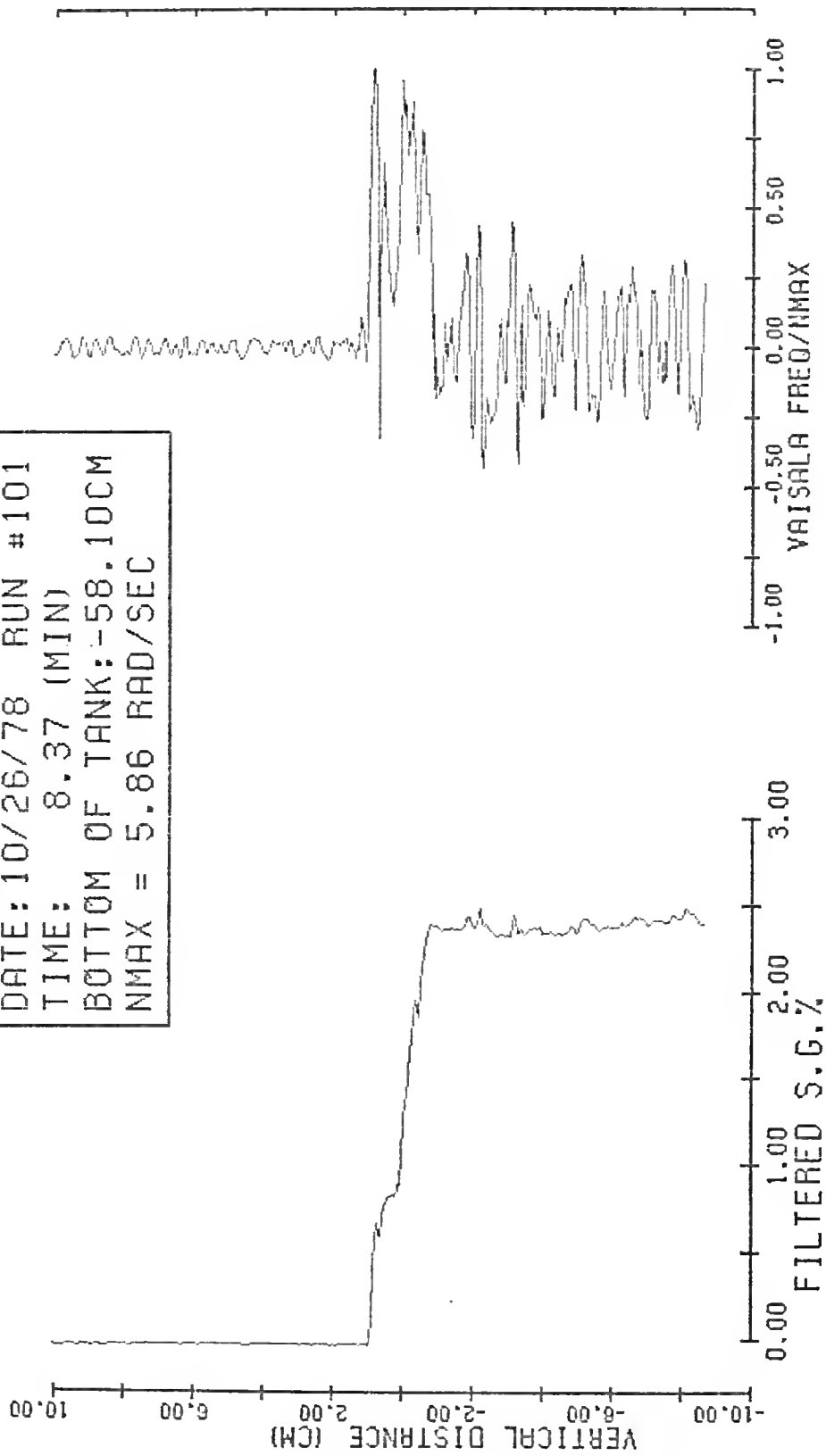




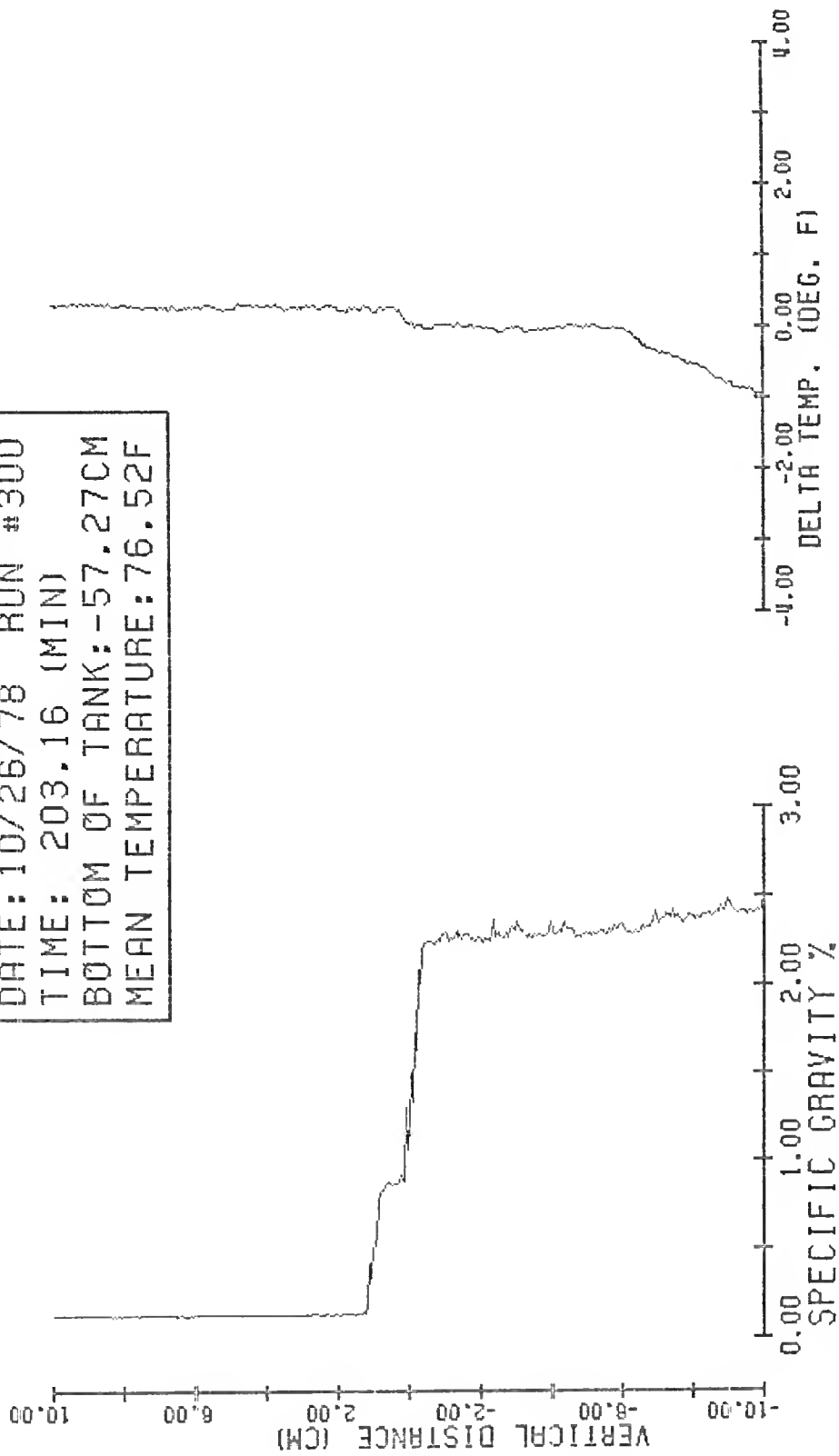
DATE: 10/26/78 RUN #101
TIME: 8.37 (MIN)
BOTTOM OF TANK: -58.10CM
MEAN TEMPERATURE: 74.78F



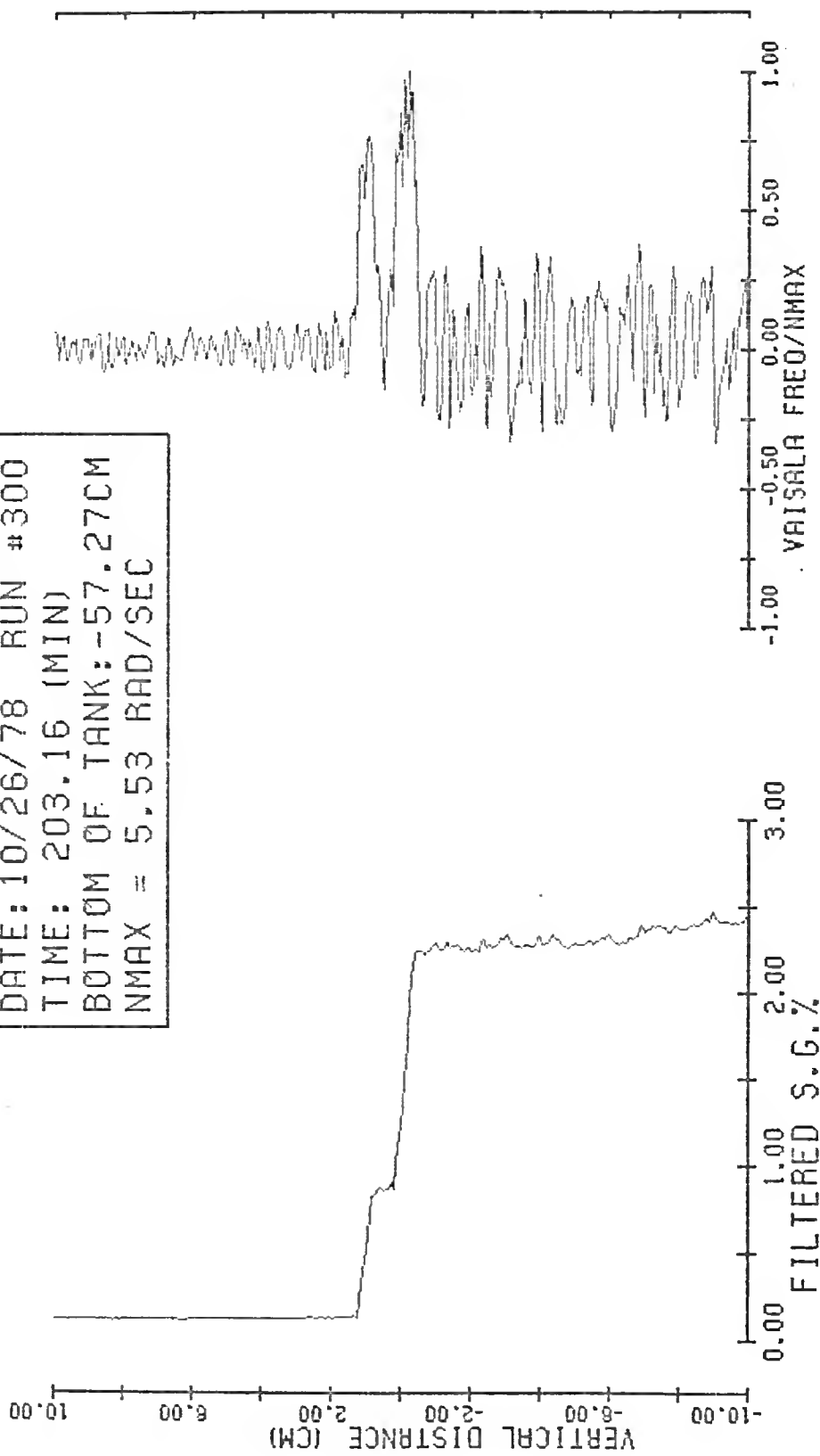
DATE: 10/26/78 RUN #101
TIME: 8.37 (MIN)
BOTTOM OF TANK: -58.10CM
NMAX = 5.86 RAD/SEC



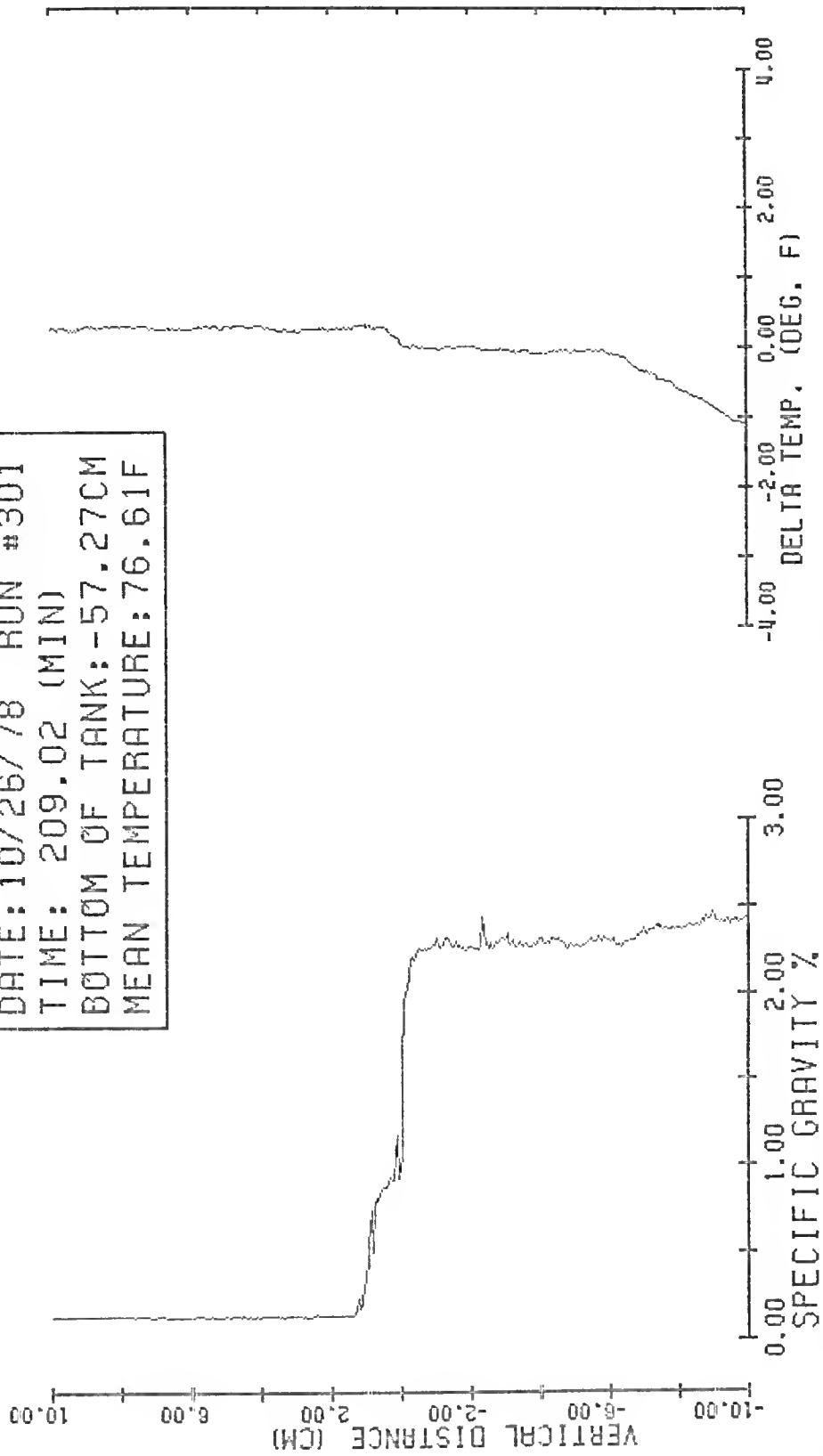
DATE: 10/26/78 RUN #300
TIME: 203.16 (MIN)
BOTTOM OF TANK: -57.27CM
MEAN TEMPERATURE: 76.52F



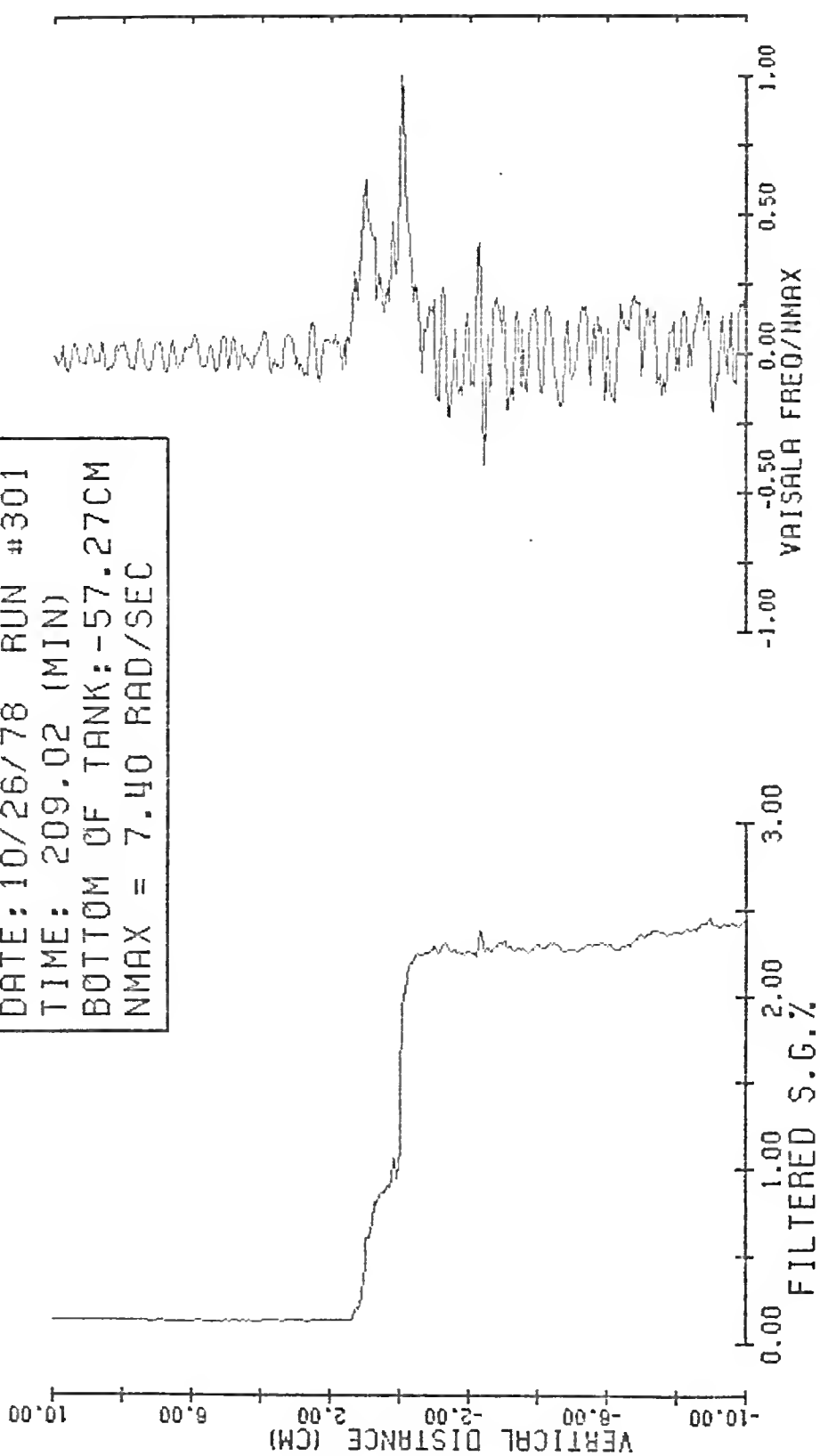
DATE: 10/26/78 RUN #300
TIME: 203.16 (MIN)
BOTTOM OF TANK: -57.27CM
NMAX = 5.53 RAD/SEC



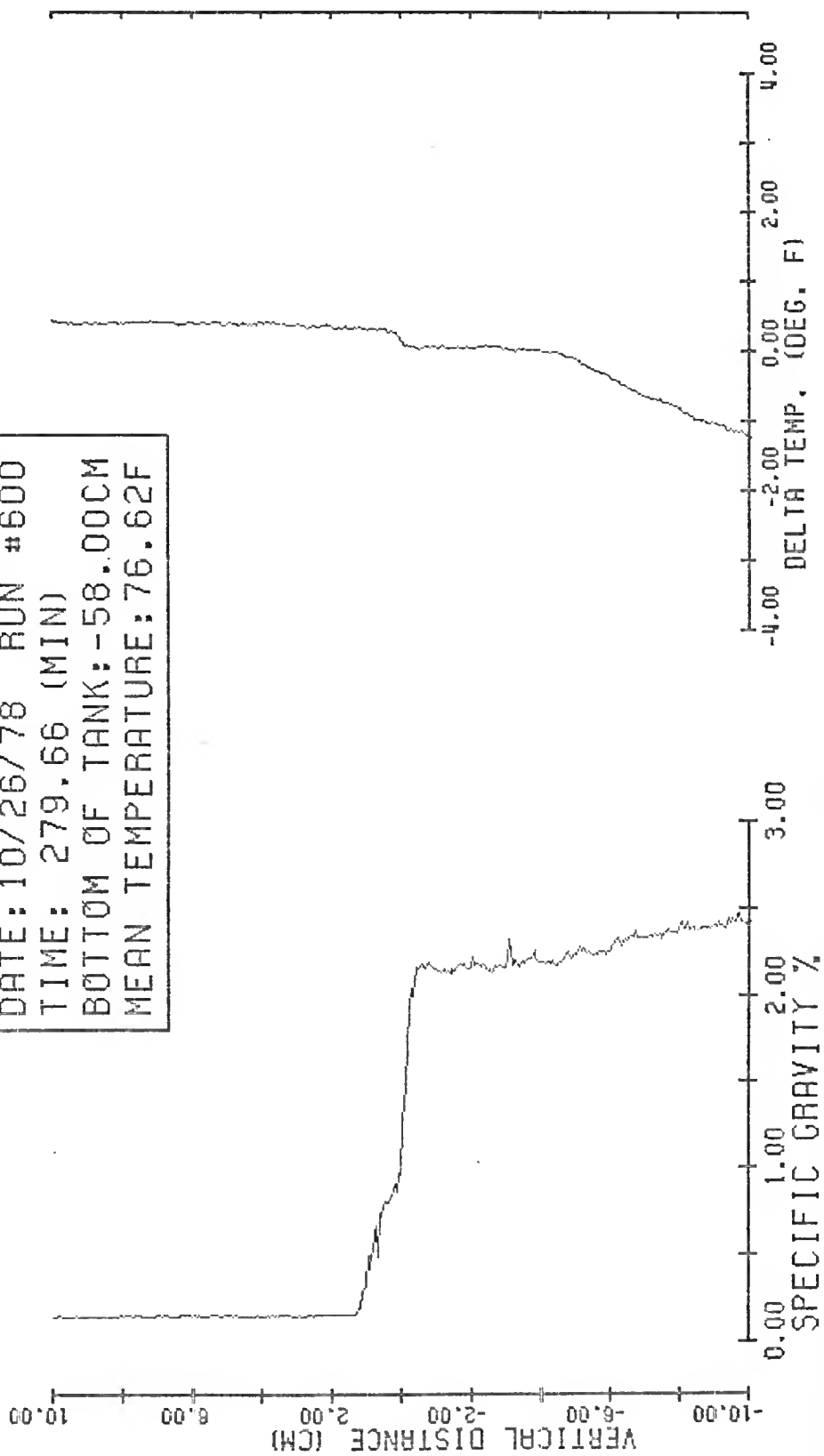
DATE: 10/26/78 RUN #301
TIME: 209.02 (MIN)
BOTTOM OF TANK: -57.27CM
MEAN TEMPERATURE: 76.61F



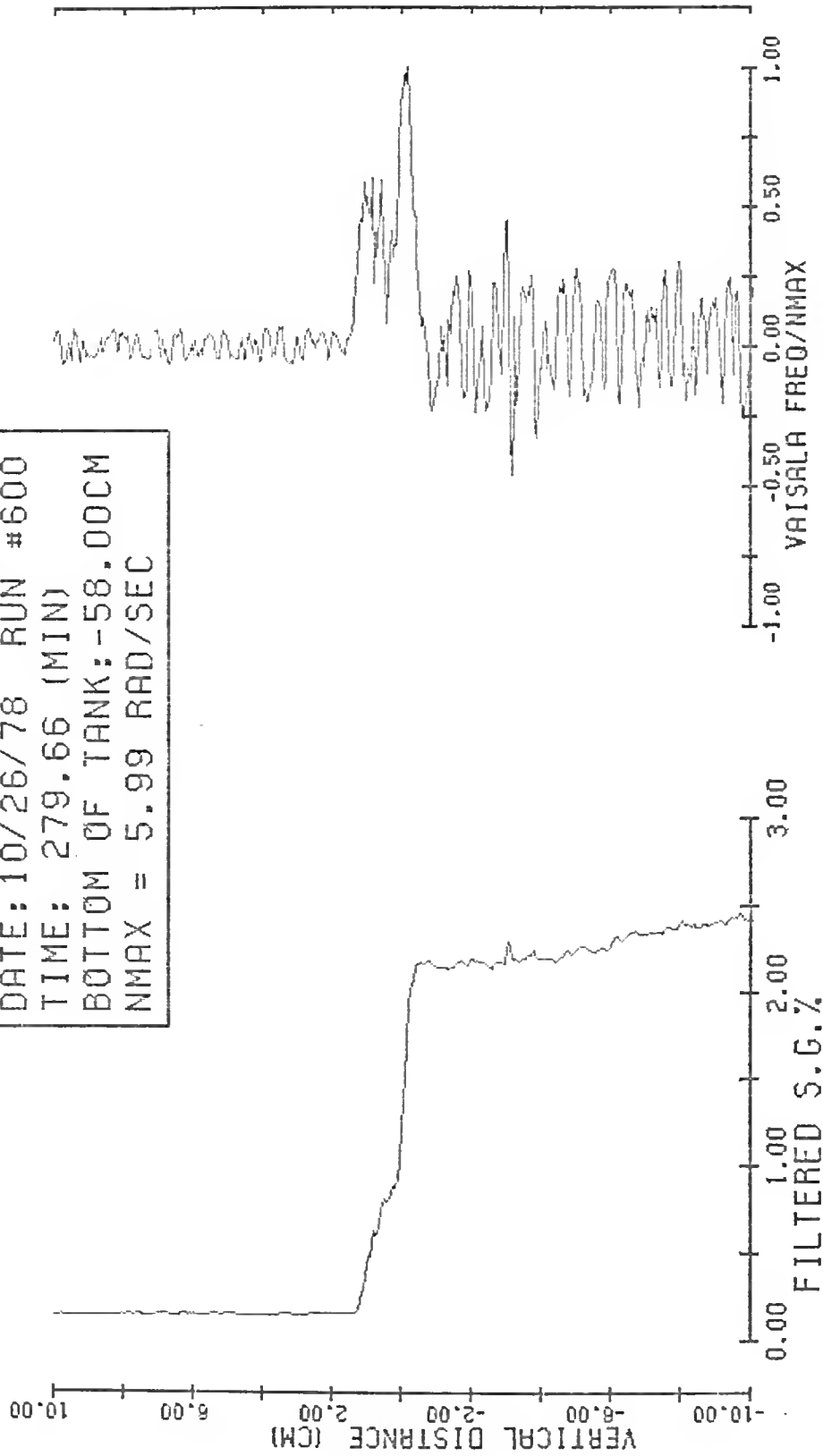
DATE: 10/26/78 RUN #301
TIME: 209.02 (MIN)
BOTTOM OF TANK: -57.27CM
NMAX = 7.40 RAD/SEC

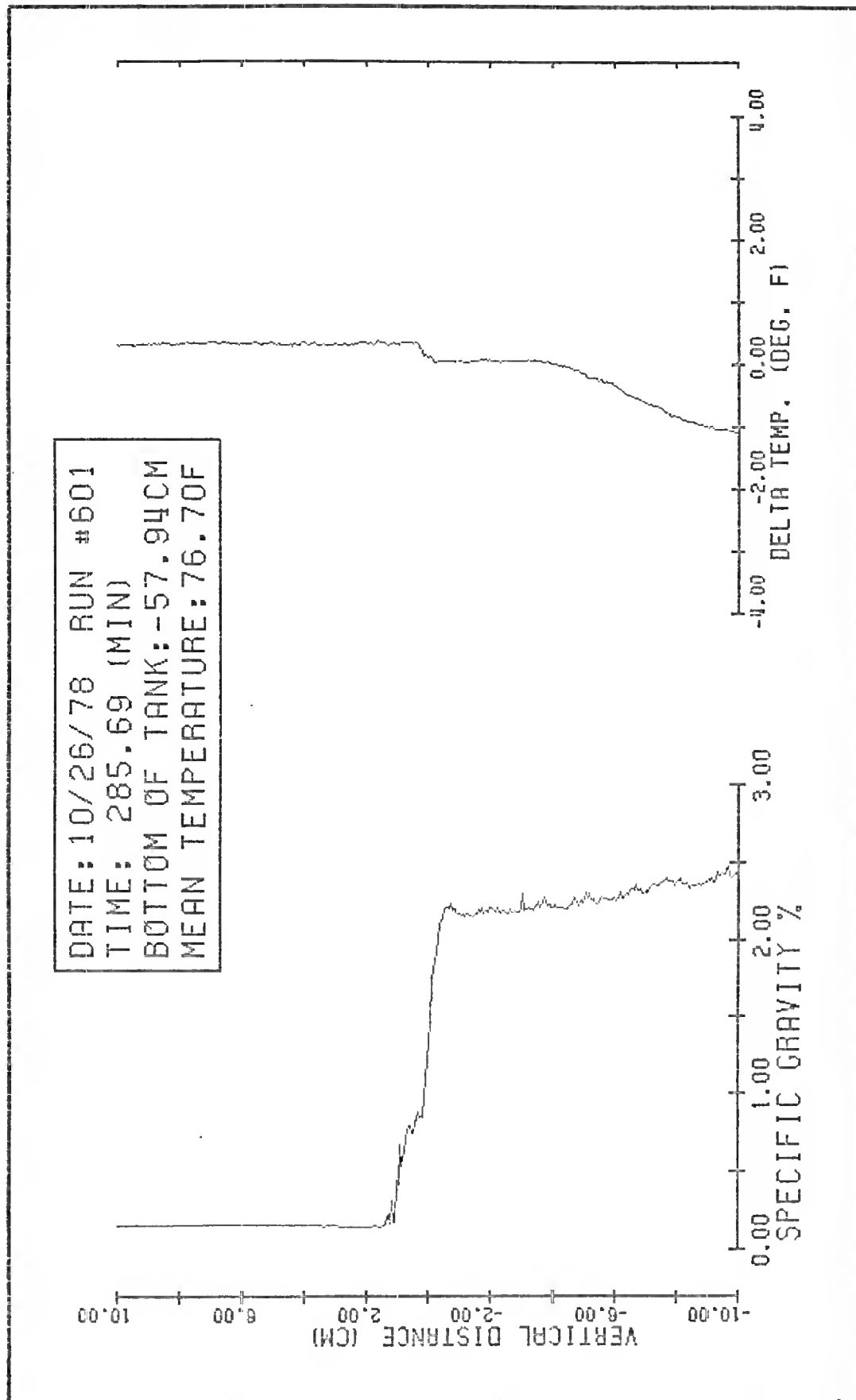


DATE: 10/26/78 RUN #600
TIME: 279.66 (MIN)
BOTTOM OF TANK: -58.00CM
MEAN TEMPERATURE: 76.62F

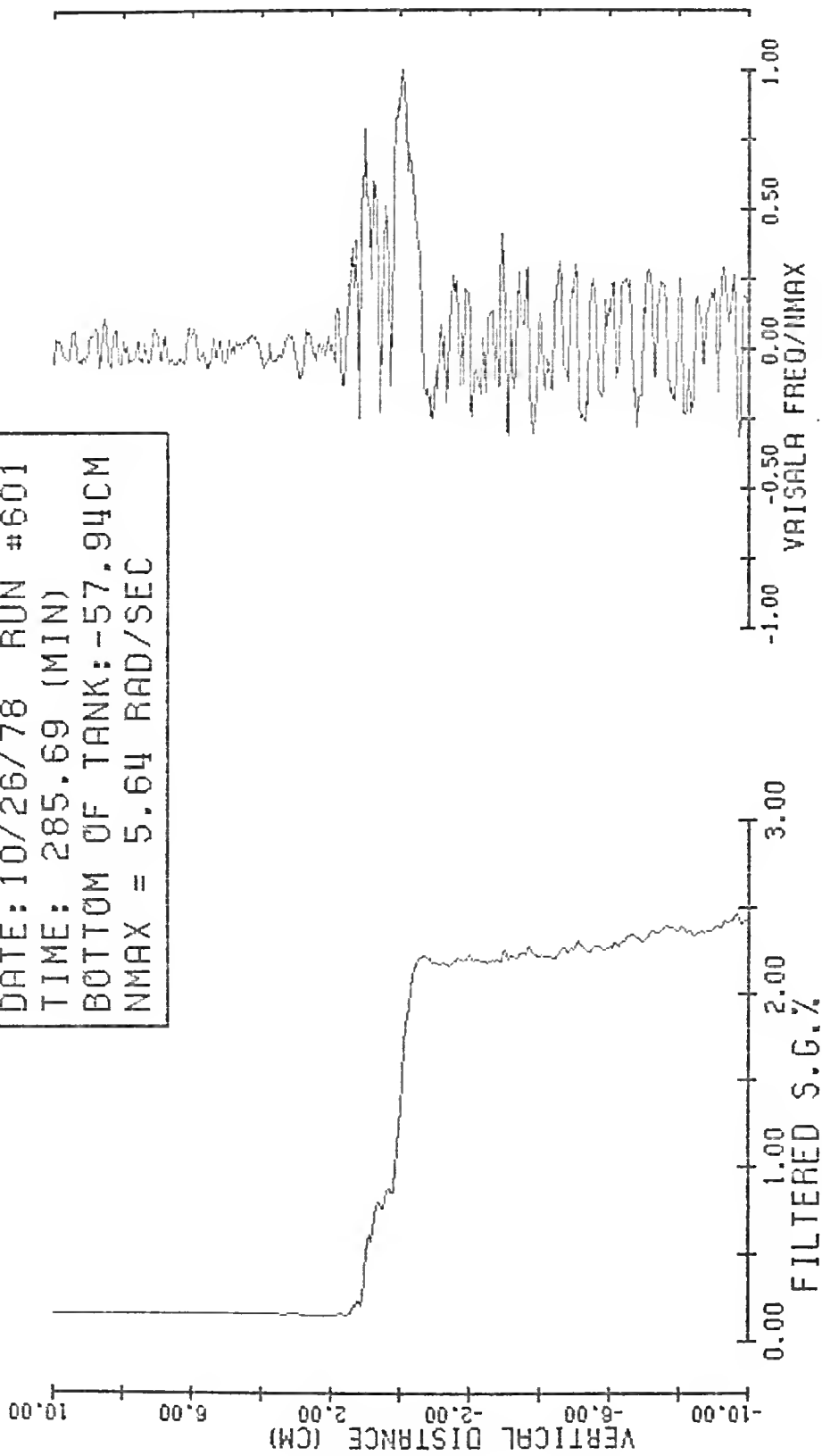


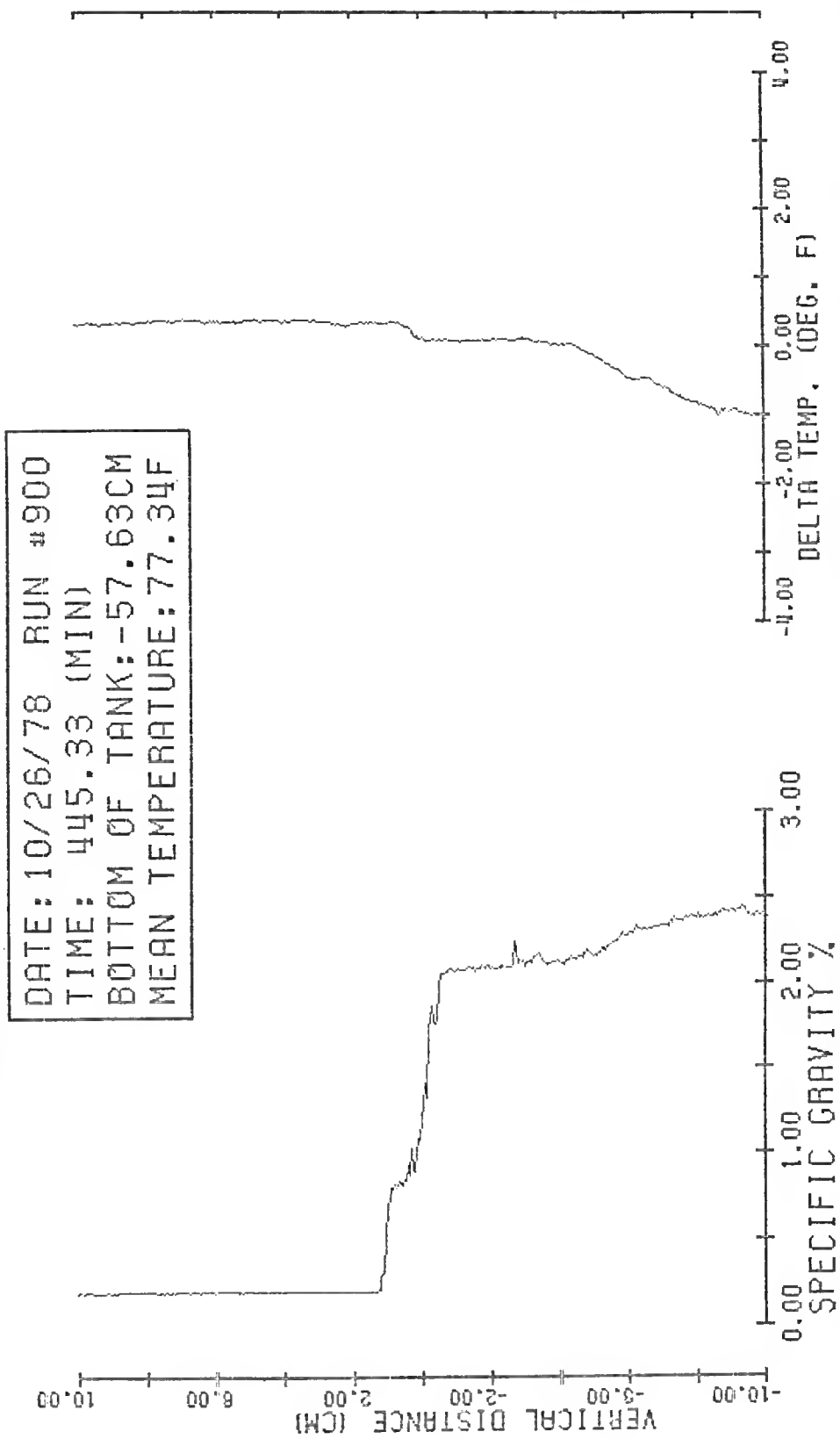
DATE: 10/26/78 RUN #600
TIME: 279.66 (MIN)
BOTTOM OF TANK: -58.00CM
NMAX = 5.99 RAD/SEC



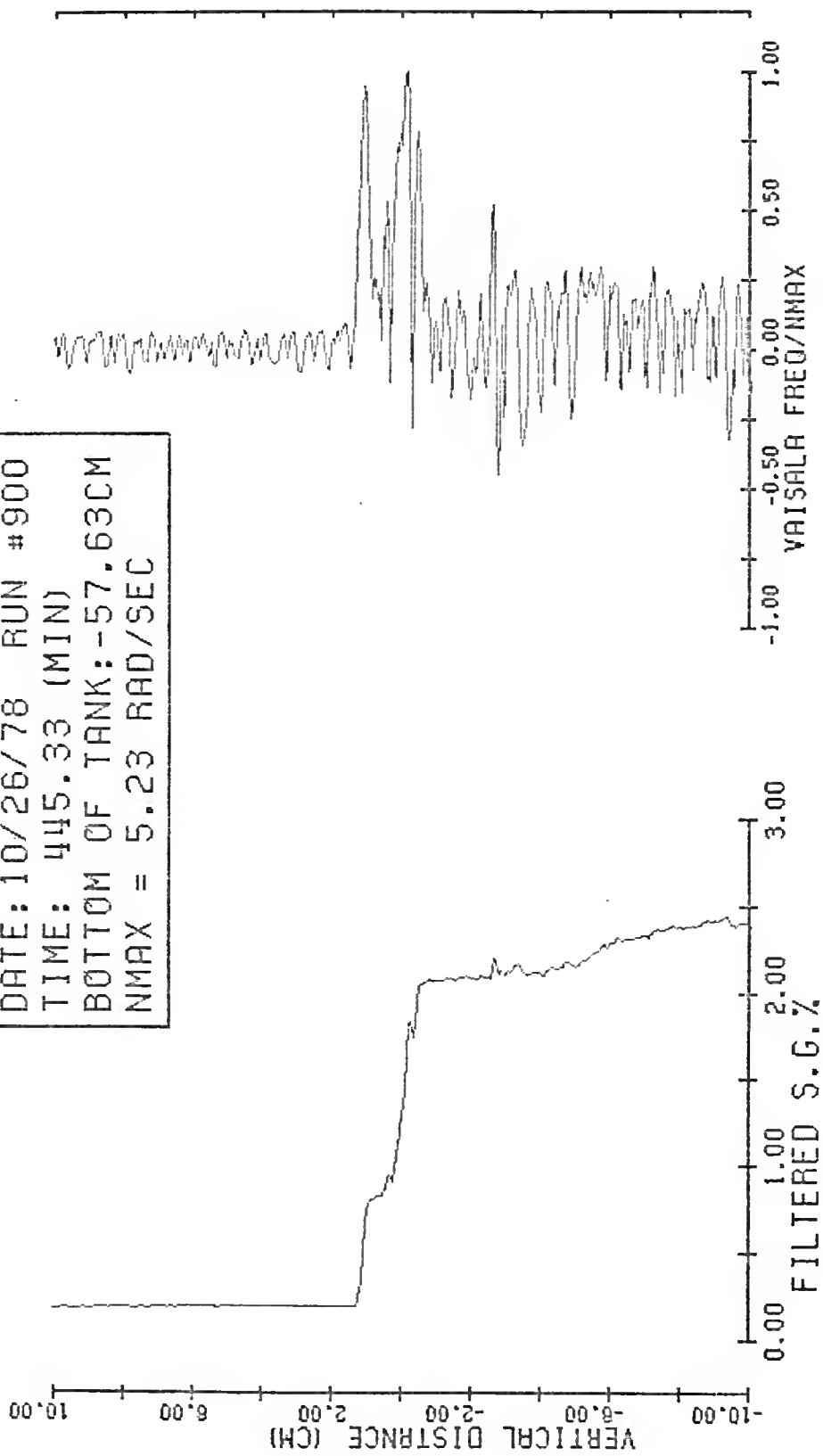


DATE: 10/26/78 RUN #601
TIME: 285.69 (MIN)
BOTTOM OF TANK: -57.94CM
NMAX = 5.64 RAD/SEC

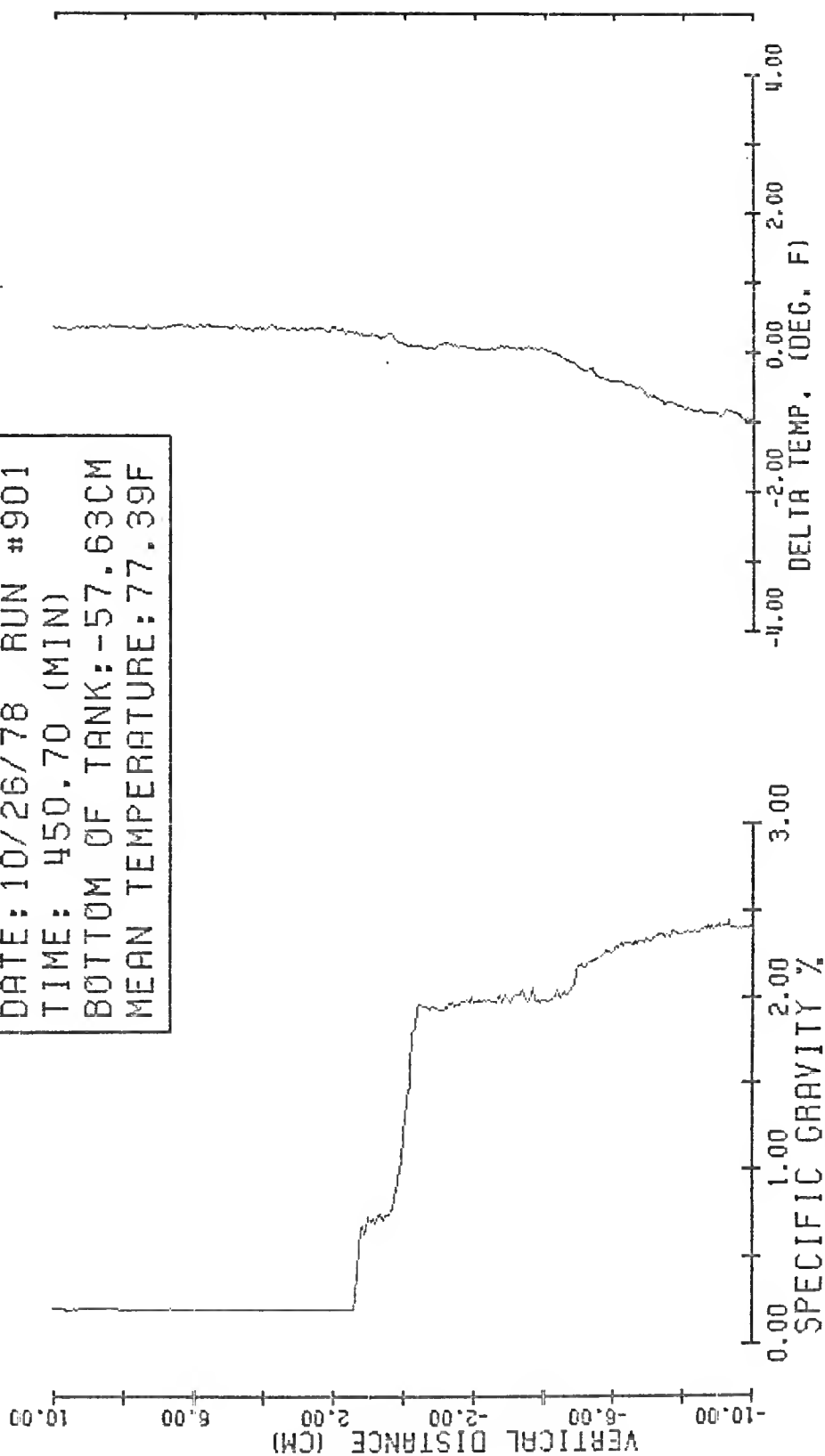




DATE: 10/26/78 RUN #900
TIME: 445.33 (MIN)
BOTTOM OF TANK: -57.63CM
NMAX = 5.23 RAD/SEC



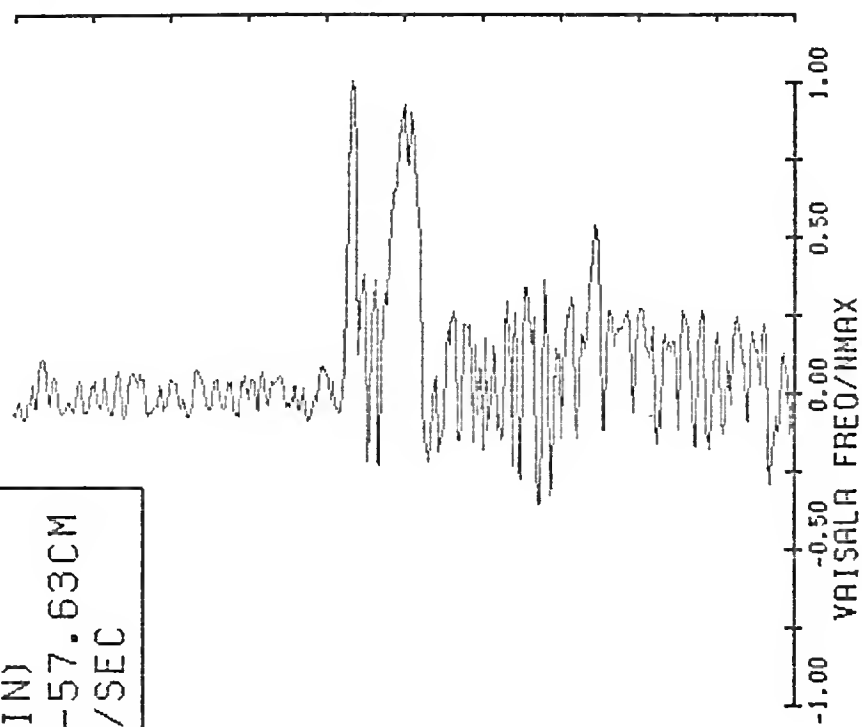
DATE: 10/26/78 RUN #901
TIME: 450.70 (MIN)
BOTTOM OF TANK: -57.63CM
MEAN TEMPERATURE: 77.39F



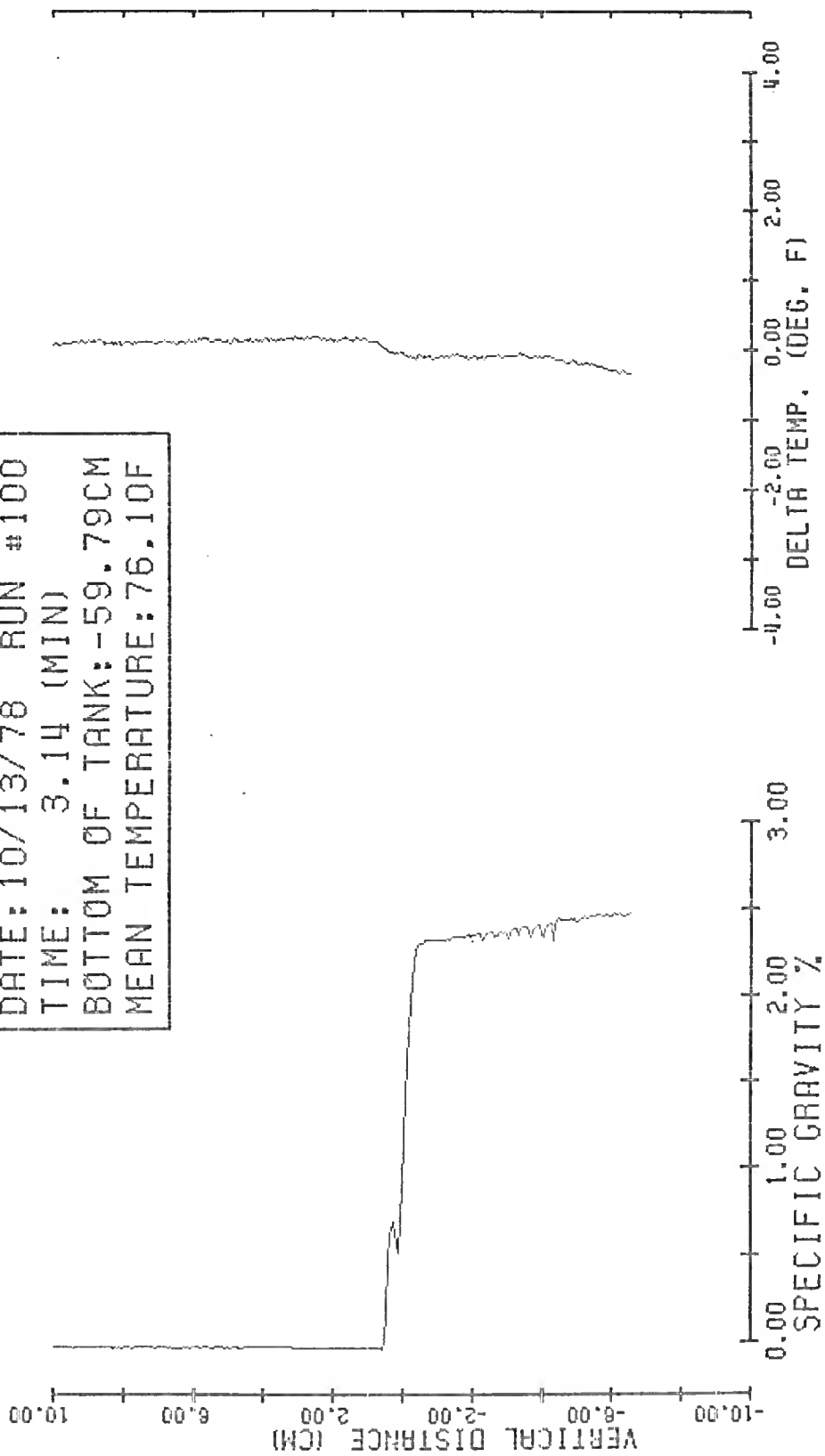
DATE: 10/26/78 RUN #901
TIME: 450.70 (MIN)
BOTTOM OF TANK: -57.63CM
NMAX = 4.91 RAD/SEC

VERTICAL DISTANCE (CM)

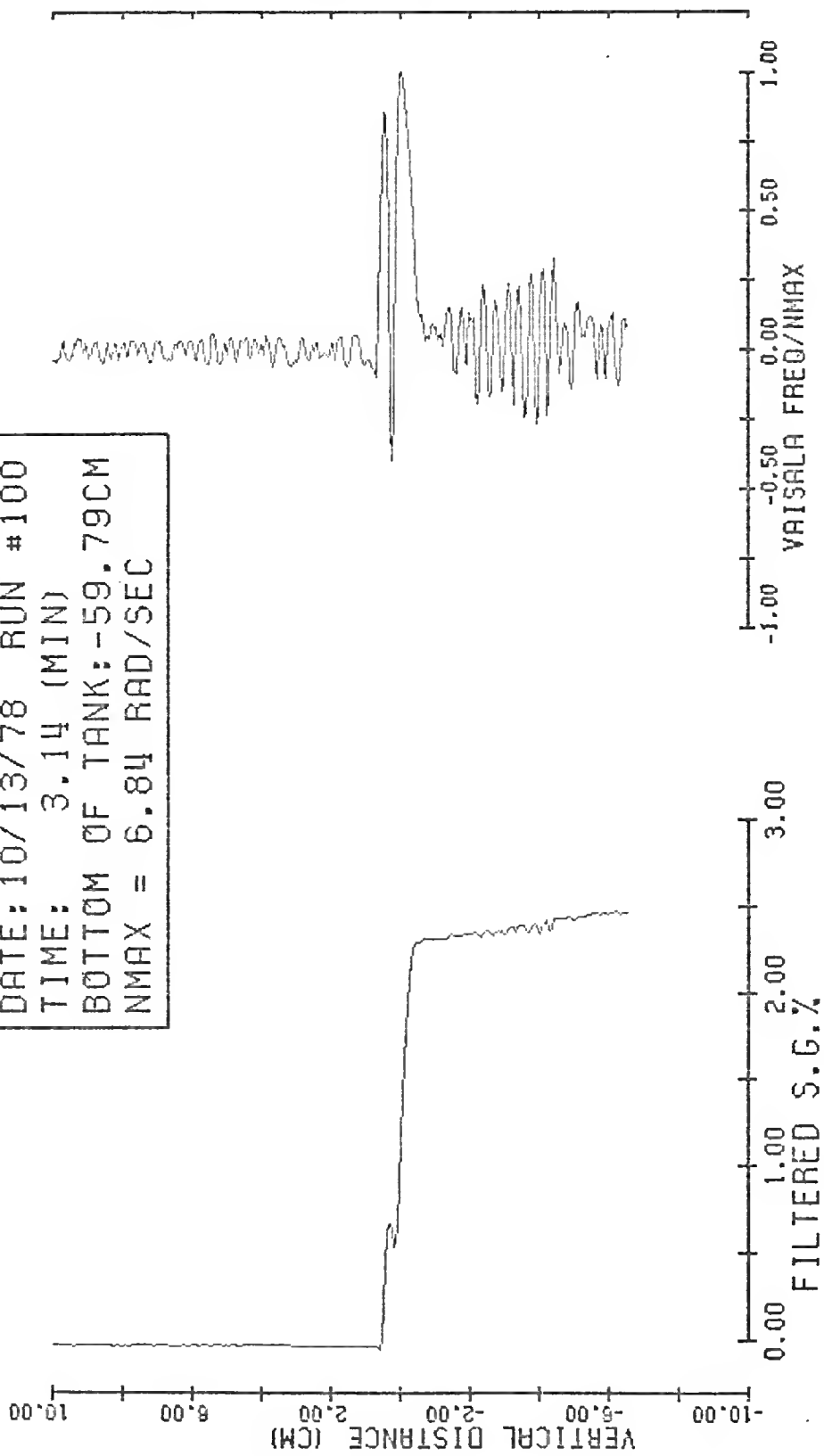
0.00 1.00 2.00 3.00
FILTERED S.G. %



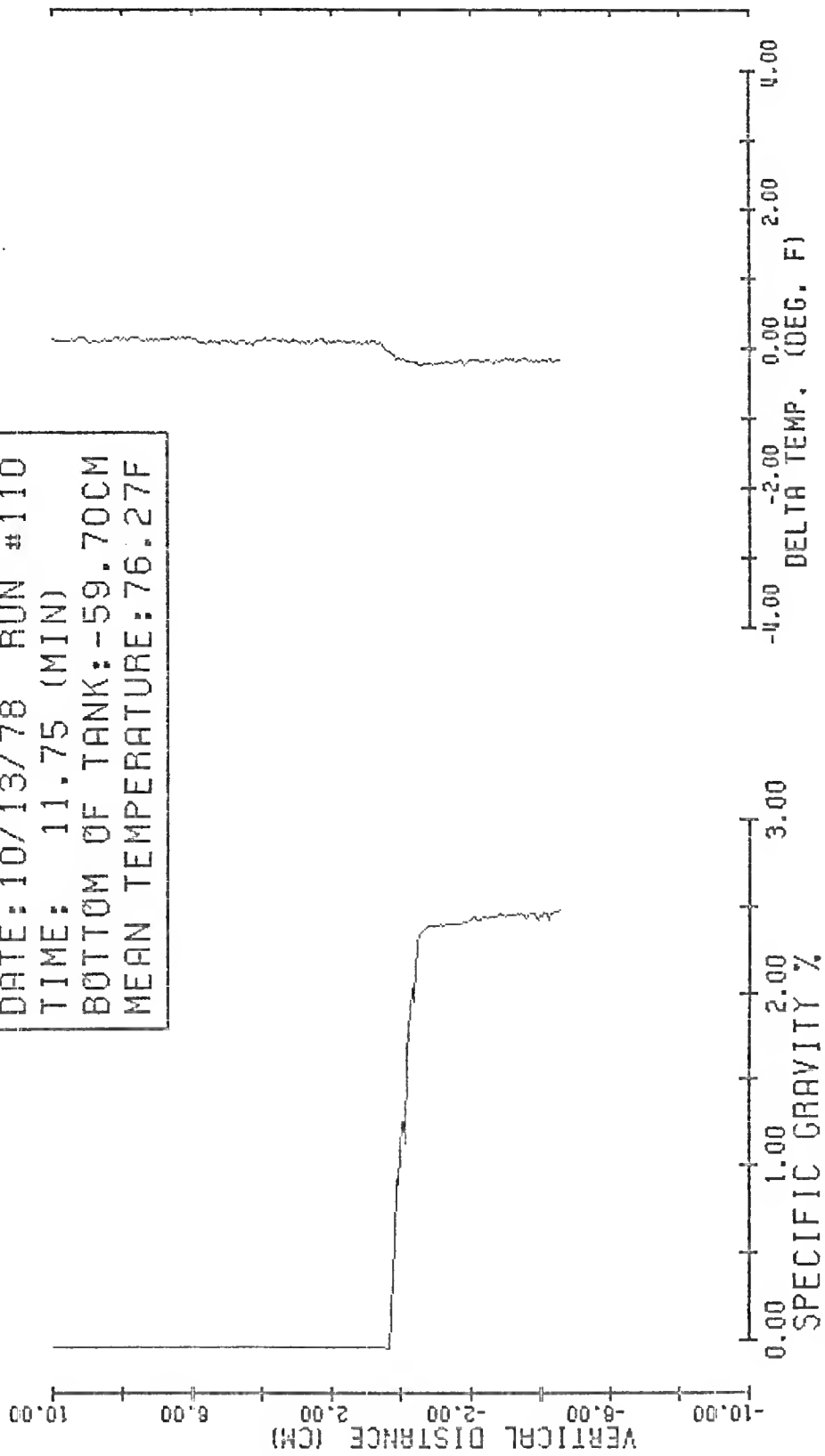
DATE: 10/13/78 RUN #100
TIME: 3.14 (MIN)
BOTTOM OF TANK: -59.79CM
MEAN TEMPERATURE: 76.10F



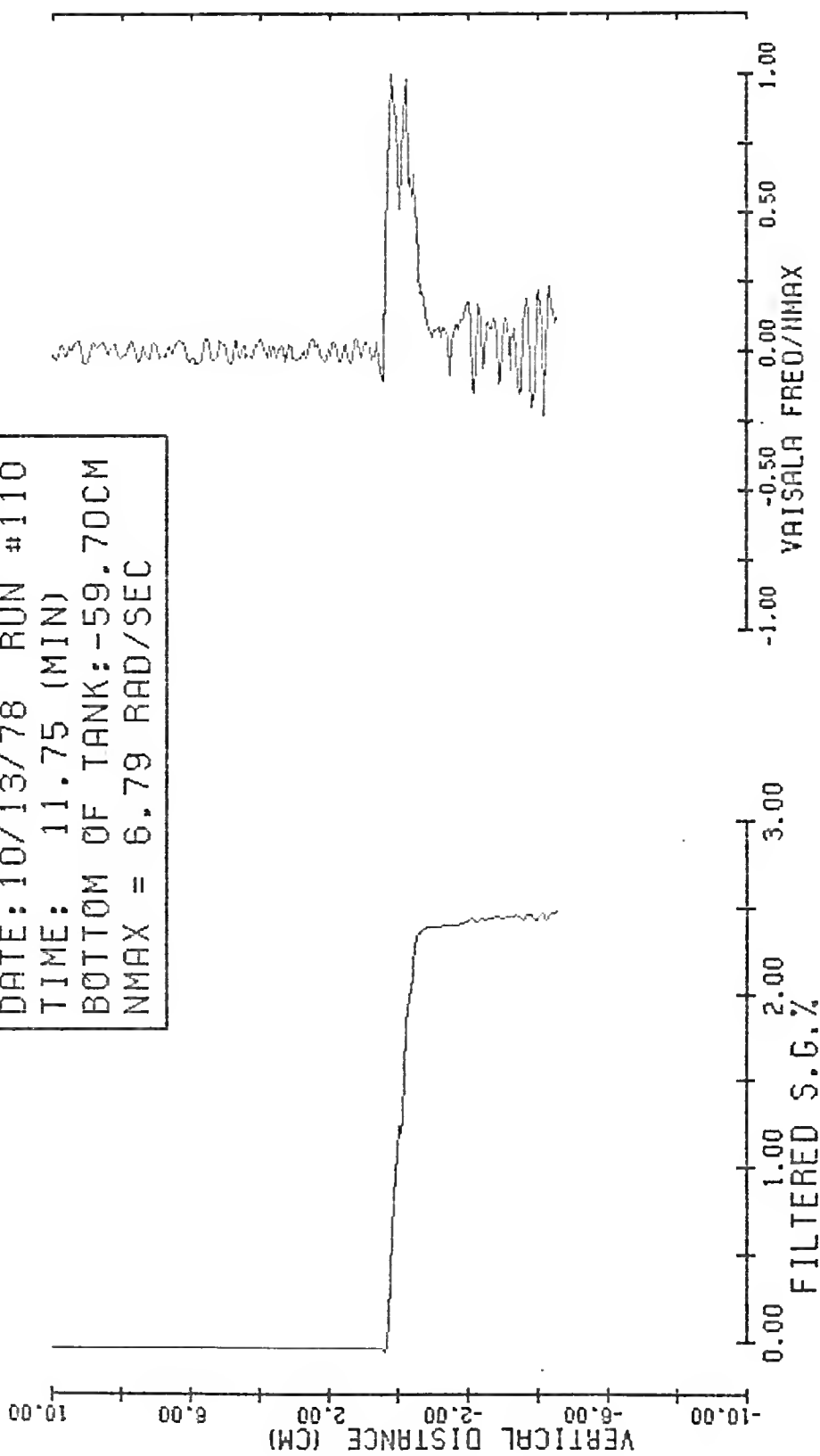
DATE: 10/13/78 RUN #100
TIME: 3.14 (MIN)
BOTTOM OF TANK: -59.79CM
NMAX = 6.84 RAD/SEC



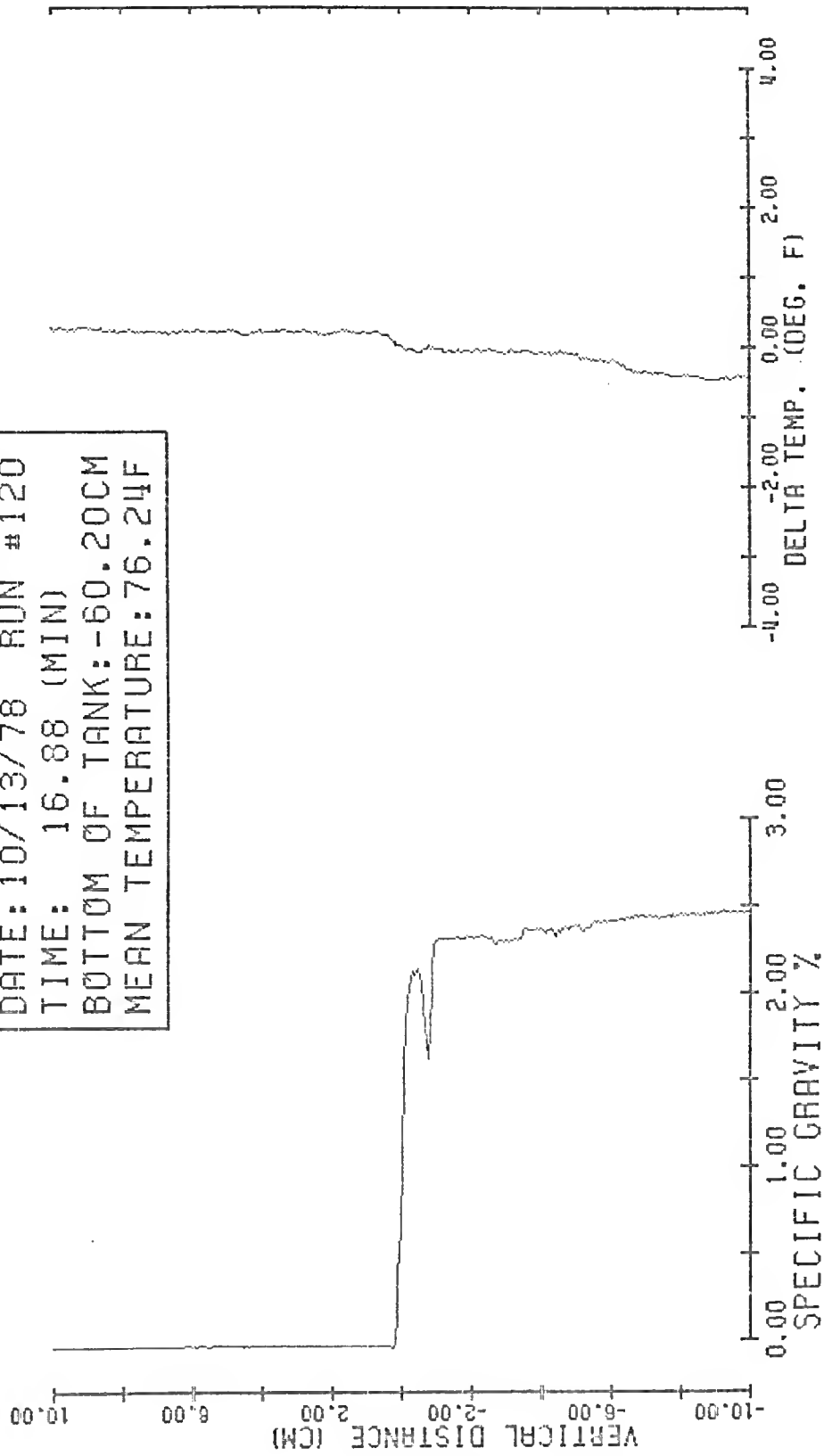
DATE: 10/13/78 RUN #110
TIME: 11.75 (MIN)
BOTTOM OF TANK: -59.70CM
MEAN TEMPERATURE: 76.27F



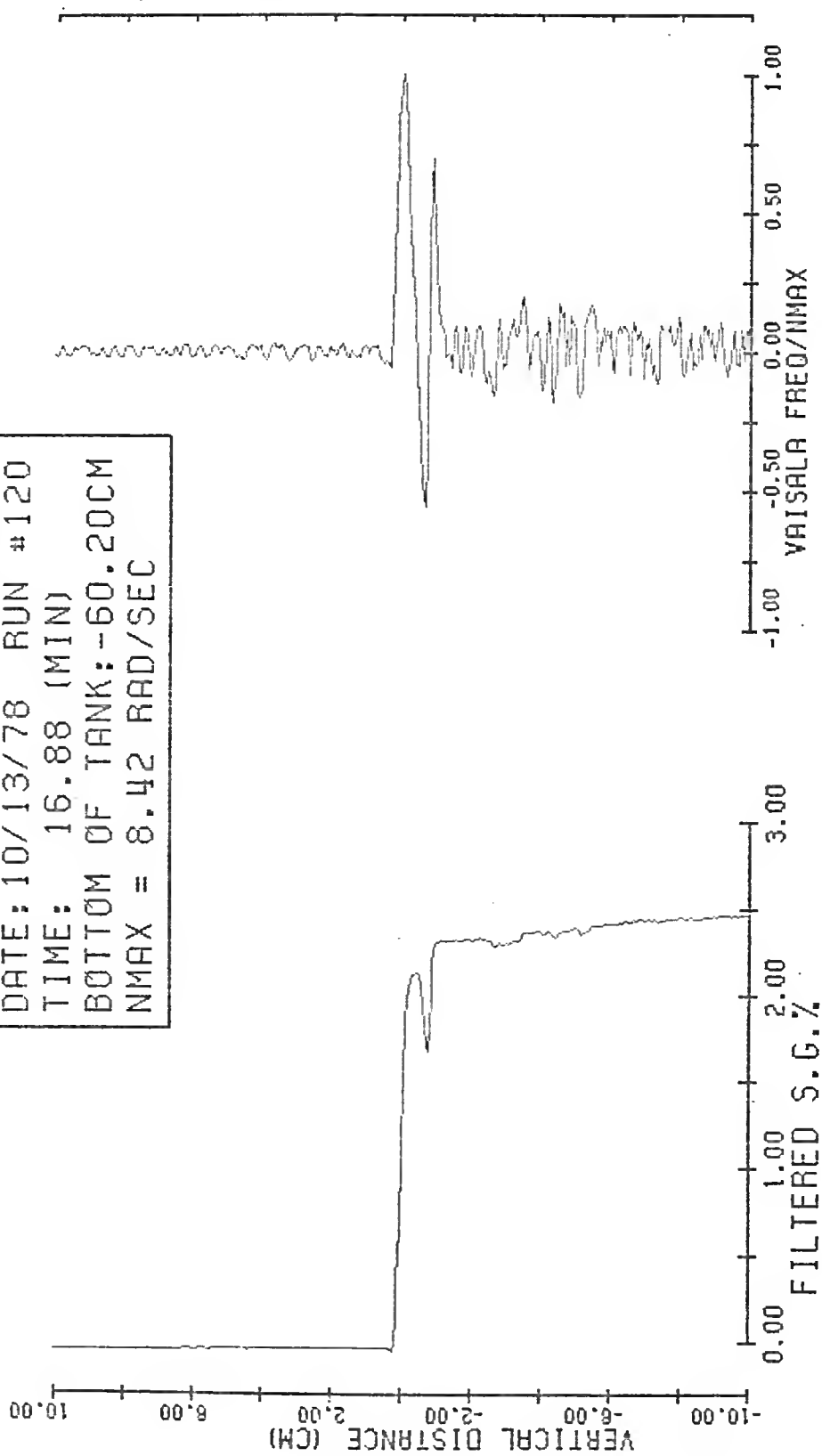
DATE: 10/13/78 RUN #110
TIME: 11.75 (MIN)
BOTTOM OF TANK: -59.70CM
NMAX = 6.79 RAD/SEC

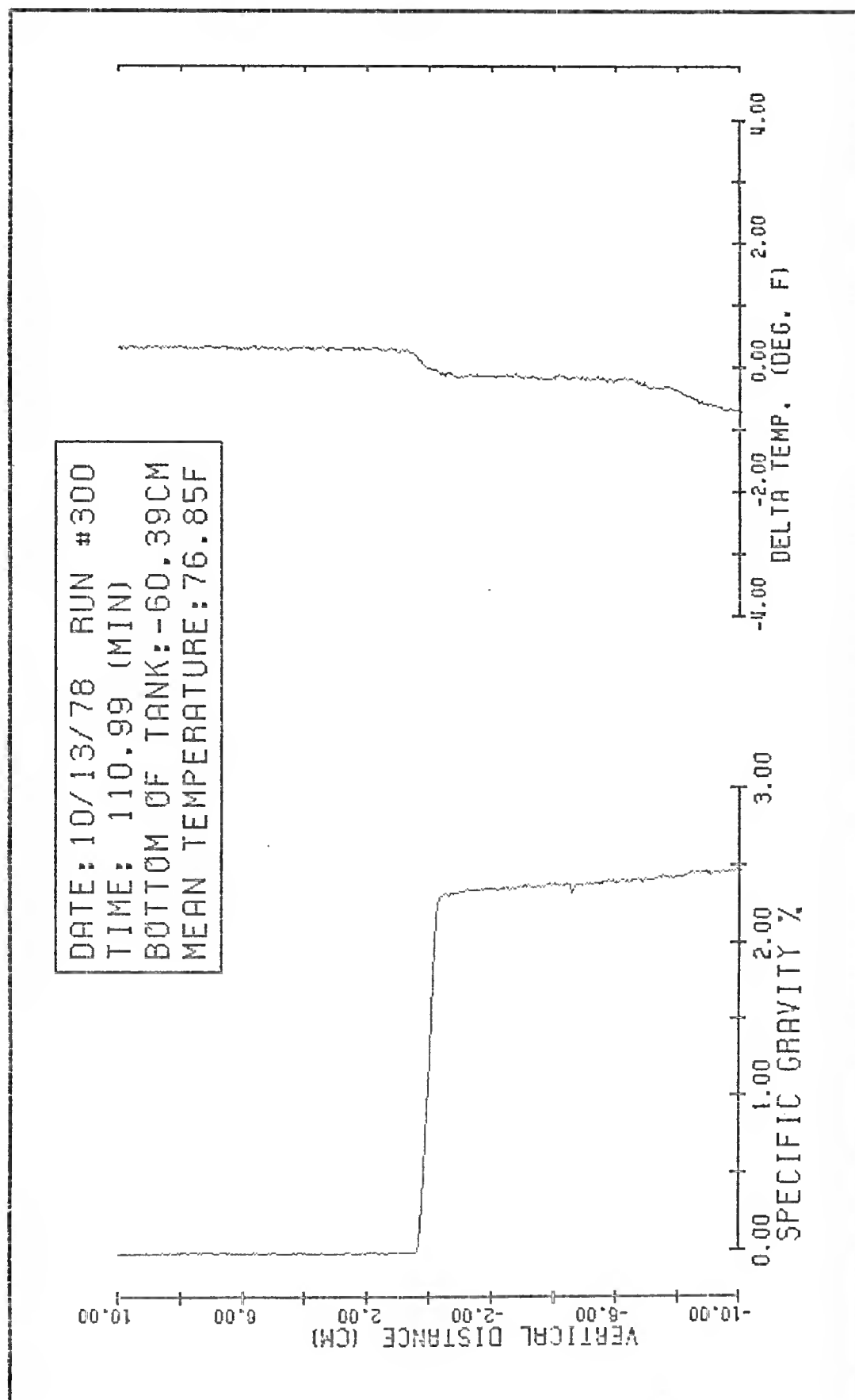


DATE: 10/13/78 RUN #120
TIME: 16.88 (MIN)
BOTTOM OF TANK: -60.20CM
MEAN TEMPERATURE: 76.24F

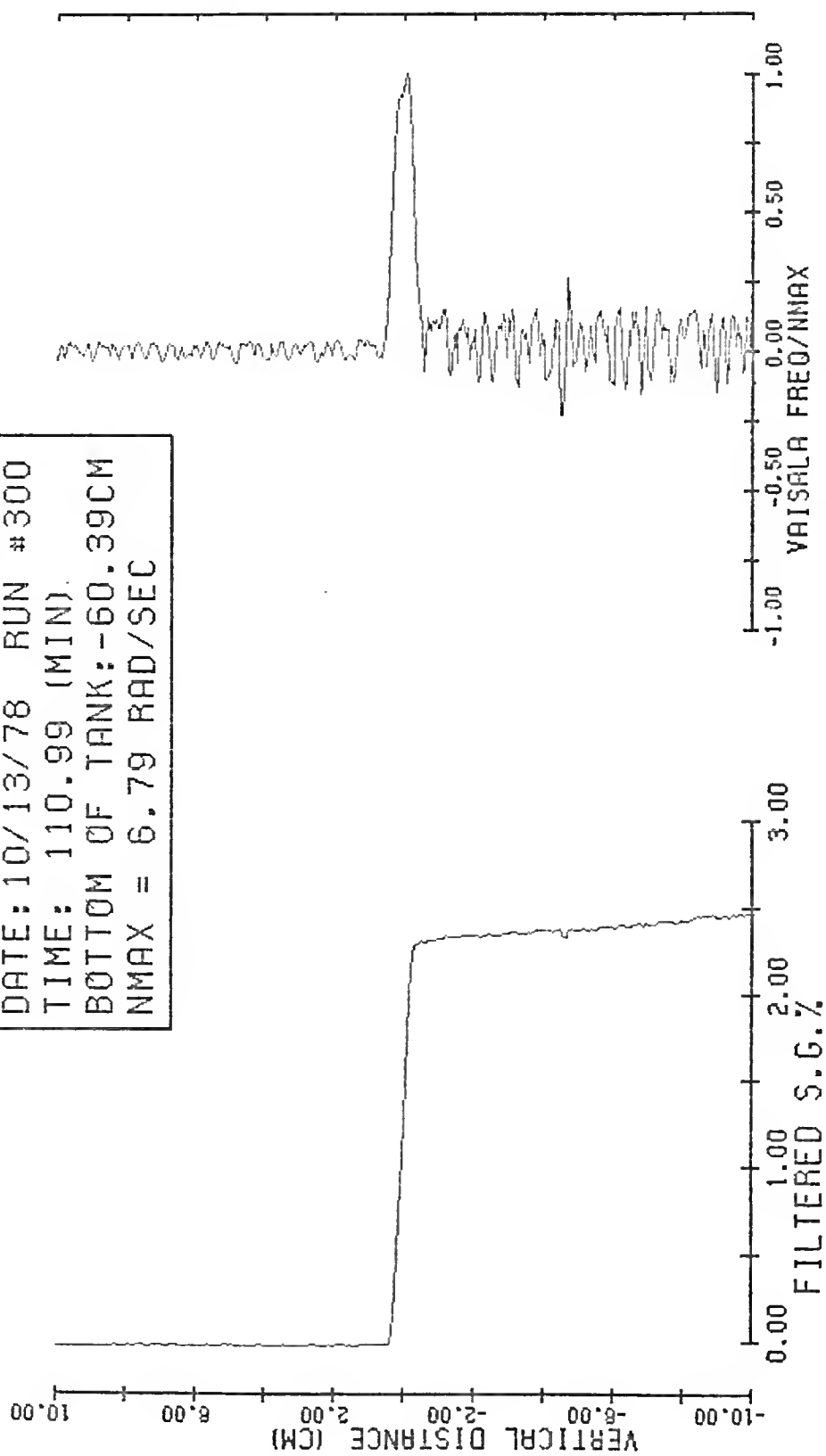


DATE: 10/13/78 RUN #120
TIME: 16.88 (MIN)
BOTTOM OF TANK: -60.20CM
NMAX = 8.42 RAD/SEC

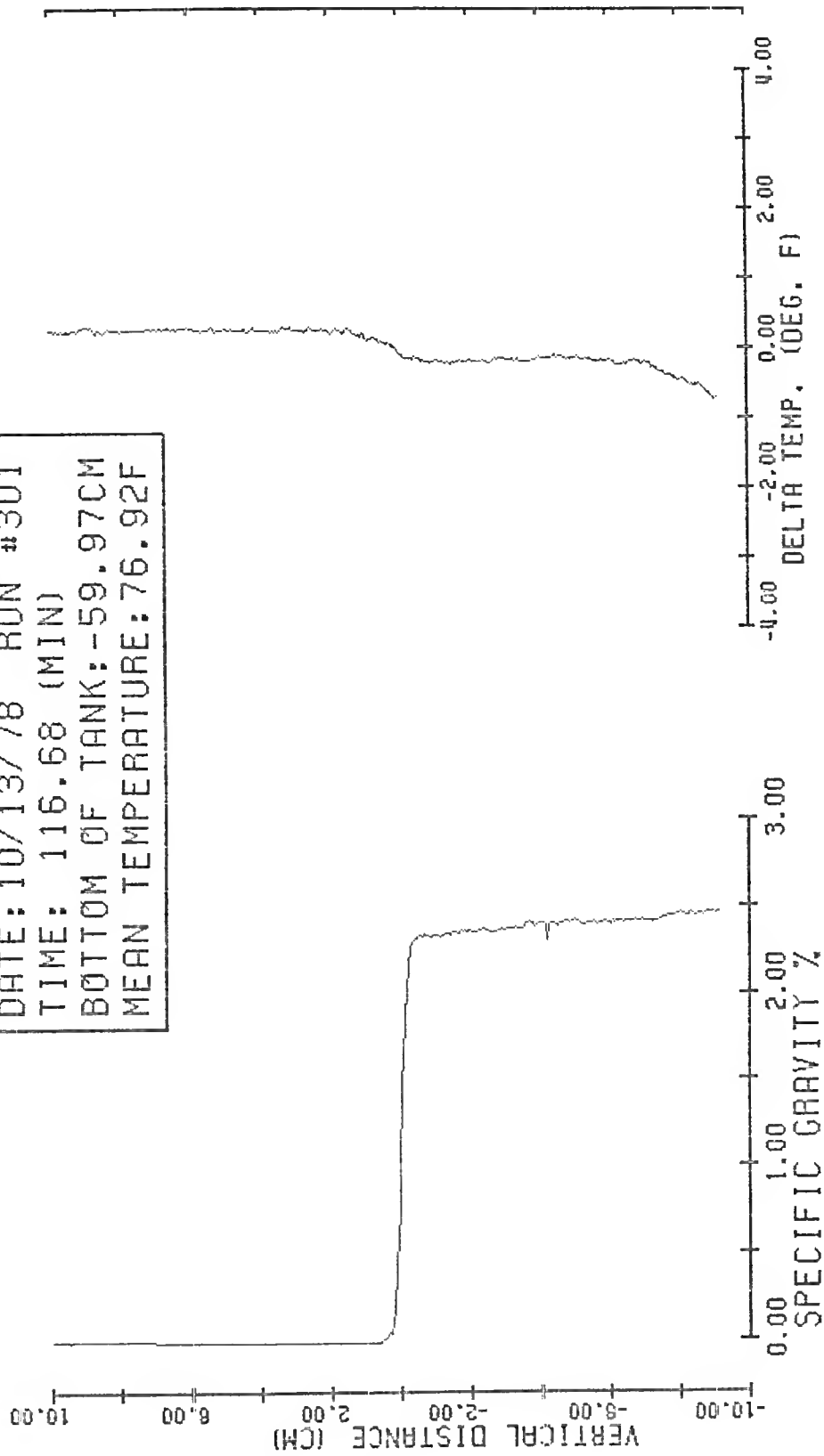


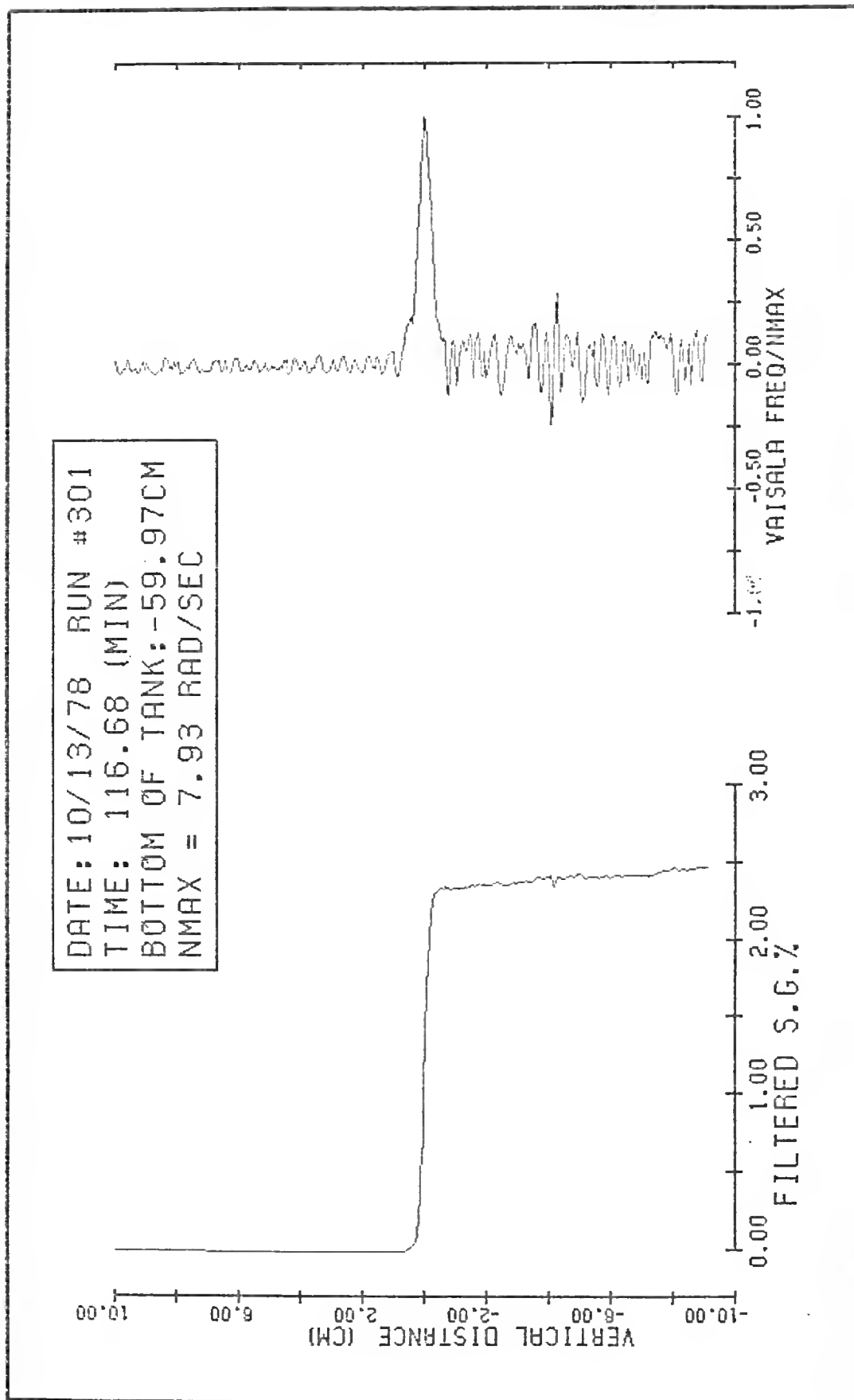


DATE: 10/13/78 RUN #300
TIME: 110.99 (MIN).
BOTTOM OF TANK: -60.39CM
NMAX = 6.79 RAD/SEC

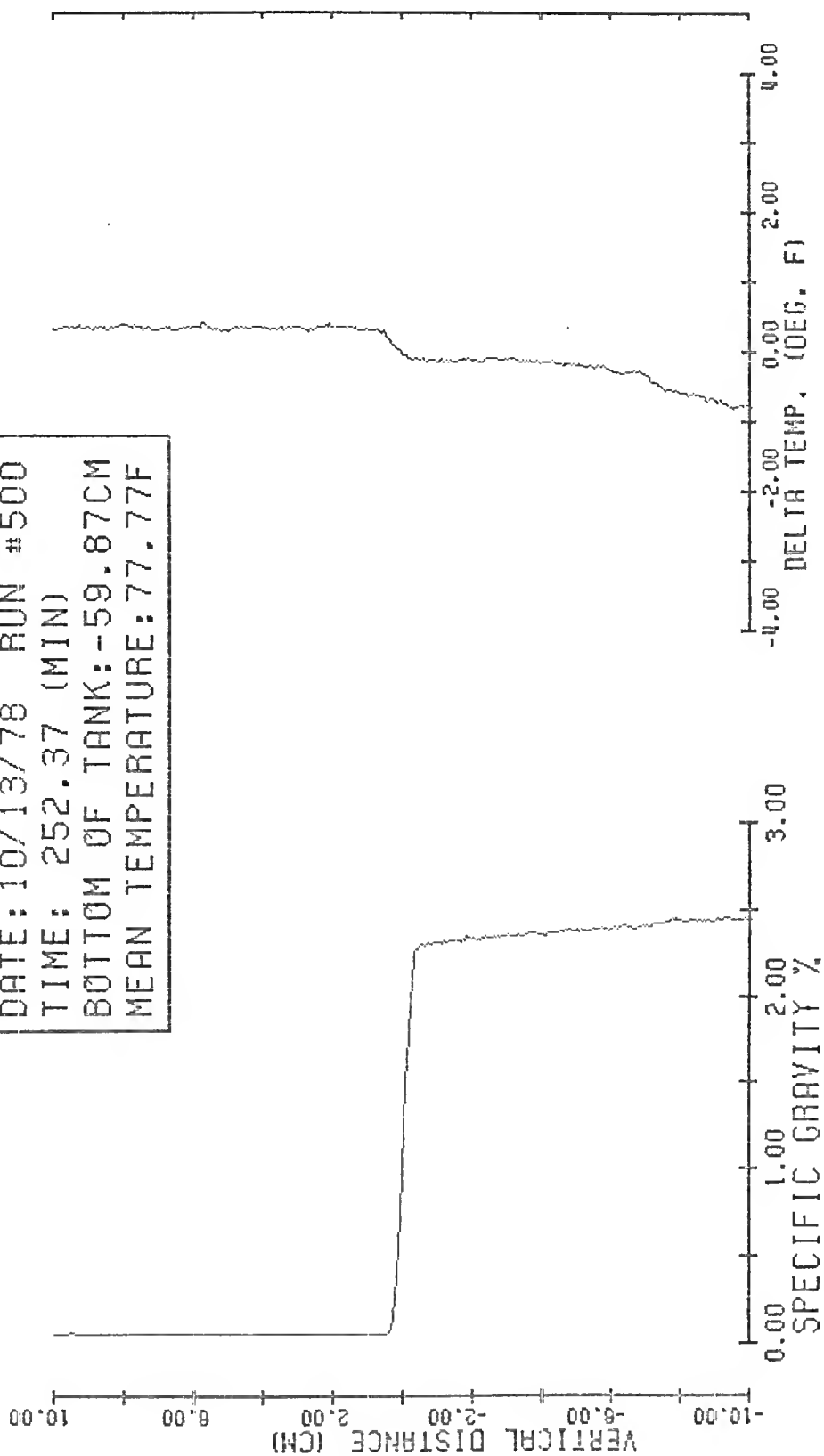


DATE: 10/13/78 RUN #301
TIME: 116.68 (MIN)
BOTTOM OF TANK: -59.97CM
MEAN TEMPERATURE: 76.92F

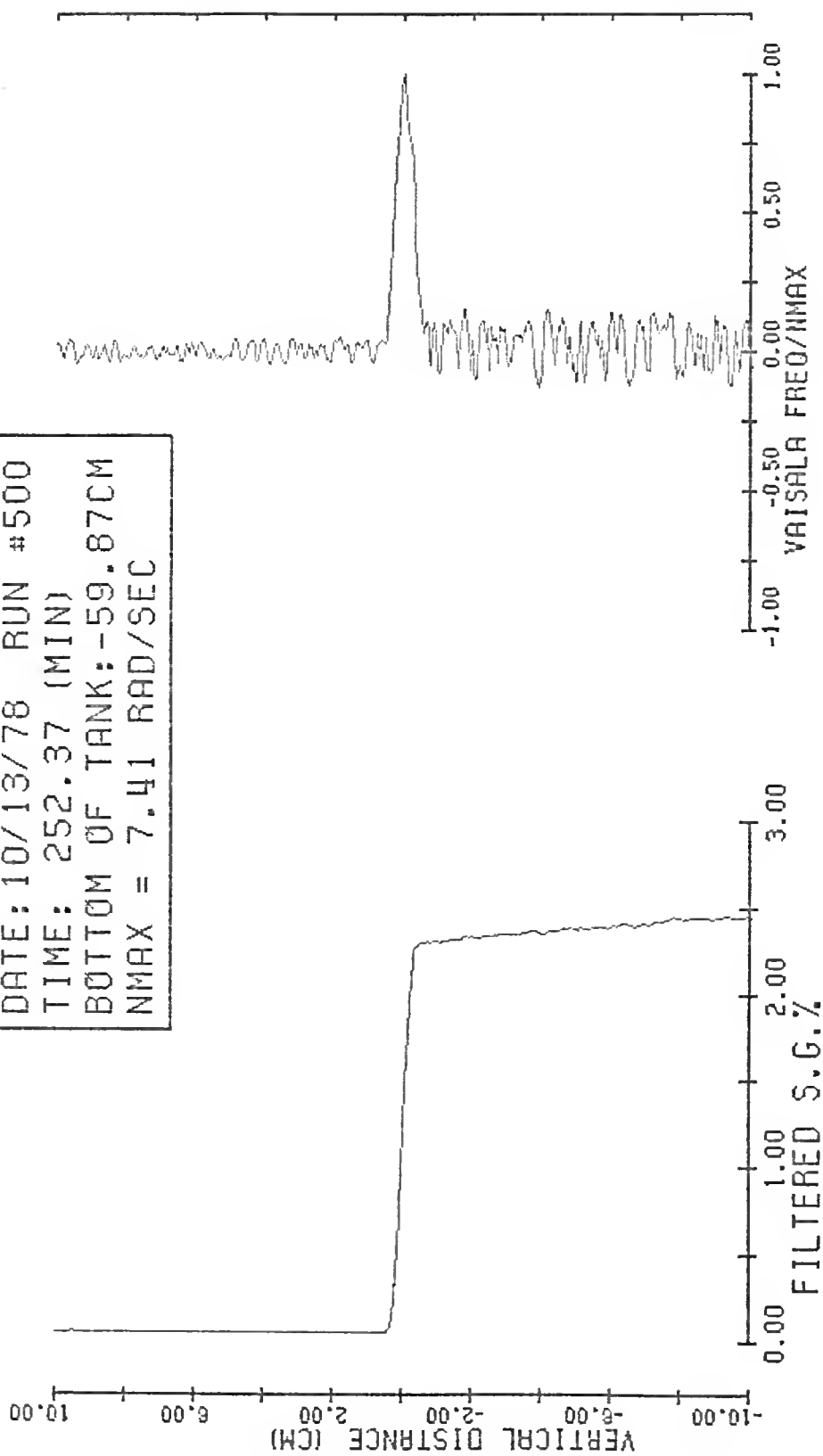




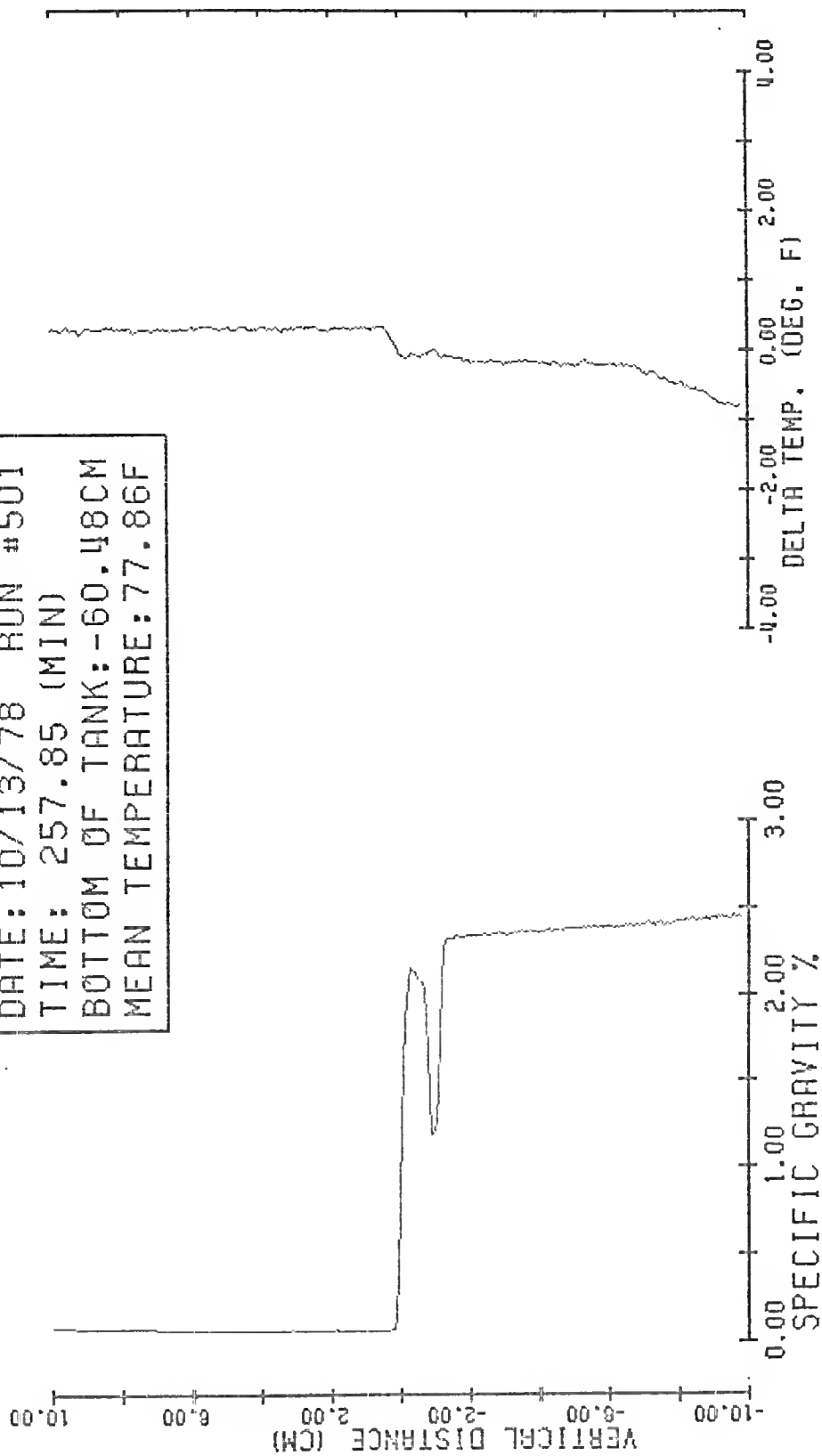
DATE: 10/13/78 RUN #500
TIME: 252.37 (MIN)
BOTTOM OF TANK: -59.87CM
MEAN TEMPERATURE: 77.77F



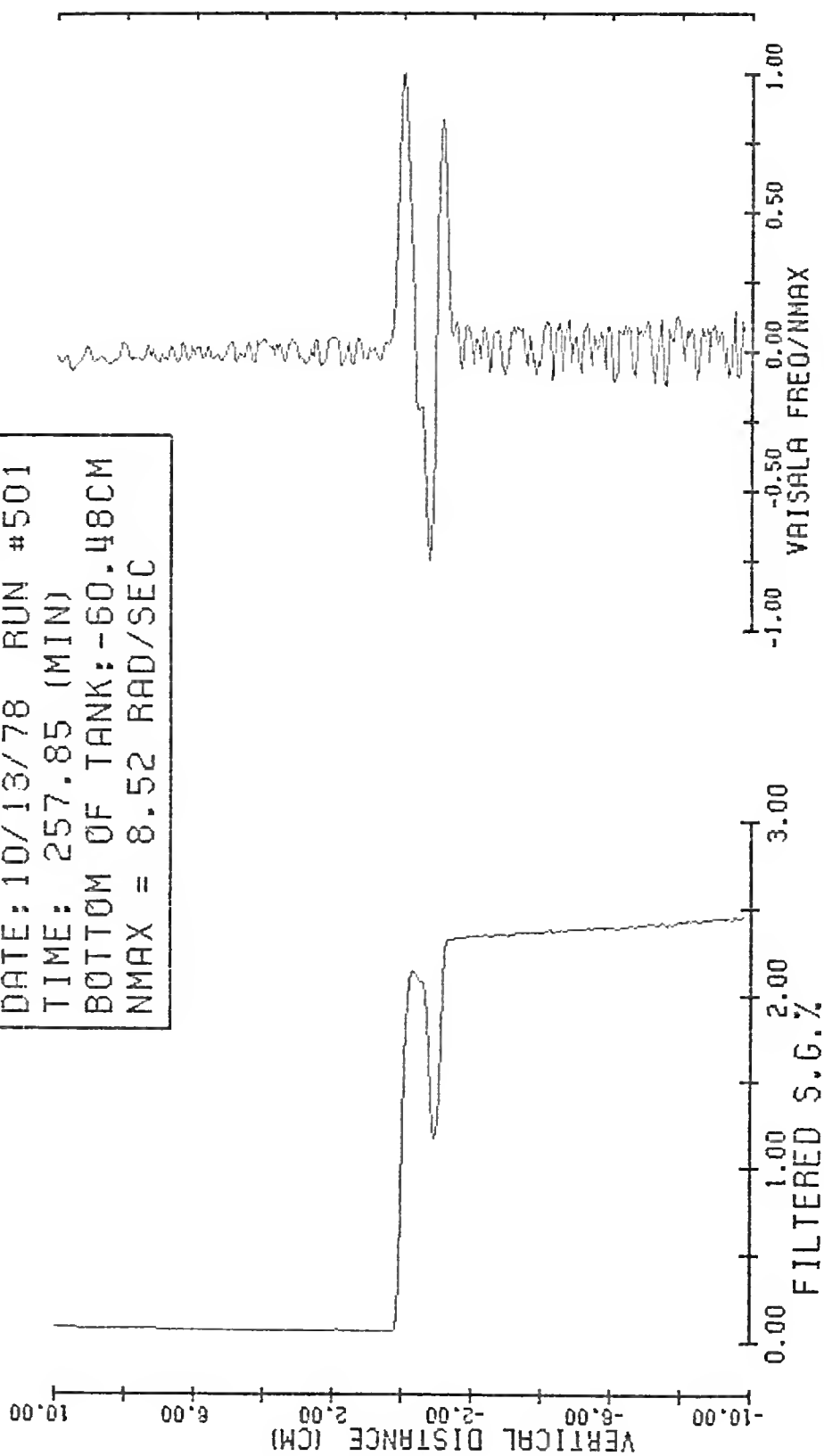
DATE: 10/13/78 RUN #500
TIME: 252.37 (MIN)
BOTTOM OF TANK: -59.87CM
NMAX = 7.41 RAD/SEC

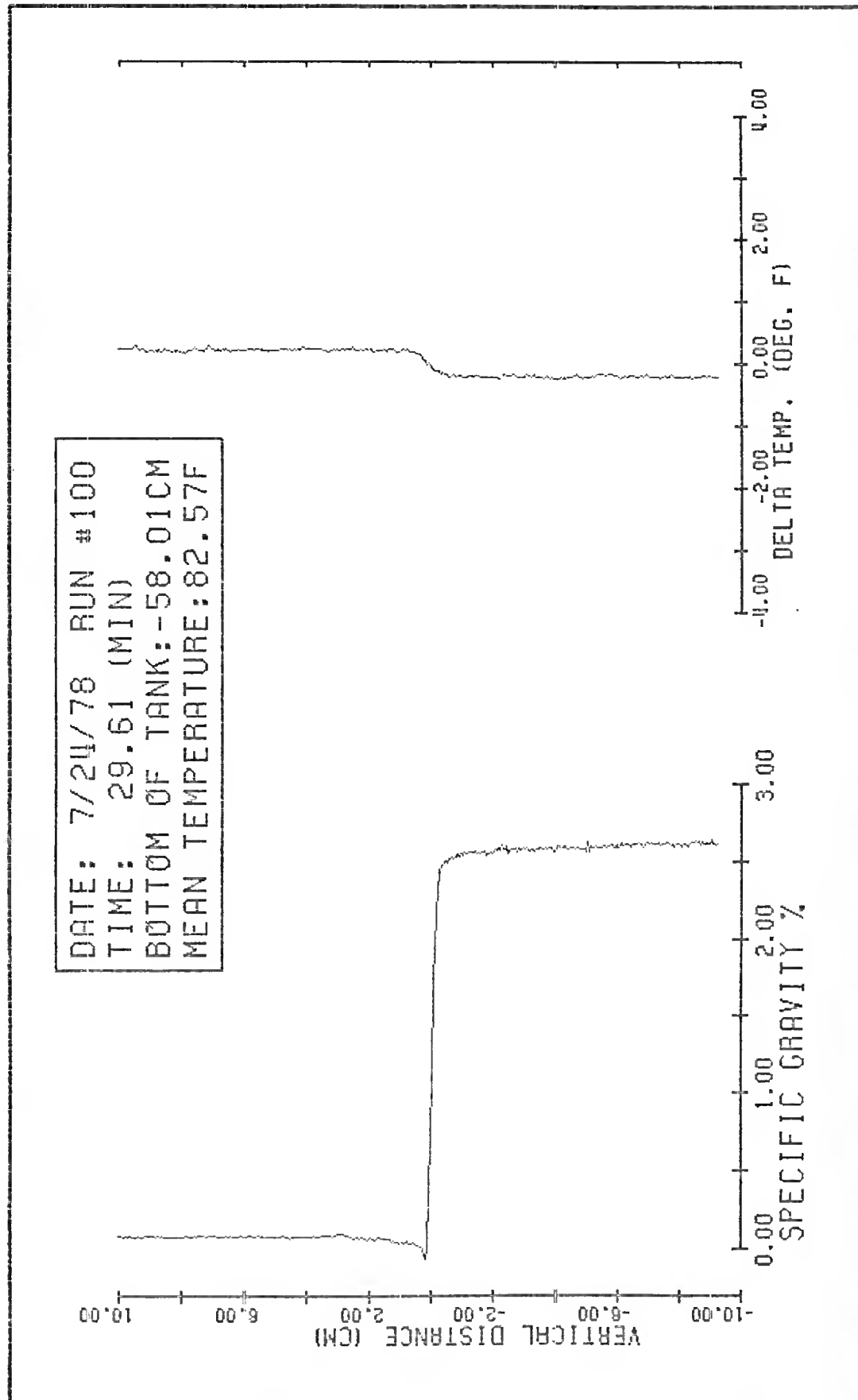


DATE: 10/13/78 RUN #501
TIME: 257.85 (MIN)
BOTTOM OF TANK: -60.48CM
MEAN TEMPERATURE: 77.86F

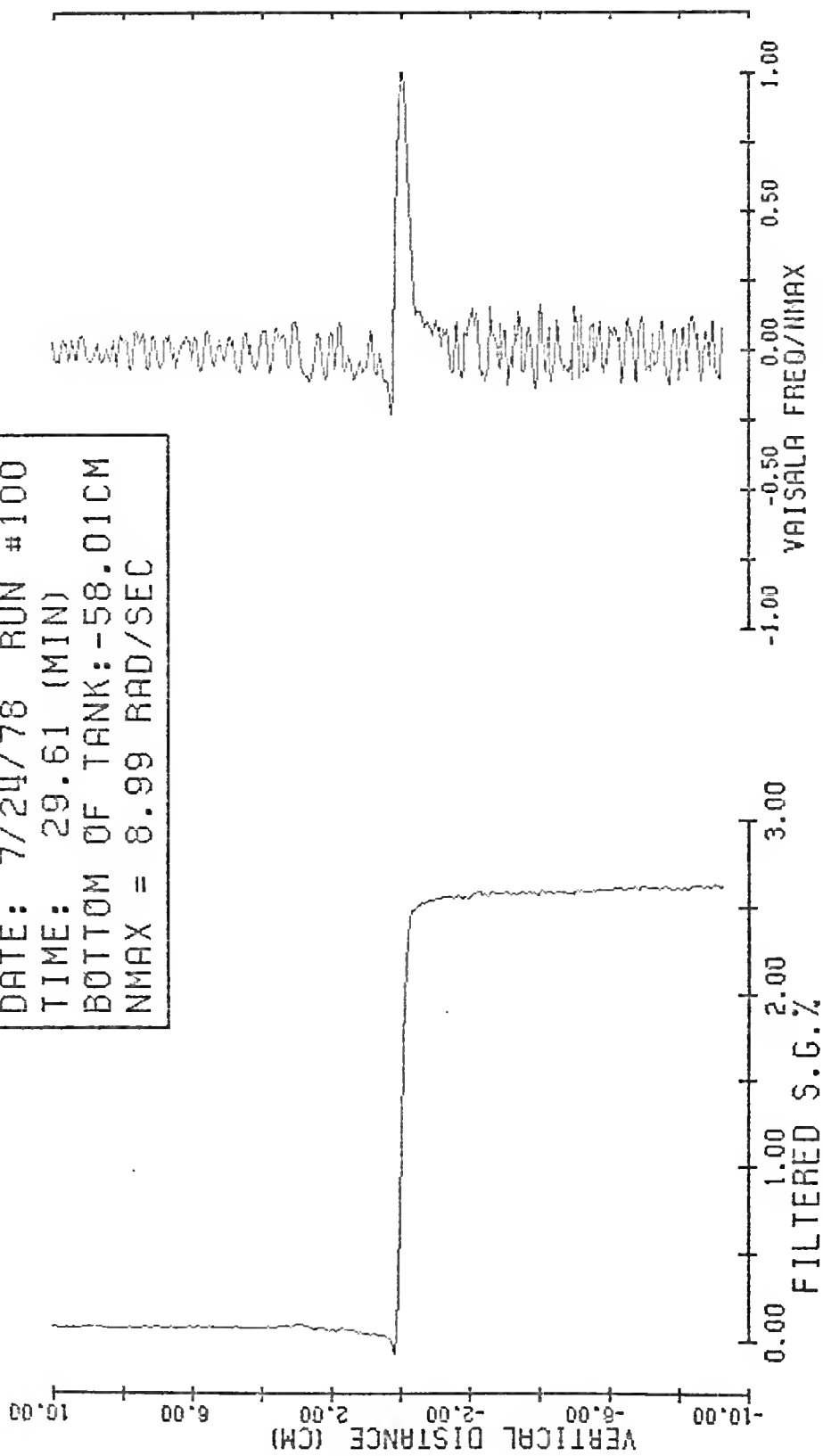


DATE: 10/13/78 RUN #501
TIME: 257.85 (MIN)
BOTTOM OF TANK: -60.48CM
NMAX = 8.52 RAD/SEC

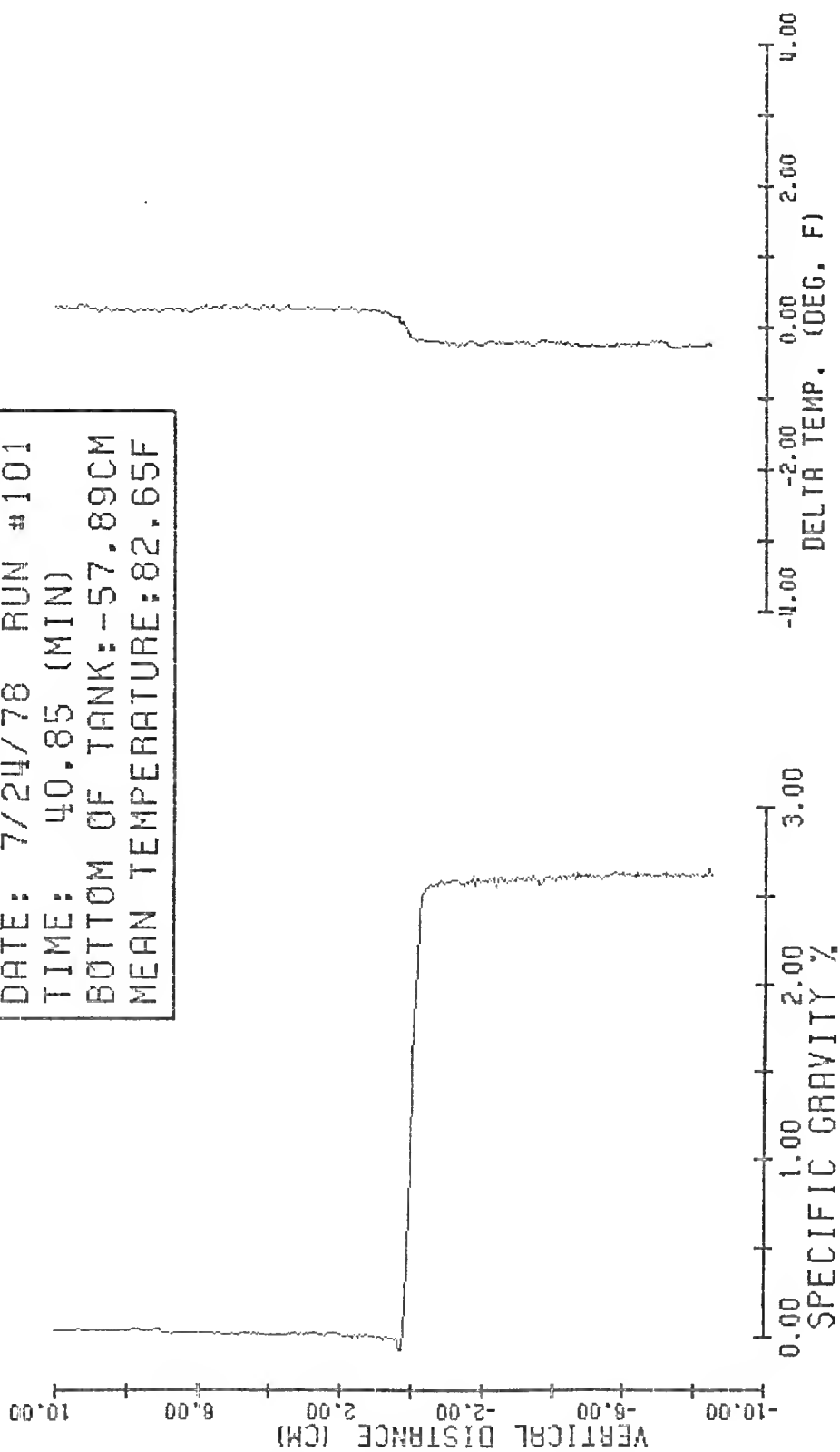




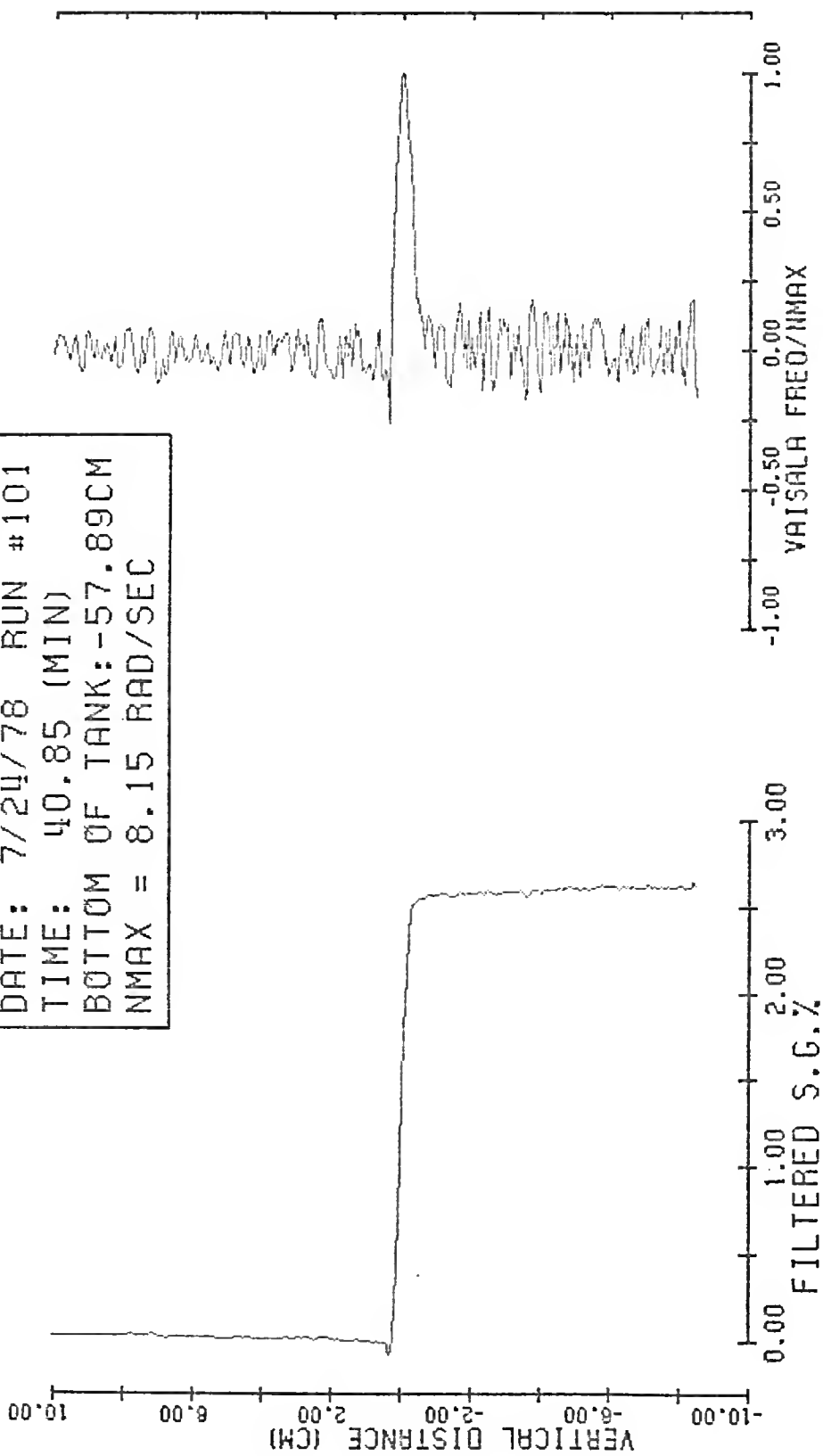
DATE: 7/24/78 RUN #100
TIME: 29.61 (MIN)
BOTTOM OF TANK: -58.01CM
NMAX = 8.99 RAD/SEC



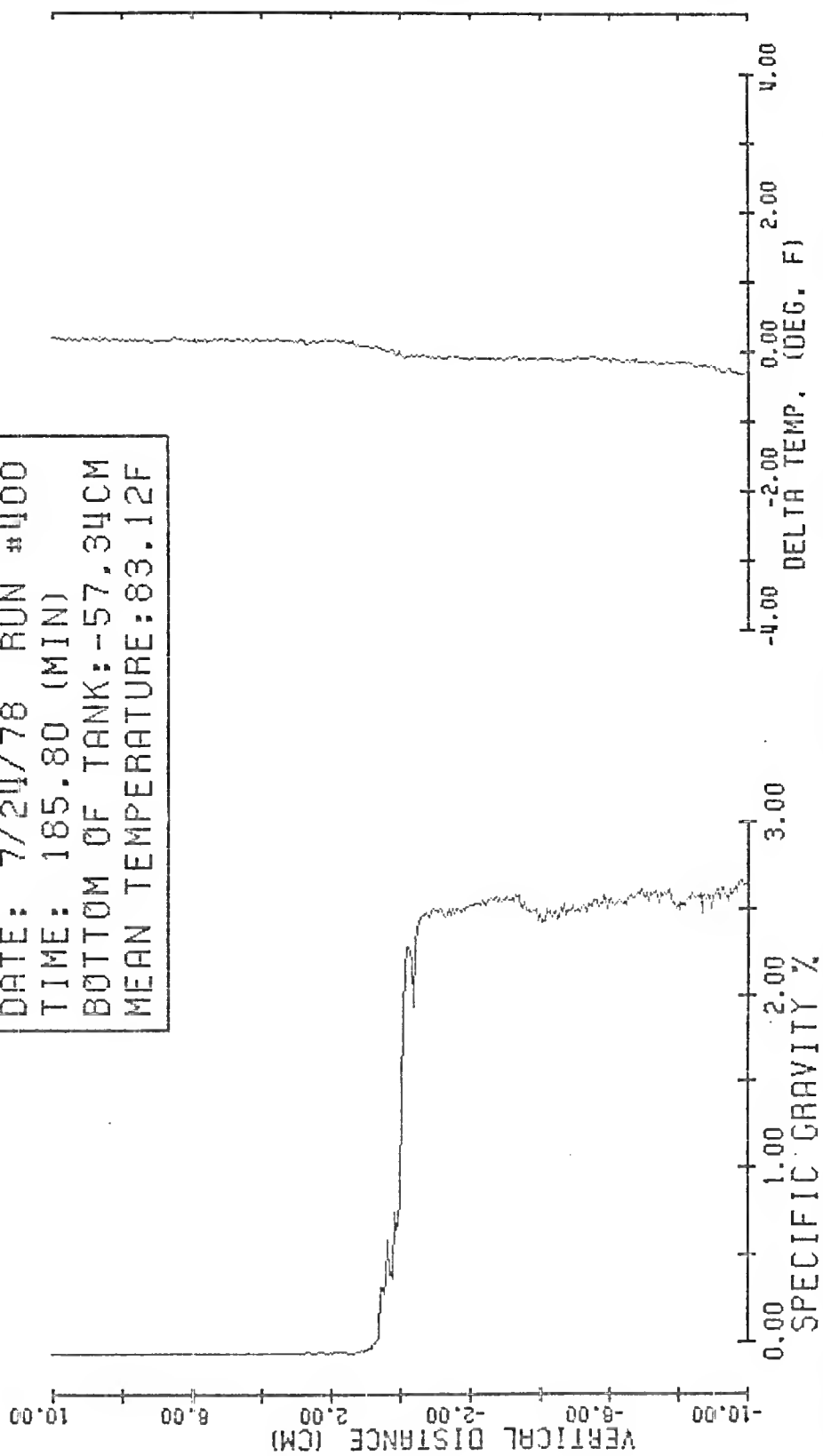
DATE: 7/24/78 RUN #101
TIME: 40.85 (MIN)
BOTTOM OF TANK: -57.89CM
MEAN TEMPERATURE: 82.65F



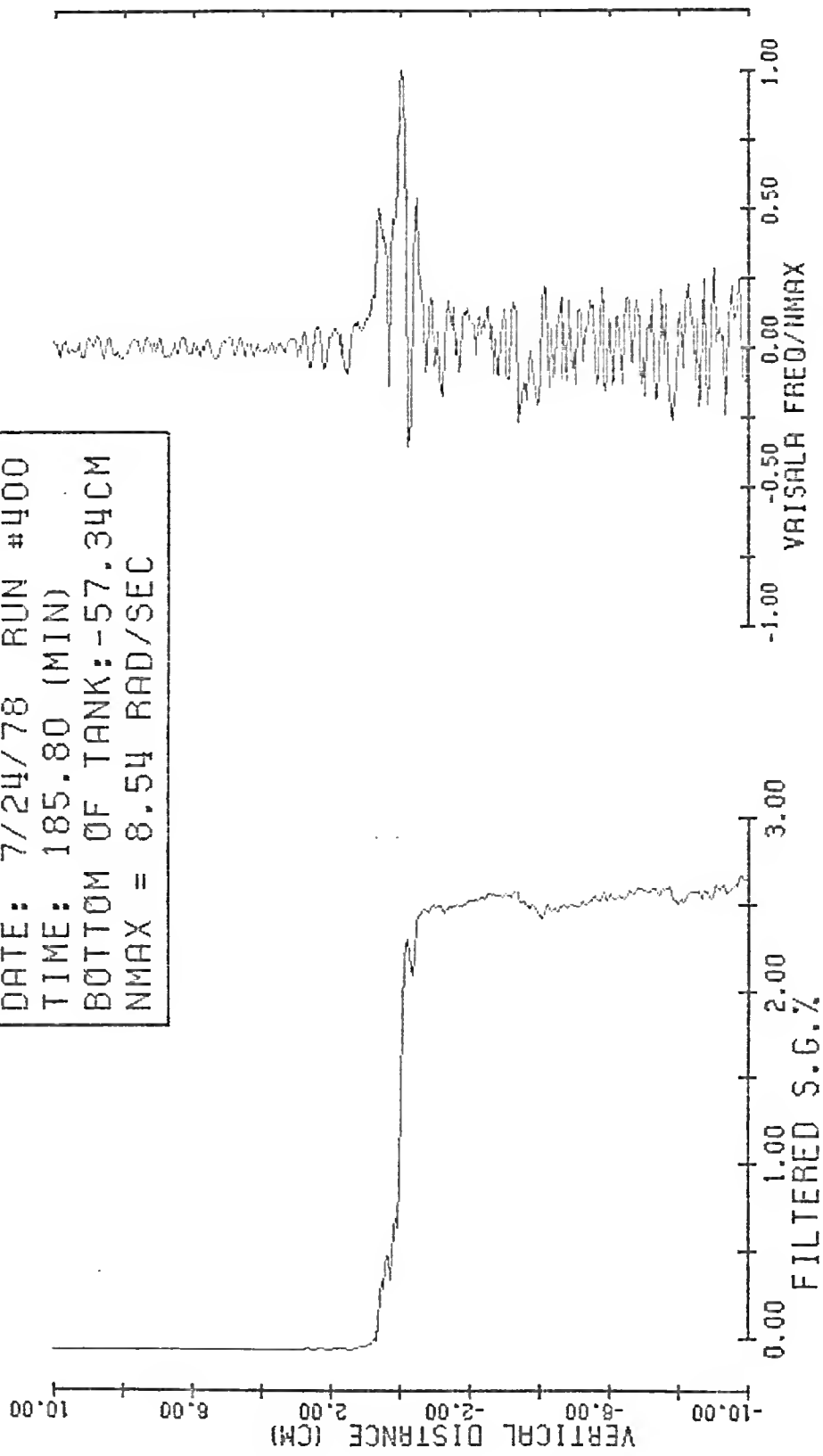
DATE: 7/24/78 RUN #101
TIME: 40.85 (MIN)
BOTTOM OF TANK: -57.89CM
NMAX = 8.15 RAD/SEC



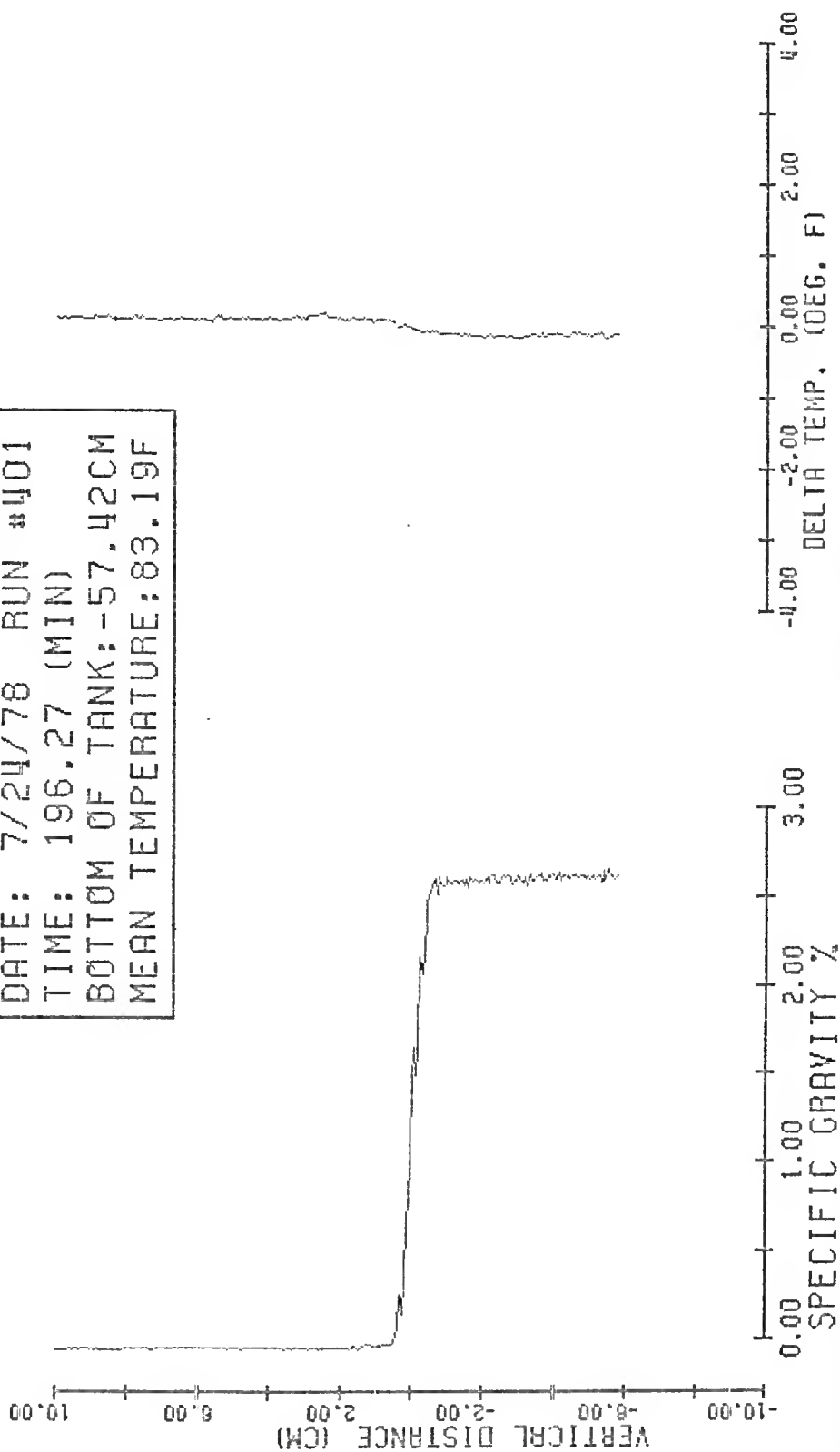
DATE: 7/24/78 RUN #400
TIME: 185.80 (MIN)
BOTTOM OF TANK: -57.34CM
MEAN TEMPERATURE: 83.12F



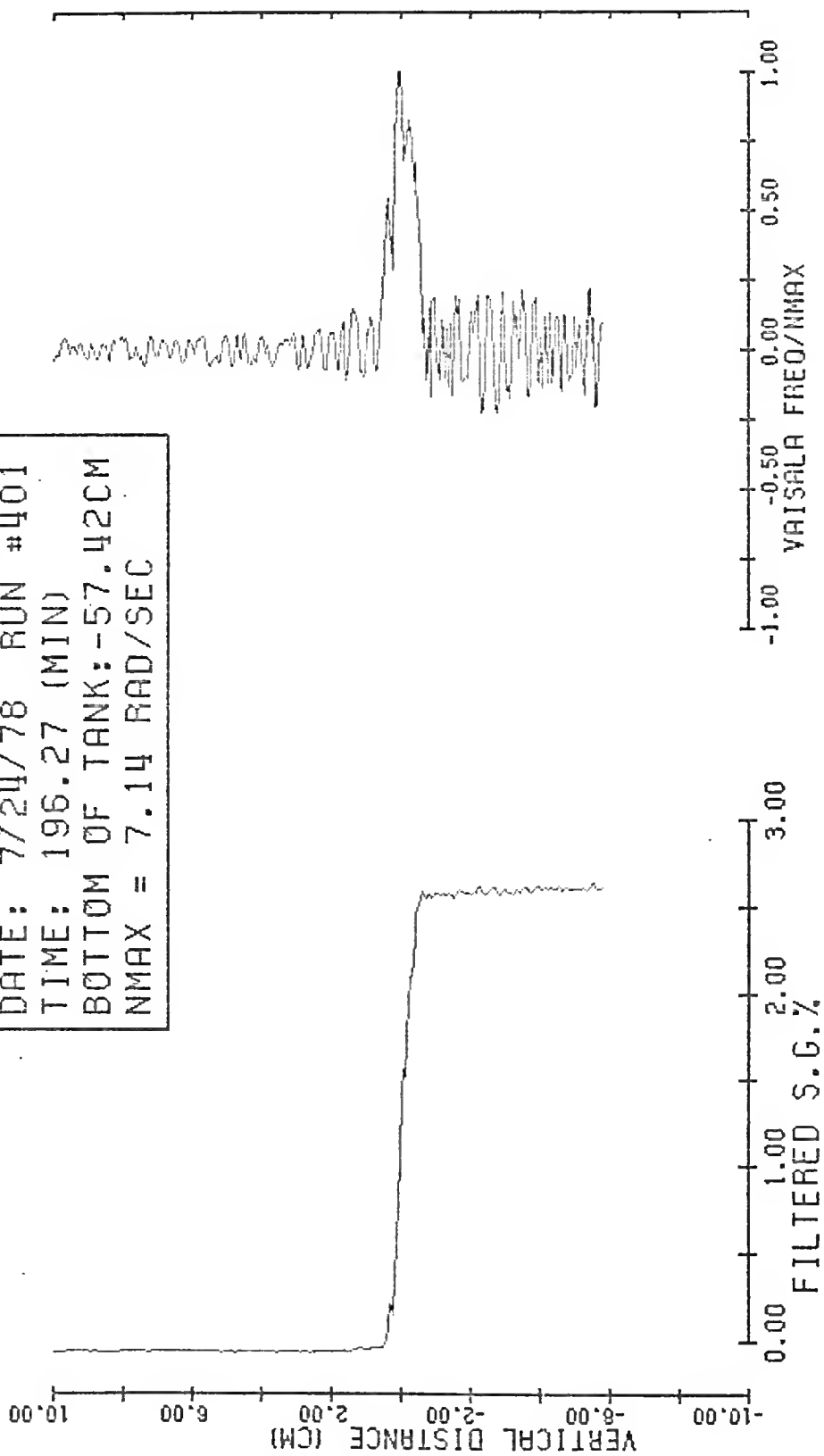
DATE: 7/24/78 RUN #400
TIME: 185.80 (MIN)
BOTTOM OF TANK: -57.34CM
NMAX = 8.54 RAD/SEC



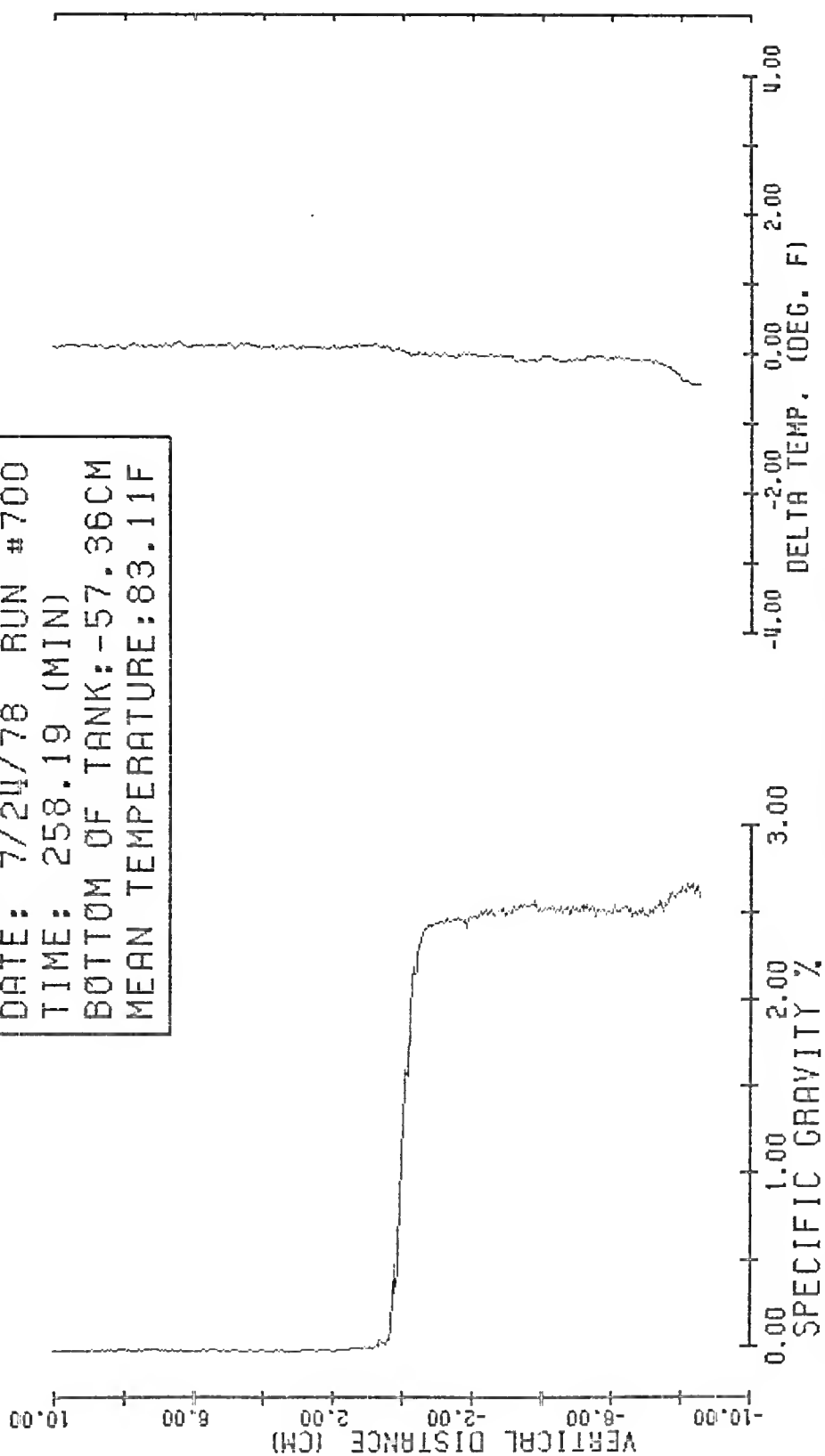
DATE: 7/24/78 RUN #401
TIME: 196.27 (MIN)
BOTTOM OF TANK: -57.42CM
MEAN TEMPERATURE: 83.19F



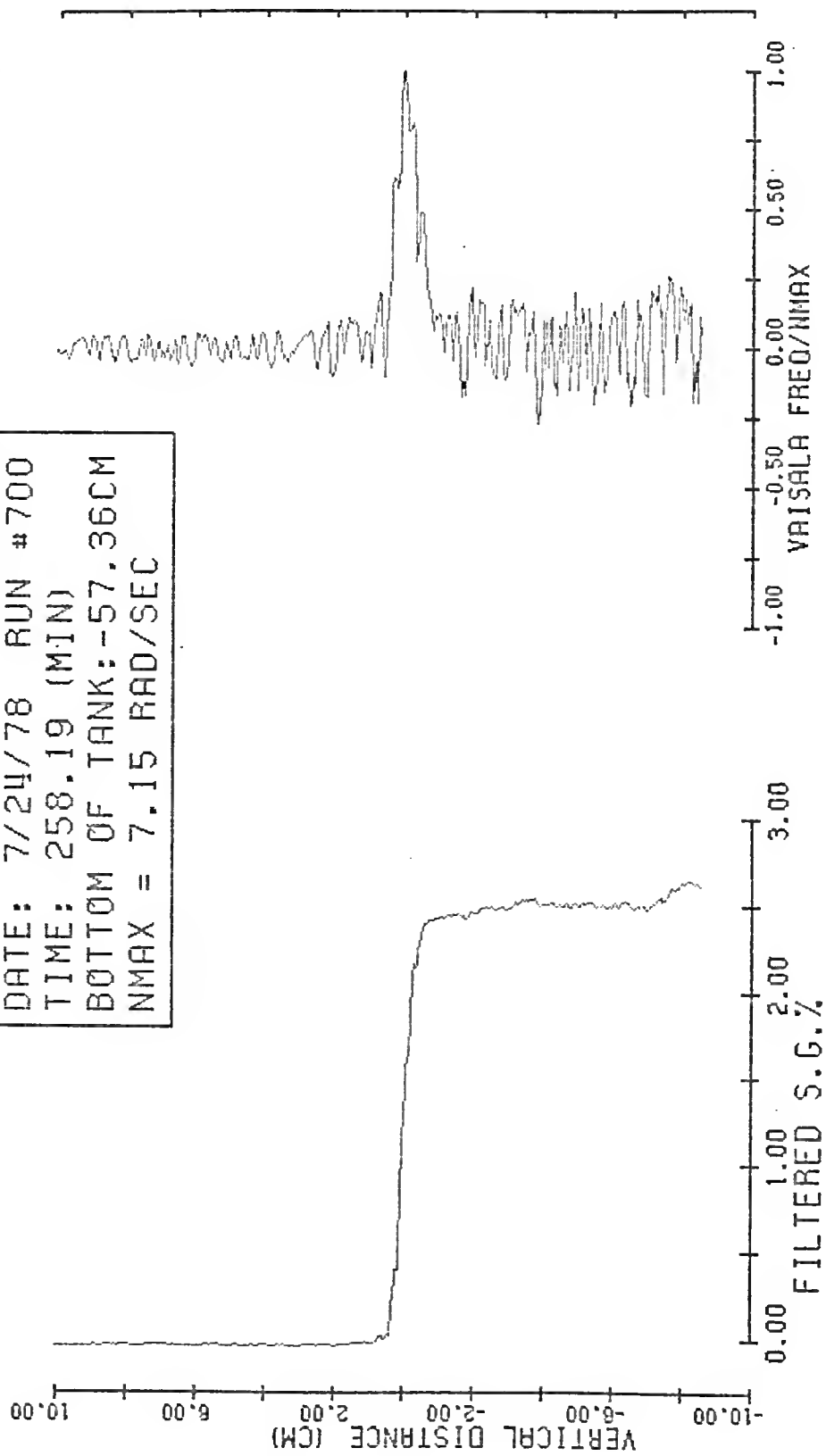
DATE: 7/24/78 RUN #401
TIME: 196.27 (MIN)
BOTTOM OF TANK: -57.42CM
NMAX = 7.14 RAD/SEC



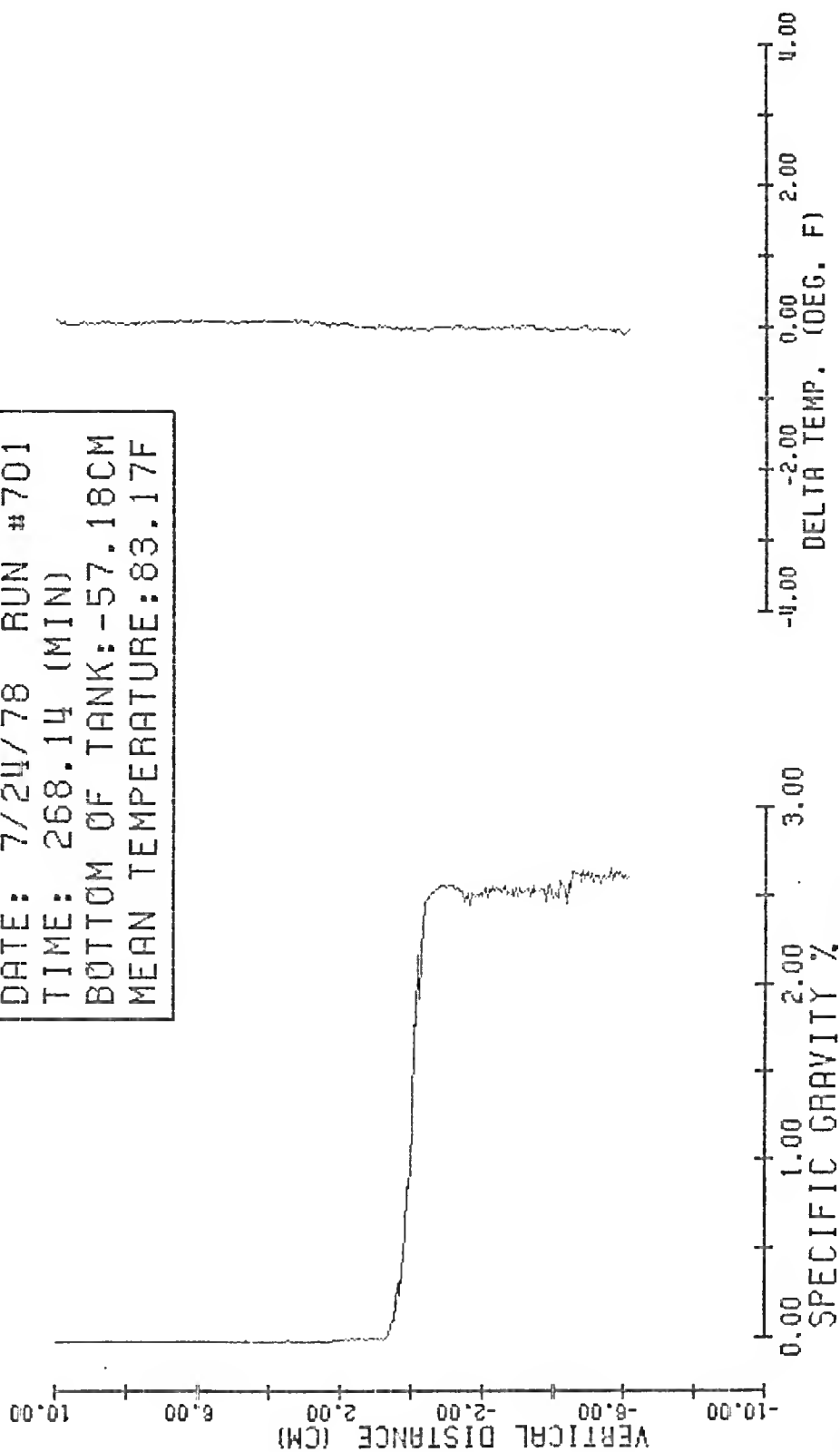
DATE: 7/24/78 RUN #700
TIME: 258.19 (MIN)
BOTTOM OF TANK: -57.36CM
MEAN TEMPERATURE: 83.11F



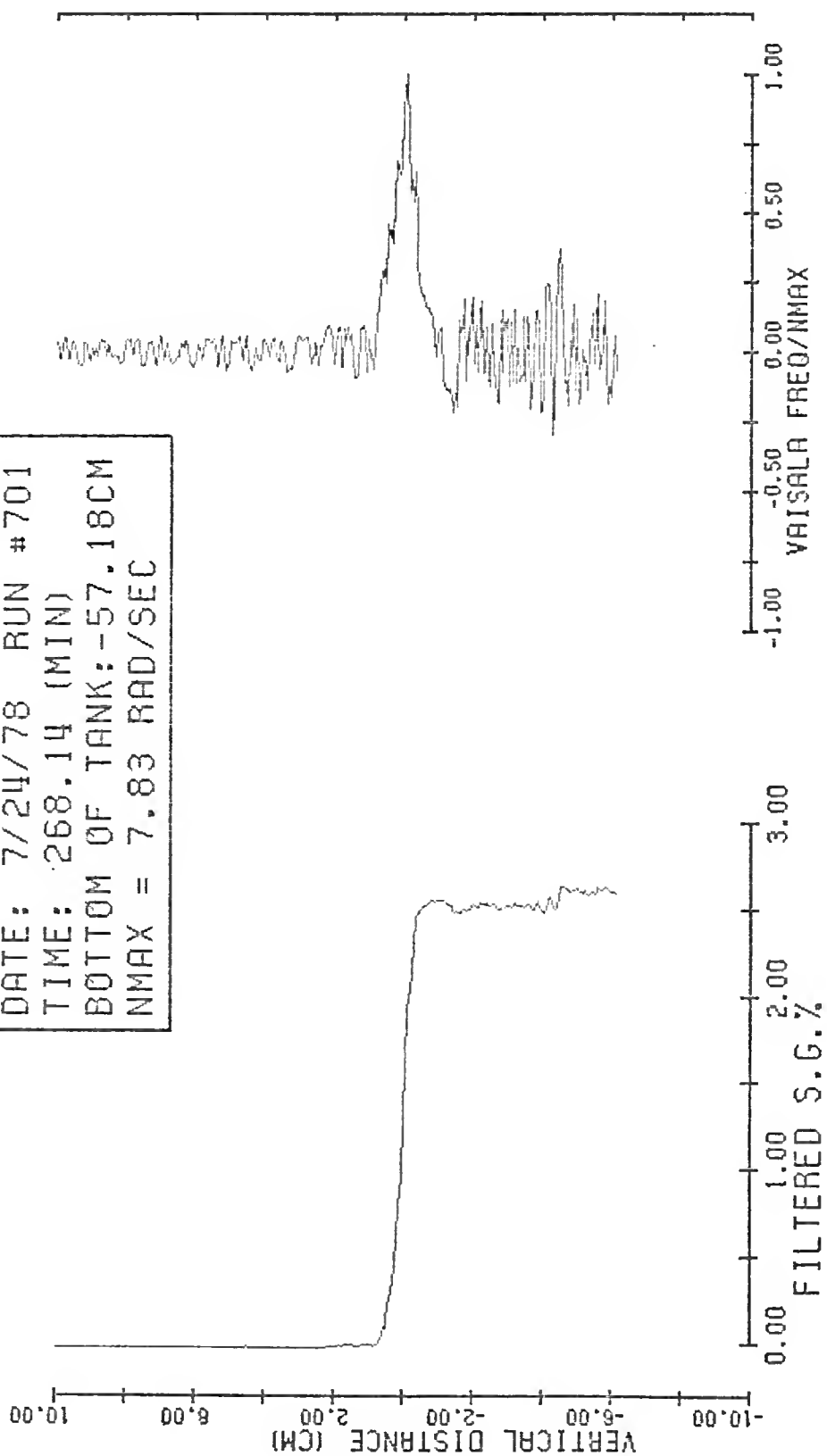
DATE: 7/24/78 RUN #700
TIME: 258.19 (MIN)
BOTTOM OF TANK: -57.36CM
NMAX = 7.15 RAD/SEC



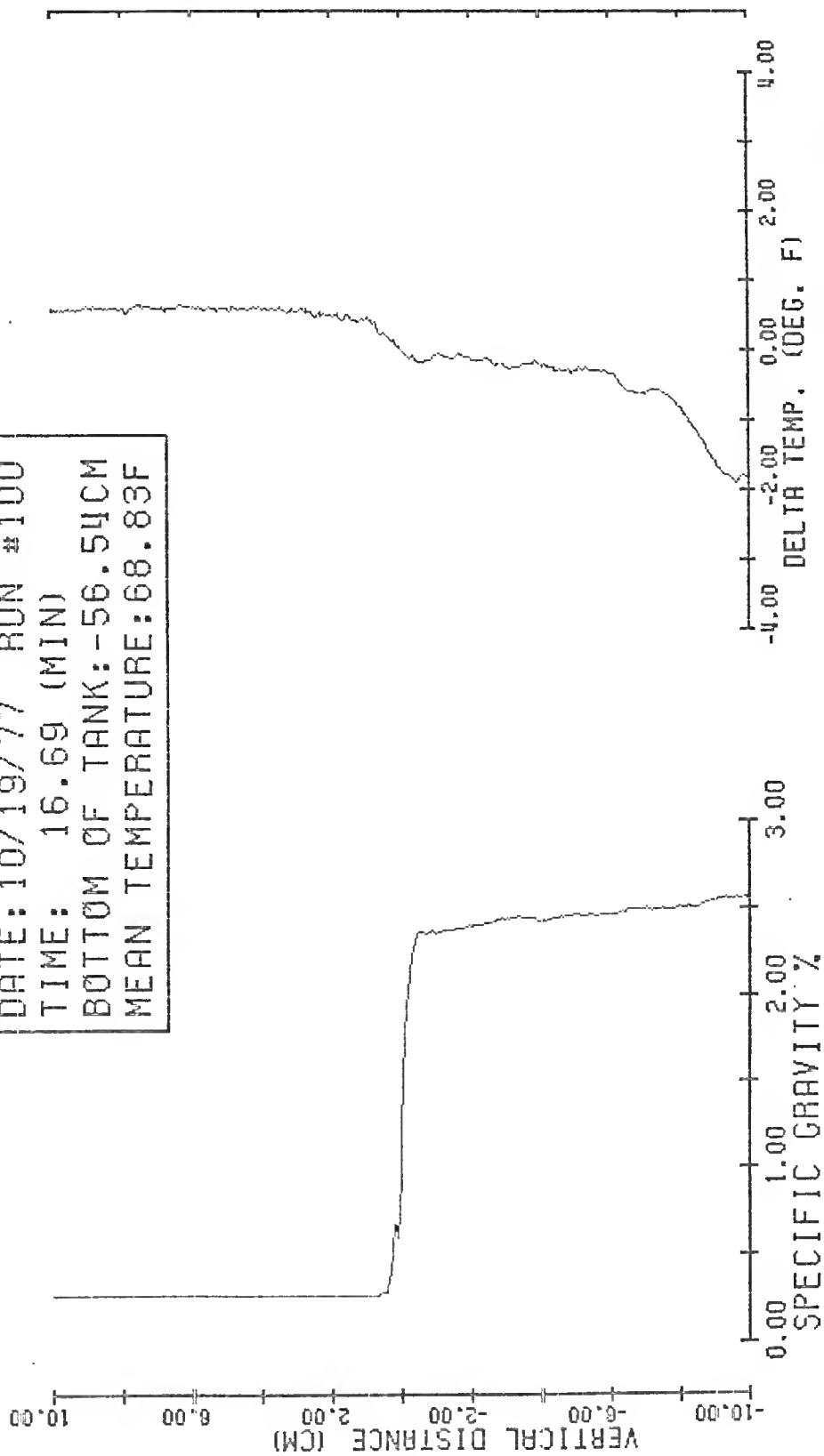
DATE: 7/24/78 RUN #701
TIME: 268.14 (MIN)
BOTTOM OF TANK: -57.18CM
MEAN TEMPERATURE: 83.17F

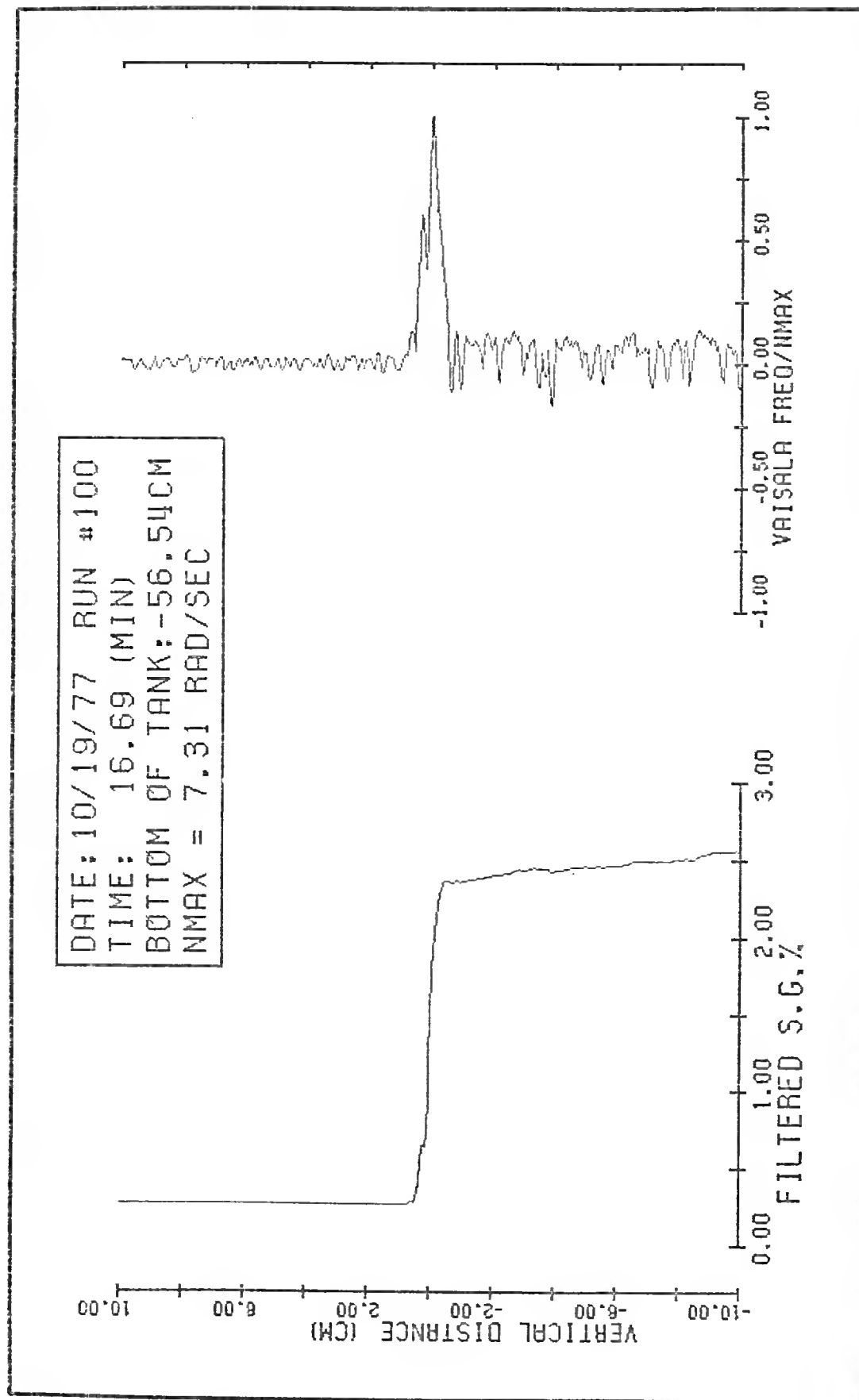


DATE: 7/24/78 RUN #701
TIME: 268.14 (MIN)
BOTTOM OF TANK: -57.18CM
NMAX = 7.83 RAD/SEC

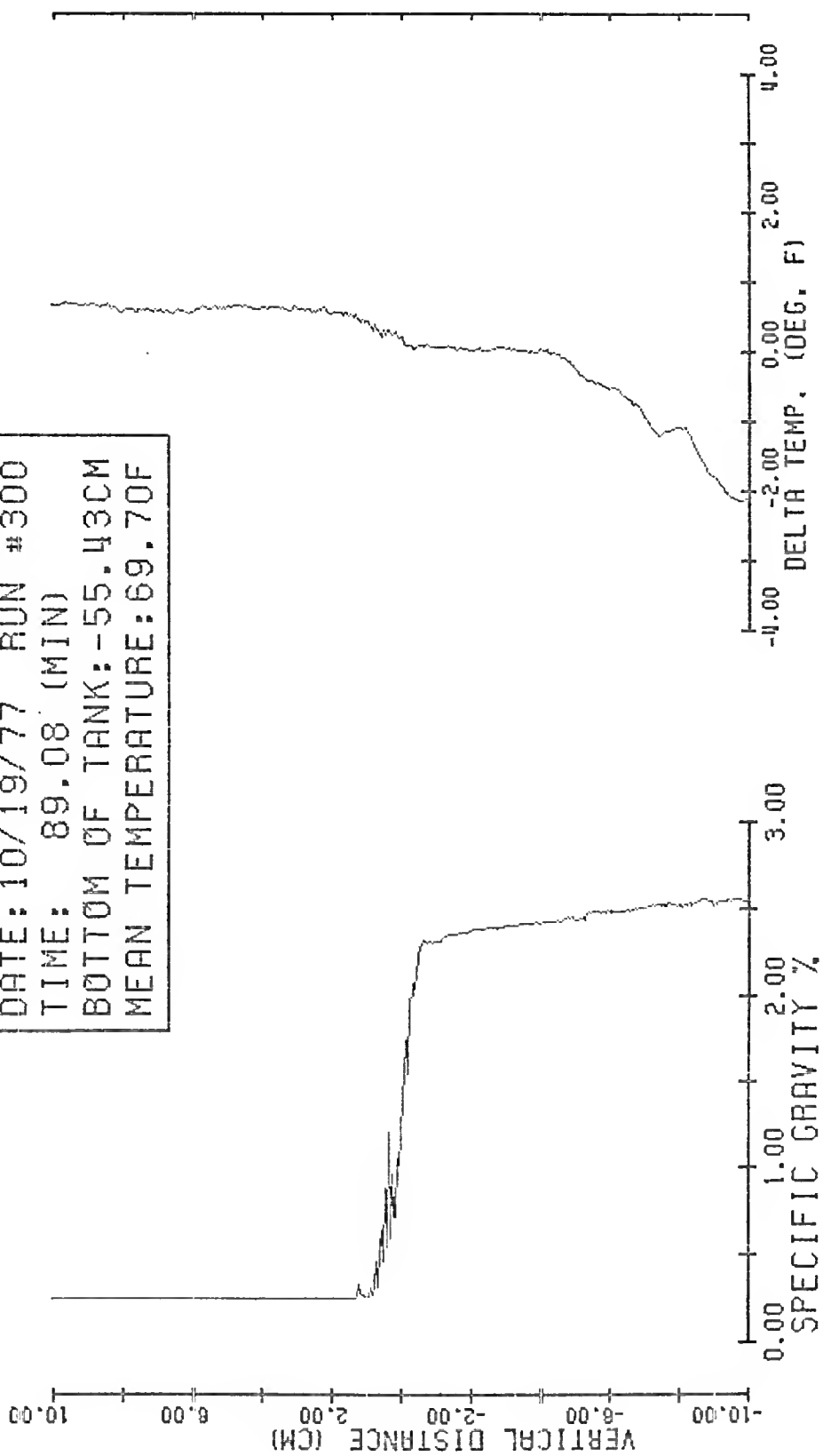


DATE: 10/19/77 RUN #100
TIME: 16.69 (MIN)
BOTTOM OF TANK: -56.54CM
MEAN TEMPERATURE: 68.83F

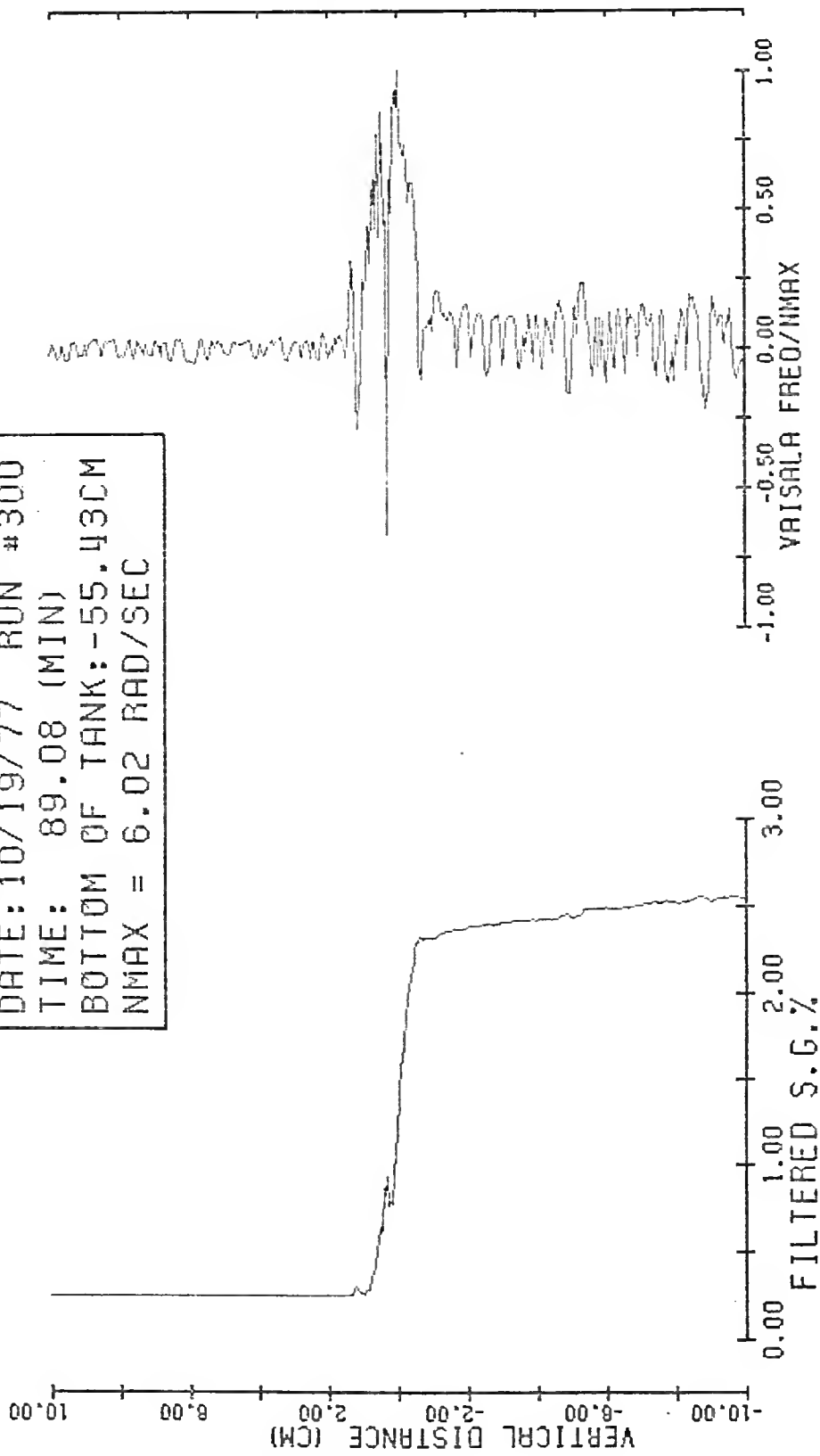




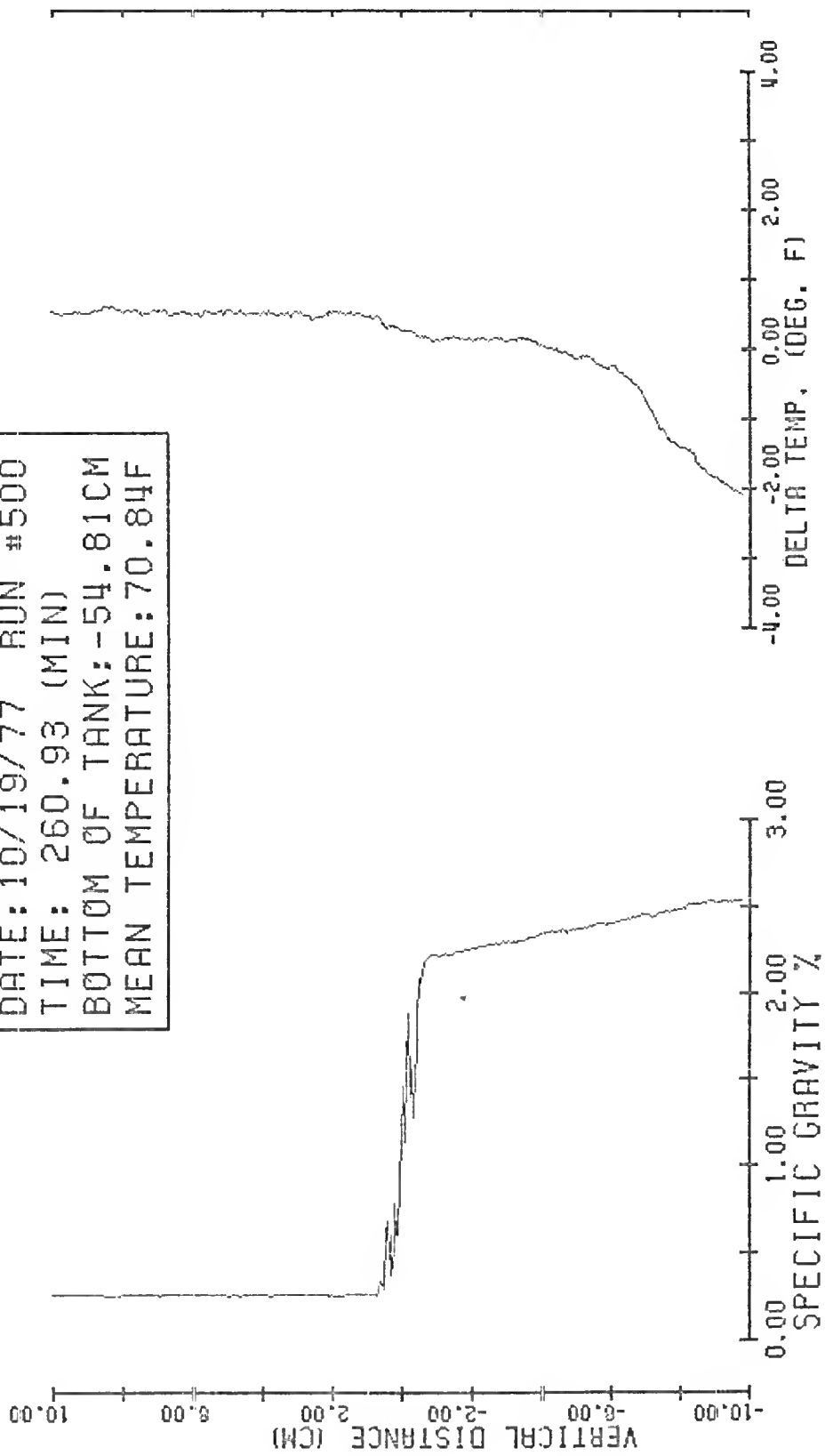
DATE: 10/19/77 RUN #300
TIME: 89.08 (MIN)
BOTTOM OF TANK: -55.43CM
MEAN TEMPERATURE: 69.70F



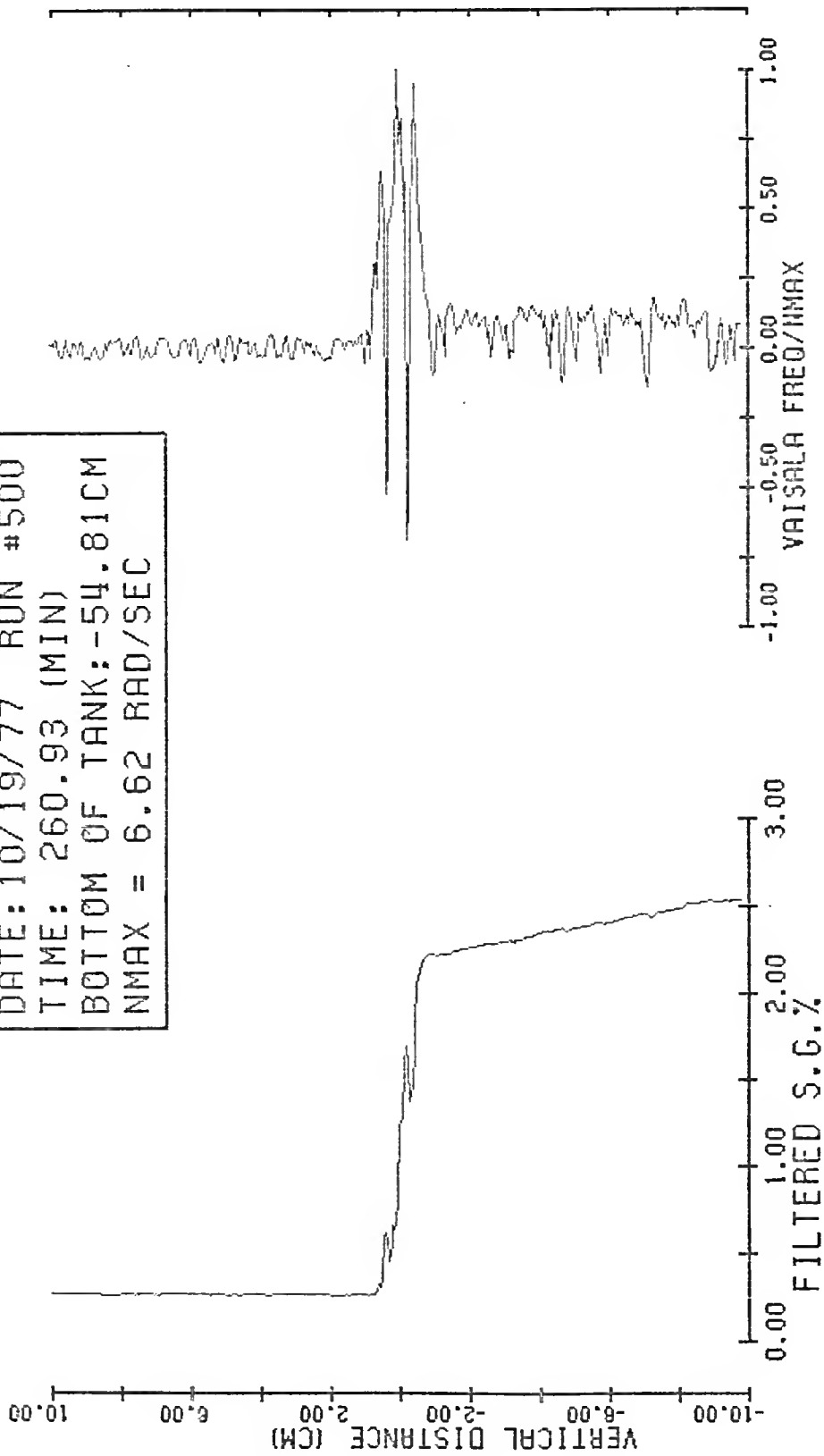
DATE: 10/19/77 RUN #300
TIME: 89.08 (MIN)
BOTTOM OF TANK: -55.43CM
NMAX = 6.02 RAD/SEC

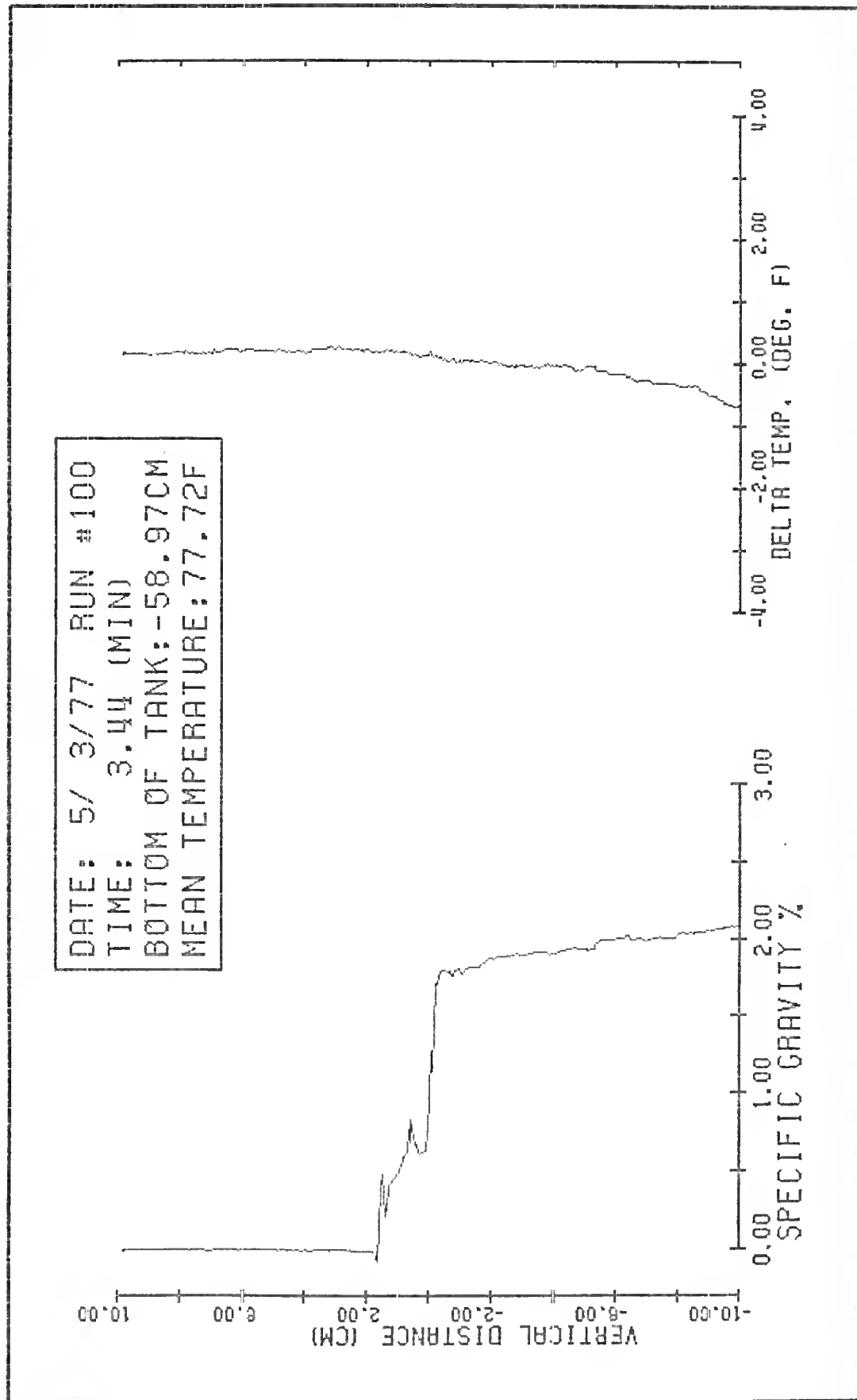


DATE: 10/19/77 RUN #500
TIME: 260.93 (MIN)
BOTTOM OF TANK: -54.81CM
MEAN TEMPERATURE: 70.84F

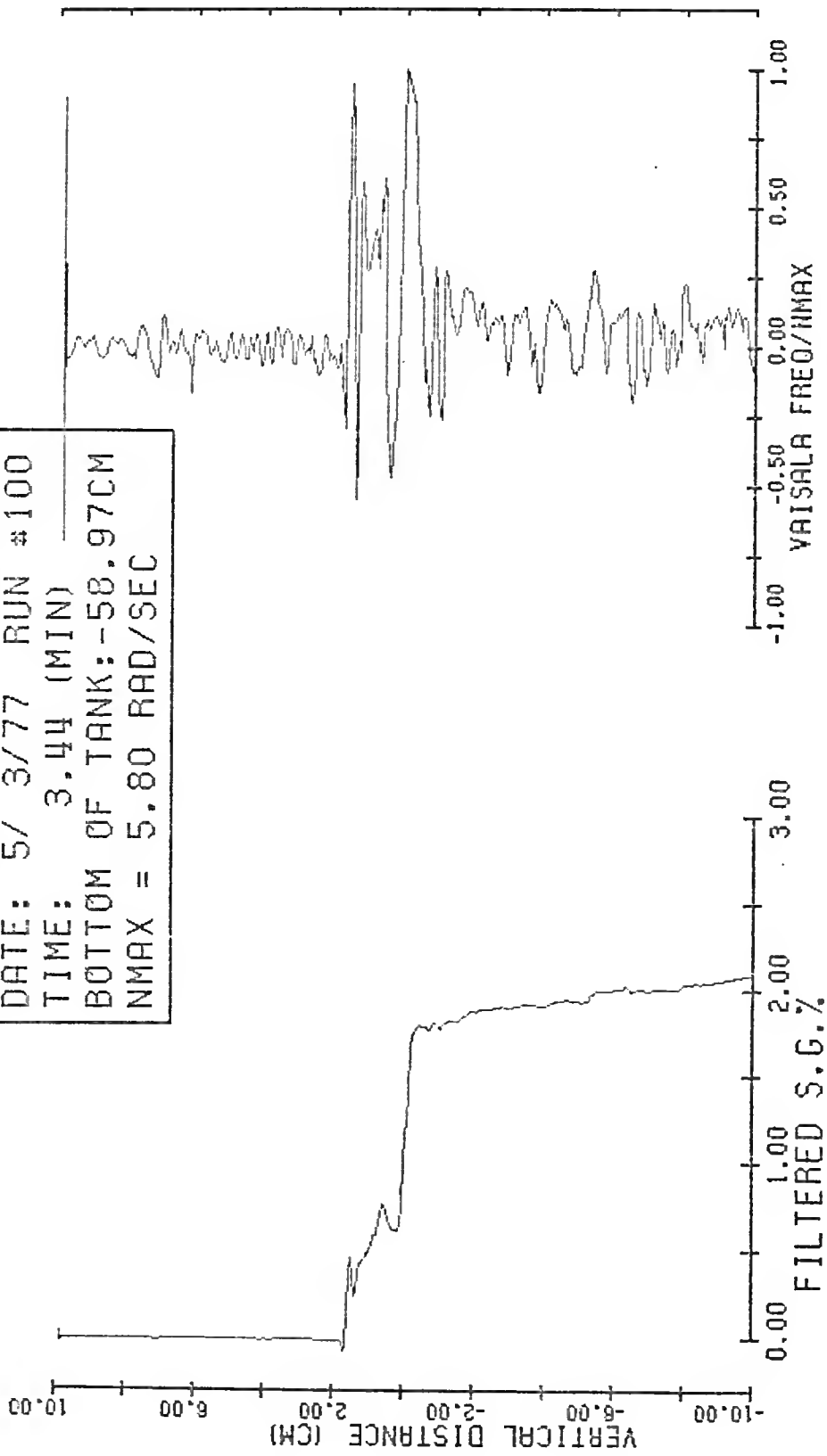


DATE: 10/19/77 RUN #500
TIME: 260.93 (MIN)
BOTTOM OF TANK: -54.81 CM
NMAX = 6.62 RAD/SEC

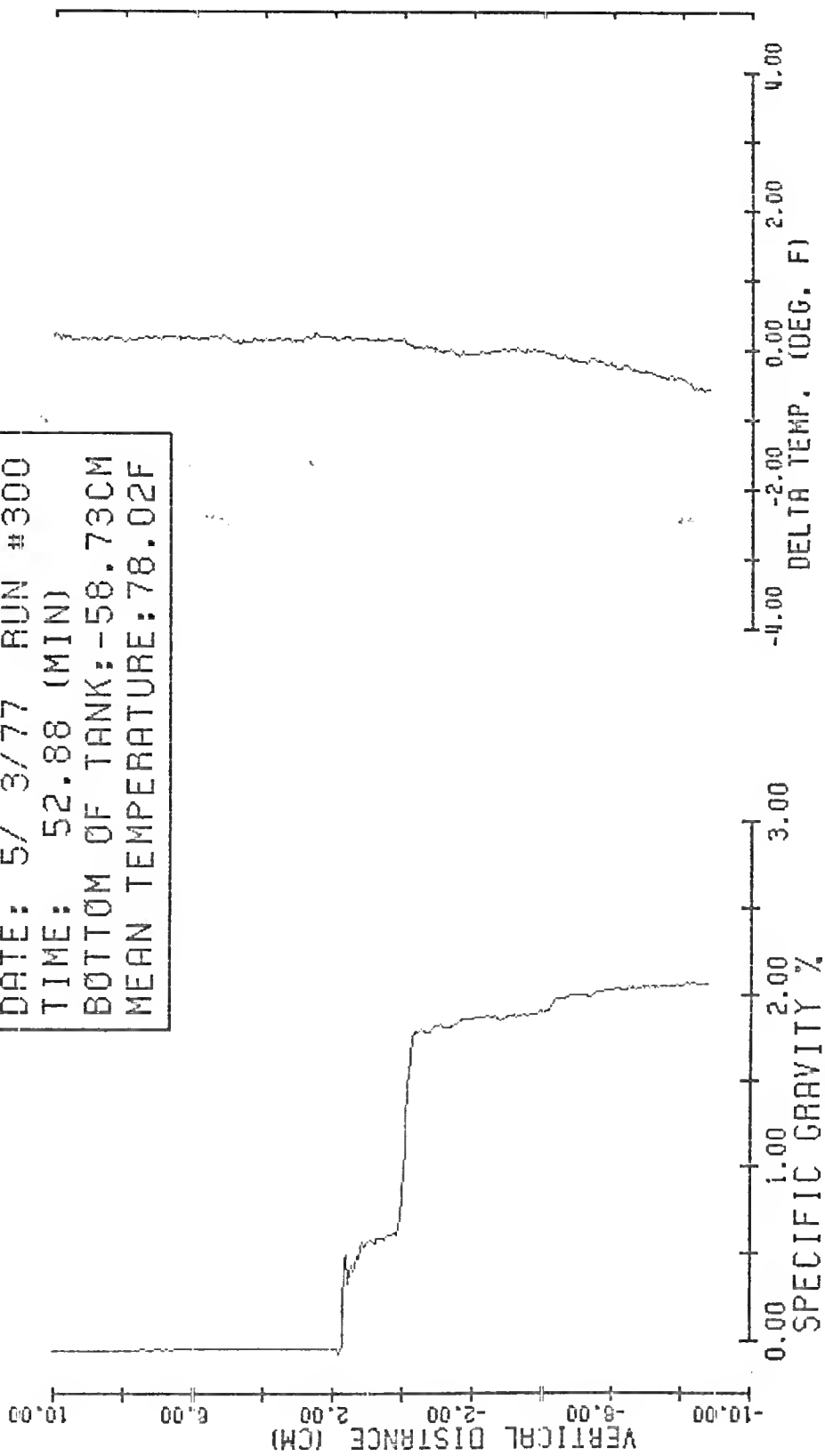




DATE: 5/ 3/77 RUN #100
TIME: 3.44 (MIN)
BOTTOM OF TANK: -58.97CM
NMAX = 5.80 RAD/SEC



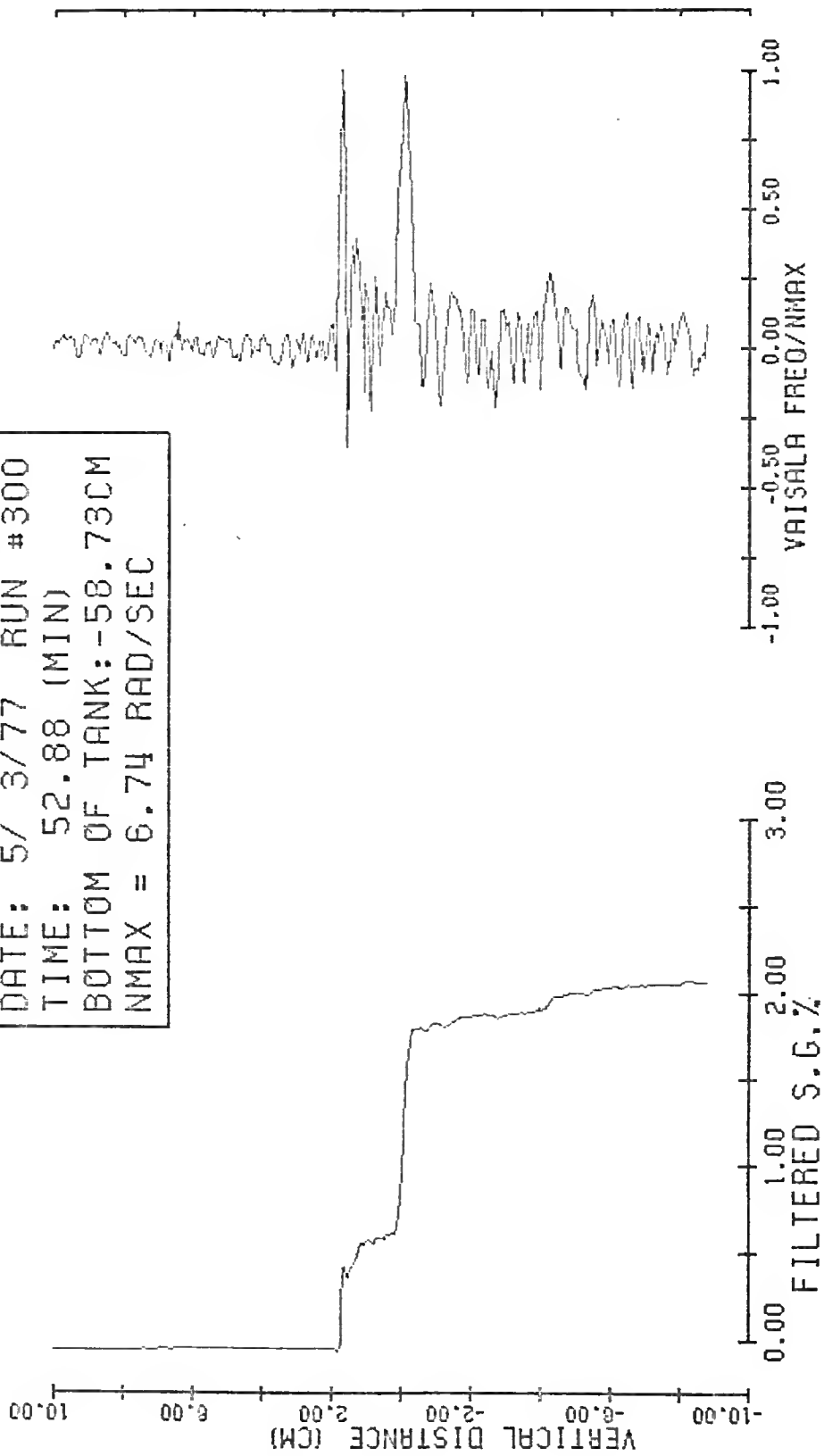
DATE: 5/ 3/77 RUN #300
TIME: 52.88 (MIN)
BOTTOM OF TANK: -58.73CM
MEAN TEMPERATURE: 78.02F



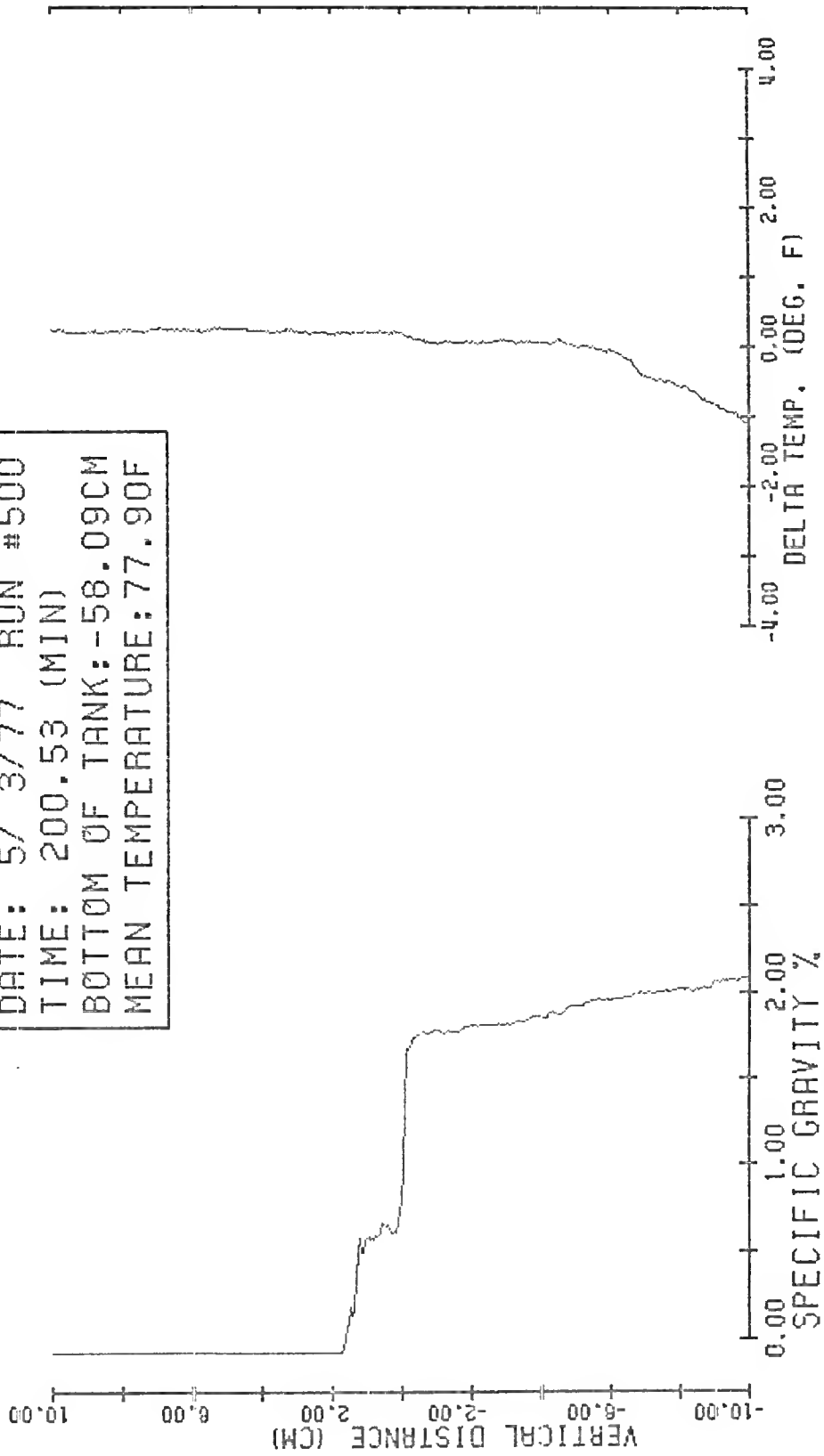
DELTA TEMP. (DEG. F)

DELTA TEMP. (DEG. F)	VERTICAL DISTANCE (CM)
-4.00	-2.00
-2.00	-2.00
0.00	2.00
2.00	2.00
4.00	2.00

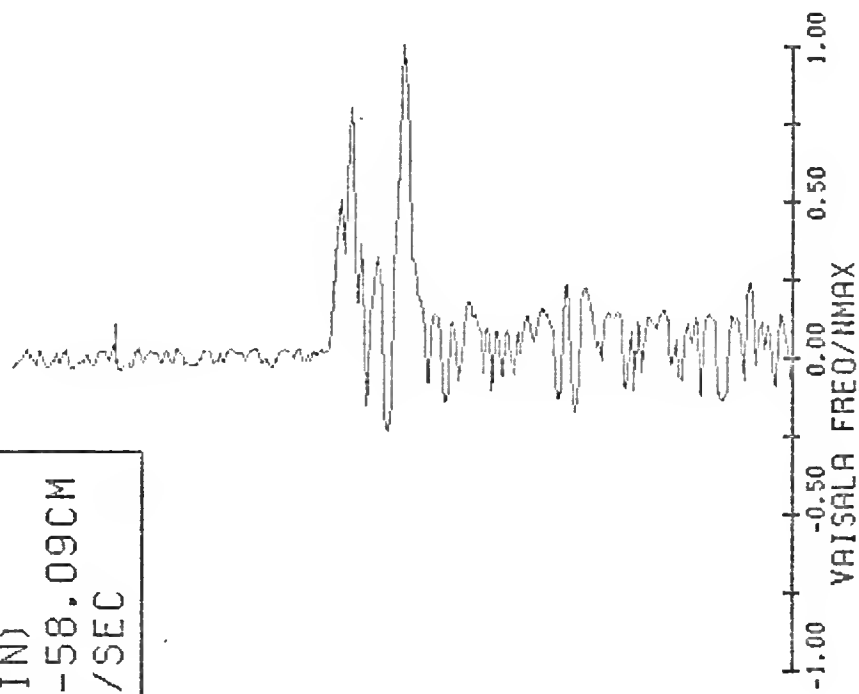
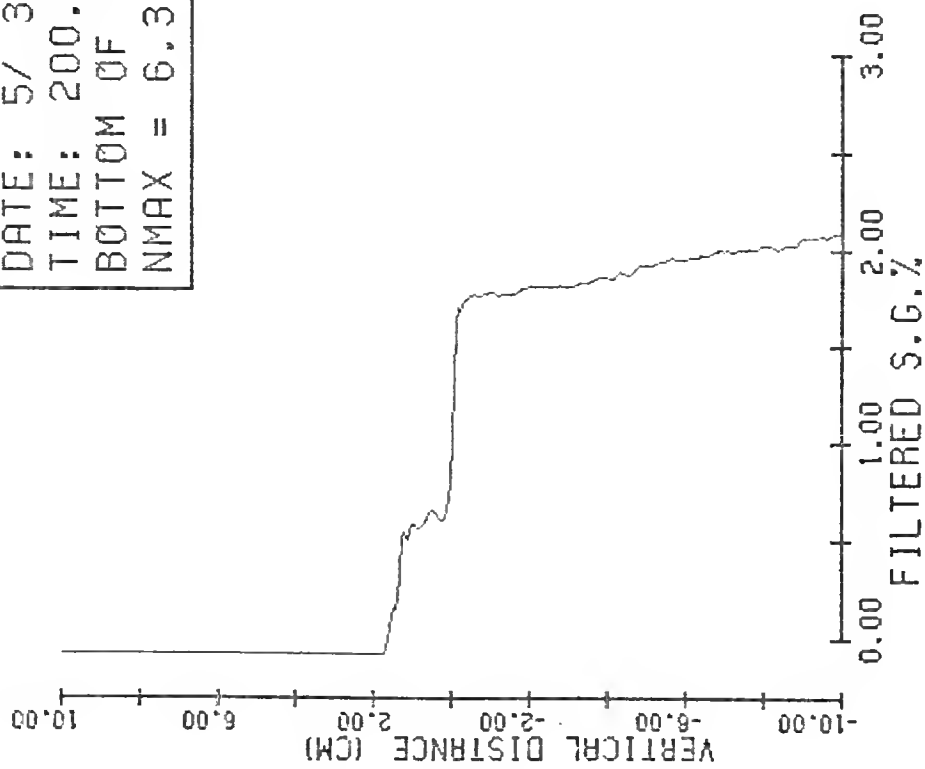
DATE: 5/ 3/77 RUN #300
TIME: 52.88 (MIN)
BOTTOM OF TANK: -58.73CM
NMAX = 6.74 RAD/SEC

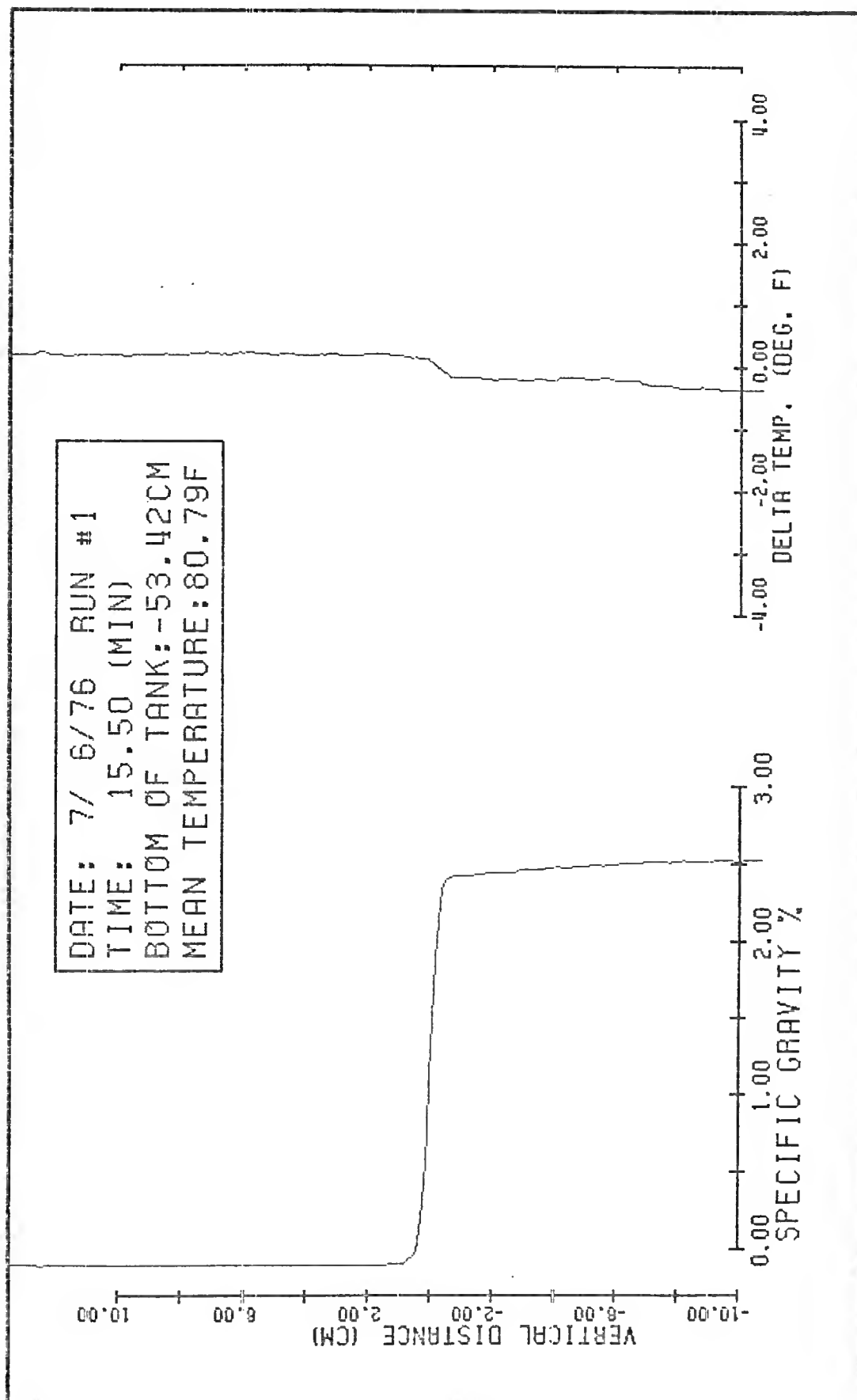


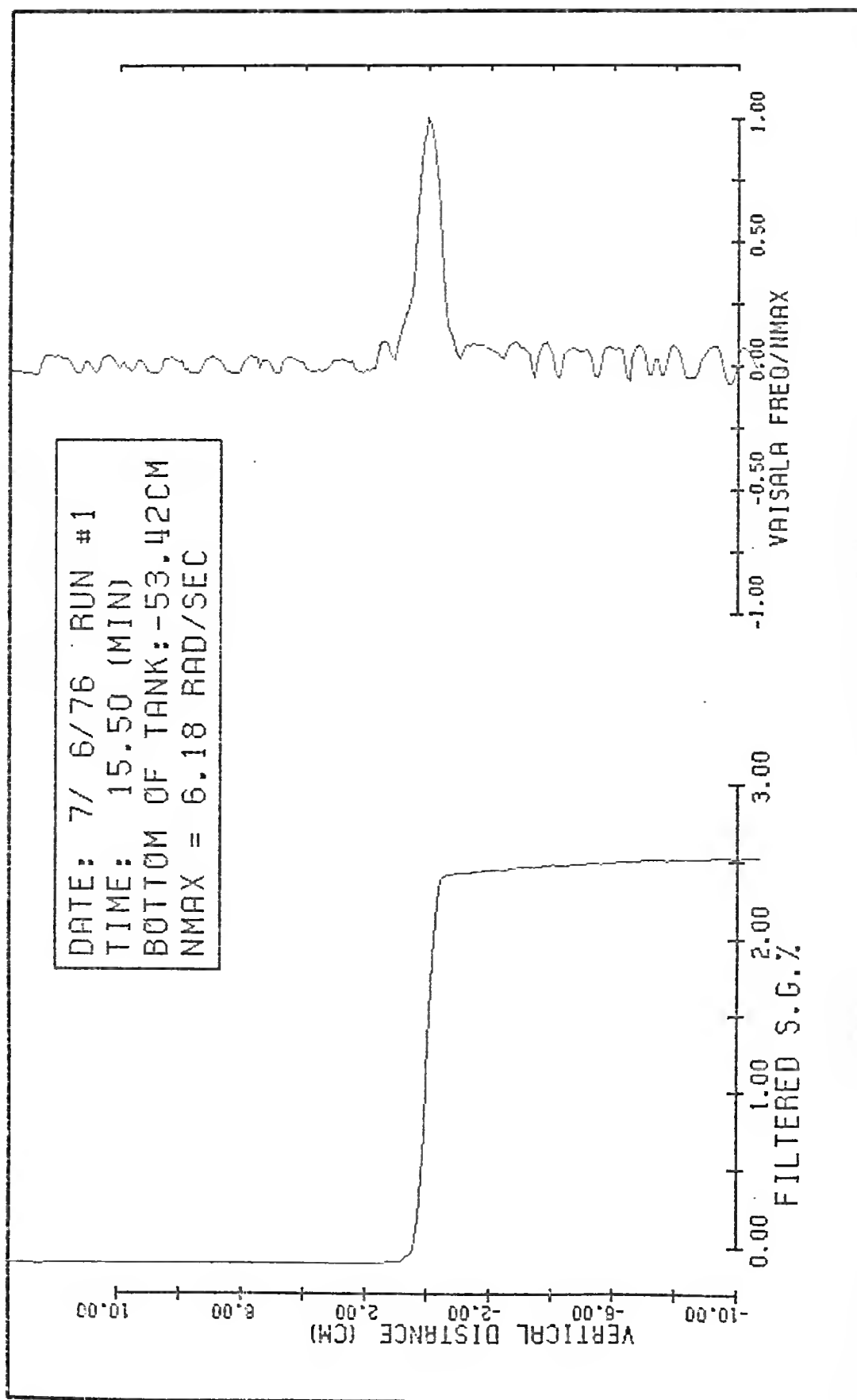
DATE: 5/ 3/77 RUN #500
TIME: 200.53 (MIN)
BOTTOM OF TANK: -58.09CM
MEAN TEMPERATURE: 77.90F

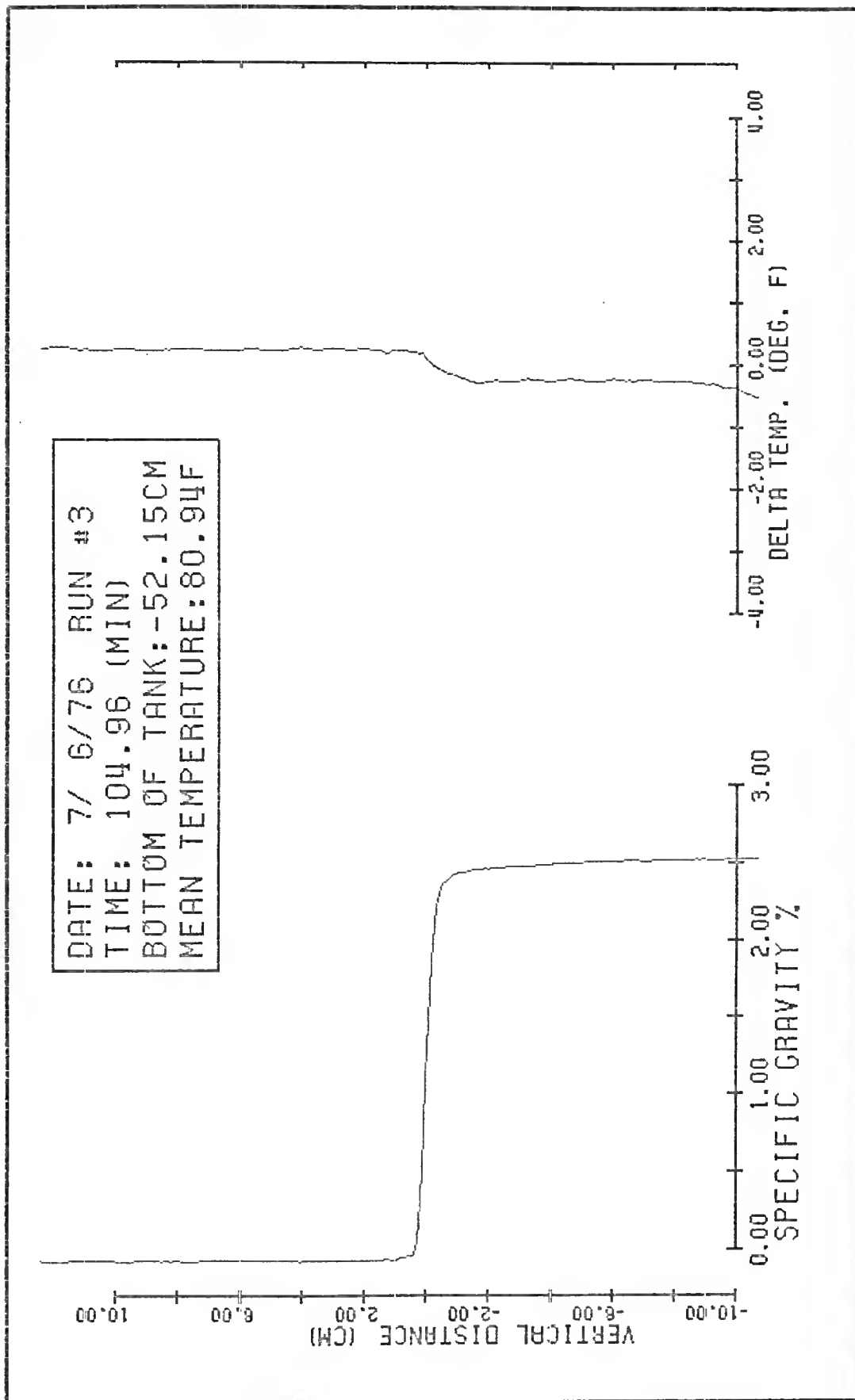


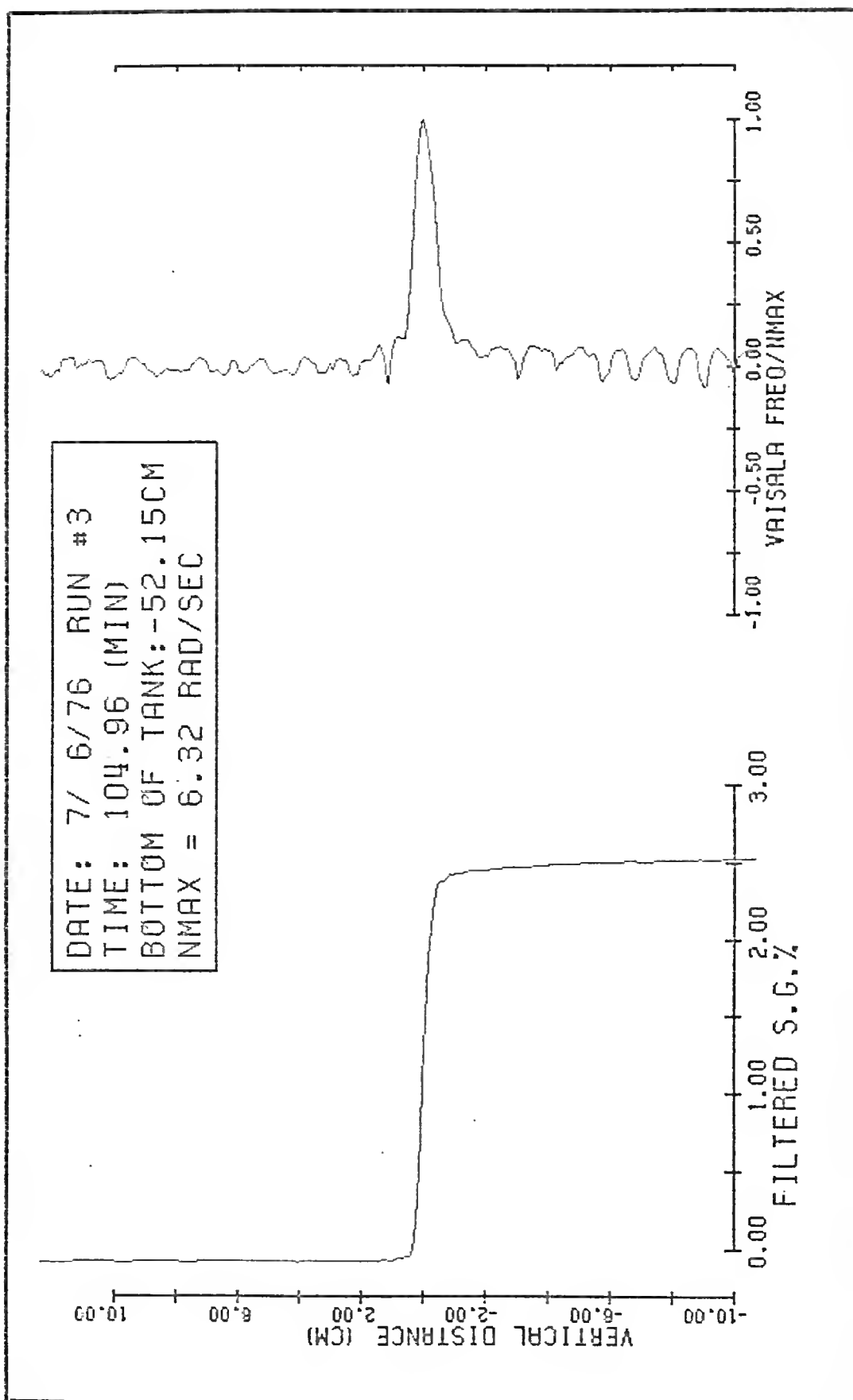
DATE: 5/ 3/77 RUN #500
TIME: 200.53 (MIN)
BOTTOM OF TANK: -58.09CM
NMAX = 6.36 RAD/SEC

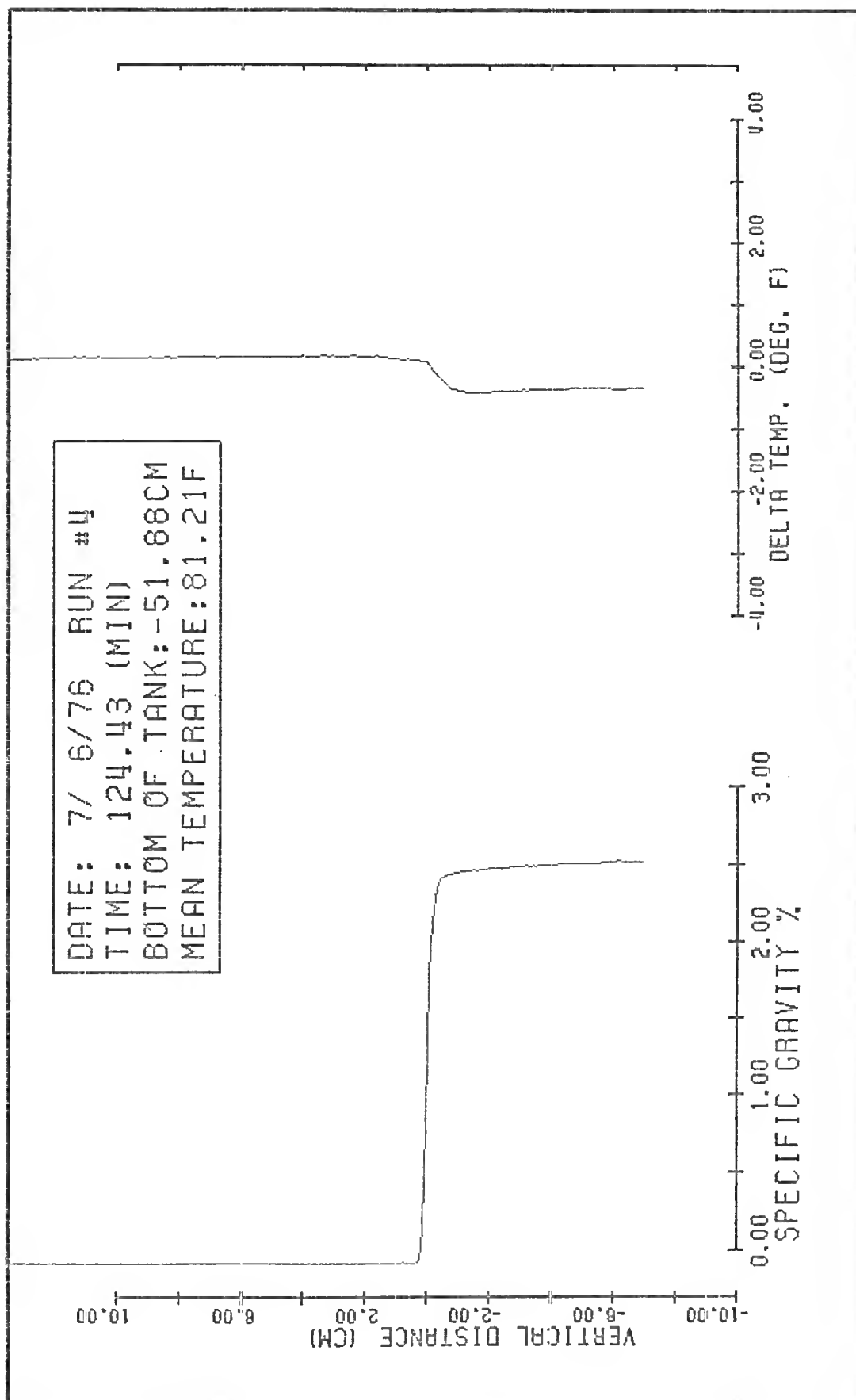


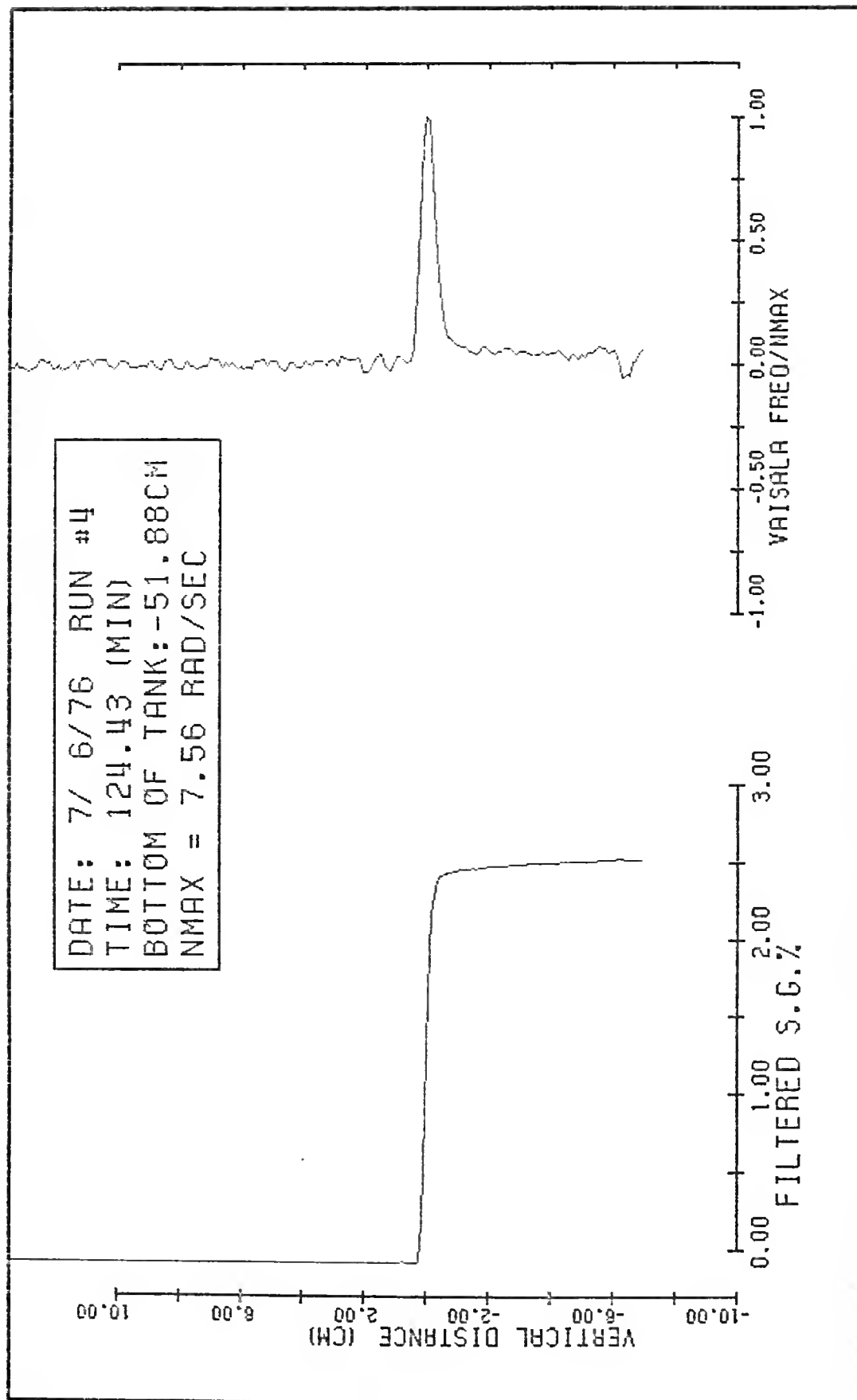










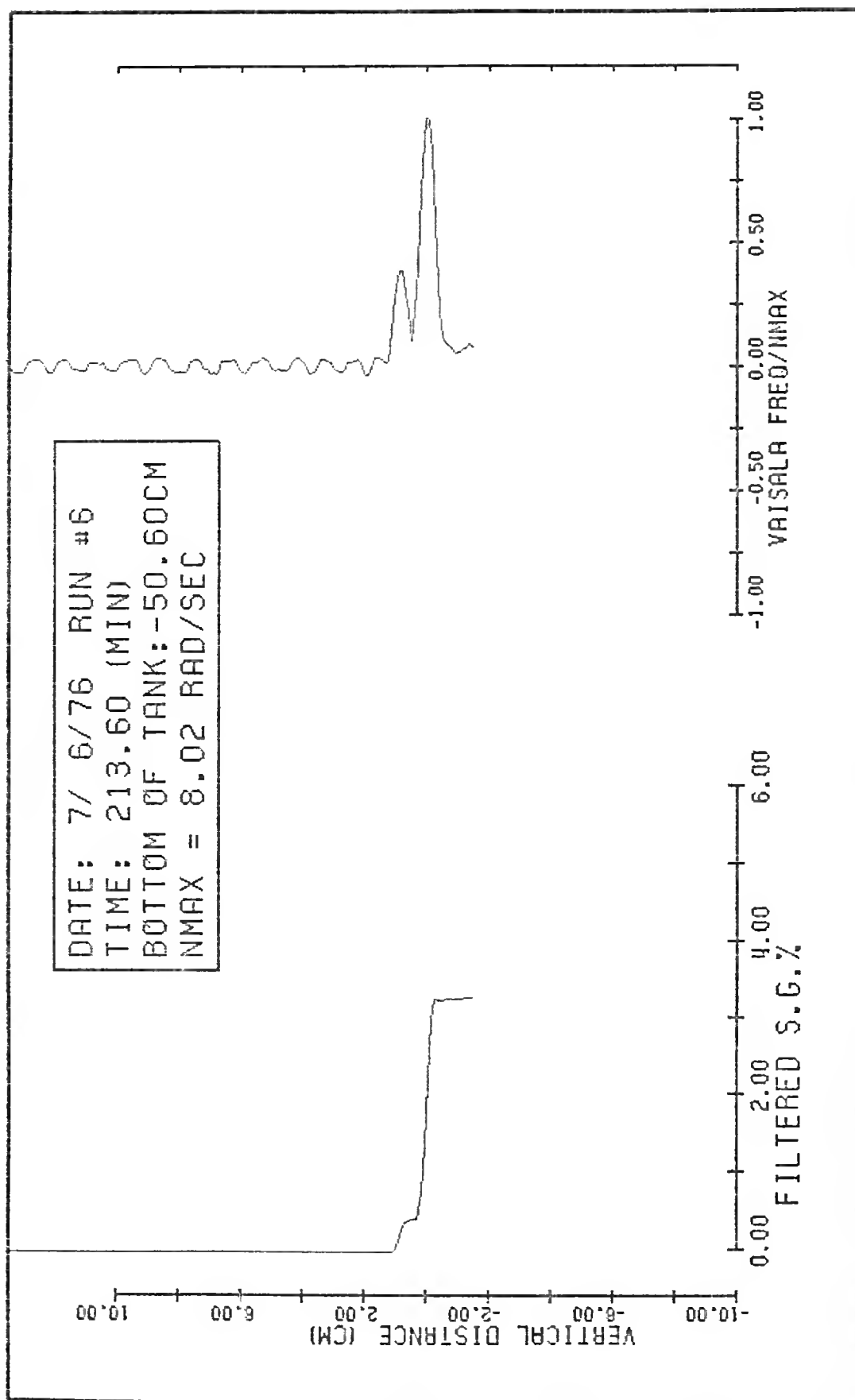


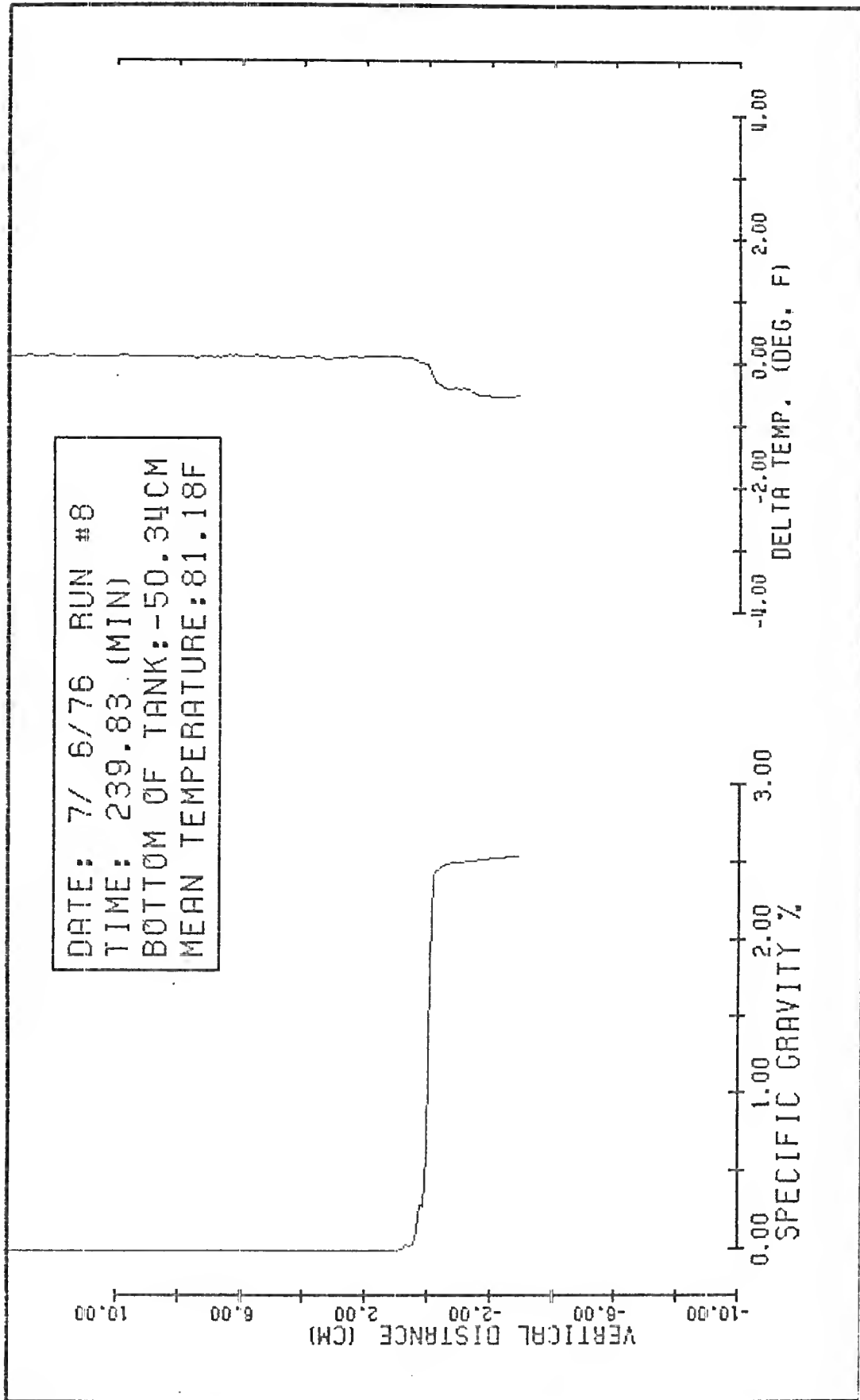
DATE: 7/ 6/76 RUN #6
TIME: 213.60 (MIN)
BOTTOM OF TANK: -50.60CM
MEAN TEMPERATURE: 81.22F

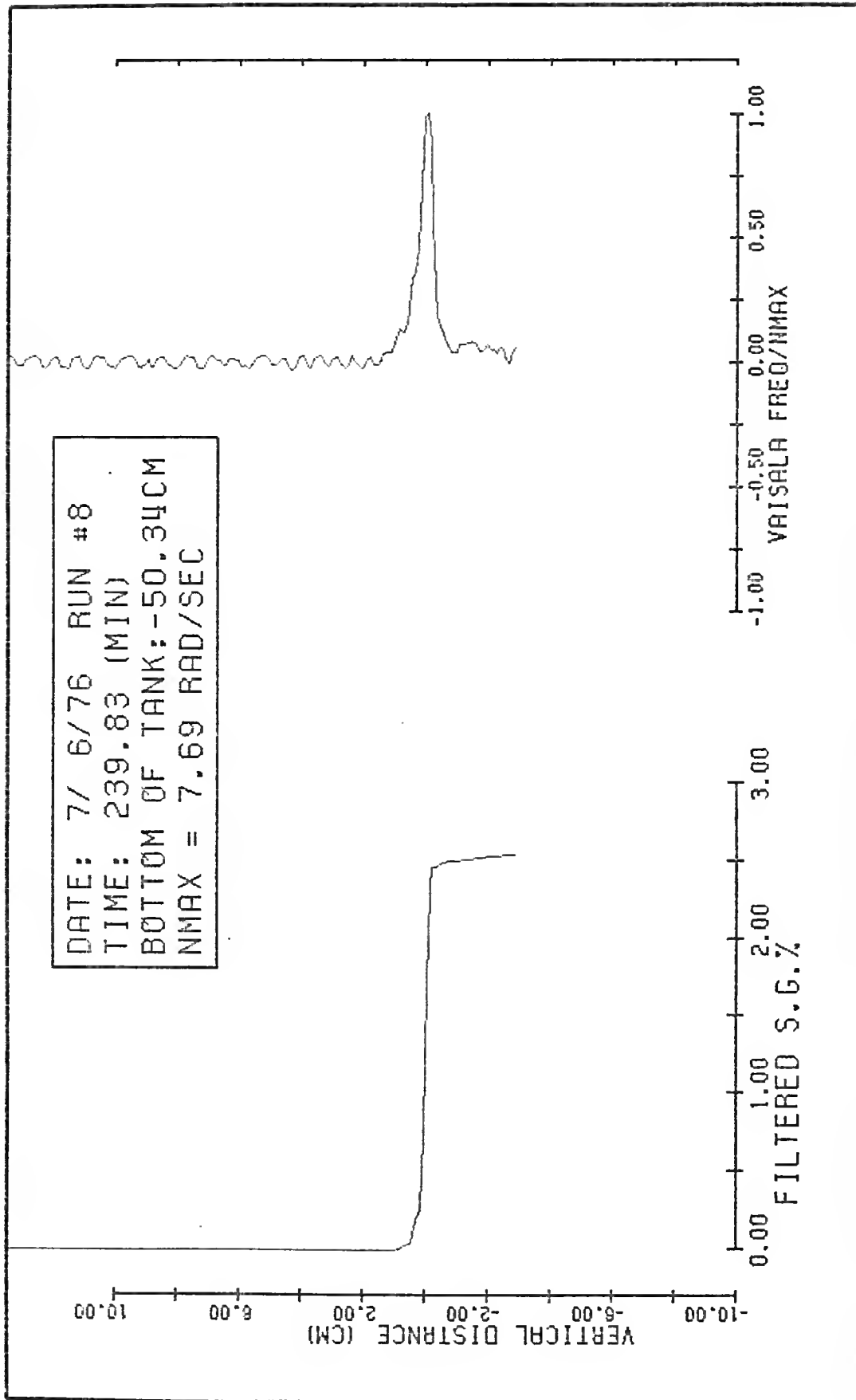
VERTICAL DISTANCE (CM)

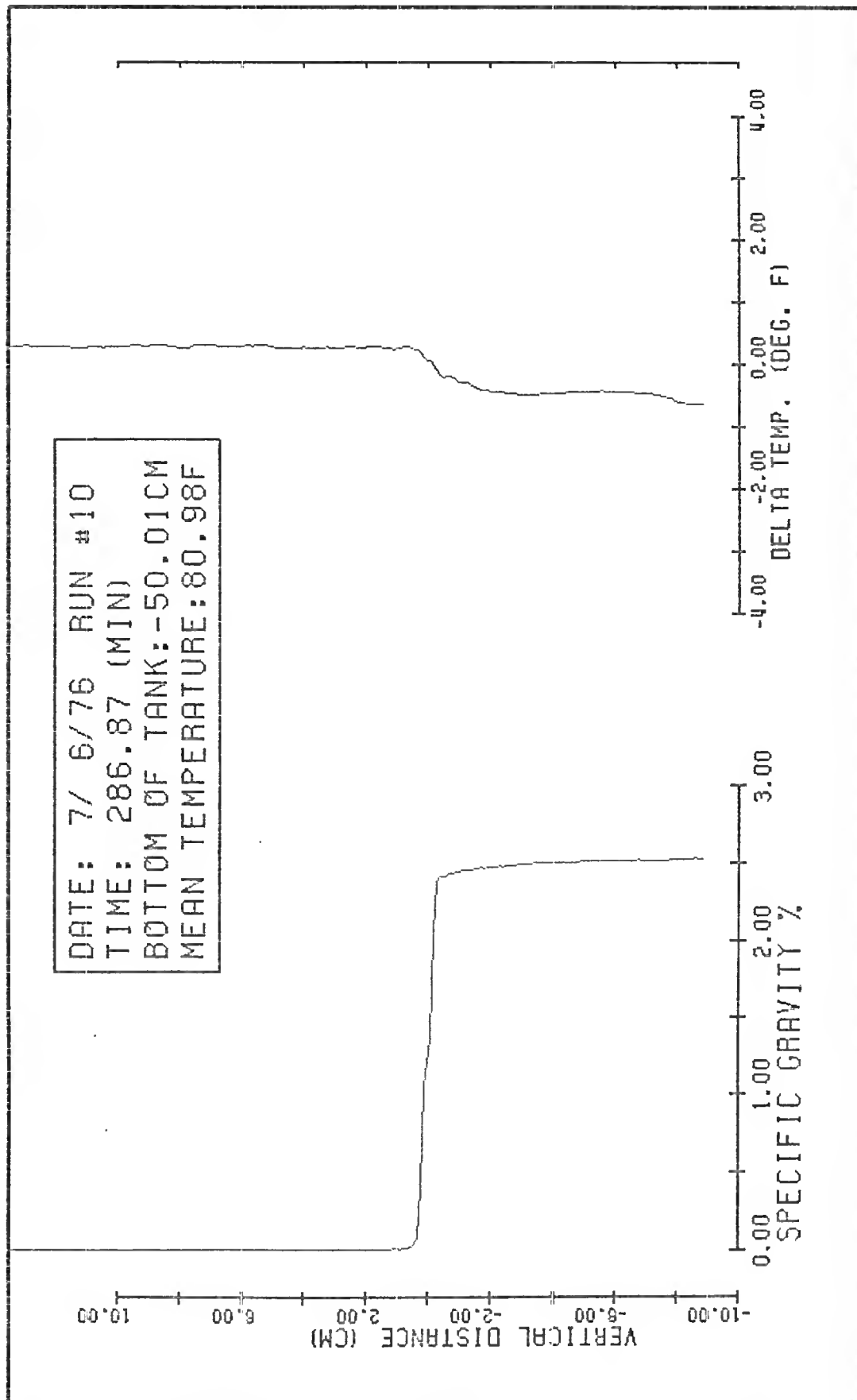
0.00 2.00 4.00 6.00
SPECIFIC GRAVITY %

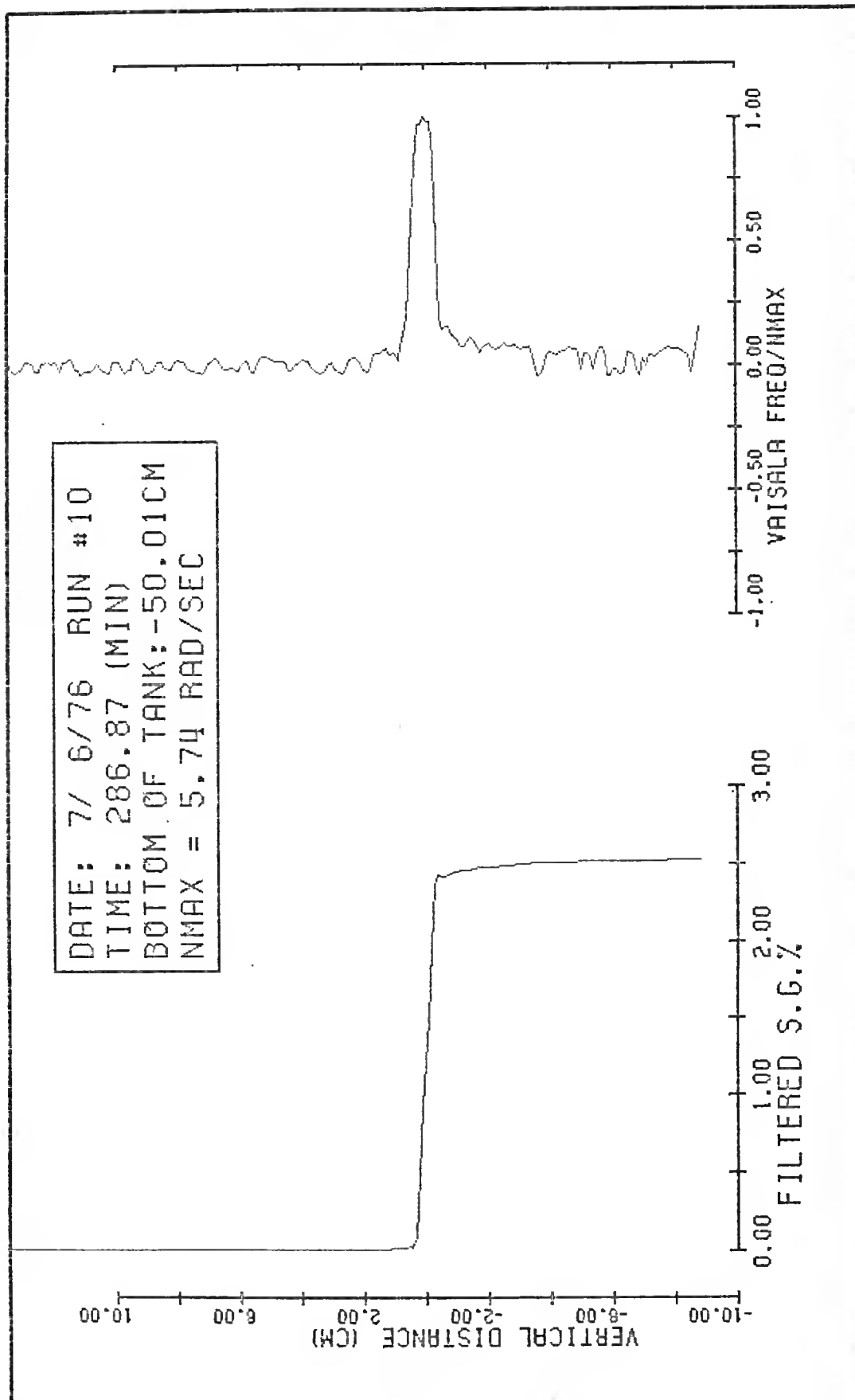
-4.00 -2.00 0.00 2.00 4.00
DELTA TEMP. (DEG. F)

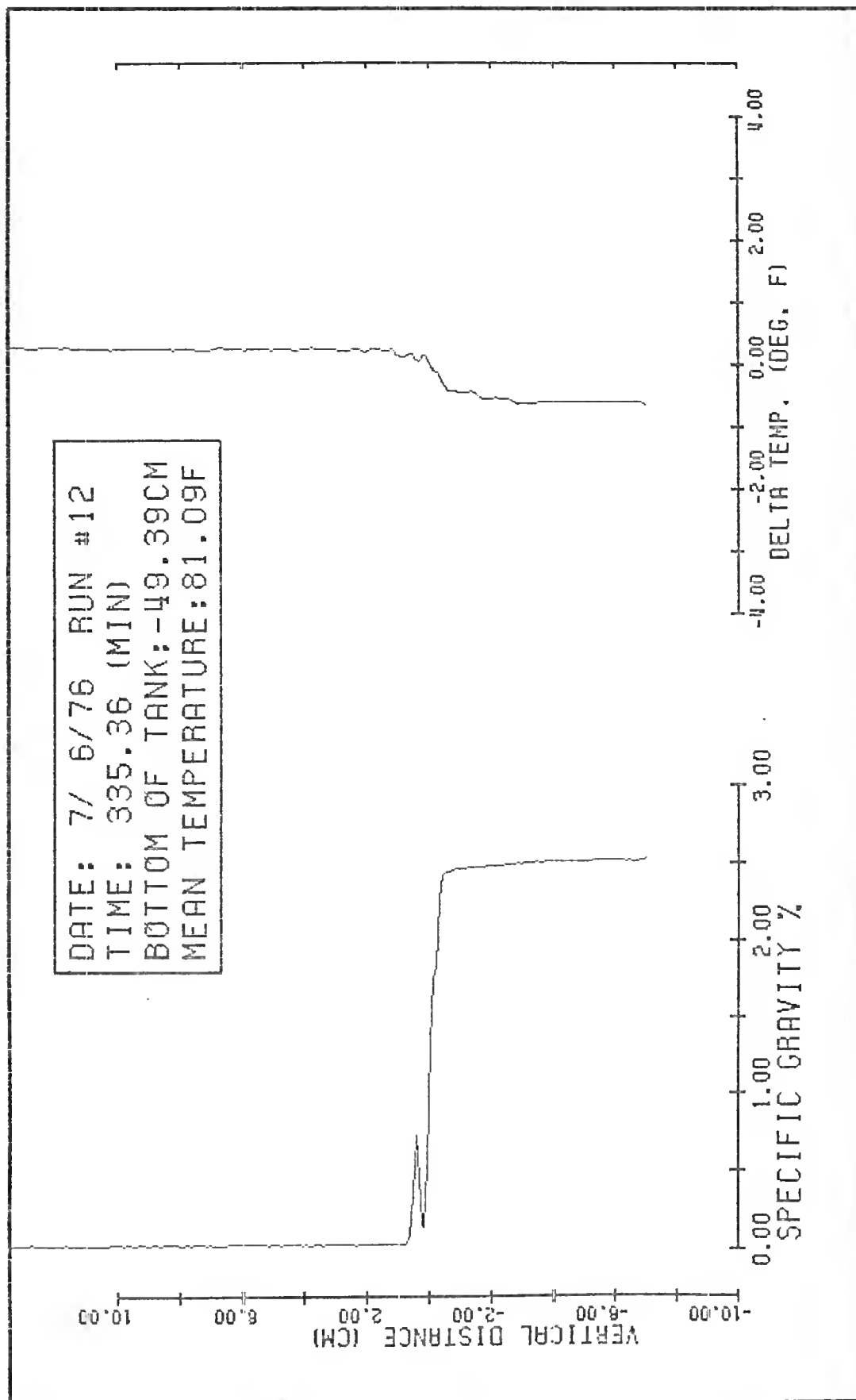


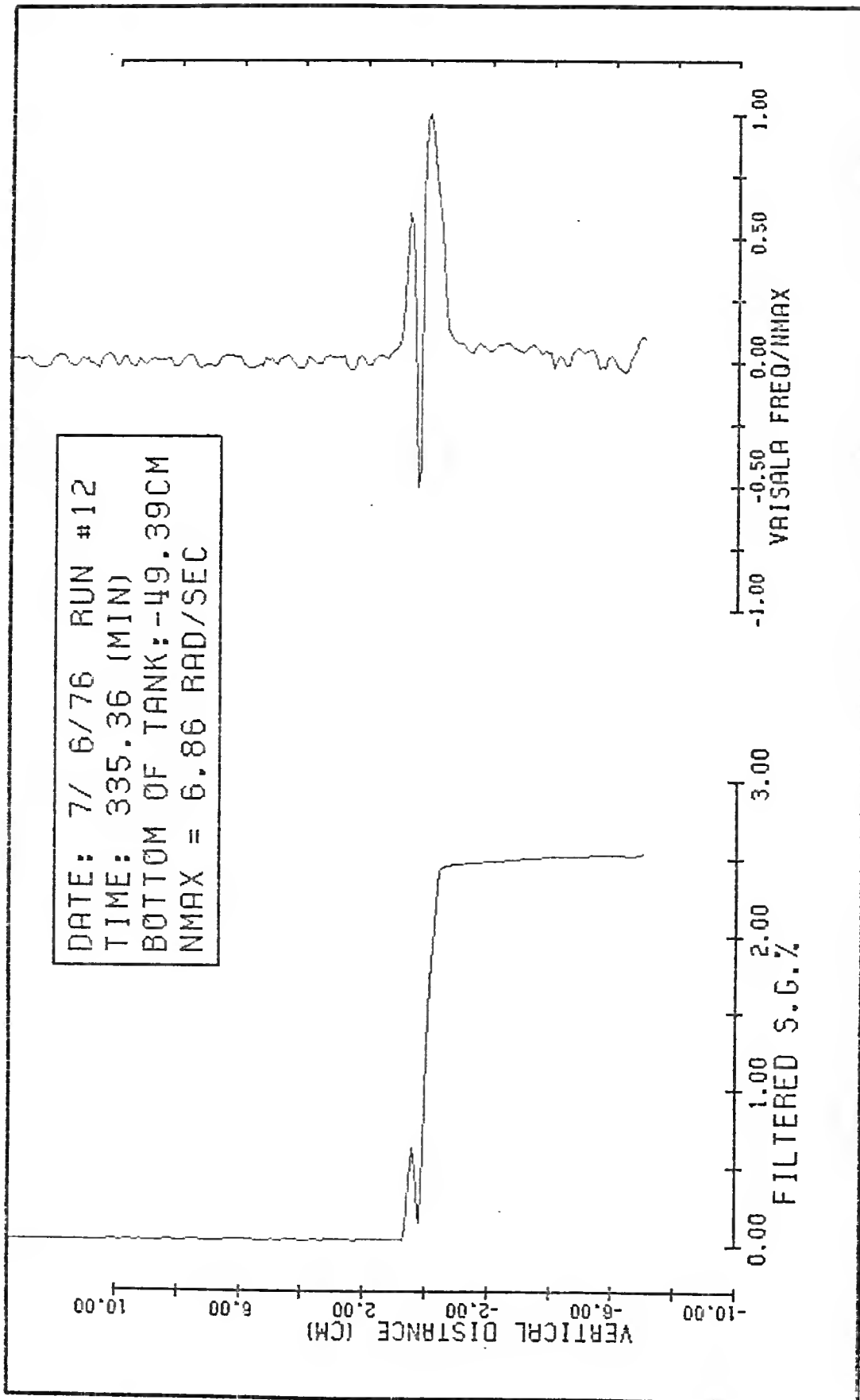












APPENDIX C

THE ERROR IN ASSUMING $D\rho/Dt = 0$

The complete continuity equation is given by,

$$\frac{D\rho}{Dt} + \rho \vec{\nabla} \cdot \vec{u} = 0, \quad C.1$$

where the material derivative is,

$$\frac{D}{Dt} = \frac{\partial}{\partial t} + \vec{u} \cdot \vec{\nabla},$$

ρ is the fluid density and \vec{u} is the velocity. The density of salt water is, in the most general case, dependent on the specific internal energy, e , the salinity, S , and the pressure, P , such that

$$\frac{D\rho}{Dt} = \frac{De}{Dt} \left(\frac{\partial \rho}{\partial e} \right)_{S,P} + \frac{DS}{Dt} \left(\frac{\partial \rho}{\partial S} \right)_{e,P} + \frac{DP}{Dt} \left(\frac{\partial \rho}{\partial P} \right)_{S,e} \quad C.2$$

The equation for the conservation of energy, under the conditions that there is no internal heat source, no radiative heat transfer and a constant coefficient of heat conduction, k , is given by,

$$\frac{De}{Dt} = \frac{-P}{\rho} \vec{\nabla} \cdot \vec{u} + \frac{k}{\rho} \nabla^2 T + \frac{\mu}{\rho} \Phi, \quad C.3$$

where Φ is the viscous dissipation function, T the temperature, and μ is the fluid viscosity.

The equation governing the conservation of salt, assuming a constant coefficient of diffusion, is given by,

$$\frac{DS}{Dt} = \gamma_s \nabla^2 S - S \vec{\nabla} \cdot \vec{u}, \quad C.4$$

where γ_s is the molecular coefficient of diffusion for salt in water and S is the salinity defined as the mass of salt/unit volume.

Substituting equations C.2, C.3, C.4 into equation C.1 gives,

$$\begin{aligned} \vec{\nabla} \cdot \vec{u} = & \left(\frac{\partial \rho}{\partial e} \right)_{S,p} \frac{\mu}{\rho f} \phi + \left(\frac{\partial \rho}{\partial e} \right)_{S,p} \frac{k}{\rho f} \nabla^2 T \\ & + \left(\frac{\partial \rho}{\partial S} \right)_{e,p} \frac{\gamma_s}{f} \nabla^2 S + \left(\frac{\partial \rho}{\partial P} \right)_{e,S} \frac{1}{f} \frac{DP}{Dt} \end{aligned} \quad C.5$$

$$\text{where } f = \left(\frac{\partial \rho}{\partial e} \right)_{S,p} \frac{P}{\rho} + \left(\frac{\partial \rho}{\partial S} \right)_{e,p} S - \rho.$$

For salt water at atmospheric pressure and room temperature the following hold:

$$\rho \approx 1.0 \text{ g/cm}^3$$

$$k \approx 5.6 \times 10^4 \text{ dynes/sec } ^\circ\text{C}$$

$$\gamma_s \approx 1.1 \times 10^{-5} \text{ cm}^2/\text{sec}$$

$$P \approx 10^6 \text{ dynes/cm}^2$$

$$S \approx 0.03 \text{ g/cm}^3$$

$$\frac{\partial \rho}{\partial S} \approx 1.0$$

$$\frac{\partial \rho}{\partial e} \approx 4.3 \times 10^{-12} \text{ g sec}^2/\text{cm}^5$$

$$\frac{\partial \rho}{\partial P} \approx 5.0 \times 10^{-11} \text{ sec}^2/\text{cm}^2$$

$$\Delta T = \text{maximum temperature deviation} < 2^\circ\text{C}$$

$\mu\Phi$ is the energy dissipation/unit volume; for flow in a channel the following estimation is made,

$$\mu\Phi \approx \frac{\tau \bar{U}}{R_h},$$

where τ is the stress on the walls of the channel, \bar{U} is the mean velocity through the channel and R_h is the hydraulic radius of the channel.

For the flow studied herein,

$$\tau \leq .1 \text{ dynes/cm}^2$$

$$\bar{U} \leq 10 \text{ cm/sec}$$

$$R_h = 40 \text{ cm}$$

$$\mu\Phi \leq .03$$

The Kolmogorov length scale which corresponds to the above dissipation rate is,

$$\lambda = \frac{(.01)^{3/4}}{(.03)^{1/4}} = .07 \text{ cm}$$

From the above values the following estimates are made:

$$\nabla^2 T \leq \frac{\Delta T}{\lambda^2} \leq \frac{2.0}{(.07)^2} = 408$$

$$\nabla^2 S \leq \frac{\Delta S}{\lambda^2} \leq \frac{.03}{(.07)^2} = 6.12$$

$$\frac{DP}{Dt} \leq \rho g U \leq 10^4$$

$$f \approx 4.3 \times 10^{-6} + .03 - 1.0 \approx 1.0$$

and

$$\begin{aligned} \vec{v} \cdot \vec{u} \approx & (4.3)(.03)(10^{-12}) + (4.3)(5.6)(4.08)(10^{-6}) \\ & + (1.0)(1.1)(6.12)(10^{-5}) + (5.0)(10^{-7}), \end{aligned}$$

therefore,

$$\vec{v} \cdot \vec{u} \leq 2 \times 10^{-4} / \text{sec.}$$

APPENDIX D

ENERGY SPECTRA

This appendix contains the energy spectral plots of the horizontal and vertical velocity fluctuations. The measurements were made during four of the nine experiments at several positions above (one below) the density interface. Two plots were shown for each run number, the first is the energy density vs. frequency for the horizontal velocity fluctuations while the second is for the vertical velocity component.

The spectra were computed by a fast fourier transform (FFT) algorithm using the subroutines RHARM and HARM from the Scientific Subroutine Package. Before the spectra were computed, the mean and linear trend were removed from the raw data by linear regression and the ends of the data sets were tapered using a \sin^2 window over the first and last 10 percent of the data set. The data sets were overlapped 50 percent in the time domain. Each spectra plot shown is an average of several individual spectrum. The following table lists the pertinent facts about the spectra:

<u>EXP. NO.</u>	<u>DATE</u>	<u>SAMPLE RATE</u>	<u>TNP¹</u>	<u>NSA²</u>
9	12/6/78	20 Hz	16,384	62
3	10/19/77	30 Hz	24,576	93
2	5/3/77	30 Hz	24,576	93
1	7/6/76	20 Hz	4,096	15

¹Total number of points used to compute spectrum.

²Number of spectra averaged to obtain spectral plot.

DEC. 6.1978

RUN #700

POSITION= 68.89 CM

MEAN VELOCITY= 4.071 CM/SEC

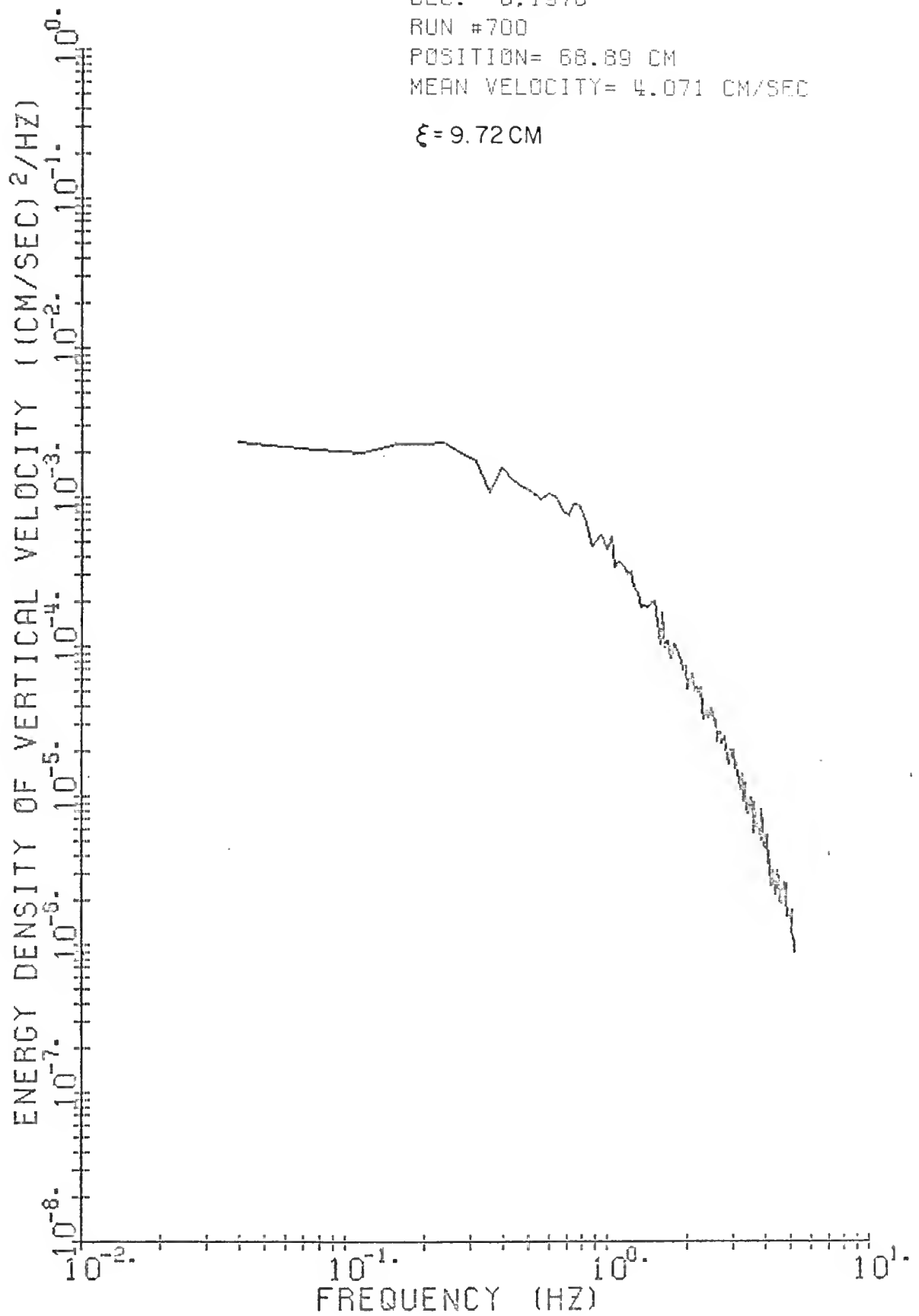
 $\xi = 9.72$ CM

DEC. 6, 1978

RUN #700

POSITION= 68.89 CM

MEAN VELOCITY= 4.071 CM/SEC

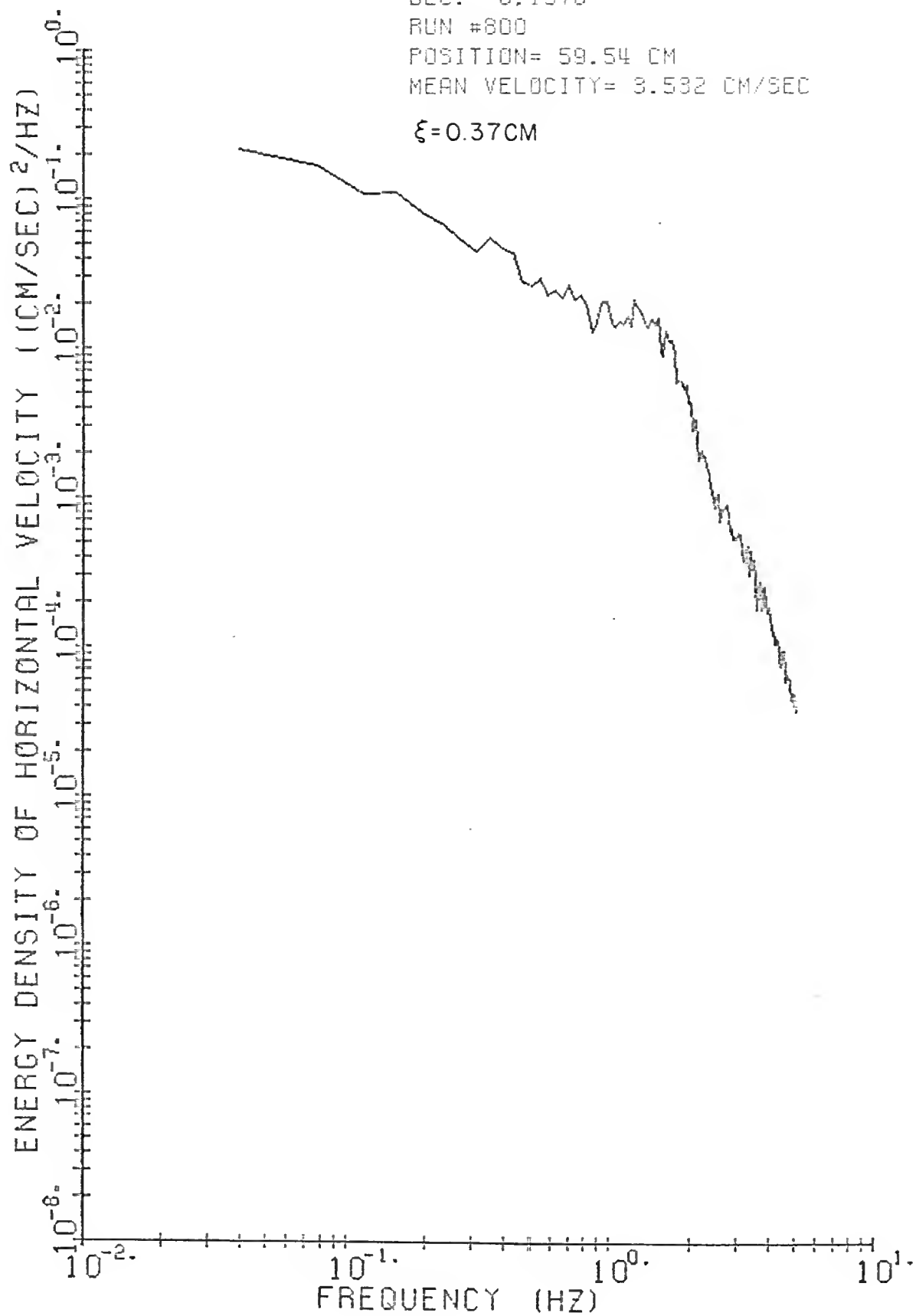
 $\xi = 9.72$ CM

DEC. 6, 1978

RUN #600

POSITION= 59.54 CM

MEAN VELOCITY= 3.532 CM/SEC

 $\xi = 0.37 \text{ CM}$ 

DEC. 6.1978

RUN #800

POSITION= 59.54 CM

MEAN VELOCITY= 3.532 CM/SEC

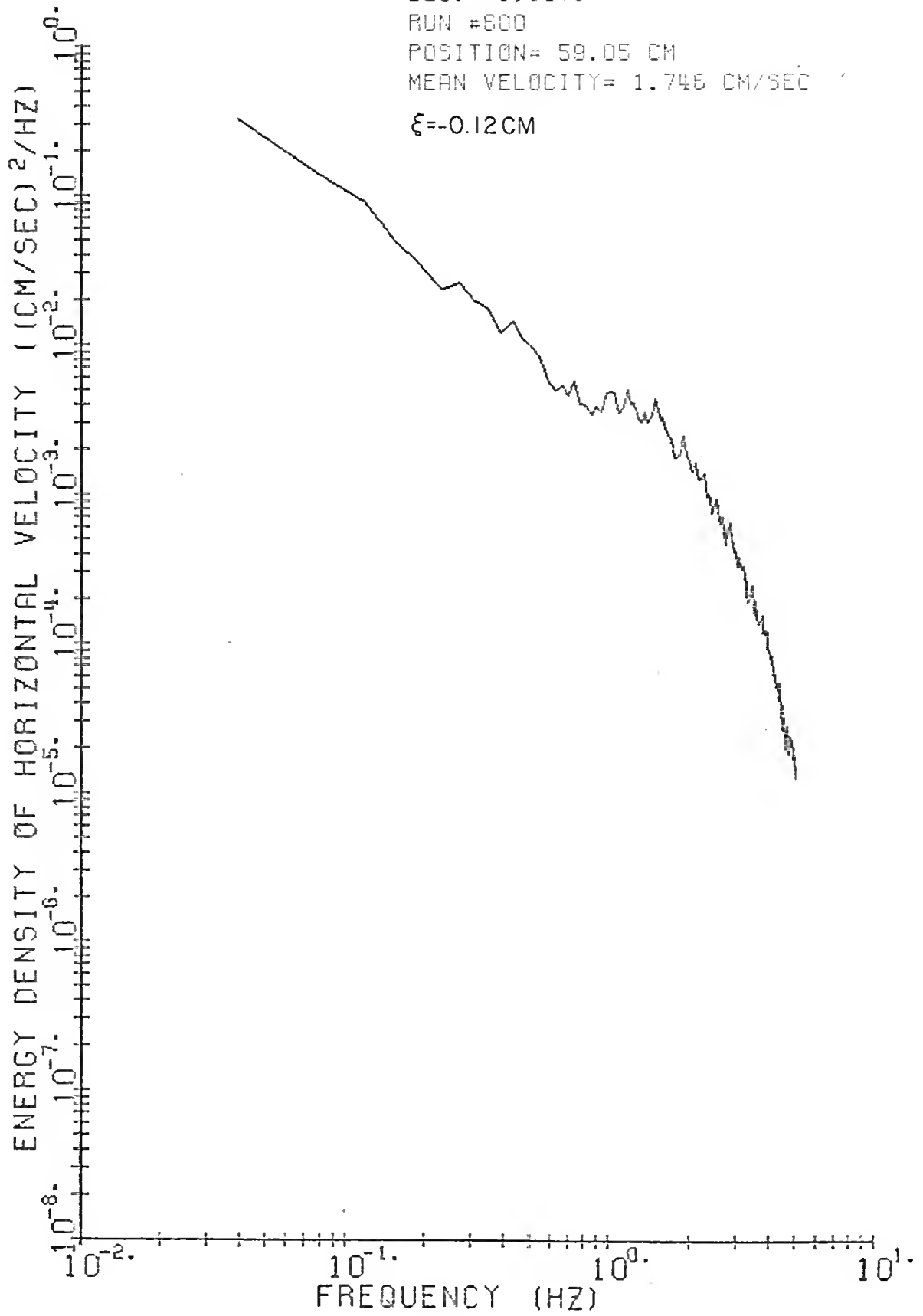
 $\xi = 0.37$ CM

DEC. 6, 1978

RUN #800

POSITION= 59.05 CM

MEAN VELOCITY= 1.746 CM/SEC

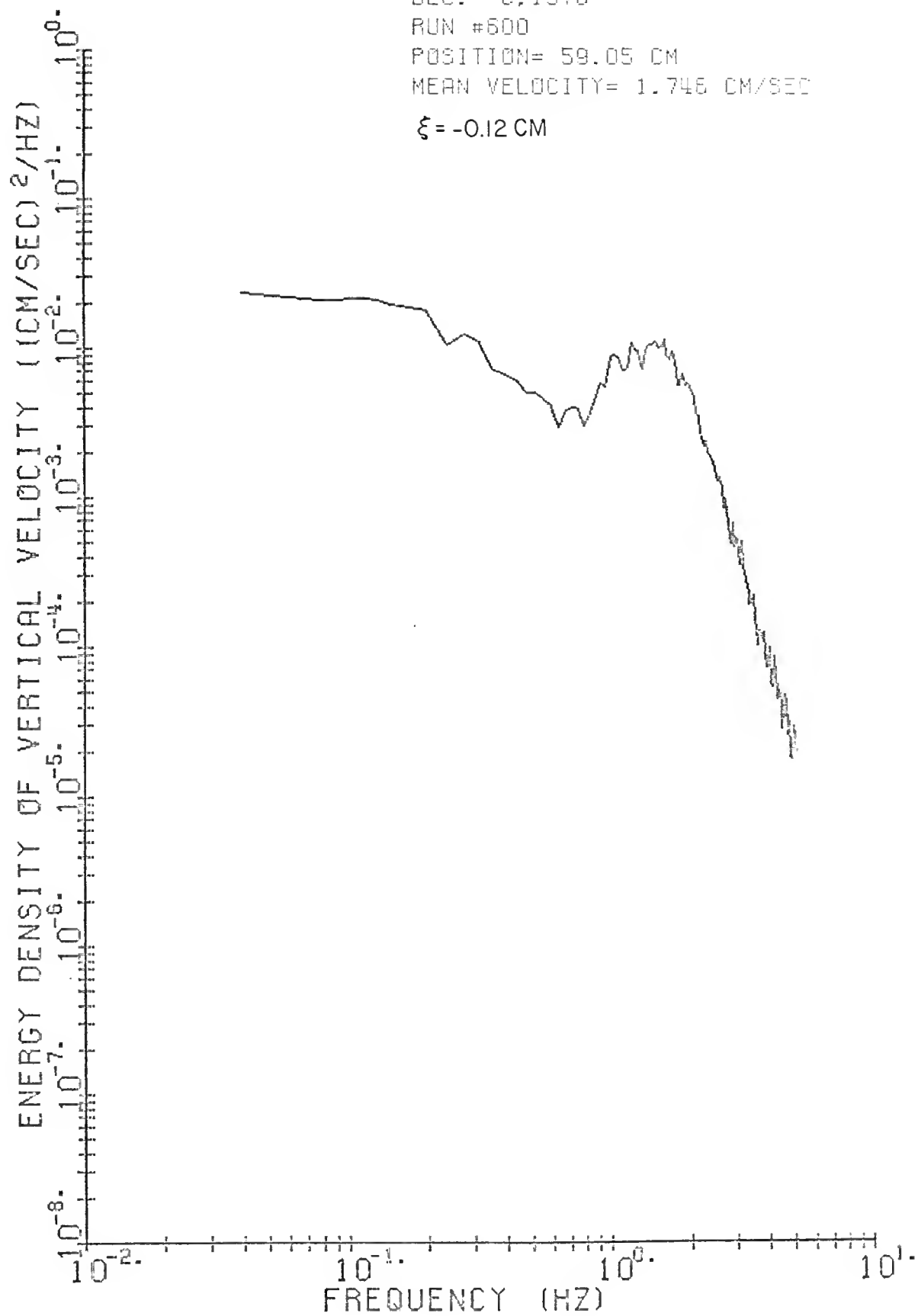
 $\xi = -0.12$ CM

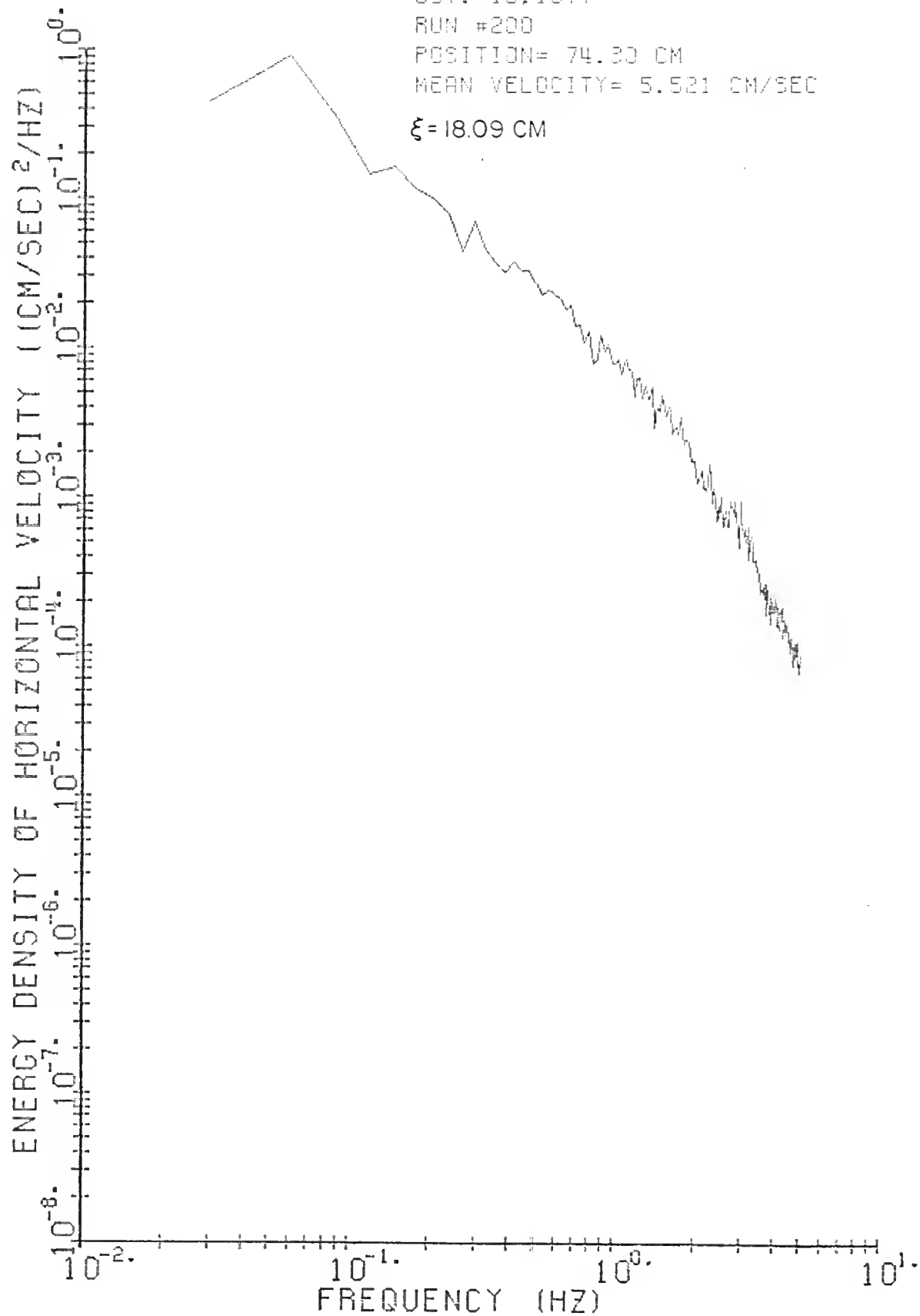
DEC. 6, 1978

RUN #600

POSITION= 59.05 CM

MEAN VELOCITY= 1.746 CM/SEC

 $\xi = -0.12$ CM

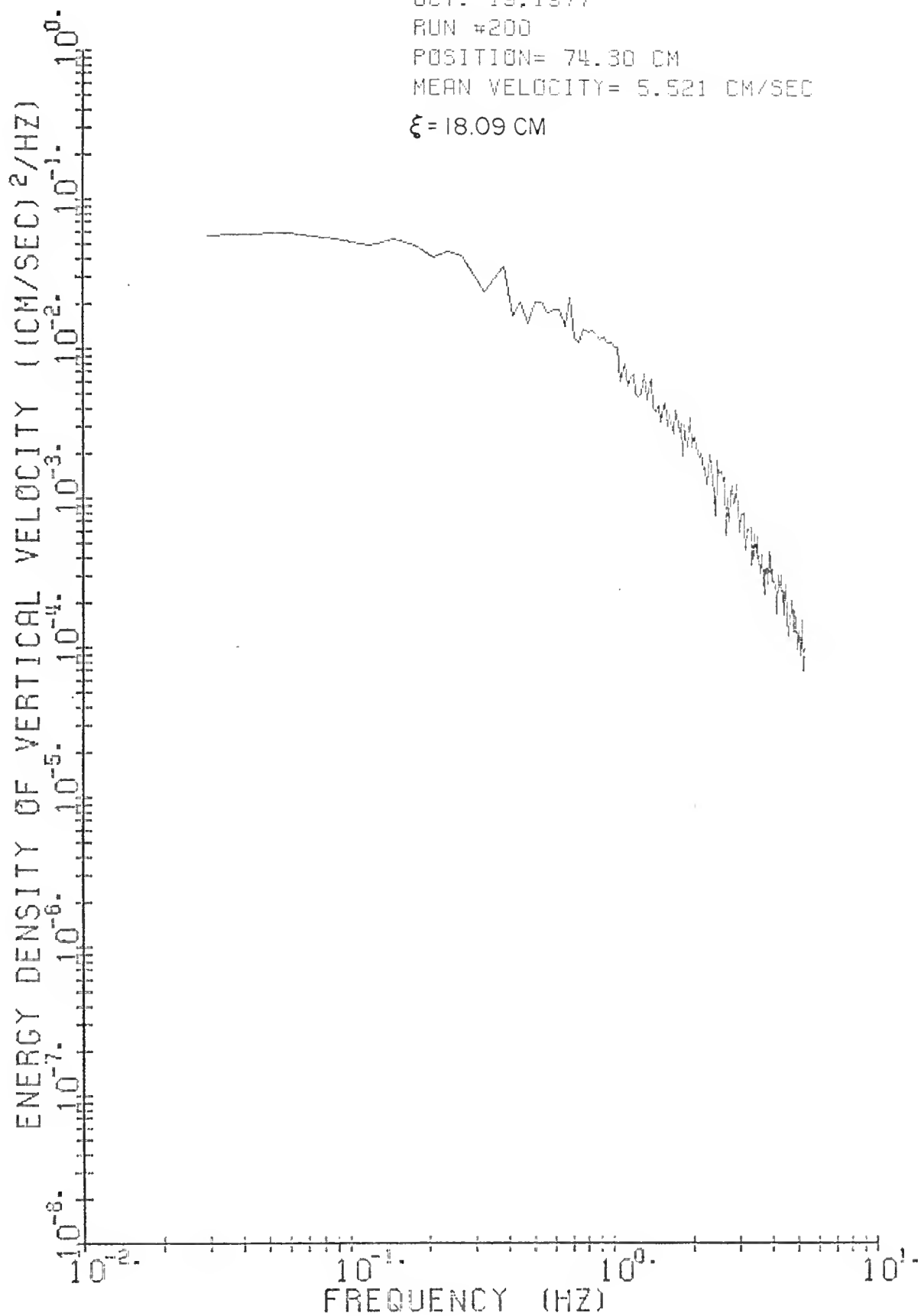


OCT. 19.1977

RUN #200

POSITION= 74.30 CM

MEAN VELOCITY= 5.521 CM/SEC

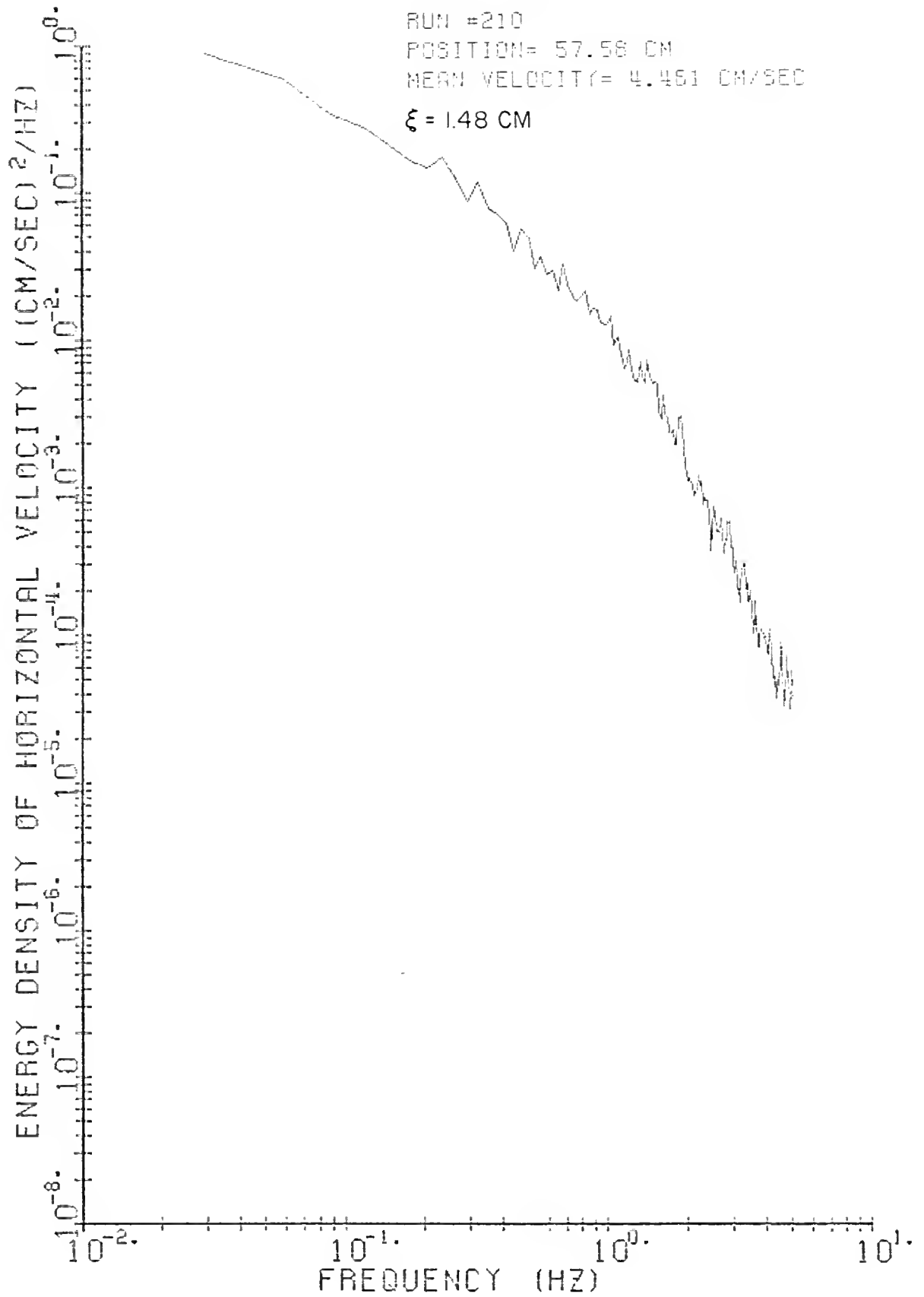
 $\xi = 18.09$ CM

OCT. 19. 1977

RUN #210

POSITION= 57.58 CM

MEAN VELOCITY= 4.461 CM/SEC

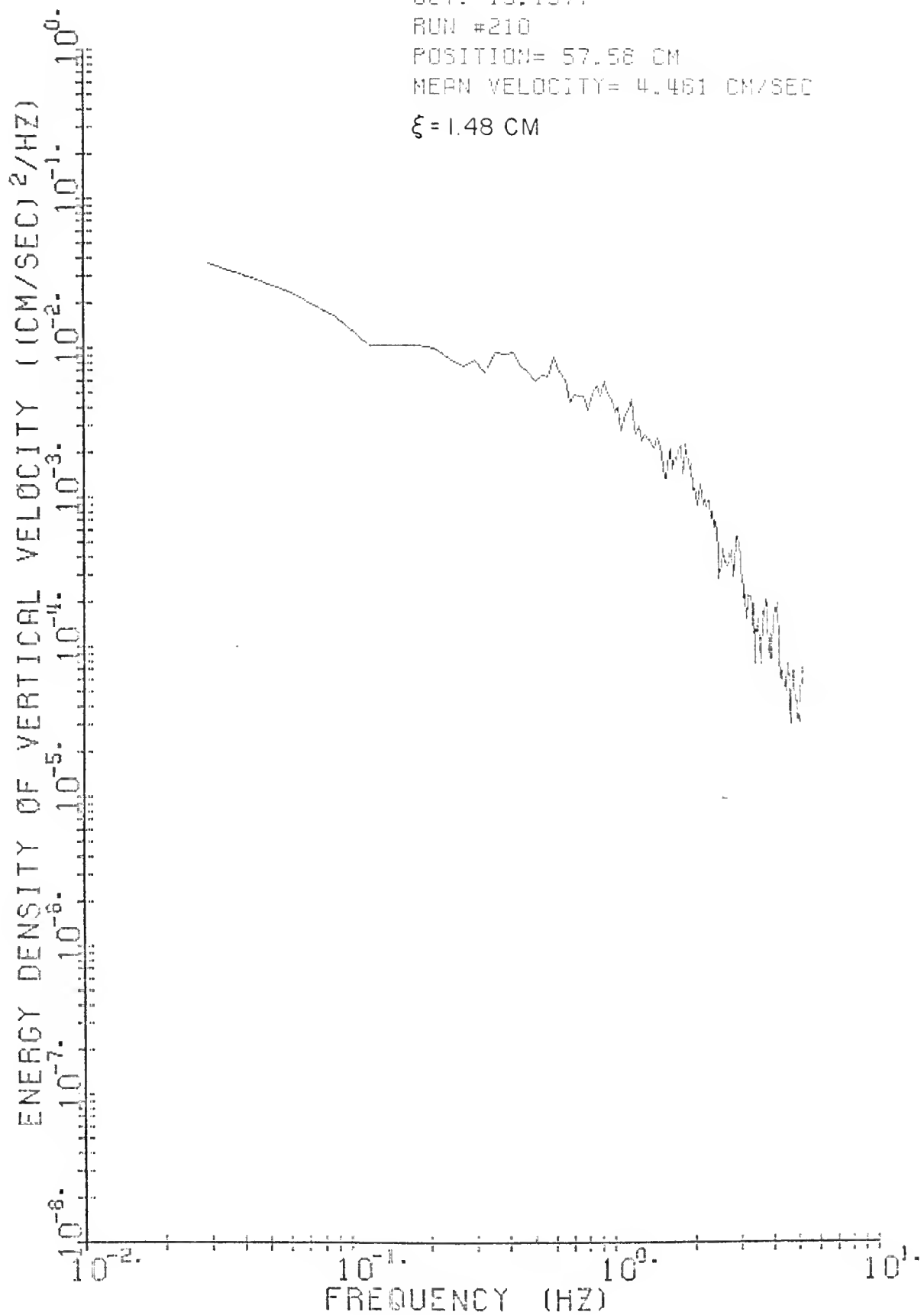
 $\xi = 1.48$ CM

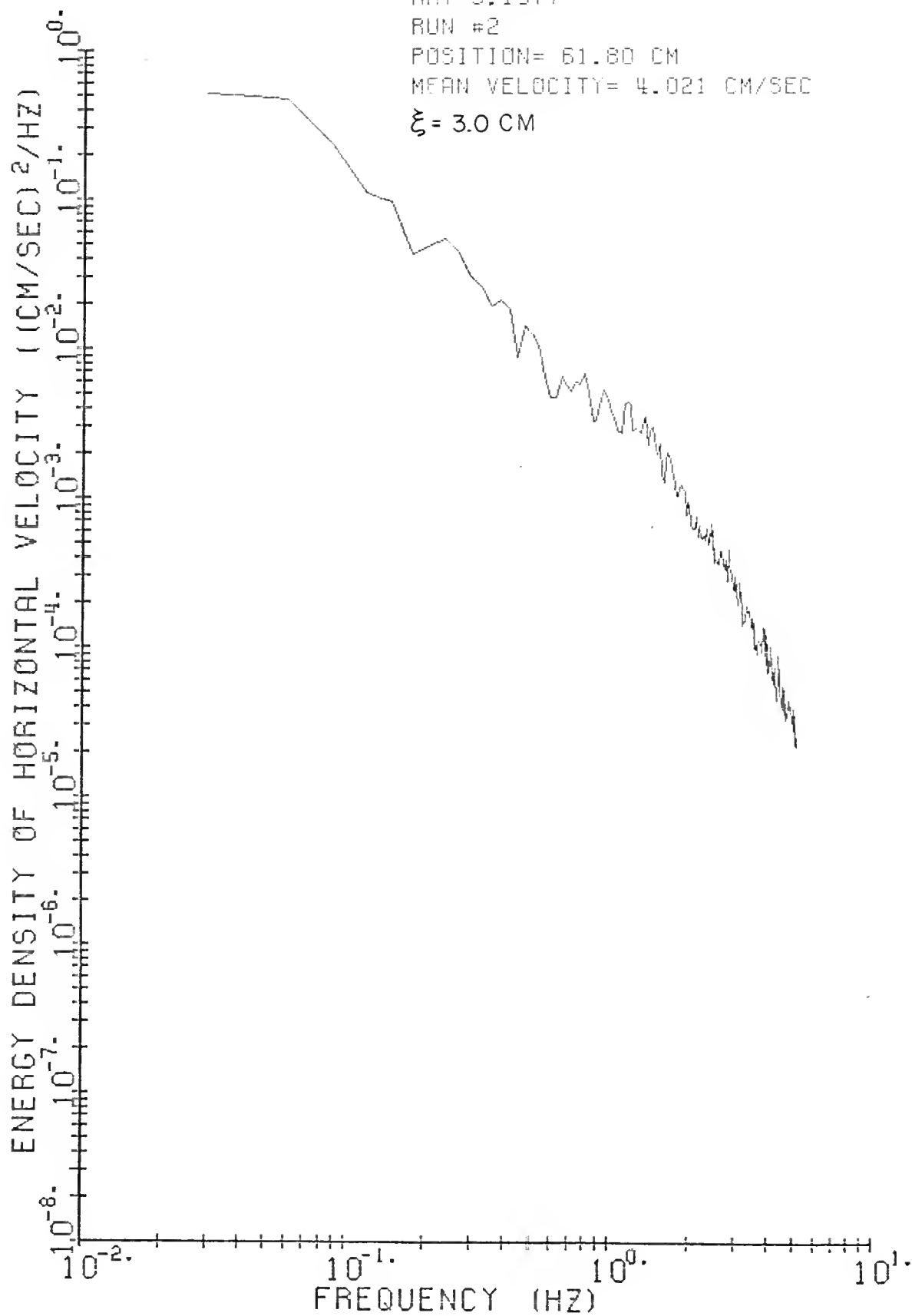
OCT. 19.1977

RUN #210

POSITION= 57.58 CM

MEAN VELOCITY= 4.461 CM/SEC

 $\xi = 1.48$ CM

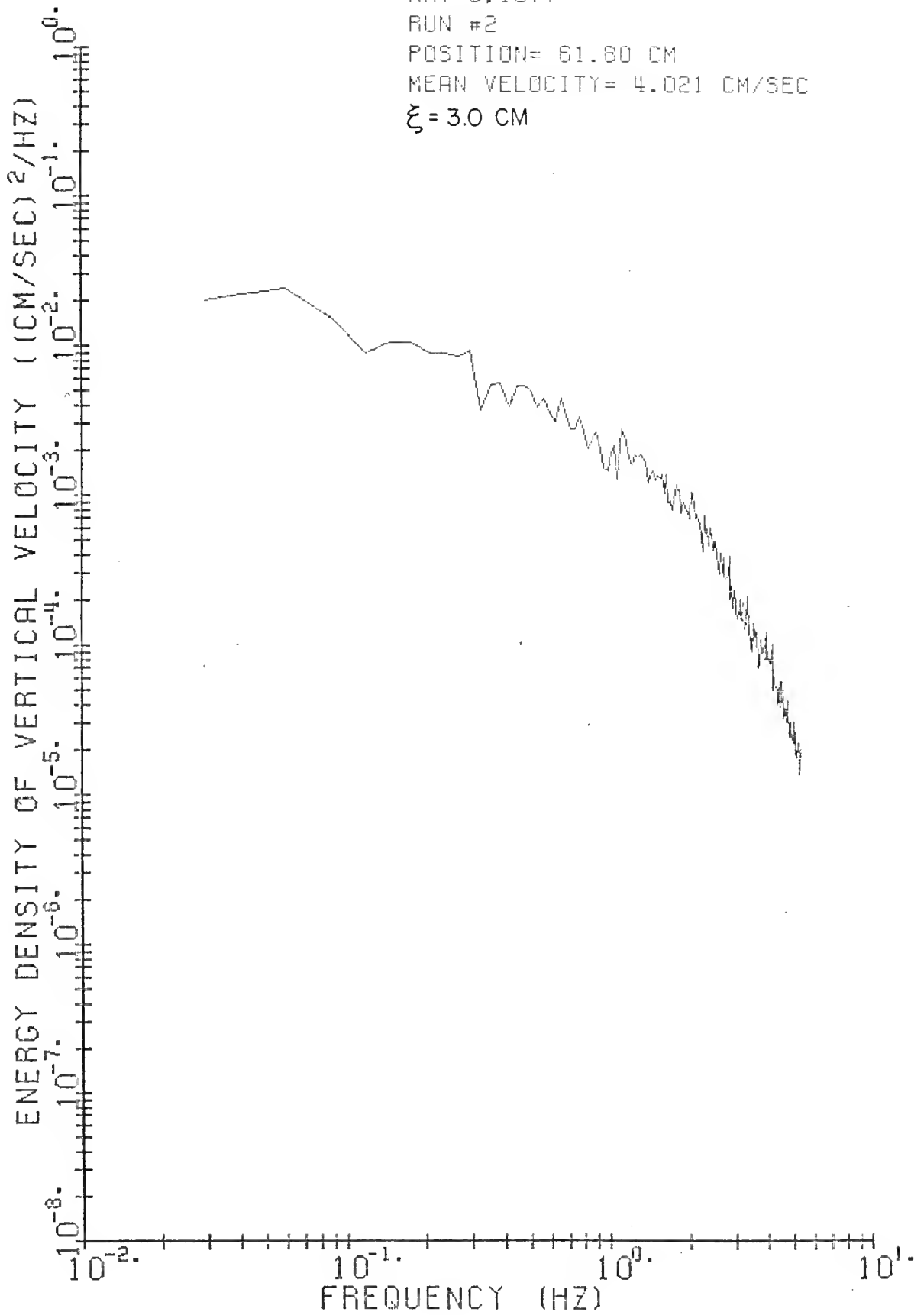


MAY 3, 1977

RUN #2

POSITION= 61.80 CM

MEAN VELOCITY= 4.021 CM/SEC

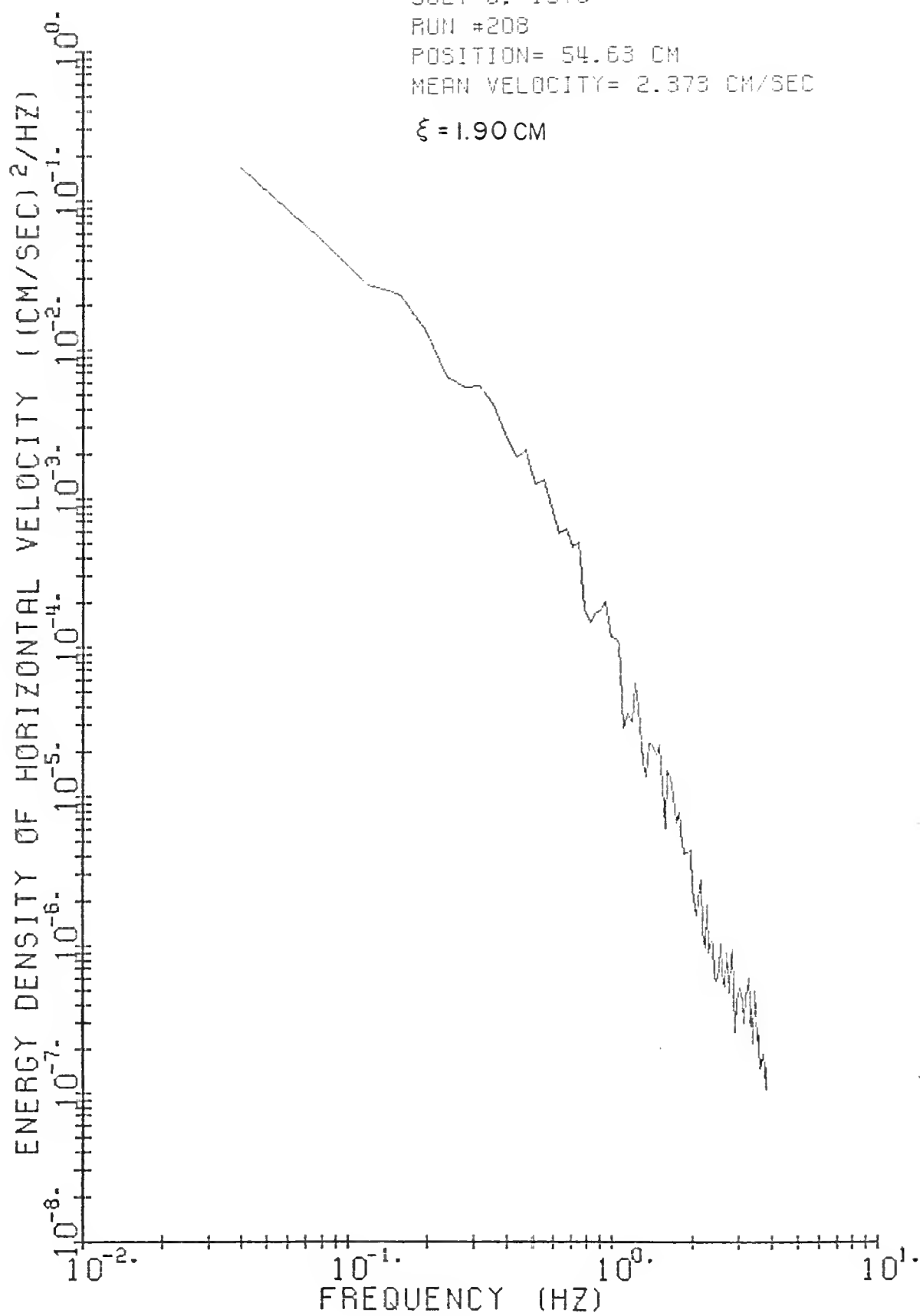
 $\xi = 3.0$ CM

JULY 6, 1976

RUN #208

POSITION= 54.63 CM

MEAN VELOCITY= 2.373 CM/SEC

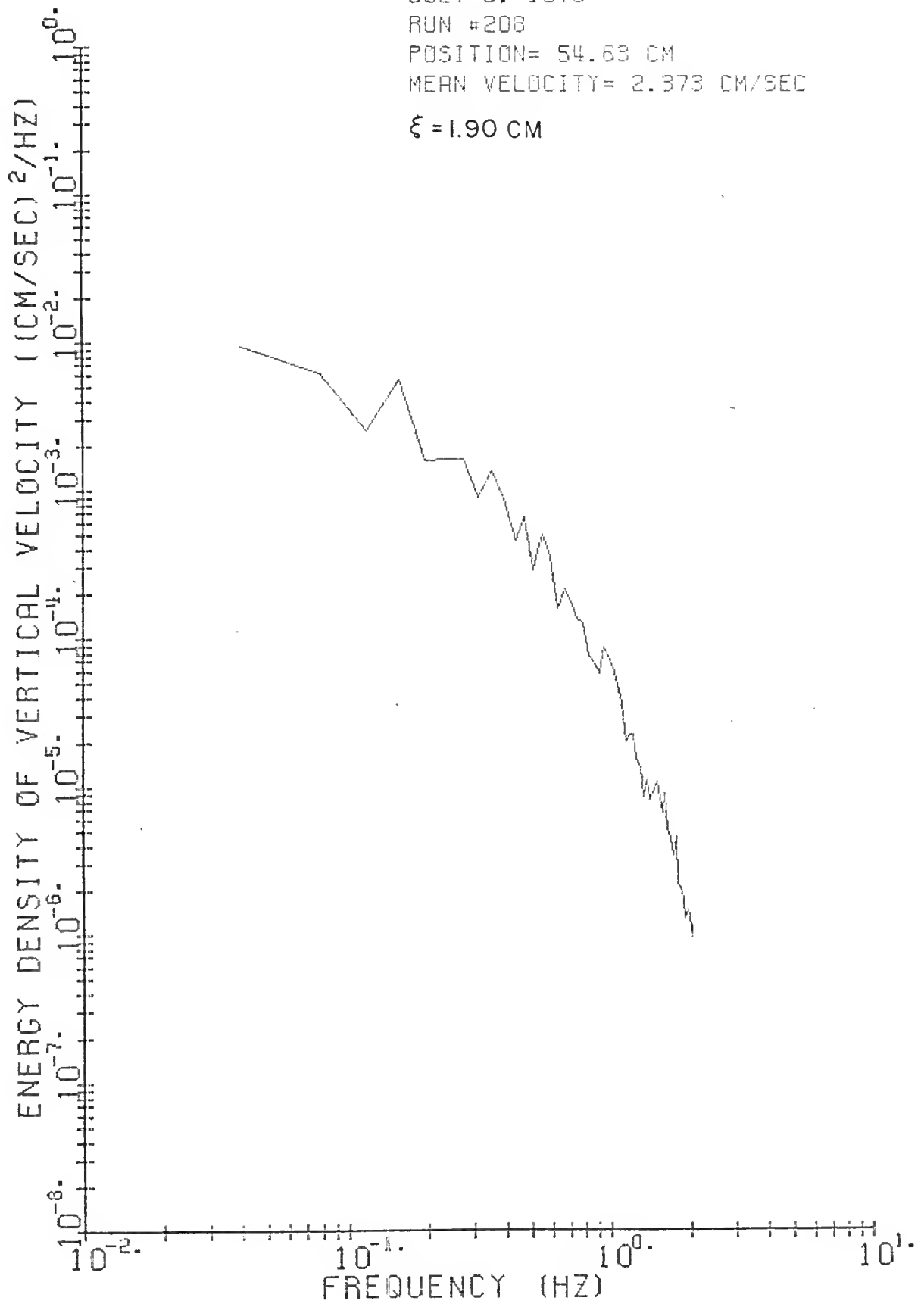
 $\xi = 1.90$ CM

JULY 6. 1976

RUN #208

POSITION= 54.63 CM

MEAN VELOCITY= 2.373 CM/SEC

 $\xi = 1.90$ CM

JULY 6, 1976

RUN #212

POSITION= 52.95 CM

MEAN VELOCITY= 1.730 CM/SEC

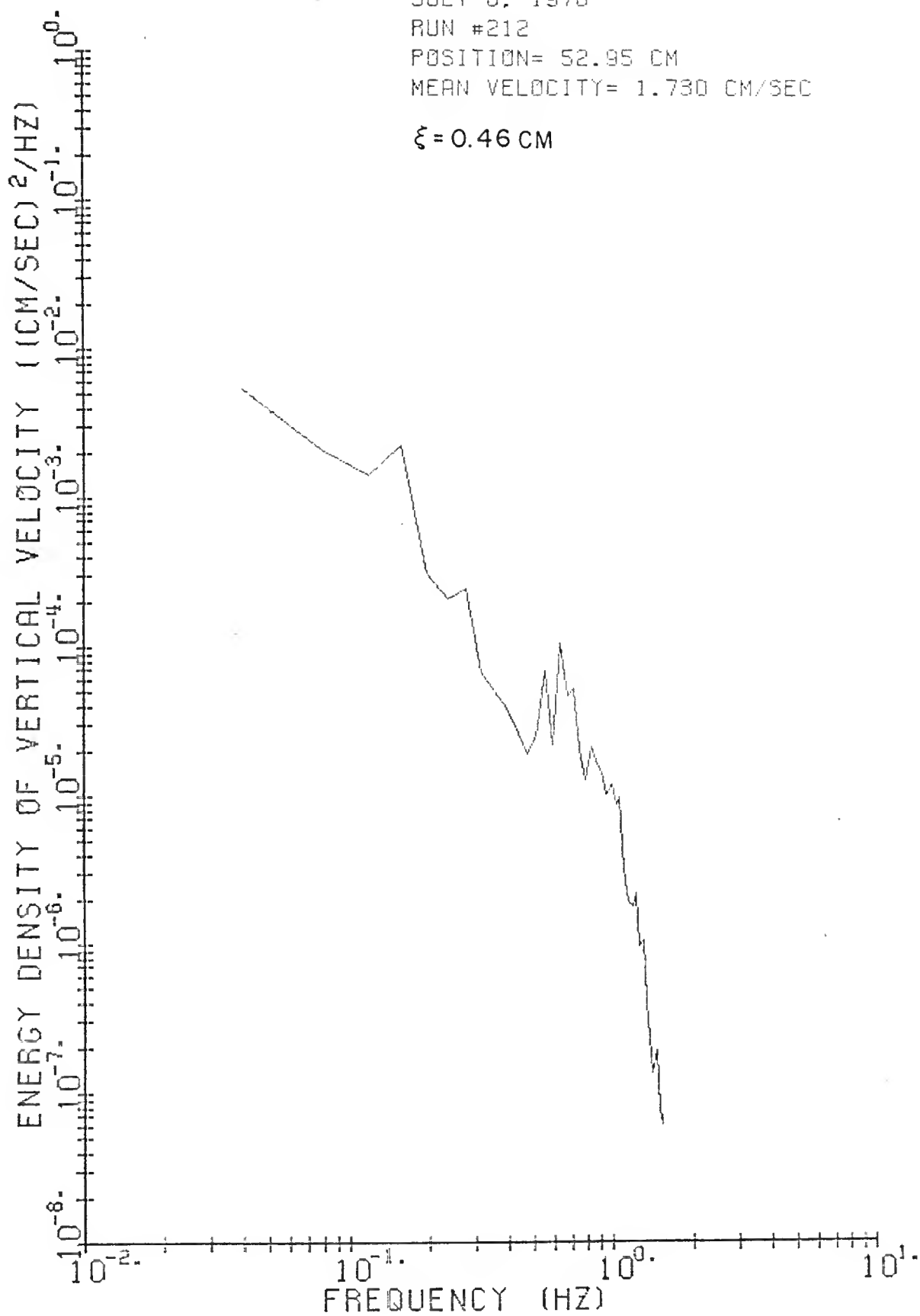
 $\xi = 0.46$ CM

JULY 6, 1976

RUN #212

POSITION= 52.95 CM

MEAN VELOCITY= 1.730 CM/SEC

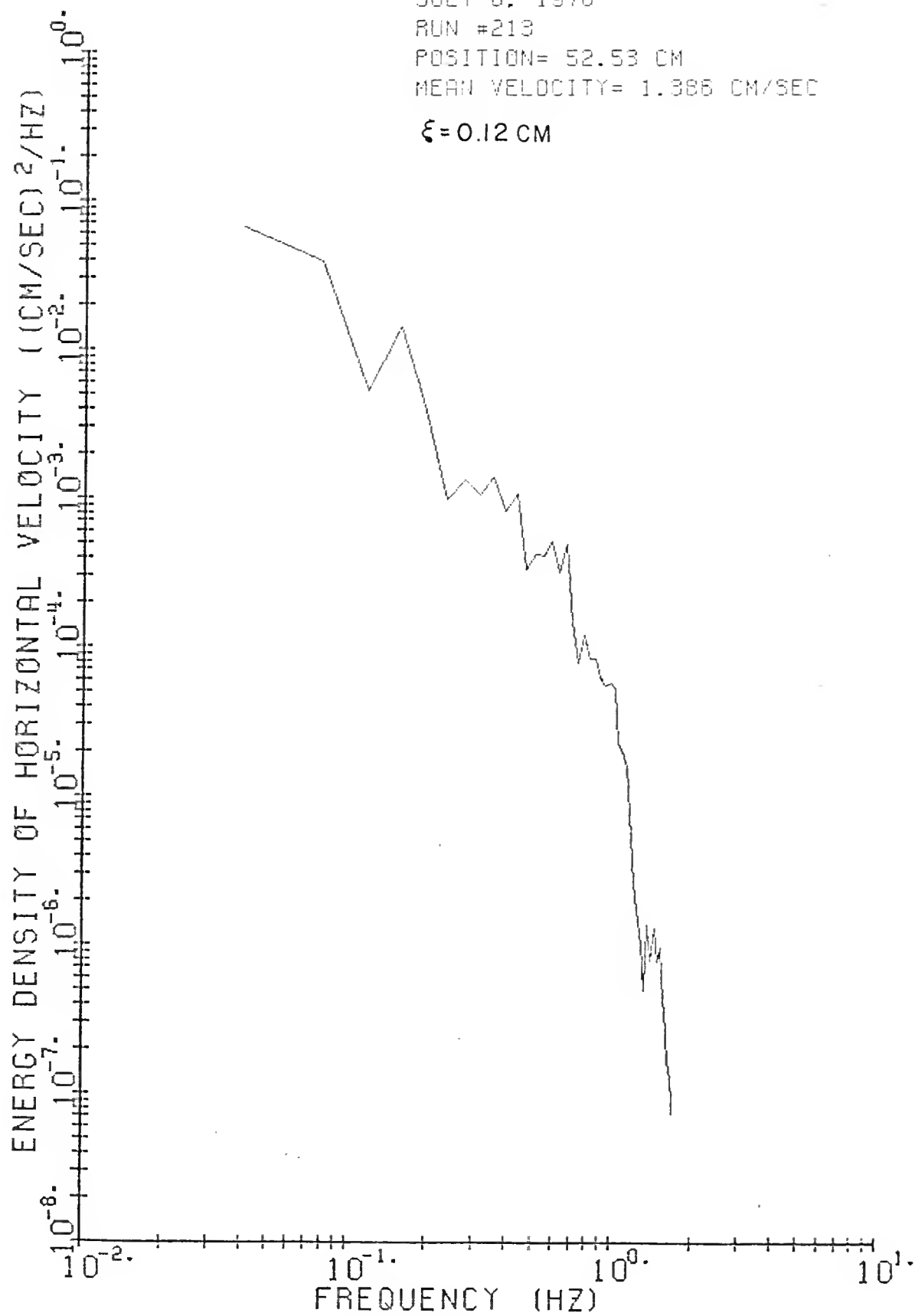
 $\xi = 0.46$ CM

JULY 6, 1976

RUN #213

POSITION= 52.53 CM

MEAN VELOCITY= 1.386 CM/SEC

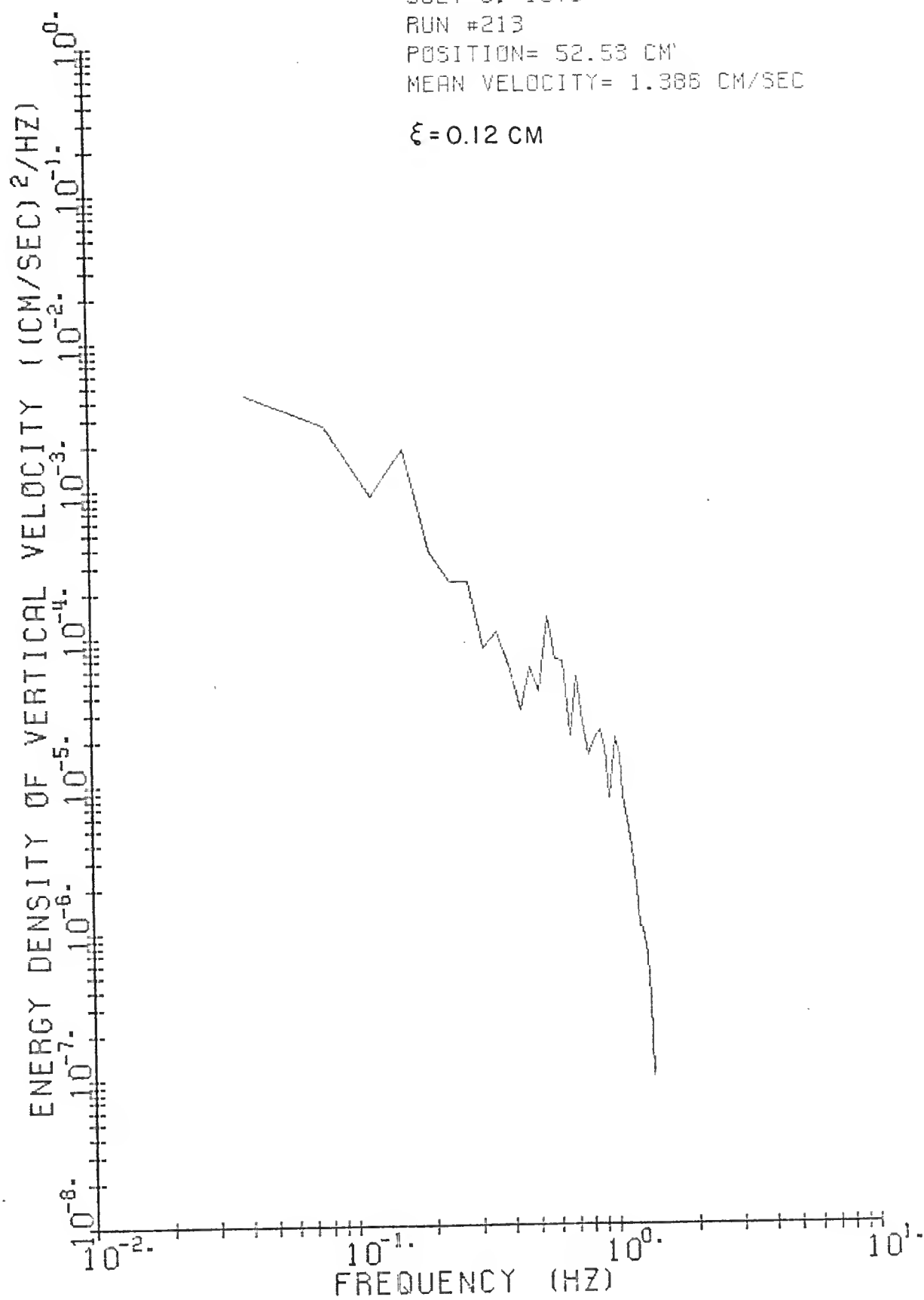
 $\xi = 0.12$ CM

JULY 6, 1976

RUN #213

POSITION= 52.53 CM

MEAN VELOCITY= 1.386 CM/SEC

 $\xi = 0.12$ CM

APPENDIX E

VERTICAL SHEAR STRESS PROFILE

The analysis presented in this appendix is carried out in two major steps. First, equations 2.1 through 2.4 are developed in a systematic way from the differential form of the continuity and Navier-Stokes equations, by expanding the latter equations using the Reynolds decomposition technique. After the complete equations are derived, various terms are eliminated until equations 2.1 through 2.4 emerge. This should allow the reader a better understanding of what assumptions are implied by the use of equations 2.1 through 2.4.

Following this, equations 2.1, 2.2 and 2.3 are integrated to determine the vertical shear stress profile, $\tau_{xy}(x,y,z=0)$. An assumption is made a priori to simplify the integration. The velocity and density profiles are assumed to be self-similar, requiring only one length scale, δ_u and δ respectively, to nondimensionalize each of the profiles.

The continuity equation for an incompressible, nondiffusive, nonconductive, nondissipative flow is given by

$$\frac{\partial u}{\partial x} + \frac{\partial v}{\partial y} + \frac{\partial w}{\partial z} = 0, \quad \text{E.1}$$

where u , v , w are the instantaneous velocities in the x , y , z directions, respectively. In a real fluid equation E.1 is only approximately correct; however, for the range of conditions studied herein the

error resulting from the use of equation E.1 is less than 2×10^{-4} /sec. Detailed arguments supporting this statement are presented in Appendix C.

The momentum equations for an incompressible, Newtonian fluid with constant viscosity are:

$$\rho \left[\frac{\partial u}{\partial t} + u \frac{\partial u}{\partial x} + v \frac{\partial u}{\partial y} + w \frac{\partial u}{\partial z} \right] = -\frac{\partial P}{\partial x} + \mu \left[\frac{\partial^2 u}{\partial x^2} + \frac{\partial^2 u}{\partial y^2} + \frac{\partial^2 u}{\partial z^2} \right], \quad E.2$$

$$\rho \left[\frac{\partial v}{\partial t} + u \frac{\partial v}{\partial x} + v \frac{\partial v}{\partial y} + w \frac{\partial v}{\partial z} \right] = -\frac{\partial P}{\partial y} - \rho g + \mu \left[\frac{\partial^2 v}{\partial x^2} + \frac{\partial^2 v}{\partial y^2} + \frac{\partial^2 v}{\partial z^2} \right], \quad E.3$$

$$\rho \left[\frac{\partial w}{\partial t} + u \frac{\partial w}{\partial x} + v \frac{\partial w}{\partial y} + w \frac{\partial w}{\partial z} \right] = -\frac{\partial P}{\partial z} + \mu \left[\frac{\partial^2 w}{\partial x^2} + \frac{\partial^2 w}{\partial y^2} + \frac{\partial^2 w}{\partial z^2} \right], \quad E.4$$

where ρ and P are the instantaneous density and pressure, respectively, μ is the fluid viscosity and g is the gravitational acceleration. The variation in the fluid viscosity resulting from salinity and temperature variations is less than four percent for the flow studied herein, therefore, the fluid viscosity is considered constant.

Employing Reynolds decomposition technique, the dependent variables are represented as the sum of fluctuating and time independent components as follows:

$$\left. \begin{aligned} \rho(x,y,z,t) &= \rho_o(x,y,z) + \rho'(x,y,z,t), \\ P(x,y,z,t) &= P_o(x,y,z) + P'(x,y,z,t), \\ u(x,y,z,t) &= U(x,y,z) + u'(x,y,z,t), \\ v(x,y,z,t) &= V(x,y,z) + v'(x,y,z,t), \\ w(x,y,z,t) &= W(x,y,z) + w'(x,y,z,t). \end{aligned} \right\} \quad E.5$$

The time average of any fluctuating quantity, $f'(t)$, is defined by,

$$\overline{f'(t)} = \lim_{T \rightarrow \infty} \frac{1}{2T} \int_{-T}^{+T} f'(t) dt,$$

and is denoted in the equations to follow by an overbar. By definition,

$$\overline{\rho'} = \overline{P'} = \overline{u'} = \overline{v'} = \overline{w'} = 0.$$

Substituting equations E.5 into equation E.1 gives

$$\frac{\partial U}{\partial x} + \frac{\partial V}{\partial y} + \frac{\partial W}{\partial z} + \frac{\partial u'}{\partial x} + \frac{\partial v'}{\partial y} + \frac{\partial w'}{\partial z} = 0. \quad E.6$$

Time averaging equation E.6 reduces it to

$$\frac{\partial U}{\partial x} + \frac{\partial V}{\partial y} + \frac{\partial W}{\partial z} = 0, \quad E.7$$

and subtracting equation E.7 from equation E.6 results in

$$\frac{\partial u'}{\partial x} + \frac{\partial v'}{\partial y} + \frac{\partial w'}{\partial z} = 0. \quad E.8$$

Thus, not only is the dilatation of the mean flow zero, but at any instant in time, the divergence of the turbulent velocity fluctuations is also zero.

In a parallel manner, the momentum equations governing the mean flow of a turbulent stratified fluid are derived by substituting equation E.5 into equations E.2, E.3 and E.4. After time averaging and much simple but tedious manipulation using equations E.7 and E.8, equations E.2, E.3 and E.4 become:

$$\begin{aligned}
& \left[1 + \frac{\overline{\rho' u'}}{\rho_o U} \right] U \frac{\partial U}{\partial x} + \left[1 + \frac{\overline{\rho' v'}}{\rho_o V} \right] V \frac{\partial U}{\partial y} + \left[1 + \frac{\overline{\rho' w'}}{\rho_o W} \right] W \frac{\partial U}{\partial z} \\
& + \frac{U}{\rho_o} \frac{\partial}{\partial x} \overline{\rho' u'} + \frac{V}{\rho_o} \frac{\partial}{\partial y} \overline{\rho' u'} + \frac{W}{\rho_o} \frac{\partial}{\partial z} \overline{\rho' u'} \\
& + \frac{1}{\rho_o} \frac{\partial}{\partial x} \overline{\rho' u' u'} + \frac{1}{\rho_o} \frac{\partial}{\partial y} \overline{\rho' v' u'} + \frac{1}{\rho_o} \frac{\partial}{\partial z} \overline{\rho' w' u'} \\
& = \frac{-1}{\rho_o} \frac{\partial P_o}{\partial x} + \frac{\partial}{\partial x} \overline{-u' u'} + \frac{\mu}{\rho_o} \frac{\partial^2 U}{\partial x^2} - \frac{\overline{u' u'}}{\rho_o} \frac{\partial \rho_o}{\partial x} \\
& \quad + \frac{\partial}{\partial y} \overline{-u' v'} + \frac{\mu}{\rho_o} \frac{\partial^2 U}{\partial y^2} - \frac{\overline{u' v'}}{\rho_o} \frac{\partial \rho_o}{\partial y} \\
& \quad + \frac{\partial}{\partial z} \overline{-u' w'} + \frac{\mu}{\rho_o} \frac{\partial^2 U}{\partial z^2} - \frac{\overline{u' w'}}{\rho_o} \frac{\partial \rho_o}{\partial z}
\end{aligned}$$

E.9

$$\begin{aligned}
& \left[1 + \frac{\overline{\rho' u'}}{\rho_o U} \right] U \frac{\partial V}{\partial x} + \left[1 + \frac{\overline{\rho' v'}}{\rho_o V} \right] V \frac{\partial V}{\partial y} + \left[1 + \frac{\overline{\rho' w'}}{\rho_o W} \right] W \frac{\partial V}{\partial z} \\
& + \frac{U}{\rho_o} \frac{\partial}{\partial x} \overline{\rho' v'} + \frac{V}{\rho_o} \frac{\partial}{\partial y} \overline{\rho' v'} + \frac{W}{\rho_o} \frac{\partial}{\partial z} \overline{\rho' v'} \\
& + \frac{1}{\rho_o} \frac{\partial}{\partial x} \overline{\rho' u' v'} + \frac{1}{\rho_o} \frac{\partial}{\partial y} \overline{\rho' v' v'} + \frac{1}{\rho_o} \frac{\partial}{\partial z} \overline{\rho' w' v'} \\
& = \frac{-1}{\rho_o} \frac{\partial P_o}{\partial y} - g + \frac{\partial}{\partial x} \overline{-u' v'} + \frac{\mu}{\rho_o} \frac{\partial^2 V}{\partial x^2} - \frac{\overline{u' v'}}{\rho_o} \frac{\partial \rho_o}{\partial x} \\
& \quad + \frac{\partial}{\partial y} \overline{-v' v'} + \frac{\mu}{\rho_o} \frac{\partial^2 V}{\partial y^2} - \frac{\overline{v' v'}}{\rho_o} \frac{\partial \rho_o}{\partial y} \\
& \quad + \frac{\partial}{\partial z} \overline{-w' v'} + \frac{\mu}{\rho_o} \frac{\partial^2 V}{\partial z^2} - \frac{\overline{w' v'}}{\rho_o} \frac{\partial \rho_o}{\partial z}
\end{aligned}$$

E.10

$$\begin{aligned}
& \left[1 + \frac{\overline{\rho' u'}}{\rho_o U} \right] U \frac{\partial W}{\partial x} + \left[1 + \frac{\overline{\rho' v'}}{\rho_o V} \right] V \frac{\partial W}{\partial y} + \left[1 + \frac{\overline{\rho' w'}}{\rho_o W} \right] W \frac{\partial W}{\partial z} \\
& + \frac{U}{\rho_o} \frac{\partial}{\partial x} \overline{\rho' w'} + \frac{V}{\rho_o} \frac{\partial}{\partial y} \overline{\rho' w'} + \frac{W}{\rho_o} \frac{\partial}{\partial z} \overline{\rho' w'} \\
& + \frac{1}{\rho_o} \frac{\partial}{\partial x} \overline{\rho' u' w'} + \frac{1}{\rho_o} \frac{\partial}{\partial y} \overline{\rho' v' w'} + \frac{1}{\rho_o} \frac{\partial}{\partial z} \overline{\rho' w' w'} \\
& = \frac{-1}{\rho_o} \frac{\partial P_o}{\partial z} + \frac{\partial}{\partial x} \overline{-u' w'} + \frac{\mu}{\rho_o} \frac{\partial^2 W}{\partial x^2} - \frac{u' w'}{\rho_o} \frac{\partial \rho_o}{\partial x} \\
& \quad + \frac{\partial}{\partial y} \overline{-v' w'} + \frac{\mu}{\rho_o} \frac{\partial^2 W}{\partial y^2} - \frac{v' w'}{\rho_o} \frac{\partial \rho_o}{\partial y} \\
& \quad + \frac{\partial}{\partial z} \overline{-w' w'} + \frac{\mu}{\rho_o} \frac{\partial^2 W}{\partial z^2} - \frac{w' w'}{\rho_o} \frac{\partial \rho_o}{\partial z}
\end{aligned} \tag{E.11}$$

Equations E.7 through E.11 have been developed from the differential form of the continuity and momentum equations while invoking a minimum number of assumptions; therefore, these equations enjoy general applicability. However, because of their complexity and the problem of closure, the system cannot be solved. In order to reduce the equations to a form which can be solved, assumptions must be made regarding the nature of the specific flow of interest.

First, if at the center of the tank ($z=0$), where the measurements presented in Chapter IV were made, the flow is assumed to be nearly two dimensional and free of any secondary currents, then

$$W = \frac{\partial W}{\partial z} = \frac{\partial U}{\partial z} = \frac{\partial V}{\partial z} = \frac{\partial P_o}{\partial z} = \frac{\partial \rho_o}{\partial z} = \overline{\rho' w'} = 0 .$$

Under these assumptions, equation E.7 reduces to

$$\frac{\partial U}{\partial x} + \frac{\partial V}{\partial y} = 0. \quad \text{E.12}$$

Next, if the pressure throughout the fluid is assumed to be hydrostatic, equation E.10 reduces to

$$\frac{\partial P_o}{\partial y} = -g \rho_o(x,y) \quad \text{E.13}$$

Finally, if the mean advective acceleration, the horizontal pressure gradient, the side wall shear stress and the interfacial shear stress are assumed to be the only significant terms in the x-component momentum equation and if ρ_o is approximately equal to ρ_u , so that the Boussinesq approximation holds, then equation E.9 becomes

$$\frac{\partial U^2}{\partial x} + \frac{\partial UV}{\partial y} = \frac{-1}{\rho_u} \frac{\partial P_o}{\partial x} + \frac{\partial}{\partial y} \tau_{xy} + \frac{\partial}{\partial z} \tau_{xz}, \quad \text{E.14}$$

where

$$\tau_{xz} = -\overline{u'w'} + \frac{\mu}{\rho_u} \frac{\partial U}{\partial z}$$

is the shear stress produced by the side walls and

$$\tau_{xy} = -\overline{u'v'} + \frac{\mu}{\rho_u} \frac{\partial U}{\partial y}$$

is the shear stress in the plane $z=0$.

Equation E.14 can be further simplified if the flow does not change with the distance downstream and the side wall stresses are insignificant. Under these conditions equation E.14 becomes

$$\frac{1}{\rho_u} \frac{\partial P_o}{\partial x} = \frac{\partial \tau_{xy}}{\partial y}. \quad \text{E.15}$$

For an ideal two layer freesurface flow, equations E.13 and E.15 predict a linear shear stress profile which is zero at the freesurface and maximum at the interface. The more complete model, given by

equations E.12 through E.14, accounts for the side wall friction, nonhomogenous density and advective accelerations due to boundary layer development. Next, these equations are solved to determine the shear stress profile at the center of the tank ($z=0$).

Intergrating equation E.12 from the free surface, $y = \nabla(x)$, to y gives

$$V(x, y, 0) = \int_y^{\nabla(x)} \frac{\partial}{\partial x} U(x, y) dy + U(x, \nabla) \frac{d\nabla}{dx}, \quad \text{E.16}$$

under the assumption that a fluid particle at the surface remains at the surface (i.e. $V(x, \nabla) = U(x, \nabla) d\nabla/dx$).

Invoking the self-similarity hypothesis, the mean velocity profile can be defined by

$$U(x, \xi^*) \equiv \bar{U}(x) f(\xi^*), \quad \text{E.17}$$

where f is a nondimensional function of the nondimensional variable ξ^* , $\bar{U}(x)$ is the freestream velocity, and

$$\xi^* \equiv \frac{\xi - \eta(x)}{\delta_u(x)} = \frac{y - D(x) - \eta(x)}{\delta_u(x)}, \quad \text{E.18}$$

where $D(x)$ is the distance from the bottom of the tank to the density interface, $\eta(x)$ is the vertical shift between the density and velocity profiles and $\delta_u(x)$ is the thickness of the velocity transition layer above the interface. By definition, in the freestream,

$$f(\xi^*) = 1 \quad ; \quad \frac{\nabla - D - \eta}{\delta_u} \geq \xi^* \geq 2.$$

Making the proper substitutions, equation E.16 can be rewritten as

$$V(x, \xi^*, 0) = \delta_u(x) \int_{\xi^*}^{(\nabla - D - \eta)/\delta_u} \frac{\partial}{\partial x} U(x, \xi^*) d\xi^* + \bar{U}(x) \frac{d\nabla}{dx}, \quad \text{E.19}$$

where

$$\frac{\partial}{\partial x} U(x, \xi^*) = \frac{d\bar{U}(x)}{dx} f(\xi^*) + \bar{U}(x) f'(\xi^*) \frac{\partial \xi^*}{\partial x}, \quad \text{E.20}$$

and

$$\frac{\partial \xi^*}{\partial x} = \frac{-\xi^*}{\delta_u(x)} \frac{d\delta_u}{dx} - \frac{1}{\delta_u} \left(\frac{dD}{dx} + \frac{d\eta}{dx} \right). \quad \text{E.21}$$

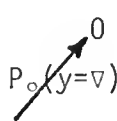
Substituting equations E.20 and E.21 into E.19 gives

$$\begin{aligned} V(x, \xi^*, 0) &= \delta_u(x) \frac{d\bar{U}(x)}{dx} \int_{\xi^*}^{(\nabla-D-\eta)/\delta_u} f(\xi^*) d\xi^* - \bar{U}(x) \frac{d\delta_u}{dx} \int_{\xi^*}^{(\nabla-D-\eta)/\delta_u} f'(\xi^*) \xi^* d\xi^* \\ &\quad - \bar{U}(x) \left(\frac{dD}{dx} + \frac{d\eta}{dx} \right) (1 - f(\xi^*)) + \bar{U}(x) \frac{d\nabla}{dx}. \end{aligned}$$

Integrating the second term on the right hand side by parts gives

$$\begin{aligned} V(x, \xi^*, 0) &= \left[\delta_u(x) \frac{d\bar{U}(x)}{dx} + \bar{U}(x) \frac{d\delta_u}{dx} \right] \int_{\xi^*}^{(\nabla-D-\eta)/\delta_u} f(\xi^*) d\xi^* \\ &\quad + \bar{U}(x) \frac{d\delta_u}{dx} \xi^* f(\xi^*) - \bar{U}(x) \left(\frac{dD}{dx} + \frac{d\eta}{dx} \right) (1 - f(\xi^*)) \\ &\quad + \bar{U}(x) \frac{d\nabla}{dx} - \bar{U}(x) \frac{d\delta_u}{dx} \frac{(\nabla-D-\eta)}{\delta_u}. \end{aligned} \quad \text{E.22}$$

Integrating equation E.13 from the freesurface, $y = \nabla(x)$, to y gives

$$P_o(x, y) = g \int_y^{\nabla(x)} \rho_o(x, y) dy + P_o(x, y=\nabla) \quad \text{E.23}$$


Differentiating equation E.23 with respect to x , gives, after applying Leibnitz's Rule,

$$\frac{\partial P_o(x,y)}{\partial x} = g \int_y^{\nabla(x)} \frac{\partial \rho_o}{\partial x} dy + g \rho_o(x, \nabla) \frac{d\nabla}{dx} . \quad \text{E.24}$$

If the density distribution is also self-similar, it can be represented by

$$\rho_o(\xi^+) = \rho_u + \Delta\rho \rho^*(\xi^+), \quad \text{E.25}$$

where ρ^* is a nondimensional function of the nondimensional vertical coordinate ξ^+ , $\Delta\rho$ is the density change across the interface and

$$\xi^+ = \frac{\xi}{\delta(x)} = \frac{y-D(x)}{\delta(x)}, \quad \text{E.26}$$

where $D(x)$ is the distance from the bottom of the tank to the density interface and $\delta(x)$ is the thickness of the density interface. By definition

$$\begin{aligned} \rho^* &= 0 & ; & \quad \xi^+ \geq 3 \\ \rho^* &= 1 & ; & \quad \xi^+ \leq -3 \end{aligned}$$

Making the above substitutions, equation E.24 becomes

$$\begin{aligned} \frac{\partial P_o(x, \xi^+)}{\partial x} &= g\Delta\rho \frac{d\delta}{dx} \left(\xi^+ \rho^*(\xi^+) + \int_{\xi^+}^{(\nabla-D)/\delta} \rho^*(\xi^+) d\xi^+ \right) \\ &+ g\Delta\rho \frac{dD}{dx} \rho^*(\xi^+) + g \rho_u \frac{d\nabla}{dx} . \end{aligned} \quad \text{E.27}$$

Next, assuming the shear stress maintained by the side walls can be written as a linear function of z times the value of the stress at the side wall, then

$$\tau_{xz}(x,y,z) = - \tau_w(x,y) z/W, \quad \text{E.28}$$

where W is the half width of the tank and τ_w is the shear stress at the side walls. Differentiating equation E.28 with respect to z gives,

$$\frac{\partial \tau_{xz}}{\partial z} = - \frac{\tau_w(x,y)}{W}.$$

Furthermore, if the side wall shear stress can be represented by

$$\tau_w(x,y) = \frac{f_o(x,y)}{8} U^2(x,y,0) = \frac{f_o(x,\xi^*)}{8} \bar{U}^2(x) f^2(\xi^*),$$

where f_o is the side wall friction factor, then

$$\frac{\partial \tau_{xz}}{\partial z} = - \frac{f_o(x,\xi^*)}{8W} \bar{U}^2(x) f^2(\xi^*). \quad \text{E.29}$$

The value of f_o depends on the Reynolds number and may depend on the density distribution. Therefore, f_o may be a function of ξ^* .

Integrating equation E.14 from the free surface to y gives,

$$\begin{aligned} & \int_y^{\nabla(x)} \frac{\partial}{\partial x} U^2(x,y) dy + U(x,\nabla) V(x,\nabla) - U(x,y) V(x,y) \\ &= \frac{-1}{\rho_u} \int_y^{\nabla(x)} \frac{\partial P_o}{\partial x} dy + \cancel{\tau_{xy}(x,\nabla)}^0 - \tau_{xy}(x,y) + \int_y^{\nabla(x)} \frac{\partial}{\partial x} \tau_{xz}(x,y) dy. \end{aligned}$$

The above equation can be transformed into the ξ^* and ξ^+ coordinate system by substituting equations E.17, E.18, E.21, E.22, E.27, and E.29.

The resulting equation is

$$\begin{aligned}
 \tau_{xy}(x, \xi^*, \xi^+) &= -g \frac{d\bar{\nabla}}{dx} \delta \left(\frac{\bar{\nabla}-D}{\delta} - \xi^+ \right) \quad (\text{Slope of freesurface}) \quad \text{E.30} \\
 &- g \frac{\Delta\rho}{\rho} \frac{dD}{dx} \delta \int_{\xi^+}^{(\bar{\nabla}-D)/\delta} \rho^*(\xi^+) d\xi^+ \quad (\text{Slope of interface}) \\
 (\text{Diffusion of I.F.}) &- g \frac{\Delta\rho}{\rho} \frac{d\delta}{dx} \delta \left[\int_{\xi^+}^{(\bar{\nabla}-D)/\delta} \rho^*(\xi^+) d\xi^+ d\xi^+ + \int_{\xi^+}^{(\bar{\nabla}-D)/\delta} \xi^+ \rho^*(\xi^+) d\xi^+ \right] \\
 (\text{Side wall shear}) &- \frac{\bar{U}^2(x)}{8W} \delta_u \int_{\xi^*}^{(\bar{\nabla}-D-\eta)\delta_u} f_0 f^2(\xi^*) d\xi^* \\
 (\text{Advective acceleration due to nonuniformity of the flow}) &+ \bar{U}^2(x) \left(\frac{dD}{dx} + \frac{d\eta}{dx} - \frac{d\bar{\nabla}}{dx} \right) (1 - f(\xi^*)) \\
 &+ \bar{U} \frac{d\bar{U}}{dx} \delta_u \left[f(\xi^*) \int_{\xi^*}^{(\bar{\nabla}-D-\eta)\delta_u} f(\xi^*) d\xi^* - 2 \int_{\xi^*}^{(\bar{\nabla}-D-\eta)\delta_u} f^2(\xi^*) d\xi^* \right] \\
 (\text{Advective acceleration due to growth of the boundary layer}) &+ \bar{U}^2(x) \frac{d\delta_u}{dx} \left[f(\xi^*) \int_{\xi^*}^{(\bar{\nabla}-D-\eta)/\delta_u} f(\xi^*) d\xi^* - \int_{\xi^*}^{(\bar{\nabla}-D-\eta)/\delta_u} f^2(\xi^*) d\xi^* \right. \\
 &\quad \left. + \frac{(\bar{\nabla}-D-\eta)}{\delta_u} (1 - f(\xi^*)) \right].
 \end{aligned}$$

Given the velocity and density profile at a fixed value of X , equation E.30 becomes a linear equation in seven parameters.

The seven parameters are:

$\frac{d\bar{v}}{dx}$ the slope of the freesurface,

$\frac{dD}{dx}$ the slope of the interface,

$\frac{dU}{dx}$ the horizontal gradient of the mean velocity in the uniform portion of the velocity profile,

$\frac{d\delta_u}{dx}$ the spacial rate of growth of the velocity boundary layer,

f_o the side wall friction factor,

$\frac{d\eta}{dx}$ the spacial rate of growth of the separation distance between the density and velocity interfaces,

$\frac{d\delta}{dx}$ the spacial rate of growth of the density transition region due to diffusion.

The values of the parameters are determined as follows:

f_o was set equal to .02 (the value for hydraulically smooth walls). Several values ranging from .01 to .035 were tried and the effect on the shear stress profile was always minor.

$\frac{d\delta}{dx}$ was determined from experimental data to be about 2.5×10^{-4} (see the section in this chapter on the density structure). Again, several values ranging from 0 to 10^{-3} were tried with little effect on the shear stress profile.

$\frac{d\bar{v}}{dx}$ and $\frac{dD}{dx}$ The data, as well as visual observation, indicates that the velocity drops to a very small value or zero at a point 1 to 3 centimeters below the interface. Since there is no motion below this point, the equations of motion reduce to a balance between the hydrostatic pressure gradients imposed by the freesurface set-down and the interfacial set-up. $d\bar{v}/dx$ and dD/dx were determined by requiring the shear stress to be zero in the region of no motion.

$\frac{dU}{dx}$, $\frac{d\eta}{dx}$, $\frac{d\delta_u}{dx}$ These parameters were determined by either fitting the shear stress to the experimental data using a least square error technique or by fixing one or more of the three parameters and solving for the remaining parameters by the least square approach.

The results of this analysis are shown in Figure 33.

BIBLIOGRAPHY

- Benjamin, T.B. (1963), "The Threefold Classification of Unstable Disburbances in Flexible Surfaces Bounding Inviscid Flows," Journal of Fluid Mechanics, Vol. 16, pp. 436-450.
- Browand, F.K. and Wang, Y.H. (1972), "An Experiment on the Growth of Small Disturbances at the Interface Between Two Streams of Different Densities and Velocities," International Symposium on Stratified Flows, Novosibirsk.
- Browand, F.K. and Winant, C.D. (1973), "Laboratory Observations of Shear-Layer Instability in a Stratified Fluid," Boundary-Layer Meteorology, Vol. 5, p. 67.
- Brown, G.L. and Roshko, A. (1974), "On Density Effects and Large Structure in Turbulent Mixing Layers," Journal of Fluid Mechanics, Vol. 64, Part 4, pp. 775-816.
- Browning, K.A. (1971), "Structure of the Atmosphere in the Vicinity of Large-Amplitude Kelvin-Helmholtz Billows," Quart. J. Roy. Meteorol. Soc., Vol. 97, pp. 283-299.
- Browning, K.A. and Watkins, C.D. (1970), "Observations of Clear Air Turbulence by High Power Radar," Nature, Vol. 227, pp. 260-263.
- Crapper, P.F. and Linden, P.F. (1974), "The Structure of Turbulent Density Interfaces," Journal of Fluid Mechanics, Vol. 65, Part 1, pp. 45-63.
- Cromwell, T. (1960), "Pycnoclines Created by Mixing in an Aquarium Tank," Journal of Marine Research, Vol. 18, pp. 73-82.
- Csanady, G.T. (1978), "Turbulent Interface Layers," Journal of Geophysical Research, Vol. 83, No. C5, p. 2329.
- Delisi, D.P. and Corcos, G. (1973), "A Study of Internal Waves in a Wind Tunnel," Boundary-Layer Meteorology, Vol. 5, pp. 121-137.
- Drazin, P. and Howard, L. (1966), "Hydrodynamic Stability of Parallel Flow of Inviscid Fluid," Adv. App. Math., Vol. 9, pp. 1-89.
- Ellison, T.H. and Turner, J.S. (1959), "Turbulent Entrainment in Stratified Flows," Journal of Fluid Mechanics, Vol. 6, p. 423.

- Emmanuel, C.B. (1973), "Richardson Number Profiles Through Shear Instability Wave Regions Observed in the Lower Planetary Boundary Layer," Boundary-Layer Meteorology, Vol. 5, pp. 19-27.
- Gage, K.S. (1973), "Linear Viscous Stability Theory for Stably Stratified Shear Flow: A Review," Boundary-Layer Meteorology, Vol. 5, pp. 3-17.
- Goldstein, S. (1931), "On the Stability of Superposed Streams of Fluid of Different Densities," Proc. Roy. Soc. A, 132, pp. 524-548.
- Hazel, P. (1972), "Numerical Studies of the Stability of Inviscid Stratified Flows," Journal of Fluid Mechanics, Vol. 51, pp. 39-61.
- Helmholtz, H. (1868), "Ueber Discontinuirliche Flussigkeitsbewegungen," Berl. Monatsber.
- Holmboe, J. (1962), "On the Behavior of Symmetric Waves in Stratified Shear Layers," Geofys. Publ., 24, p. 78.
- Hopfinger, E.J. and Toly, J.A. (1976), "Spatially Decaying Turbulence and Its Relation to Mixing Across Density Interfaces," Journal of Fluid Mechanics, Vol. 78, Part 1, pp. 155-178.
- Jeffreys, H. (1926), "Formation of Water Waves by Wind," Proc. Roy. Soc., A, 110, p. 241.
- Kantha, Lakshmi H. (1975), "Turbulent Entrainment at the Density Interface of a Two-Layer Stably Stratified Fluid System," Johns Hopkins University, Department of Earth and Planetary Science, Technical Report 75-1.
- Kato, H. and Phillips, O.M. (1969), "On the Penetration of a Turbulent Layer into a Stratified Fluid," Journal of Fluid Mechanics, Vol. 37, pp. 643-656.
- Kelvin, W. (1871), "The Influence of Wind on Waves in Water Supposed Frictionless," Phil. Mag., (4) 42, pp. 368-374.
- Keulegan, G.H. (1944), "Laminar Flow at the Interface of Two Liquids," J. Res. Nat. Bureau of Stand., Vol. 32, pp. 303-327.
- Keulegan, G.H. (1949), "Interfacial Instability and Mixing in Stratified Flows," J. of Res. of the Nat. Bureau of Stand., Vol. 43, pp. 487-500.
- Koop, C.G. (1976), "Instability and Turbulence in a Stratified Shear Layer," Ph.D. Thesis, University of Southern California.
- Linden, P.F. (1975), "The Deepening of a Mixed Layer in a Stratified Fluid," Journal of Fluid Mechanics, Vol. 71, pp. 385-405.

- Lock, R.C. (1951), "The Velocity Distribution in the Laminar Boundary Layer Between Parallel Streams," Quart. J. Mech. and Applied Math., Vol. 4, pp. 42-63.
- Lofquist, K. (1960), "Flow and Stress Near an Interface Between Stratified Liquids," Physics of Fluids, Vol. 3, p. 158.
- Long, R.R. (1975), "The Influence of Shear on Mixing Across Density Interfaces," Journal of Fluid Mechanics, Vol. 70, Part 2, pp. 305-320.
- Maslowe, S.A. and Thompson, J.M. (1971), "Stability of a Stratified Free Shear Layer," Physics of Fluids, Vol. 14, p. 453.
- Miles, J.W. (1961), "On the Stability of Heterogeneous Shear Flows," Journal of Fluid Mechanics, Vol. 10, pp. 496-508.
- Miles, J.W. (1963), "On the Stability of Heterogeneous Shear Flows, Part 2," Journal of Fluid Mechanics, Vol. 16, pp. 209-227.
- Moore, J.M. and Long, R.R. (1971), "An Experimental Investigation of Turbulent Stratified Shearing Flow," Journal of Fluid Mechanics, Vol. 49, Part 4, pp. 635-655.
- Osborne, T. and Cox, C. (1972), "Oceanic Fine Structure," Geophys. Fluid Dynamics, Vol. 3, p. 321.
- Phillips, O.M. (1969), The Dynamics of the Upper Ocean, Cambridge University Press, New York, N.Y.
- Roshko, A. (1976), "Structure of Turbulent Shear Flows: A New Look," AIAA Journal, Vol. 14, No. 10, pp. 1349-1357.
- Rouse, H. and Dodu, J. (1955), "Turbulent Diffusion Across a Density Discontinuity," Houille Blanche, Vol. 10, p. 530.
- Scotti, R.S. and Corcos, G.M. (1969), "Measurements on the Growth of Small Disturbances in a Stratified Shear Layer," Radio Science, Vol. 4, pp. 1309-1313.
- Sheppard, D.M. and Doddington, J.W. (1977), "Laboratory Instrument for Measuring Electrical Conductivity in Stratified NaCl Solutions," Rev. Sci. Instrum., Vol. 48, No. 3.
- Sheppard, D.M., Shemdin, O.H. and Wang, Y.H. (1973), "A Multipurpose Internal Wave Facility," Coastal and Oceanographic Engineering Laboratory, UF/COEL/TR-019.
- Taylor, G.I. (1931), "Effect of Variation of Density on the Stability of Superposed Streams of Fluid," Proc. Roy. Soc., A, 132, pp. 499-523.

- Thorpe, S.A. (1968), "A Method of Producing a Shear Flow in a Stratified Fluid," Journal of Fluid Mechanics, Vol. 32, pp. 693-704.
- Thorpe, S.A. (1969), "Experiments on the Instability of Stratified Shear Flows: Immiscible Fluids," Journal of Fluid Mechanics, Vol. 39, pp. 25-48.
- Thorpe, S.A. (1973), "Experiments on Instability and Turbulence in a Stratified Shear Flow," Journal of Fluid Mechanics, Vol. 61, p. 731.
- Turner, J.S. (1968), "The Influence of Molecular Diffusivity on Turbulent Entrainment Across a Density Interface," Journal of Fluid Mechanics, Vol. 33, p. 639.
- Turner, J.S. (1973), Buoyancy Effects in Fluids, Cambridge University Press, New York, N.Y.
- Wang, Yu-Hwa (1975), "An Experimental Study of the Instability of a Stably Stratified Free Shear Layer," Journal of Fluid Mechanics, Vol. 71, Part 3, pp. 563-575.
- Woods, J.D. (1968), "Wave-Induced Instability in the Summer Thermocline," Journal of Fluid Mechanics, Vol. 32, pp. 791-800.
- Woods, J.D. and Wiley, R.L. (1972), "Billow Turbulence and Ocean Microstructure," Deep-Sea Res., Vol. 19, p. 87.
- Yih, Chia-Shun (1965), Dynamics of Nonhomogeneous Fluids, The Macmillan Company, New York, N.Y.

BIOGRAPHICAL SKETCH

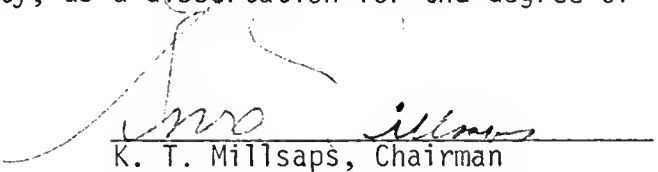
Gregory M. Powell was born November 1, 1949, in Milwaukee, Wisconsin. While he was still an infant, his parents moved to Miami, Florida, where he spent his youth through high school. It was during this time, living near the ocean and through the "space race," that he developed an interest in both aerospace engineering and marine sciences. In June 1968, he was graduated from North Miami Senior High School and in September of the same year entered the University of Florida.

The four and one-half years he spent as an undergraduate were eventful ones: Vietnam, the draft, Kent State, the Woodstock Music Festival, the Richard Nixon/George McGovern presidential election and the end of the "space race." In December 1972, he received a Bachelor of Science degree in aerospace engineering from the University of Florida. The following year he entered graduate school at the University of Florida in the Department of Coastal and Oceanographic Engineering.

On September 15, 1973, he married Carol Brady. In March 1975, he received a Master of Engineering degree in coastal and oceanographic engineering. On June 3, 1978, his mother died.

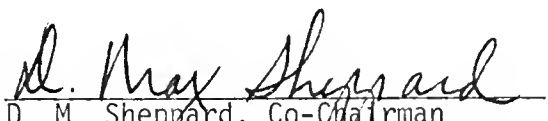
After graduation he continued work toward the Doctor of Philosophy degree through the Department of Engineering Sciences. He has worked as a graduate assistant while earning both the Master of Engineering and the Doctor of Philosophy degrees. He has also worked part-time since September 1977 for Environmental Science and Engineering, Inc.

I certify that I have read this study and that in my opinion it conforms to acceptable standards of scholarly presentation and is fully adequate, in scope and quality, as a dissertation for the degree of Doctor of Philosophy.



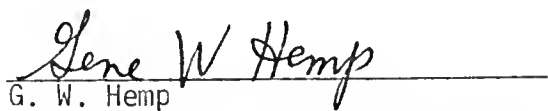
K. T. Millsaps, Chairman
Professor and Chairman of
Engineering Sciences

I certify that I have read this study and that in my opinion it conforms to acceptable standards of scholarly presentation and is fully adequate, in scope and quality, as a dissertation for the degree of Doctor of Philosophy.




D. M. Sheppard, Co-Chairman
Associate Professor and Acting
Chairman of Coastal and
Oceanographic Engineering

I certify that I have read this study and that in my opinion it conforms to acceptable standards of scholarly presentation and is fully adequate, in scope and quality, as a dissertation for the degree of Doctor of Philosophy.

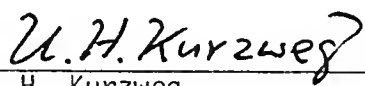


G. W. Hemp
Professor of Engineering Sciences
and Associate Vice President of
Academic Affairs

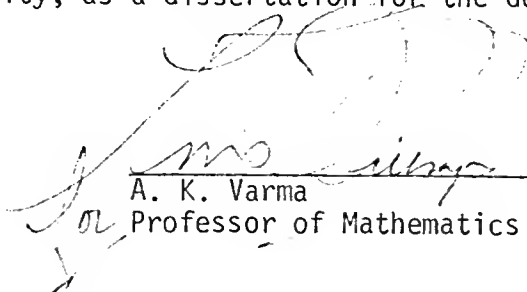
I certify that I have read this study and that in my opinion it conforms to acceptable standards of scholarly presentation and is fully adequate, in scope and quality, as a dissertation for the degree of Doctor of Philosophy.


C. C. Hsu, Associate Professor
of Engineering Sciences

I certify that I have read this study and that in my opinion it conforms to acceptable standards of scholarly presentation and is fully adequate, in scope and quality, as a dissertation for the degree of Doctor of Philosophy.

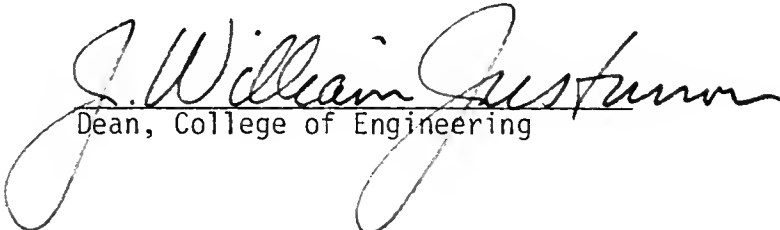

U. H. Kurzweg
Professor of Engineering
Sciences

I certify that I have read this study and that in my opinion it conforms to acceptable standards of scholarly presentation and is fully adequate, in scope and quality, as a dissertation for the degree of Doctor of Philosophy.


A. K. Varma
Professor of Mathematics

This dissertation was submitted to the Graduate Faculty of the College of Engineering and to the Graduate Council, and was accepted as partial fulfillment of the requirements for the degree of Doctor of Philosophy.

June, 1979


Dean, College of Engineering

Dean, Graduate School

